THÈSE

Pour obtenir le grade de

DOCTEUR DE L'UNIVERSITÉ GRENOBLE ALPES

École doctorale : PHYS - Physique
Spécialité : Physique des matériaux
Unité de recherche : Institut LAUE LANGEVIN

Détermination de la structure nucléaire et magnétique de couches minces épitaxiées d'oxyde de manganèse: étude par diffraction de rayons X et de neutrons

Determination of the nuclear and magnetic structure of manganese oxide epitaxial thin films: an X-ray and neutron diffraction study

Présentée par :

Himanshu HIMANSHU

Direction de thèse :

Charles SIMON DIRECTEUR DE RECHERCHE, Université Grenoble Alpes	Directeur de thèse
Elisa REBOLINI Scientifique à l'ILL, Institut Laue Langevin	Co-encadrante de thèse

Rapporteurs :

Nathalie VIART
PROFESSEURE DES UNIVERSITES, Université de Strasbourg
Stéphane PAILHéS
DIRECTEUR DE RECHERCHE, CNRS Délégation Rhöne Auvergne

Thèse soutenue publiquement le **29 novembre 2023**, devant le jury composé de :

Nathalie VIART PROFESSEURE DES UNIVERSITES, Université de Strasbourg	Rapporteure
Stéphane PAILHéS DIRECTEUR DE RECHERCHE, CNRS Délégation Rhöne Auvergne	Rapporteur
Pascal MANUEL SENIOR SCIENTIST, ISIS Facility	Examinateur
Thierry KLEIN PROFESSEUR DES UNIVERSITES, Université Grenoble-Alpes	Président

Acknowledgments

I would like to express my heartfelt gratitude to all those who have been involved in the completion of my PhD thesis. This academic journey has been a challenging yet rewarding experience, and I could not have reached here without the support and encouragement of numerous individuals.

First and foremost, I am deeply thankful to my PhD supervisors; Charles Simon and Elisa Rebolini. I would like to acknowledge Charles for trusting me with an opportunity to start an exciting new project. In the beginning of my thesis, he carefully introduced me to the area of magnetic thin films and diffraction, and explained in details the challenges and physics behind this project. He has given me the space to do things independently and at the same time, also made sure that the work was maintained timely on track. Whenever in doubt, his knowledge and experience in this field has been my go-to solution.

I would like to express my gratitude to Elisa, who kindly accepted to be my PhD supervisor at the beginning of second year. Since then she has been guiding me in every aspect of this journey not only as a supervisor but as a mentor too. Her systematic way of guidance was crucial in shaping my work and in my training as a researcher. She always managed to take out time for discussions on a regular basis. Her invaluable insights throughout the last two years have helped me greatly in completing this project.

I would like to extend my thanks to Ketty Beauvois who was my supervisor during the first year of PhD. She helped me in understanding the science behind neutron diffraction and getting familiar with the D10 instrument at ILL. I am grateful for her support in helping me settle in during my initial days. I am thankful for her dedication to our various beamtimes at ILL.

Special thanks goes to the members of our team whose expertise in respective areas have made this work better: Bachir Ouladdiaf for his support and insights in our experiments on D10, Marie-Bernadette Lepetit for her work on DFT calculations and constant support during the analysis. I would also like to appreciate Stéphane Grenier for his commitment to the XRD studies and making extra effort in coordinating the measurements on SmartLab.

This thesis would not have been possible at all without the help of Bernard Mercey, who supplied all the samples. He has provided us excellent quality samples and was available to help in anyway possible. I would also like to appreciate the work done by Late Bernadette Domenges on these samples, which was very useful for this thesis.

I would like to appreciate the support of ILL people from the Diffraction group,

and the human resources staff for quick resolution of the everyday life matters.

I would like to thank my family and friends in India, whose belief and support has sustained me through the challenges. Their love provided the emotional strength and encouragement to always give my best.

I am blessed to have Ritwika as my constant support. With her, I understand life a bit better.

Last but not the least, I am grateful to have shared these three years with many good friends at ILL and in Grenoble. It was lovely to have lunch and coffee breaks with people from all over the world at ILL. Be it sports or just hanging out on a weekend, I shared some very memorable moments with them. Special mention to my cricket group in Grenoble, who made my Saturday mornings even more enjoyable.

Each person mentioned here has played a significant role in making this achievement possible. I am deeply grateful to all of you for being a part of this journey.

Abstract

The search of new materials for magnetic thin films in spin-based devices, has been the focus of research for more than a decade. In particular, epitaxial $La_{1-x}Sr_xMnO_3$ (LSMO) films, known for their intriguing properties like magnetoresistance and half-metallicity, hold promise for spintronic applications. This thesis aims to unravel the nuclear and magnetic structure of LSMO epitaxial films and super-lattices, employing single crystal X-ray and neutron diffraction, complemented by SQUID magnetometry.

On one sample, a 40.9 nm LSMO film on Si substrate with a $SrTiO_3$ (STO) buffer layer, we showcase a successful single crystal diffraction study. X-ray measurements, which required innovative measurement and structural refinement routes, revealed I *4/m* nuclear space group. Thanks to the D10+ instrument at Institute Laue-Langevin, the magnetic ordering in the sample was resolved by measuring magnetic diffraction Bragg peaks. Combination of neutron diffraction and SQUID measurements disclosed a predominantly in-plane ferromagnetic alignment with slight out-of-plane component, indicating incomplete strain relaxation at this thickness.

We also explored the impact of strain on the magnetic properties using super-lattice samples comprising LSMO and $BaTiO_3$ (BTO) layers deposited on STO substrate. In particular, the $(LSMO)_3/(BTO)_3$ structure is known for showing magnetism above 600 K. We conducted neutron diffraction measurements on this sample at D10 and analyzed the nuclear structure with the help of DFT calculations, revealing the arrangements of layers in the system. X-ray diffraction peaks confirmed that the strain is maintained throughout the film due to intercalation of BTO layers. SQUID measurements displayed signs of possible spin-flop transition along [100] and antiferromagnetic behavior.

The effect of change in number of layers (LSMO or BTO) was studied using $(LSMO)_3/(BTO)_2$ and $(LSMO)_2/(BTO)_3$ samples. SQUID results showed that all the super-lattice samples are antiferromagnetic in nature with slight differences in spin alignment. Notably in $(LSMO)_3/(BTO)_2$, the LSMO layers are expected to be coupled magnetically through the BTO layers. Structural analysis suggested low layer-width modulation in 3-2 and 2-3 as compared to 3-3 via weak satellite peaks.

In summary, through this thesis, we have established that the prevention of strain relaxation on LSMO films via super-lattice structures leads to change in magnetic ordering from FM to AFM. This way, by precisely controlling the strain implementation via substrate, we can create artificial structures for desired technological applications. In addition, this thesis provides a foundational study to decipher nuclear and magnetic structures in epitaxial thin films using single crystal diffraction methods.

Résumé

La recherche de nouveaux films minces magnétiques constitue un domaine prometteur. En particulier les films épitaxiés de $La_{1-x}Sr_xMnO_3$ (LSMO), connus pour leurs propriétés remarquables comme la magnétorésistance et la demi-métallicité, semblent prometteurs pour des applications en spintronique. Cette thèse vise à déterminer la structure nucléaire et magnétique des films épitaxiés de LSMO ainsi que des superréseaux à base de LSMO, en utilisant la diffraction des rayons X et des neutrons, complétée par de la magnétométrie.

Sur un film de LSMO de 40,9 nm déposé sur un substrat de silicium avec une couche tampon de $SrTiO_3$ (STO), nous présentons une étude de diffraction de type monocristal. Les mesures aux rayons X, qui ont nécessité des méthodes de mesure et d'affinement de structure innovantes, ont révélé un groupe d'espace nucléaire I *4/m*. Grâce à l'instrument D10+ de l'Institut Laue-Langevin, l'ordre magnétique a été déterminé par la mesure de l'intensité des pics de Bragg correspondant à la structure magnétique. La combinaison de la diffraction des neutrons et des mesures d'aimantation au magnétomètre à SQUID a révélé un alignement ferromagnétique principalement dans le plan, avec un léger angle vers l'extérieur, preuve de l'existence pour cette épaisseur des films d'une relaxation incomplète de la déformation du réseau.

Nous avons également exploré l'impact de cette déformation sur les propriétés magnétiques en utilisant des échantillons de superréseau composés de couches de LSMO et de $BaTiO_3$ (BTO) déposées sur un substrat STO. En particulier, la structure $(LSMO)_3/(BTO)_3$ est connue pour son magnétisme au-dessus de 600 K. Nous avons effectué des mesures de diffraction neutronique sur cet échantillon sur D10 et analysé la structure nucléaire à l'aide de calculs DFT, révélant les arrangements spatiaux des différentes couches. Les pics de diffraction rayons X ont confirmé que la déformation est maintenue tout au long du film en raison de l'intercalation des couches de BTO. Les mesures SQUID ont montré les signes d'une possible transition de spin-flop le long de [100] et d'un comportement antiferromagnétique.

L'effet du changement du nombre de couches (LSMO ou BTO) a été étudié en utilisant des échantillons $(LSMO)_3/(BTO)_2$ et $(LSMO)_2/(BTO)_3$. Les résultats d'aimantation ont montré que tous les superréseaux sont de nature antiferromagnétique, avec de légères différences dans l'alignement des spins. En particulier, dans l'échantillon $(LSMO)_3/(BTO)_2$, les couches de LSMO sont couplées magnétiquement à travers les couches de BTO. L'analyse structurelle suggère une faible modulation de la largeur de couche en 3-2 et 2-3 par rapport à 3-3 via de faibles pics satellites.

En résumé, cette thèse nous a permis d'établir que le passage de films épais de LSMO vers des super-réseaux conduit à un changement de l'ordre magnétique de FM à AFM. Ainsi, en contrôlant précisément la mise en œuvre de la déformation de la maille cristalline via le substrat, nous pouvons créer de nouvelles structures artificielles pour les applications technologiques souhaitées. En outre, cette thèse fournit une étude fondamentale qui pourra servir à déterminer les structures nucléaires et magnétiques dans les structures épitaxiales en utilisant des méthodes de diffraction monocristalline.

Acronyms

AFM Anti-ferromagnetic

DE Double exchange

DFT Density functional theory

DM Diamagnetic

FM Ferromagnetic

FP FullProf

IP In-Plane

LSMO $La_{0.67}Sr_{0.33}MnO_3$

MBE Molecular Beam Epitaxy

ND Neutron Diffraction

OOP Out-Of-Plane

PLD Pulsed Laser Depostion

PM Paramagnetic

RHEED Reflection High Energy Electron Diffraction

RT room temperature

SQUID Superconducting Quantum Interference Device

STO $SrTiO_3$

T_c Curie temperature

T_M Magnetic transition temperature

TEM Transmission Electron Microscopy

U-mat U-matrix

UB-matrix Orientation matrix

XRD X-Ray Diffraction

Contents

Chapter 1

Introduction

Materials have been at the center of most technological innovations that have been accomplished so far. From all the mundane little things in our daily lives such as a humble milk bottle, to the pinnacle of creation as an unmanned rover roaming on Mars, material research and development constitute the foundational basis. It is the relentless pursuit of understanding, manipulating, and engineering the properties of materials, that has led to countless advancements and propels our technological progress. The materials at play have been meticulously designed, tested, and refined to meet the demands of their respective applications whether it's the durability of a smartphone screen or the performance of a cricket bat and ball.

In this quest, researchers have explored diverse avenues, from fundamental studies of material properties to the synthesis of novel compounds with remarkable characteristics. One such field of research is *Spintronics*. In the present "digital age", there is an ever increasing demand of better and faster computing and electronic devices, and spintronics is at the core of this discipline. Spintronics harnesses the intrinsic magnetic properties and charge of the electrons (hence the name 'spin+electronics') to create devices such as spin transistors, spin logic gates and magnetic storage of information. To keep up with the demands and maintain technological progress, it is imperative not only to understand the physical behavior of magnetic materials used in these devices, but also to design artificial ones tailored to specific applications. Spintronics devices are typically based on materials in the form of thin layers or films deposited on a base material called substrate. Naturally, magnetic thin films have been a subject of rising importance and interest among researchers.

In addition, to ensure efficiency and practicality, specific material properties are requisite for spintronic applications. There are qualities necessary for the material integration into devices such as thermal stability, non-volatility and compatibility with semiconductor fabrication processes. On top of this, spin dependent transport studies are used to quantify a material performance. Specifically, if we take the example of magnetic storage devices, they store bits of information via magnetic spins on small regions of the film. Essentially, for devices to operate in everyday applications, one of the most critical requirement is to have films that show magnetism at room temperature (RT). In other words, the transition temperature signifying the

loss of magnetic ordering in the system should be significantly higher than RT. In addition, materials that show a preferred direction of magnetic moment alignment (anisotropy) are also the area of focus. They are found to be more reliable in terms of data storage and retention.

Recently, materials with anti-parallel alignment of moments, known as antiferromagnets, have come up as the materials for the next generation of spintronic devices [1, 2]. This is because they possess numerous features such as no stray fields, robustness against perturbation and ultrafast dynamics [3, 4]. The frequency of spin dynamics in antiferromagnets is of the order of THz, considerably faster compared to parallelly aligned moments in ferromagnets (GHz) [5].

Thin films are famous for exhibiting a set of properties different from their bulk counterparts. As the thickness of bulk materials is reduced to below μm, surface and interface (substrate-film) effects come into play, that lead to emergence of new and exciting physical properties in thin films (more on this at the beginning of the next chapter). In the thin films for spintronics, the prime importance is given to magnetic properties, which are a major factor in governing their performance in different spin-based devices. In general, the origin of new physical properties is found in atomic structure of the crystalline systems. This is why, structure-property relations are so important to study and it has been one of the main objectives for investigating magnetic thin films to understand the reasoning behind their exciting properties.

There are several techniques that are commonly used to study the behavior of magnetic thin films such as reflectivity, magnetometry, microscopy, magnetic resonance and magneto-optical kerr effect to name a few. All these techniques can record different physical properties of magnetic thin films and give insights into the possible origin(s) of them. Reflectivity can provide information on the film thickness and interface roughness [6, 7]. Magnetometry provides only the macroscopic knowledge of the sample magnetic behavior [8, 9]. Ferromagnetic resonance is used to study dynamic properties in the films [10]. Magneto-optical Kerr effect measures polarization of reflected light under magnetic field [11]. This technique can give insights into magnetic anisotropy and domains in the system. However, none of these techniques are suitable enough to obtain detailed information on the crystal and magnetic structure of the film. This is where diffraction comes into the picture. Single crystal X-ray and neutron diffraction are well-developed ways to resolve nuclear and magnetic structure of crystalline materials. For decades, researchers have been utilizing these techniques to study and investigate crystallography of bulk compounds in different areas of research [12–15]. Building on this, one of the goals in this thesis is to make use of diffraction methods to solve nuclear and magnetic structure of epitaxial thin films for spintronic applications, in the hope of understanding their structure-property relations better.

We have chosen manganese oxides for this study focusing on epitaxial thin film structures made of $La_{2/3}Sr_{1/3}MnO_3$ (LSMO) perovskite compounds. These films show a plethora of interesting properties and are considered as potential candidates for the spintronic devices. These properties include dramatic changes in electric resistance under magnetic field-Giant MagentoResistance (GMR) and Colossal MagnetoResis-

tance (CMR), magnetically anisotropic behavior and electric conductance for only one direction of spins [16–19]. Furthermore, these properties can be manipulated using several factors such as epitaxial strain, level of Sr doping etc. [20, 21]. Overall, such exciting materials have complex magnetic phase diagrams and need to be well understood for their successful and efficient integration into devices.

What makes this study challenging is that X-ray and ND techniques are not well-established to study thin films via single crystal diffraction. These films, often nanoscale in thickness, require precise growth on substrates and specialized instrumentation for accurate measurements. The quality of sample, i.e. degree of crystallinity is the first and foremost requirement to successfully perform single crystal diffraction on epitaxial films. Factors such as strain effects, substrate influences (absorption and diffraction peaks), and potential stacking faults, add layers of complexity to data interpretation. Moreover, the small size makes it difficult to obtain sufficient diffraction signal with necessary resolution for precise measurements, especially for Neutron Diffraction (ND). Nevertheless, these challenges are met with determination, as researchers continue to push the boundaries of materials science. D10 (now D10+) at Institute Laue Langevin (ILL) is a diffractometer, which offers the possibility to perform energy analysis with four-circle mode to reduce the background and the intensity of the inelastic peaks coming from the substrate (explained in Chapter 3 in-detail). Consequently, D10 has been increasingly used for thin film studies [22–24]. We have utilized this particular instrument along with X-Ray Diffraction (XRD) SmartLab, CEA-CNRS and SQUID magnetometry, to strengthen our understanding of magnetic epitaxial thin films. A particular focus has been kept on using the strain imposition by the substrate, as a tool to control the magnetic properties of epitaxial films.

As a first step in the study of these thin films, we decided to work on a "simple" LSMO film, before moving to more complex super-lattice structures. Although LSMO films have been thoroughly studied before, the demand for complete crystallographic knowledge of LSMO films is apparent, which is one of the points of focus of this project [16, 25–27].

In addition, when engineered in a super-lattice the magnetic transition temperature of LSMO films is potentially improved for spintronic devices. As the name suggests, super-lattice structures contain epitaxial layers of different materials deposited alternatively. In this thesis, we worked on super-lattices made of LSMO and BTO ($BaTiO_3$) layers with $SrTiO_3$ (STO) as substrate. Please note that a detailed review of literature on each sample is provided in respective chapters. These materials are particularly interesting because they are believed to pave way for control and design of artificial structures with desired magnetic properties [28–31]. The fundamental scientific idea behind these super-lattices is to control the orbital occupation in Mn ions, which in turn, results in control over the magnetic properties. This control can be achieved via strains induced by the substrate. On top of this, it can also lead to the emergence of new phases that do not exist otherwise in these compounds.

The 3-3 structure of this family, contains a unit cell made of 3 layers of LSMO and 3 of BTO repeated along the surface normal direction. On this sample, it is

experimentally verified that the magnetic transition temperature is above 600 K, a quality dearly desired for spin-based memory devices [28]. It is hypothesized that the BTO layers help in preventing the strain relaxation imposed by STO and hence, lead to dramatic changes in the physical properties of the material. However, the exact relationship between the crystal structure and the massive increase in magnetic transition temperature is unknown. Moreover, the order of arrangement of moments also remain to be experimentally determined. Through this thesis, we attempt to provide an explanation for this behavior by determining the nuclear and magnetic structure of such super-lattices. This will also help us in verifying the theory of orbital occupation that can be a significant step in the field of fabrication of artificial magnetic structures. We worked on 3 different super-lattice samples of LSMO/BTO with different distributions of LSMO and BTO in the super-lattice. The thesis is structured into 7 chapters in total (including this one) as follows.

The next 2 chapters are designed to equip the reader with essential information required to comprehend the presented results effectively. In the second chapter, fundamental concepts pertaining to the various techniques employed in the project, are introduced. The third chapter delves into the detailed descriptions of the instruments utilized to implement these techniques.

Following this, the subsequent three chapters will systematically present the results obtained from various samples, each chapter dedicated to a specific sample. The fourth chapter is devoted to the study of LSMO thin film. I present the results of the single crystal diffraction and SQUID experiments performed on this sample. This study has two major goals: First, to gain insights into the crystallographic and magnetic properties of the LSMO films and observe how they differ from the bulk LSMO crystals. Second, to establish a foundational reference for more complex investigations, such as those involving super-lattices rather than thin films, which will be the focus of subsequent chapters.

In Chapter 5, I will provide a comprehensive account of the work carried out on the 3-3 sample. Through diffraction, SQUID, and DFT, we investigate the crystallography of the super-lattice and its magnetic properties as compared to the LSMO film, thereby shedding light on the effect of BTO intercalation.

In a similar way, we studied 2 more samples: 3-2 and 2-3, which are presented in Chapter 6. As the name suggests, these samples comprise 2 layers of either LSMO or BTO instead of 3. The idea behind this work is to examine the effects of modifying the numbers of layers in the 3-3 super-lattice on its magnetic properties.

Finally, in the last chapter, we will discuss the main conclusions and highlight the overall impact of this project.

Chapter 2

Concepts and methods

Contents

What to expect in this chapter

This chapter is assigned to get the reader acquainted with general terms and methods behind the results and analyses presented in this thesis. It starts with a brief introduction to the basics of thin films, with a specific focus on the role of strain in epitaxial thin films. Subsequently, we will go through the underlying concepts of magnetism and different types of magnetic interactions. We will also get familiar with essential macroscopic parameters employed for characterizing magnetic materials. We will explore the diffraction technique as a way to study microscopic nature of single crystals including epitaxial thin films. This part also includes an overview of the relevant concepts integral to conducting diffraction experiments. In the end, a succinct introduction to DFT is presented. All the experimental details and instrument specifications are given in the following chapter.

2.1 Epitaxial thin films and strain

In this section, I will define some thin film specific key concepts such as epitaxy, lattice-mismatch and strain, which are critical to the understanding of this PhD thesis.

2.1.1 Film-substrate interface and epitaxy

Thin films are solid materials with thickness in the range from few nm to μm. These structures are fragile by themselves and need to be supported to prevent their breaking and deforming. This support is provided by a "base" material called *substrate* on which the films are usually deposited.

In addition to providing structural support, substrates also exert a significant influence on the physical properties of the deposited film. The film-substrate interaction at the interface can essentially govern the film behavior [32–36]. In addition, at such low thickness of below μm, surface effects come into play leading to emergence of fascinating physical properties. Moreover, subtle alterations to the lattice, and crystal structure can further modify the film characteristics. Since thin films are very sensitive to these perturbations, they can be used to stabilize phases that do not exist in their bulk counterparts. Due to this versatility of thin films to provide tailored properties, today they are widely used in a variety of devices [37–39].

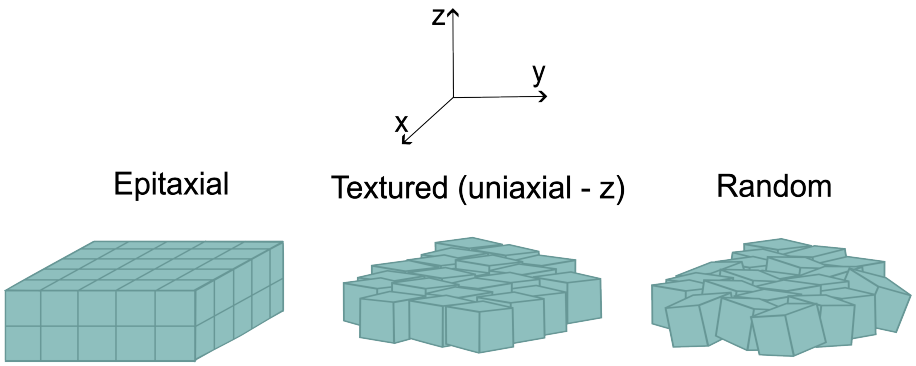

Figure 2.1: Schematic representing different types of film structures: Epitaxial (complete 3D periodicity), uniaxial textured (aligned only along z-axis) and random.

Based on the type of film structure with respect to the substrate, they can be broadly classified into 3 categories; random, textured and epitaxial. As shown in the schematic in Figure 2.1, in random films, the crystal structure of the film does not follow any periodicity in any direction. In the case of textured, the film structure is oriented along only 1 or 2 directions (uniaxial or biaxial textured), while it is randomly arranged along the rest. The epitaxial films, on the other hand, show periodic arrangement of its constituents in 3D space resembling a single crystal structure. The unit which is repeated periodically is called a unit cell and its shape is characterized by 3 lattice vectors $(\vec{a}, \vec{b}, \vec{c})$. In these films, substrate plays a big role on the film structure and hence, properties as well. The quality of epitaxy depends

on the chosen substrate and in an ideal case, the atomic rows of the film and the substrate overlap with complete continuity at the interface. If the two bulk materials (of the film and the substrate) have exactly the same size of unit cell, one is in an ideal case otherwise there is some degree of strain as the film tries to accommodate the difference. To keep the discussion relevant to the thesis, we will only discuss the epitaxial films in what follows.

2.1.2 Lattice mismatch and strain

The misfit between substrate and the bulk nature of film material is quantified by *lattice mismatch* δ, given by:

$$\delta = \frac{a_s - a_b}{a_s} \times 100 \tag{2.1}$$

where, a_s and a_b are in-plane lattice parameters of the substrate and the bulk structure of film material, respectively.

Lattice mismatch factor is of prime importance in determining the chances of obtaining an epitaxial film. Usually, $|\delta| < 2.5\%$ is considered good for epitaxial growth. If δ is very small, the film will be able to follow the substrate structure easily and grow with minimal defects. With increase in δ, there is a "competition" between the bulk and substrate structure, leading to strain in the film. This strain from the substrate imposes the substrate In-Plane (IP) lattice parameters and symmetry onto the film. In reaction to this, the film tries to reduce the strain by either gradually changing the lattice parameters back to bulk value or by forming defects such as edge dislocation and stacking faults. This phenomenon is called strain relaxation and its nature depends on several factors including deposition conditions, temperature and material properties.

In general, the film can be under two types of strain. For $\delta < 0$ ($a_s < a_b$, the IP lattice parameter of the bulk form of film material is greater than the substrate one), the film will be under compressive strain to be able to follow the lattice constraint from the substrate. For the other case with $\delta > 0$ ($a_s > a_b$), the film will be under tensile strain as its lattice will be extended IP compared to the bulk.

Strain engineering is a well-known tool in thin film field, used to significantly alter the electrical, magnetic and mechanical properties of the films for device applications. While there are many ways to impose strain in thin film structures, lattice-mismatch with substrate is one of the most popular methods for epitaxial perovskite films [40–42]. If we take the example of $La_{1-x}Sr_xMnO_3$ epitaxial thin films, a variety of perovskite substrates have been used for these films such as $LaAlO_3$, $NdGaO_3$ etc. Their magnetic and electric properties have been reported to be predominantly varying with the substrate choice [43–46]. The lattice mismatch with substrate leads to different strain induced distortions in the film structure and as a consequence, changes in physical properties are observed. For instance, the magnetic transition temperature in these films decreases with increase in tensile strain, whereas resistivity increases with it [47, 48]. The physical properties of LSMO film are discussed in-detail in Chapter 4, where we present our results obtained on this thin film.

In this thesis, I focused on the magnetic properties of LSMO-based thin films, where the strain is coming either from the substrate only or is maintained throughout the film via some interlayers. To understand the structure-property relations in these thin films, I first need to define the magnetic properties that I will be presenting, which is given in Section 2.2, then the different experimental and theoretical methods, which will be used through this manuscript, are in section 2.3.

2.2 Basics of magnetism

In this section, we will read about the fundamental concepts and properties of magnetic materials. We will start with the source of magnetism at atomic level and progress towards experimentally measurable parameters that allow us to study their behavior.

2.2.1 Microscopic origin of magnetism

Magnetism in materials is a physical phenomenon mainly associated with the motion of unpaired electrons in an atom. The fundamental quantity in magnetism is the intrinsic magnetic moment $\vec{\mu}$. It has two distinct contributions related to orbital and spin momentum of electrons. The nucleus of an atom also possesses a magnetic moment of spin but it is often neglected due to its relatively low value and it won't be considered in what follows. The orbital magnetic moment $\vec{\mu_\ell}$ arises from the movement of an electron around the nucleus, which can be assimilated to a current circuit containing only one electron. For an electron associated with the orbital and magnetic quantum number ℓ and m_ℓ respectively, the moment norm can be expressed as:

$$\mu_\ell = -g_\ell \mu_B m_\ell \tag{2.2}$$

where, g_ℓ is the orbital g-factor ($g_\ell = 1$) and μ_B is the Bohr magneton, a convenient unit for describing the size of atomic magnetic moments. It takes the value $9.27 \times 10^{-24} Am^2$ and is given by $\frac{e\hbar}{2m_e}$ ($\hbar$ is the reduced Planck constant $= 1.05 \times 10^{-34} Js$, m_e the electron rest mass ($9.1 \times 10^{-31} kg$), e the electron charge ($1.6 \times 10^{-19} C$)).

Electrons also have an intrinsic spin angular moment leading to the existence of spin magnetic moment. The norm of the spin magnetic moment $\mu_s = -g_s \mu_B m_s$. In this expression, g_s is the spin g-factor (≈ 2) and m_s is the component of spin angular momentum.

Electrons are fermions, which means that they possess half integral spins. This leads to $m_s = \pm\frac{1}{2}$, commonly referred to as 'up' and 'down' spins, which actually represent the direction of spin angular momentum with respect to reference axis (usually taken as z-axis in quantum mechanics). Thus, for a spin of $+\frac{1}{2}$, the spin magnetic moment will be approximately $-\mu_B$ and vice-versa.

The orbital and spin magnetic moments can also interact together, and this is through the so-called spin-orbit coupling (relativistic effect). Taking spin-orbit coupling as a perturbation, one finds that for an atom in its ground state, the total angular momentum, j, takes values in the range $|\ell - s|$ to $|\ell + s|$ (where, ℓ and s are orbital and spin quantum numbers respectively). The expression for total magnetic moment is:

$$\mu_{tot} = -g_J \mu_B m_j \tag{2.3}$$

here, g_J is the Lande's g-factor of total angular momentum related to g_ℓ and g_s via quantum-mechanical arguments, and m_j the quantum number associated with total angular momentum j. In some cases such as in transition metals, the $3d$ orbitals are prone to interact with the crystal field i.e. electric potential due to charge distribution

on lattice sites. This leads to quenching of orbital momentum and hence, the total magnetic moment consists only of the spin contribution. A detailed discussion on this is provided in the subsequent sections. First, let's take a brief overview of the various categories of magnetic materials.

2.2.2 Types of magnetic materials

Magnetic materials are classified into various categories based on the arrangement of magnetic moments. Here is how one can identify them based on the moment configuration. Macroscopic quantities that can experimentally differentiate between different materials are discussed in Section 2.2.4.

- Diamagnetic (DM) materials are characterized by their tendency to "shield" themselves from external magnetic fields. In these materials, the electrons tend to repel the applied magnetic field by inducing a magnetic moment opposite to the direction of applied field. In a classical framework, this behavior is explained in terms of Lenz's law, which states that the orbital motion of an electron opposes the applied field by inducing current in the opposite direction. All materials show some degree of diamagnetism however in many cases there can be other domnating effects (magnetic interactions) and the diamangetic contribution is negligible. There is no intrinsic magnetic ordering in DM as they don't have any unpaired electrons.

- Paramagnetic (PM) materials have unpaired electrons and exhibit weak attraction to external magnetic fields. In these materials, magnetic field induces a magnetization (magnetic moment per unit volume) in the same direction as the applied field. However, without any applied field, the atomic moments point in random directions leading to zero net moment in the material (black in Figure 2.2). The atomic moments in paramagnets interact very weakly with the neighboring moments and can be considered as independent (weaker than thermal effects). These atomic moments tend to align parallel to the applied field.

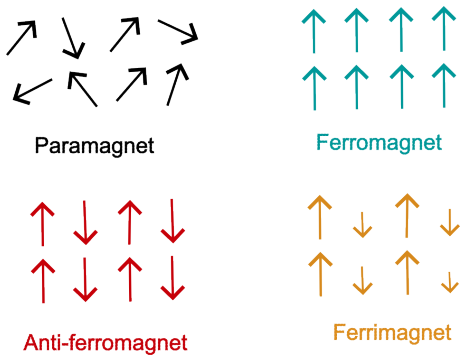

Figure 2.2: Schematic representation of different types of moment configurations in magnetic materials.

- Ferromagnetic (FM) materials are signified by spontaneous parallel alignment of atomic moments, even in the absence of external magnetic field (sea green in Figure 2.2). These materials exhibit strong and permanent magnetization.
- Anti-ferromagnetic (AFM) materials are counterparts of FM. They have moments that spontaneously align anti-parallel to each other, cancelling out the net magnetization to zero ideally (red in Figure 2.2). AFM materials do not exhibit any macroscopic magnetization in the absence of an external field.
- Ferrimagnets are the class of materials with non-zero magnetization with anti-parallel alignment of moments. In these materials, the two moments are not equal in magnitude and have a net magnetization due to partial cancellation (yellow in Figure 2.2).

From the above mentioned categories, FM, AFM and Ferrimagnetic materials have strong interactions among different atomic moments. As a result, they possess long range ordering of moments. One should note that a same system can exist in different magnetic states depending on its temperature. All FM, AFM and ferrimagnets become PM above a given temperature. Now, we will discuss few types of these microscopic magnetic interactions, keeping the scope of the thesis in mind.

2.2.3 Magnetic interactions

In a magnetic material, such as a crystal lattice of atoms or ions, the individual atomic magnetic moments interact through various mechanisms, leading to specific arrangements of these moments. The nature and strength of these interactions plays a crucial role in determining the overall magnetic behavior of the material. Let's review some of them.

Dipolar interaction
Two moments $(\vec{\mu_1}, \vec{\mu_2})$ can have dipolar interactions among them depending on their separation $(\vec{r})$ and alignment. The energy of this interaction is given by:

$$E = \frac{\mu_0}{4\pi r^3}[\vec{\mu_1}.\vec{\mu_2} - \frac{3}{r^2}(\vec{\mu_1}.\vec{r})(\vec{\mu_2}.\vec{r})] \tag{2.4}$$

where, μ_0 is physical constant representing magnetic permeability in free space ($= 4\pi \times 10^{-7} N/A^2$). The order of magnitude of this interaction is usually weak ($< 1\mu eV$, for $\mu = 1\mu_B$ and $r = 1\mathring{A}$) and is considered important only in materials that order at milliKelvin temperatures [49]. Stronger interactions that lead to long-range ordering at higher temperatures are called exchange interactions, which we will discuss next.

Exchange interactions
The behavior of magnetic systems can be represented by the effective Heisenberg Hamiltonian:

$$\mathcal{H} = -\sum_{ij} J_{ij} \mathbf{S}_i.\mathbf{S}_j \tag{2.5}$$

where, J_{ij} is the effective exchange constant between the i^{th} and j^{th} spins and $\mathbf{S}_i$ and $\mathbf{S}_j$ are the spin operators on sites i and j [50]. The sign of J leads to one type of spin alignment (parallel or anti-parallel) being energetically favored. If $J > 0$, the interaction is FM, while it is AFM if $J < 0$. This effective interaction is the result of several physical phenomena, which can compete with one another.

Now, we will discuss two types of exchange interactions.

1. **Direct exchange:** The origin of direct exchange interactions lies in the quantum mechanical behavior of electrons, including their spin, and how their arrangement in atomic orbitals affects the energy of the material [50]. They arise from the antisymmetry requirements of the electronic wave function (Pauli exchange principle). Direct exchange interactions are usually short range and can be considered limited to nearest neighbors only. These interactions cause neighboring atoms or ions to align their magnetic moments parallel to each other leading to stable lower energy state of the system.

2. **Indirect exchange:**
   To describe indirect exchanges, we first need to introduce the phenomenon of crystal field splitting. As the name suggests, it is the splitting (degeneracy breaking) of d orbitals due to their surrounding environment i.e. electronic repulsion from electrons in ligand orbitals (such as oxygen). The effect of repulsion from the local environment depends on the orbital shape. The d orbitals can be divided into 5 types based on their shapes as shown in Figure 2.3. They are classified into two classes; t_{2g} orbitals, which point in-between the x, y and z axes (d_{xy}, d_{yz}, d_{xz}) and e_g orbitals which lie on the axes (d_{z^2} and $\mathrm{d}_{x^2-y^2}$). A common environment in metal oxides is octahedral: a metallic ion in the center of an octahedra with an oxygen on each corner situated on the axes (x, y and z). In such environment, the electron(s) in e_g orbitals are destabilized by the electrostatic repulsion as a result of larger orbital overlap with the p orbitals along the axes as compared to the t_{2g} ones. Therefore, the e_g orbitals are higher in energy than t_{2g}. In the case of tetrahedral environment, the splitting works in opposite sense and the e_g orbitals are lower in energy.

   In $3d$ transition metal ions, crystal field leads to another effect called orbital quenching. The $3d$ orbitals are exposed to crystal field interaction, which is much stronger than spin-orbit interaction. As a result, the system chooses a ground state such that the orbital contribution to moment is zero ($L = 0$). This is known as quenching of orbital moment. For 4f ions on the other hand, the orbitals are shielded by 5s and 5p shells and hence, the crystal field interaction is not as strong.

   Superexchange through the ligand: In ionic solids, the exchange interaction can take place indirectly between non-neighboring magnetic ions mediated by orbital overlap with a non-magnetic ion (ligand) placed in-between (such as oxygen). In the case of transition-metal oxides (such as LSMO), the strength

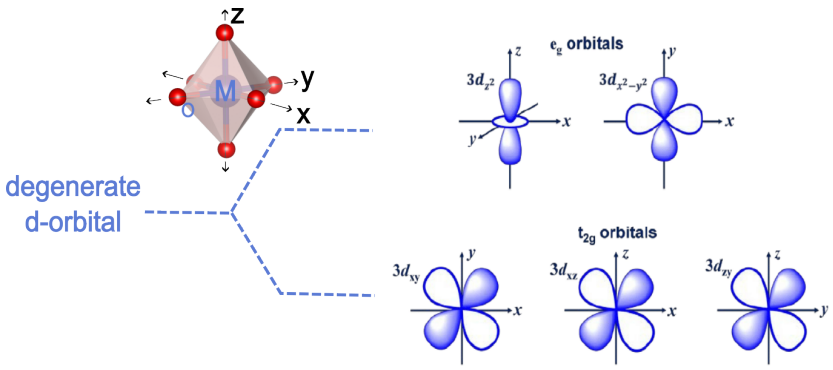

Figure 2.3: Schematic representing the crystal field splitting of d orbitals in octahedral environment [51].

and nature of ordering favored by superexchange is influenced by the occupancy of 3d orbitals and the angle of M-O-M bond (M-metal and oxygen as the intermediate ion) [50]. Goodenough, Kanamori and Anderson found some simple rules to illustrate the mechanism of this complex magnetic interaction (GKA rules) [52–54]. These rules are based on two main principles: (1) two electrons in the same orbital favor antiparallel spins as per the Pauli exclusion principle, and (2) following Hund's rules, the electrons in different orbitals of the same 3d shell favor parallel arrangement of spins. Figure 2.4 shows schematics of different possible scenarios of superexchange interaction in Mn^{3+}-O along the z-direction showing both $3d_{z^2}$ and $3d_{x^2-y^2}$ orbitals. Let's have a deeper look at these situations one-by-one.

- In the first case (Figure 2.4(a)), the Mn-O-Mn bond angle is 180°. The oxygen ion orbital (2p) overlaps with those of the Mn and forms a bond by virtual hopping of electrons. This polarizes the spin in oxygen orbital as shown in the figure. If the electron in the first Mn^{3+} ion is spin up, the oxygen electron bonding with it should be spin down (Pauli exclusion principle). Consequently, the other oxygen electron will be spin up. Since this electron is bonding with second Mn^{3+} ion, the electron there must be spin down. As a result, the magnetic ordering between the two Mn ions with 180° exchange is strong and AFM.
- Second case is the one with one occupied and one empty d_{z^2} orbital. In this case, the exchange is FM as a consequence of Hund's rule and the strenth of this type of interaction is weaker as compared to the first case.
- In another scenario with 2 filled d_{z^2} orbitals with 90° exchange, the nature of ordering is again FM and weak, due to Hund's rule coupling at the oxygen site as shown in the Figure 2.4(c).

In addition to the above described, there can be another type of electron hopping interaction in the mixed valence manganites between Mn^{3+} and Mn^{4+}. This is called double exchange, which is discussed in-detail next.

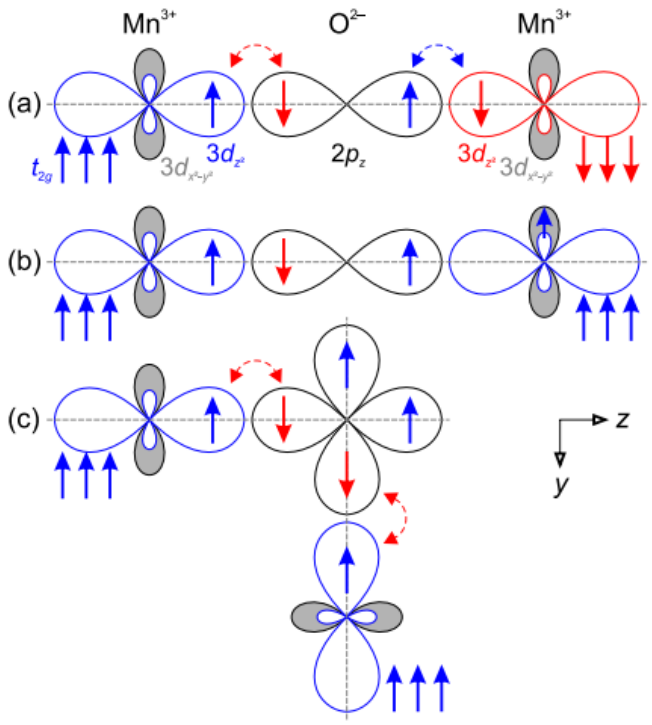

Figure 2.4: Schematic representing the Goodenough-Kanamori-Anderson rules illustrated for magnetic exchange between Mn^{3+}-O along the z-direction. Depending on the orbital overlap and occupancy, the exchange can be FM or AFM (adapted from [55]).

Double exchange

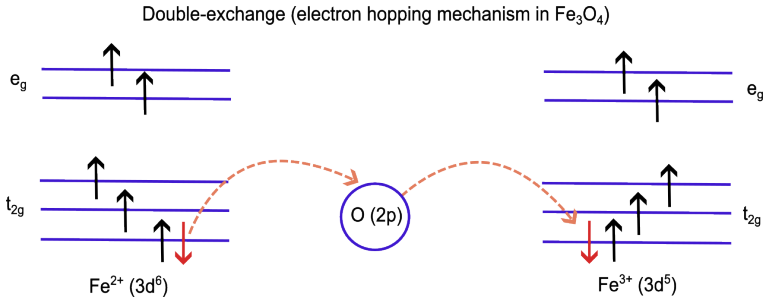

Figure 2.5: Double exchange mechanism between Fe^{2+} and Fe^{3+} in Fe_3O_4 compound. The 6^{th} electron in Fe^{2+} (in red) hops to Fe^{3+} maintaining its spin polarity giving rise to FM ordering in the system.

Double exchange (DE) occurs in oxides in which magnetic ion can show mixed valency. A common example of this is Fe_3O_4 compound. There is an equal mixture of Fe^{2+} ($3d^6$) and Fe^{3+} ($3d^5$) ions on octahedral sites in this compound.

The same number of Fe^{3+} ions sit on tetrahedral sites. The DE interaction takes place between Fe^{2+} and Fe^{3+} ions on the octahedral site. The electronic configuration of these ions is shown in Figure 2.5 with splitting between t_{2g} and e_g orbitals in octahedral environment. The 6^{th} electron in Fe^{2+} follows a hopping mechanism via oxygen to the Fe^{3+} ion as depicted in Figure 2.5. The hopping proceeds without spin-flip following Pauli exclusion principle. This process causes the electron to delocalize, which minimizes its kinetic energy.

Think of particle in a one-dimensional box scenario in quantum mechanics. The energy of this particle is proportional to B^{-2} (box length - B) [49]. Thus, the energy will be lower for a bigger box. In this case, the electron saves kinetic energy by wandering in a bigger "box". Thus, the system aligns ferromagnetically in order to save energy. Moreover, it also becomes conducting with 100% spin polarization.

These are some of the interactions among magnetic ions that govern the nature of moment ordering. Now, we will move on to the macroscopic part of magnetism, which includes different properties of these materials that can be measured experimentally to study their behavior.

2.2.4 Macroscopic magnetic properties

2.2.4.1 Magnetic susceptibility

The behavior of magnetic materials in an external field is usually described by the magnetic Susceptibility (χ_M), that relates a material magnetization, M, to the strength of applied magnetic field, H:

$$\chi_M = \frac{M}{H} \tag{2.6}$$

χ_M is a measure of how responsive a material is to the external magnetic field. Here is how it reflects the nature of a magnetic material.

- DM materials show negative χ_M values as they have a tendency to repel the applied magnetic field. Their contribution to χ_M is so small that it can simply be ignored in many cases and it is temperature independent.

- PM have positive χ_M values meaning that the applied magnetic field induces a magnetization in the same direction as applied field. Paramagnets are also temperature dependent and the variation of their χ_M against temperature is expressed by Curie law:

  $$\chi_M = \frac{C}{T} \tag{2.7}$$

  where, C is the Curie constant. Thus, as the temperature decreases, fluctuations in the moments due to thermal effects become less potent and the net magnetization in the material increases resulting in higher susceptibility at low temperature (see Figure 2.6).

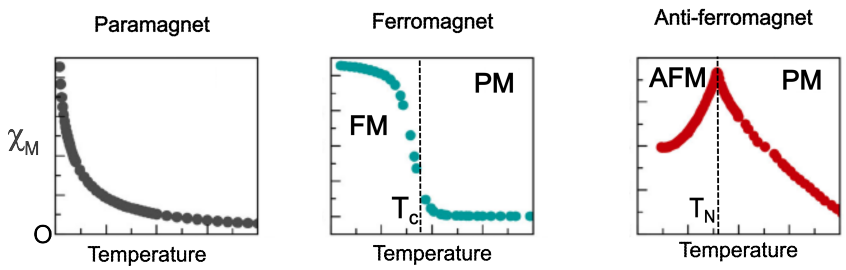

Figure 2.6: Graphical representation of variation of magnetic susceptibility with temperature of PM, FM, and AFM materials (adapted from [56]).

- FM materials' temperature dependence is expressed using an extension of Curie's law; Curie-Weiss law:

$$\chi_M = \frac{C}{T - T_c} \tag{2.8}$$

  where, T_c is the Curie temperature, above which the magnetic arrangement is PM in nature (see Figure 2.6). This equation describes the tendency of a FM material in external field in the PM phase and close to the transition temperature. Below T_c, the material possess spontaneous magnetization and χ_M is relatively higher. A typical χ_M vs temperature curve for a FM is shown in Figure 2.6.

- For AFM, the magnetic transition temperature is called the Néel temperature (T_N) and T_c in equation 2.8 is replaced by θ (intercept of the curve below T_N on x-axis).

It is to be noted that there are certain limitations of the Curie-Weiss law. It only describes the nature of χ_M of these materials in the temperature region of PM phase. Below this temperature, the behavior is more complex due to factors such as domain formation. In addition, Curie–Weiss law fails to describe the susceptibility in the immediate vicinity of the transition temperature, since it is based on a mean-field approximation.

2.2.4.2 Magnetic hysteresis

Magnetic hysteresis loops are graphical representations of the magnetic response of a material to an external field. They are traced out by measuring the magnetization (M) in varying applied field (H). At first, magnetic field is applied along the chosen direction of the sample. The field strength is the gradually reduced to zero while measuring the magnetization at regular intervals. At this point, the direction of the field is reversed and the magnitude is increased to the starting value. This measures magnetization in the opposite direction and provides information on the mechanism of moment rotation in the sample. To complete the loop, this process is repeated backwards i.e. decreasing the field strength to zero in the reversed direction and then

increasing it back to the starting point. Figure 2.7(a) shows an example of hysteresis curve with marked important parameters.

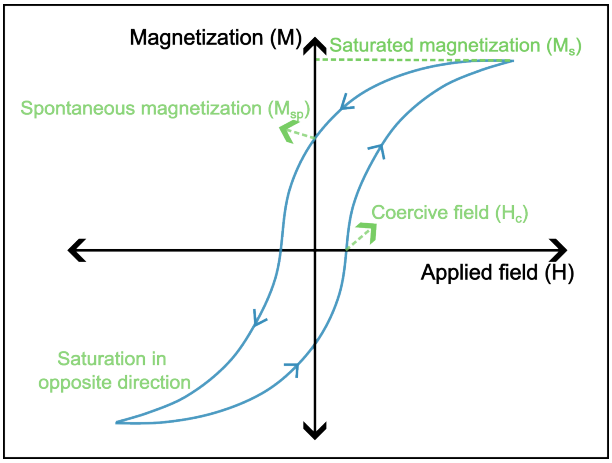

(a)

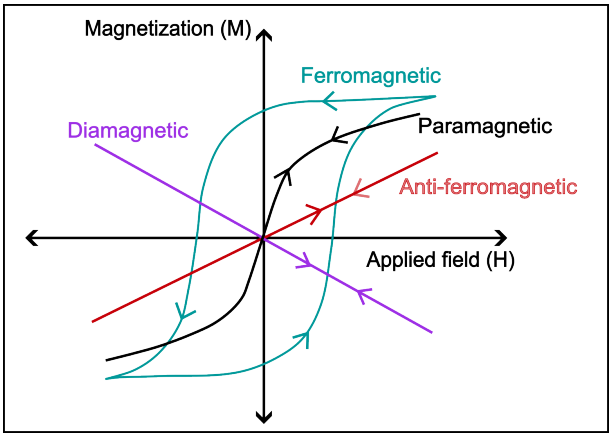

(b)

Figure 2.7: (a) Schematic of a typical magnetic hysteresis loop showing different important parameters. (b) Ideal magnetic hysteresis loops of different types of materials (not drawn to scale).

- Saturated magnetization (M_s): If the applied field is strong enough (sample dependent), it can lead to saturation of moments in the sample. This is indicated by the plateau-like region corresponding to the saturated magnetization (M_s).

- Spontaneous magnetization (M_{sp}): Some materials such as FM retain their magnetization even when applied field is removed. This is called spontaneous magnetization (M_{sp}).

- Coercive field (H_c): While reversing the field direction, it is common to see that the magnetization of the sample doesn't change its direction instantaneously.

In fact, a certain minimum strength of field is required to switch the magnetization into the opposite direction. This field is called coercive field (H_c). The magnitude of H_c determines how easily the magnetization of material can be manipulated, which is very useful in their integration into devices such as magnetic storage.

Deducing these parameters is part of hysteresis curve analysis as they provide information on the magnetic properties of the material.

The shapes of hysteresis loops can vary significantly depending on the type of material and its magnetic properties. Figure 2.7(b) shows the ideal hysteresis of some common magnetic orderings. The M_{sp} is ideally zero for AFM, DM, and PM materials. In zero-field, there is no magnetization in DM while for PM and AFM, the moments cancel out to zero net magnetization. The phenomenon of hysteresis is associated with energy dissipation, which is proportional to the area enclosed by the loop. It is more pronounced in FM materials as compared to AFM and is usually not exhibited by PM and DM.

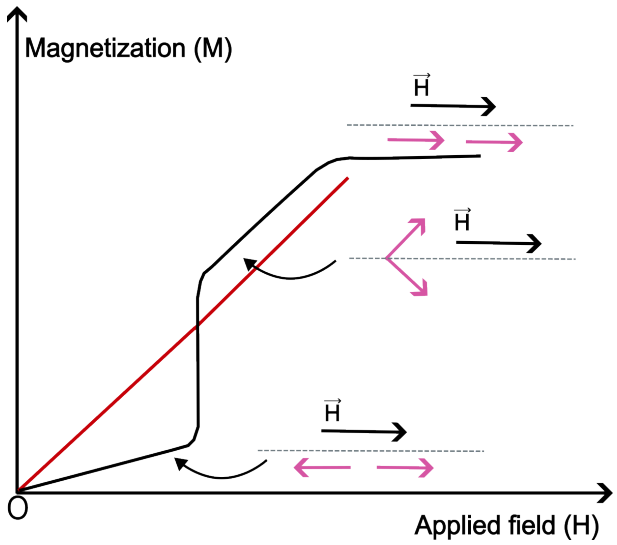

Figure 2.8: Schematic illustration of a spin flop transition reflected on the slope of magnetic hysteresis curve of an AFM material.

In addition, magnetic hysteresis can also reveal transitions in the moment alignment through changes in the slope of the curve. One such transition is *spin-flop* transition, which commonly occurs in AFM due to application of external magnetic field. If the field is applied along the crystal's preferred direction of magnetization, at a critical field the moments suddenly rotate in a direction perpendicular to the applied field. Then, a continuous rotation of moments occur upon increasing the field. This results in change in the magnetic hysteresis shape, as illustrated clearly in Figure 2.8.

2.2.4.3 Magnetic anisotropy

Certain magnetic crystals possess magnetic easy-axis and hard-axis. In such materials, the moments prefer to align along particular crystallographic directions, hence the name easy-axis and it is relatively difficult to rotate them along other directions. This property of different magnetic behavior along different directions is called magnetic anisotropy. The anisotropy effect can be observed in the measured hysteresis of a material. As an example, magnetic hysteresis of few elements are shown in Figure 2.9. The shapes of the curves for field applied along different crystal directions are compared. One can clearly notice that the moments are saturated along certain directions at lower strength of applied field suggesting easy-axis behavior.

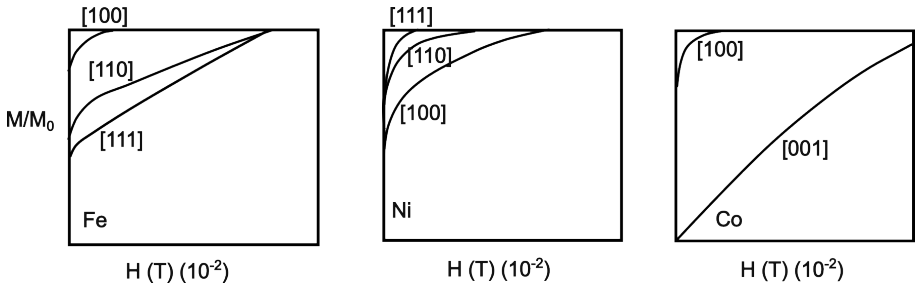

Figure 2.9: Magnetic anisotropy in Fe, Ni and Co shown by the hysteresis curves for field applied along different directions. The easy-axis for Fe and Co is [100] and it is [111] for Ni, because the moments are saturated at lower field for these directions. Adapted from [49, 57, 58].

The physical origins of magnetic anisotropy can be multiple. It can be due to directional dependence of spin-orbit interaction and orbital quenching due to crystal symmetry (magnetocrystalline anisotropy). It can also be related to sample shape such as thin films, whose magnetic behavior can be very different from their bulk counterparts. In thin films, the magnetization generally prefers to stay in-plane instead of aligning normal to the surface. This helps in lowering the magnetostatic energy in the system as the magnetic field lines occupy lesser area outside the material. In addition, magnetic interaction at the film surface are different compared to the inner film region. This leads to surface anisotropy in the system. It is inversely proportional to the thickness of the film [59]. Therefore, surface anisotropy is negligible in very thick films. Changes in crystal lattice due to strain in the film can also lead to anisotropic behavior. These are a few of the possible origins and a given material can exhibit a combination of these anisotropy types.

Magnetic anisotropy affects the formation and behavior of magnetic domains in the material. Magnetic materials form a number of small regions called domains, which are equally favorable by energy minimization. Domain formation is a way for materials to reduce the overall energy of the system. They are separated by a boundary called domain wall. The width of domain wall depends on the anisotropy because the moments inside domain walls have to align along axes other than easy-axis as they are rotating form one domain configuration to another.

SQUID magnetometer (discussed in next chapter) is a well-established technique to study the macroscopic magnetic properties of materials. However, it is not easy to obtain information on the microscopic nature of magnetic materials i.e. arrangement of magnetic moments. For this and also resolving the crystal structure, diffraction methods can be very effective. Now, we will focus on general concepts behind diffraction experiments and how they can be used to obtain atomic scale information about the material.

2.3 Diffraction

Diffraction methods are a very common tool to study nuclear and magnetic structures. X-rays and neutrons are popular probes in this field and can be used to obtain precise information about the atomic and spin arrangement in crystalline materials. In this section, the basic principles of X-ray and neutron scattering is described along with the different concepts that are used for analysis in this project. Let's start with a brief introduction to the world of crystallography.

2.3.1 Crystal symmetry

Crystalline structures are characterized by periodic arrangement of constituent particles in all 3 dimensions. This underlying periodicity can be described with the help of a building block called unit cell $(\vec{a}, \vec{b}, \vec{c})$, such that any point inside the cell is given by $\vec{v} = x\vec{a} + y\vec{b} + z\vec{c}, (x, y, z \in [0, 1])$. Usually, the unit cell is also represented using the concept of reciprocal space lattice, which is the Fourier transform of the lattice cell in real space. Indeed, it is convenient to represent a periodic object by its Fourier transformation. The reciprocal lattice concept helps in simplifying the diffraction analysis. It is constructed based on a set of the reciprocal lattice vectors $(\vec{a^*}, \vec{b^*}, \vec{c^*})$ given by the following relations:

$$\begin{aligned} \vec{a^*} &= 2\pi \frac{\vec{b} \times \vec{c}}{V}, \\ \vec{b^*} &= 2\pi \frac{\vec{c} \times \vec{a}}{V}, \\ \vec{c^*} &= 2\pi \frac{\vec{a} \times \vec{b}}{V} \end{aligned} \tag{2.9}$$

where, V is the volume of the unit cell. The two sets of vectors (real and reciprocal lattice vectors) are orthogonal and follow the relation $\vec{V_i}.\vec{V_j^*} = \delta_{ij}$. The use of reciprocal lattice to determine the diffraction condition using Ewald sphere is discussed later in section 2.3.4.1.

One should note that each atomic plane can be conveniently represented using Miller indices $(hk\ell)$. Miller indices are calculated by taking the inverse of the distance at which the chosen plane intersects the unit cell axes. For example, if a plane intersects the unit cell axes $(\vec{a}, \vec{b}, \vec{c})$ at 1/2, 1/3 and ∞ (no intersection), the Miller indices for this plane are (2 3 0).

Furthermore, the unit cell is associated with crystal lattice, which is defined by the arrangement of motifs (atom(s) at a lattice point), throughout the structure. For example, if a unit cell of cubic shape $(a = b = c)$ consists of motifs at each corner and at face centers, it is called a face-centered cubic lattice labeled as F. In total, 14 types of lattices are defined based on the 7 types of unit cells. These are called Bravais lattices named after the French physicist who was the first to correctly enumerate them. The labels used are P - Primitive, I - Body-centered, F - Face-centered and C - Base-centered. The repetition of a unit cell along with the lattice points in 3D space, generates the whole structure.

A crystal lattice description can be further simplified by identifying symmetry elements that leave the arrangement of elementary units invariant. These symmetry elements include rotation axes, mirror planes and inversion centers. So, to efficiently describe a crystal structure one needs to identify its unit cell (edge lengths and angles), lattice type and the symmetry operations present in the lattice. All this information is represented using a concept known as *space group*, that can help categorize and analyze crystal symmetries. A space group is a mathematical object that describes all the symmetry elements that leave the crystal unchanged. It characterizes the entire three-dimensional translational and rotational symmetry of a crystal. Space group defines how the positions of atoms or ions repeat within a crystal lattice and how the crystal can be rotated, inverted, or reflected while maintaining its overall structure. Thus, knowing the space group of a material can provide detailed insights into its crystal structure. Key concepts of space group theory will be given in Section 2.3.3.

Another important term is *point* symmetry. It describes the symmetry of the arrangement of atoms or ions around a specific point within a crystal structure. It focuses on the local arrangement of atoms, which can be represented by a point group. Both these concepts are crucial for understanding the structural and physical properties of crystalline materials.

2.3.2 Principle of diffraction

Before getting into the theory of diffraction on crystals, let us have a look at the scattering from atoms in general.

2.3.2.1 Interactions during scattering

The mechanism of scattering from atoms basically depends on how an incident beam of particles interact with them. The nature of interaction is related to the kind of particles used as a probe. Figure 2.10 shows a schematic of interaction of electrons, neutrons and X-rays with a basic structure of atoms. Starting from the bottom left of the figure, electrons get repelled by the electrons in an atom, preventing it from penetrating deep into the sample. They can scatter off from this repulsion, leading to deflection from their original path. Next are X-rays, high energy electromagnetic waves, which have electromagnetic interaction with the electron cloud. X-rays can penetrate slightly deeper than electrons as illustrated in the figure. Neutrons are neutral particles, which means that they interact with the nucleus through strong and short-range nuclear forces. The probability of this scattering event is low because the nucleus is considered as a point object being much smaller than the electron cloud. As a result, the scattered intensity is weak and neutrons can travel deep into the sample without interacting. If the sample is magnetic in nature, neutrons can also interact with the unpaired electrons with magnetic dipole-dipole interaction. The neutron-electron interaction has higher probability than the nuclear interaction but the magnitude of magnetic interaction is weaker. Interestingly, the overall strength of nuclear and magnetic scattering are of the same order in magnitude.

One should note that an X-ray photon, being electromagnetic, interacts strongly

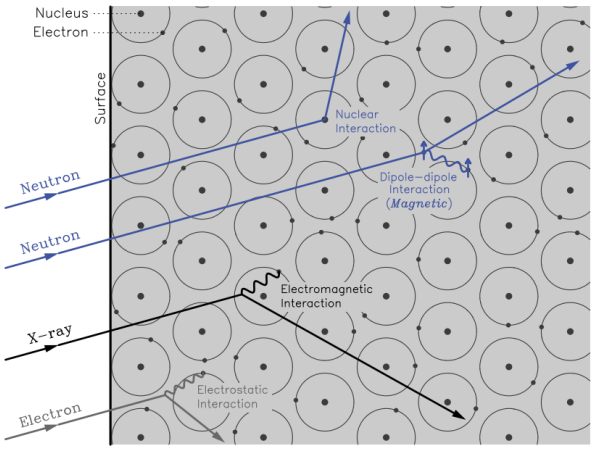

Figure 2.10: Schematic illustration of the interactions of different types of incident beams with an atom. Adapted from [60].

with the electron cloud. This interaction is between the electron charge and oscillating electric and magnetic fields of the photon. X-rays can also have magnetic dipole interaction like neutrons with the unpaired electrons, but it is very weak and high intensity beams (synchrotron sources) are required to study it.

Both neutrons and X-rays are popular probes for diffraction experiments. Both techniques are advanced and well-established and are often complimentary in terms of obtainable information. Now we have a qualitative idea of the scattering in general, let's learn about the basics of mathematical representation of a scattering event from a single atom. We will later proceed to the idea of scattering from ordered crystal structures, which helps us determine the crystal symmetry.

2.3.2.2 Mathematical representation of a scattering event

For the sake of relevance to the thesis, the description is kept limited to the elastic scattering case, where there is no exchange of energy in the process. The basic quantity that is measured in an elastic scattering experiment is the fraction of incident particles scattered in a unit solid angle direction. This is known as the differential cross-section ($\frac{\mathrm{d}\sigma}{\mathrm{d}S}$), represented schematically in Figure 2.11(a).

To derive the mathematical formulation, let us consider a beam of incident particles of wavevector $\vec{K_i}$ ($|\vec{K_i}| = K_i$), traveling in the z direction described by complex plane wave:

$$\psi_i = \psi_0 \exp(iK_i z) \tag{2.10}$$

where, ψ_0 represents the amplitude of the wave and $K_i = 2\pi/\lambda_i$, λ_i being the wavelength of the incident beam. These particles interact elastically with the scattering object (an atom) and move radially outwards. This means that the sinusoidal part of scattered beam is dependent on displacement vector $\vec{r}$ instead of only z, with origin at the point of scattering. The scattered waveform also has inverse dependence on the distance r because the number of particles per unit area decreases with distance

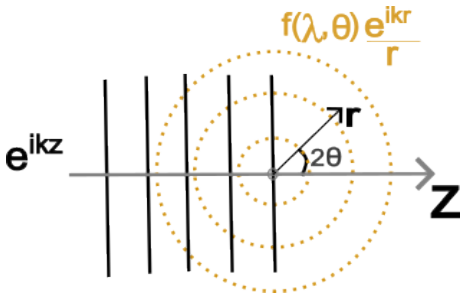

(a)

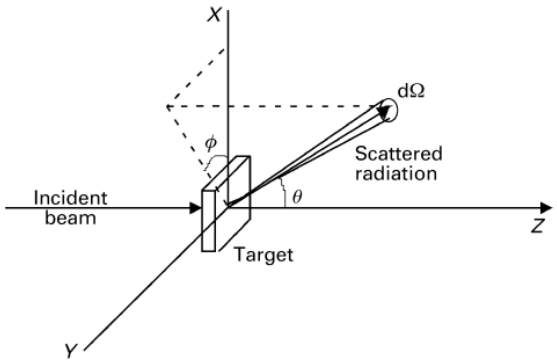

(b)

Figure 2.11: (a) Differential cross-section geometry in scattering process [61]. (b) An incident beam getting scattered isotropically and elastically by a fixed target at the origin.

away from the scattering point. Thus, it is given by:

$$\psi_f = \psi_0 f(\lambda, \theta) \frac{\exp(iK_f r)}{r} \tag{2.11}$$

where, $f(\lambda, \theta)$ is the atomic form factor representing probability that the particle of wavelength λ is deflected in the direction of angle θ by an atom (see Figure 2.11(b)), more details will be given on this in Section 2.3.2.5. Since it is elastic scattering, there is no change in magnitude of wavevector upon deflection ($K_i = K_f = K$). The differential cross-section measured in the experiment is thus given by the modulus-squared of Equation 2.11:

$$\frac{\mathrm{d}\sigma}{\mathrm{d}S} = |\psi_f|^2 = \psi_f \psi_f^* = |\psi_0|^2 \frac{f(\lambda, \theta)^2}{r^2} \tag{2.12}$$

where, $|\psi_0|^2$ is basically the incident flux.

The change in momentum in general can be written as:

$$\vec{P} = \hbar \vec{K_f} - \hbar \vec{K_i} = \hbar \vec{Q} \tag{2.13}$$

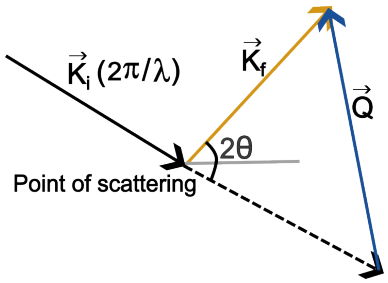

Figure 2.12: Schematic illustration of elastic scattering process showing the isosceles triangle formed by incident wavevector ($\vec{K_i}$), scattered wavevector ($\vec{K_f}$) and scattering vector ($\vec{Q}$).

where $\vec{Q}$ is the momentum transfer given by $\vec{K_f} - \vec{K_i}$ (schematically presented in Figure 2.12).

Although the momentum transfer is given by the same equation for X-rays and neutrons, their energy is related differently to the wavevector $\vec{K}$.

$$\begin{aligned} \text{For X-rays,} \quad & E = \hbar c K \\ \text{For neutrons,} \quad & E = \frac{(\hbar K)^2}{2m_n} \end{aligned} \tag{2.14}$$

where, m_n is the mass of the neutron and c is the speed of light. An X-ray photon with wavelength comparable to atomic spacing ($\approx$ 2Å) thus corresponds to energy of 6.2 keV, whereas a neutron with same wavelength has an energy of 20.4 meV. Hence, X-rays and neutrons with energies close to these values are appropriate to study atomic arrangements.

Now, we can simply extend this formalism to a large assembly of atoms. Equation 2.12 then leads to:

$$\frac{\mathrm{d}\sigma}{\mathrm{d}S} \propto \left| \sum_j f_j(\lambda, \theta) \exp\left(i\vec{Q}.\vec{r_j}\right) \right|^2 \tag{2.15}$$

where, $\vec{r_j}$ is the position vector of atom j and the summation is carried over all the atoms in the sample. Equation 2.15 shows how differential cross-section is related to the atomic structure. Now it is time to proceed to the highlight of this discussion: scattering from a perfectly ordered crystal structure. In this part, we will see the effect of crystal symmetry on the outcome of the scattering event discussed above.

2.3.2.3 Scattering from ordered crystal structures

Elastic scattering from ordered atomic planes in crystals leads to interference among the scattered beams giving rise to constructive and destructive patterns. The patterns obtained on the detector are characteristic of the material crystal structure. The recorded patterns include constructive interference peaks at specific positions given by θ (angle of incidence), at which the path difference between scattered beams is an integral multiple of λ (see Figure 2.3.2.3). This is represented by Bragg's law:

$$2d\sin\theta = n\lambda \tag{2.16}$$

where, d is the inter-planar spacing of parallel planes responsible for diffraction and n is a Natural number representing the order of diffraction. The higher order peaks come from the interference between scattered beams from the planes that are nd distance apart. For example, the second order peak for (1 0 0) reflection will be from the planes with interplanar distance ($2d_{100}$), which is at the same θ position as the first order peak of (2 0 0).

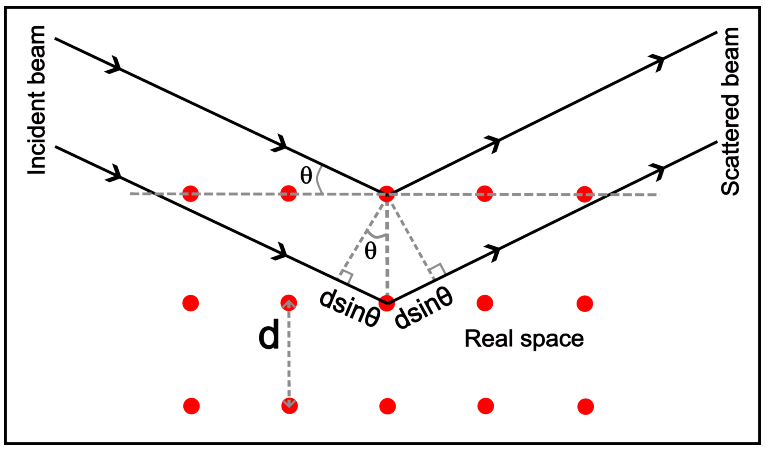

Figure 2.13: Representation of scattering of an incident beam from lattice planes.

In a periodic crystal the position of an atom can be rewritten as $\vec{r}_{Nj} = \vec{R}_N + \vec{r}_j$ where, $\vec{R}_N$ is the vector representing the position of N_{th} unit cell in 3D space and $\vec{r}_j$ is the position vector, $\vec{r_j} = x_j\vec{a} + y_j\vec{b} + z_j\vec{c}$ where, $(x_j, y_j, z_j) \in [0, 1]$ are the coordinates of atom j in the unit cell. Therefore, Equation 2.15 can be rewritten as:

$$\begin{aligned}\frac{\mathrm{d}\sigma}{\mathrm{d}S} &\propto \left|\sum_N \sum_j f_j(\lambda,\theta)\exp\Big(2\pi i(\vec{Q}.\vec{R}_N + \vec{Q}.\vec{r}_j)\Big)\right|^2 \\ &= \left|\sum_N \exp\Big(2\pi i(\vec{Q}.\vec{R}_N)\Big)\sum_j f_j(\lambda,\theta)\exp\Big(2\pi i(\vec{Q}.\vec{r}_j)\Big)\right|^2\end{aligned} \tag{2.17}$$

where, the first sum is the Fourier transform of the lattice. This only gives intensity if $\vec{Q} = \vec{Q}_{hk\ell}$ with $\vec{Q_{hk\ell}} = h\vec{a^*} + k\vec{b^*} + l\vec{c^*}$, signifying the Bragg condition and $(hk\ell)$ are the Miller indices of the atomic plane under diffraction. The scattering vector $\vec{Q}_{hk\ell}$ is thus a point in the reciprocal space representing the plane under diffraction. The second sum represents the structure factor. The measured intensity is a convolution of the 2 terms. First, the ones coming from the Bragg term, which are the sharp periodic peaks depending on the size, shape and repetition of the unit cell in real space. The structure factor term corresponds to the positions and nature of atoms in the unit cell.

Using the above relations, the structure factor equation can be derived to:

$$F_{hk\ell} = \sum_j f_j(\lambda, \theta) \exp(2\pi i(hx_j + ky_j + lz_j)) \tag{2.18}$$

This equation provides a simplified mathematical expression for diffraction on ordered crystal structures. In this thesis, we have worked with super-lattice structures, so let's review the nature of diffraction patterns on such configurations. The next section deals with how the Equation 2.18 changes for a super-lattice structure.

2.3.2.4 Diffraction on super-lattice structures

The structure factor for diffraction on super-lattices can be simplified to get a better idea of the pattern. From the Equation 2.17, we know that there are two types of terms that contribute to the diffraction pattern. For a super-lattice structure, we can further breakdown the structure factor term as follows.

Let us consider a super-lattice structure with 6 layers of thickness close to each other (the unit cell) and repeated several times along z-direction (ℓ in reciprocal space) as shown in Figure 2.14(a). On such a structure, we want to look at the diffraction pattern along $\vec{Q} = (0\ 0\ \ell)$. Considering (x_j, y_j, z_j) as the position vector of atom j, let's rewrite the structure factor term from Equation 2.17 as:

$$\begin{aligned} F_{hk\ell} &= \sum_j f_j(\lambda, \theta) exp(2\pi i(lz_j)) \\ &= \sum_n \sum_\alpha f_{n\alpha}(\lambda, \theta) exp(2\pi il(\frac{n}{6} + \sigma_{n\alpha})) \end{aligned} \tag{2.19}$$

where, n is index of monolayer in the unit cell (total 6 monolayers), α is the index of atoms in each monolayer, and $\sigma_{n\alpha}$ represents the atomic position of atom α in the monolayer n (see Figure 2.14(a)).

Assuming that all the 6 monolayers are identical in structure, $\sigma_{n\alpha}$ (and hence, $f_{n\alpha}(\lambda, \theta)$) become independent of n and we can further untangle Equation 2.19 as follows:

$$F_{hk\ell} = \sum_n exp(2\pi i \frac{nl}{6}) \sum_\alpha f_\alpha(\lambda, \theta) exp(2\pi il\sigma_\alpha) \tag{2.20}$$

where, the first term gives rise to peaks at (0 0 6), (0 0 12) and so on, owing to repetition of 6 monolayers inside the unit cell. The second term represents the intensity of these peaks as a factor of nature and positions of the atoms inside each monolayer. In addition, we also have peaks from the Bragg term as explained through Equation 2.17. So the measured diffraction pattern is a convolution of these two types of peaks.

Here we have assumed the monolayers to be of identical width. In case of variations in this width, the superstructure peaks are broadened. Thus, the final diffraction pattern can also include peaks such as (0 0 5) and (0 0 7) (see the blue peaks in Figure 2.14(b)). Thus, the presence of such peaks in the diffraction pattern is an indication of layer width modulation in the structure. In this thesis, we have referred to these peaks as *satellite* peaks. In the Chapter 6, we will see how the diffraction

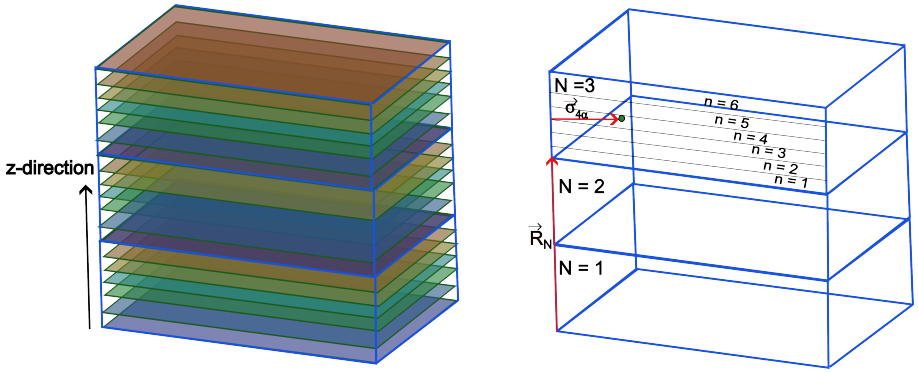

(a)

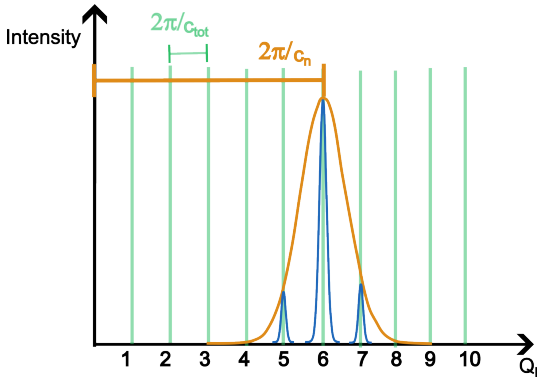

(b)

Figure 2.14: (a) Schematic of a super-lattice structure showing different layer thicknesses and arrangements. (b) Schematic showing two different types of diffraction peaks produced by the super-lattice structure; green: Bragg peaks and orange: superstructure peaks. The blue peaks represent the diffraction pattern seen experimentally i.e. convolution of the two types of peaks, not drawn to exact scaling.

pattern along (0 0 ℓ) can be used to obtain information about layer configuration in the sample.

Now we will take the attention to a crucial parameter $f_j(\lambda, \theta)$ to draw distinctions between X-ray and neutron diffraction experiments.

2.3.2.5 Atomic form factor for X-ray and neutron diffraction

Since $f_j(\lambda, \theta)$ signifies the nature of interaction between the incident particle and the sample, it is characterized using different quantities for X-rays and neutrons.

X-ray diffraction

The interaction of X-rays while scattering from an atom is long-range electromagnetic one with the electron cloud. This interaction is represented by *atomic form factor*, which has a magnitude proportional to the atomic number Z. The strength of scattering increase with the number of electrons (same as Z for a neutral atom).

Therefore, the scattered intensity in X-rays increases with atomic number and it is relatively difficult to distinguish between atoms with close atomic numbers. In addition, the atomic form factor also has dependence on incident angle θ and wavelength λ of X-rays. It decreases with increasing θ and decreasing λ. The θ dependence is because at higher incident angle, the increased path length leads to destructive interference. The direct proportionality to λ is because the low energy X-rays interact strongly with the electron cloud, leading to higher form factor. The exact nature of the decay curve is element specific. Figure 2.15 shows a typical shape of these curves plotted with respect to $\sin\theta/\lambda$, which can also be represented in terms of scattering vector $Q = 4\pi \sin\theta/\lambda$.

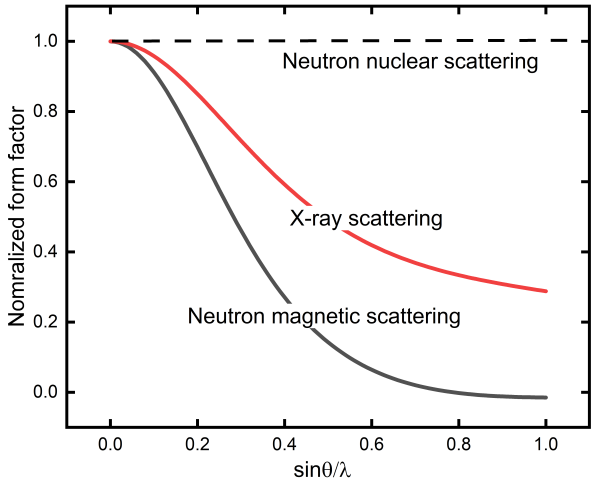

Figure 2.15: Schematic to show variation of X-ray and neutron form factors (nuclear and magnetic) with scattering vector.

Nuclear neutron diffraction

Neutrons interact with the nucleus through strong and short-range nuclear forces, and with the electron cloud via magnetic dipole moment. The nuclear interaction is characterized by scattering length (b) and unlike X-rays, this interaction is independent of θ and λ (see Figure 2.15). This is because it is short-range and the scattering is considered from a 'point object' (nucleus). The independence from λ is valid only for the elastic scattering case, and not for absorption or resonance scenarios. The quantity b has dimensions of length and is usually represented in unit of Barn (1 Barn = 10^{-28} m^2). It depends on the nuclear configuration meaning it is isotope specific and also varies with nuclear spin alignment (if non-zero) with respect to the incident neutron. The neutron-electron magnetic interaction is discussed in-detail in the next paragraph.

Magnetic neutron diffraction

One big advantage of ND is the ability to study the arrangement of magnetic spins in a magnetically ordered crystal. Neutrons are spin 1/2 particles with magnetic

moment of -1.913 nuclear magneton ($1\ \mu_N = 5 \times 10^{-27}$ JT^{-1}). This allows neutrons to interact with the magnetic spins of electrons.

At a certain temperature, magnetic materials undergo a transition from magnetically ordered to PM phase. This means that if the diffraction measurements are carried out above the transition temperature, the diffracted intensity will only include nuclear contribution as there is no long-range magnetic ordering in the system. Whereas in the magnetically ordered phase, the diffracted intensity consists of both nuclear and magnetic scattering contributions. A common strategy to find magnetic structure of crystals involves measuring data-sets in both PM and magnetically ordered phase. Then, the subtraction of PM intensity from the low temperature data-set gives only the magnetic part of the peaks, which can be used to resolve the magnetic moment configuration in the system. Both polarized and unpolarized neutrons can be used for magnetic diffraction. Considering the scope of the thesis, the description has been kept limited to unpolarized case only. The magnetic structure factor for neutrons is given by:

$$F^m_{hk\ell} = p \sum_j f^m_j(\vec{Q}) \vec{\mu_{j\perp}} \exp\Big(2\pi i(\vec{Q}.\vec{r_j})\Big) \tag{2.21}$$

where, p is a normalization constant equal to 2.69 fm (1 fm $= 10^{-15}$ m) that allows the conversion of magnetic moments in Bohr magnetons to units of scattering length (10^{-12} cm). $f^m_j(\vec{Q})$ is the magnetic form factor. In contrast to the nuclear neutron scattering length, the magnetic form factor varies with scattering vector $\vec{Q}$ (see Figure 2.15) and decreases with increase in $\vec{Q}$. $\vec{\mu_{j\perp}}$ is the component of magnetic moment of atom j, which is perpendicular to $\vec{Q}$. It is worthwhile to note that only the perpendicular component of magnetic moment contributes to magnetic scattering. It is illustrated by the schematic in Figure 2.16. For example: if the scattering vector $\vec{Q}$ = (0 0 2), then only the component of magnetic moment in the plane ($hk0$) will contribute to the magnetic intensity. Thus, an alternative way to separate the nuclear and magnetic scattering can be aligning all the moments parallel to $\vec{Q}$ by applying field, hence no magnetic intensity contribution in the pattern.

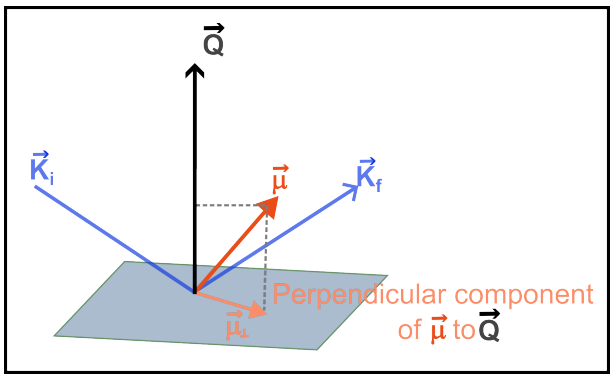

Figure 2.16: Schematic to show perpendicular component of magnetic moment to scattering vector that contributes to the diffracted intensity

2.3.3 Representation group theory for nuclear and magnetic structures

The representation group theory can be used to describe and classify the possible nuclear and magnetic structures deriving from the crystallographic space group of a material. The concept of irreducible representations and basis vectors is found to be very useful to analyze the possible arrangements of atoms and magnetic spins inside a crystal[62]. This section summarizes the principal results of representation group theory and its application to crystallography. The conventions are followed from the article of J. Rodríguez-Carvajal and F. Bourée on magnetic structures and symmetry [63]. At first, let us have a look at the definitions of some terms from group theory that are useful in this scope.

2.3.3.1 Basics of group theory

We are taking G as a group that consists of symmetry operations followed by the crystal structure in which the magnetic ordering takes place.

- **A group**
  A group is a mathematical concept representing a set of elements and an operation $(*)$ that satisfy the following four axioms:

  1. **Closure:** For any two elements of the group (a and b), $a * b = c$, should also be an element of the group.
  2. **Associative:** The group elements should also satisfy the equation, $(a * b) * c = a * (b * c)$
  3. **Identity:** There exists an identity element (e) int he group such that $a * e = e * a = a$ holds true.
  4. **Inverse:** For each element in the group, there exists an inverse element $a * a^{-1} = a^{-1} * a = e$

- **Representation of a group**
  In simple words, representation of a group is defined as a way to describe the elements of a group and its operation $(*)$, using a simpler approach. In the context of crystal symmetry, these representations are taken in the form of matrices. Each matrix (Γ) represents a symmetry operation (g) that can be applied to the coordinates of atoms and/or their magnetic moments. A set of such square matrices is considered a representation of group G if a mapping can be established with the elements of the group such that it preserves the group multiplication. Mathematically, it can be written as:

$$\Gamma = \{\Gamma(g) | g \epsilon G\}, \qquad \Gamma(g_1 g_2) = \Gamma(g_1)\Gamma(g_2) \tag{2.22}$$

- **Similarity transformations**
  An equivalent representation can be obtained by applying similarity transformation to all the matrices using unitary matrix, U $(U^{\dagger} = U^{-1})$.

$$\tilde{\Gamma}(g) = U\Gamma(g)U^{-1}, \qquad (g \epsilon G) \tag{2.23}$$

As mentioned earlier, space groups and points groups are mathematical objects that are used to describe the complete crystal symmetry of a structure. Let us take an example to illustrate how group theory concepts are used in crystallography.

Consider point group $2/m$ as an example. It consists of four different types of symmetry operations: identity (E), 2-fold axis (say along $\vec{z}$), a mirror plane (perpendicular to 2-fold axis) and an inversion center (i). One representation (irreducible type) of this group can be the set of matrices shown in the equation 2.24. Each matrix corresponds to a symmetry operation and represents the transformation of a point P in 3 dimensional Cartesian coordinate system.

$$\begin{aligned} E &\rightarrow \begin{bmatrix} 1 & 0 & 0 \\ 0 & 1 & 0 \\ 0 & 0 & 1 \end{bmatrix} \\ 2_z &\rightarrow \begin{bmatrix} -1 & 0 & 0 \\ 0 & -1 & 0 \\ 0 & 0 & 1 \end{bmatrix} \\ m &\rightarrow \begin{bmatrix} 1 & 0 & 0 \\ 0 & 1 & 0 \\ 0 & 0 & -1 \end{bmatrix} \\ i &\rightarrow \begin{bmatrix} -1 & 0 & 0 \\ 0 & -1 & 0 \\ 0 & 0 & -1 \end{bmatrix} \end{aligned} \tag{2.24}$$

The number of representations of arbitrary dimensions that can be obtained for a particular group is infinite. However, the representations can be reduced to simpler forms such as "block-diagonal matrix" using similarity transformations. A representation is reducible if one can find a similarity transformation that reduces it to block-diagonal form. In the end, irreducible representations (Irrep) are the ones of fundamental significance in representation theory. Any reducible representation can be decomposed in a direct sum of Irreps:

$$\Gamma = \sum_{\oplus\nu} n_\nu \Gamma^\nu = n_1\Gamma^1 \quad \oplus \quad n_2\Gamma^2 \quad \oplus \quad . \quad . \quad . \quad \oplus n_m\Gamma^m \tag{2.25}$$

where n_ν is the number of times a particular Irrep is present in the reducible representation, Γ. In the example presented above, the 4 matrices are in block-diagonal form and hence, can be used to construct an Irrep of point group $2/m$. The 3 elements along the diagonal of each matrix represent the 3 axes (x, y, z) respectively and combine to form Irreps. For example, the elements representing x, combine to form (1 -1 1 -1), which is an Irrep of dimension 1. A table listing all the Irreps of a group G is called the Character table of G. It reports Irreps corresponding to all the symmetry operations present in a space group or a point group. The commonly used symbol for an Irrep is Γ.

Similar to atomic positions, magnetic moments also transform under crystal symmetry operations as discussed briefly next.

2.3.3.2 Magnetic moments in crystal symmetry

Magnetic moment of an electron is generated by its spinning and orbital motion around the nucleus. We will keep the focus on spin magnetic moment which is generated by the spinning motion of electron charge (electric current). The behavior of magnetic moment can be described using axial vectors. Figure 2.17 illustrates the effect of a mirror plane symmetry on magnetic moments. The arrow's direction represents orientation of electron loop and its length is proportional to the magnitude of moment. Under the symmetry operations of crystallographic space groups, the

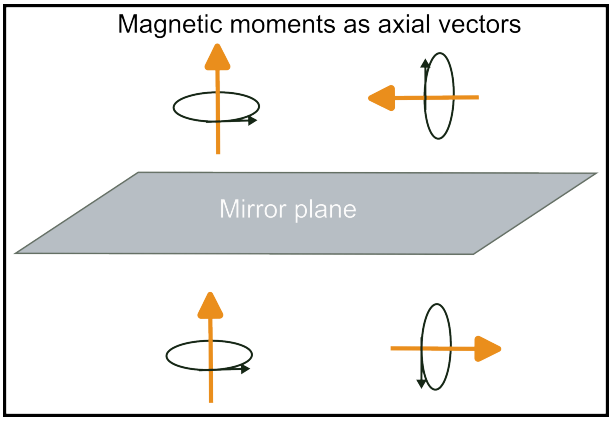

Figure 2.17: Action of a mirror plane on axial vectors

axial vectors behave differently than polar vectors. It involves an additional operator known as time reversal or spin reversal. This operator changes the direction of rotation of electron loop and hence the direction of the moment vector. This is represented by a primed symbol along with the conventional symmetry operators. Therefore, the resolved magnetic structure should be consistent with the chemical space group symmetry including the time-reversal operator.

This is where group theory and crystal symmetry combination comes into play. One can calculate the allowed magnetic moment configurations with respect to the crystal symmetry constraints. The transformations of components of magnetic moments under the crystal symmetry operations can be carried out in a similar way as the atomic positions, discussed in Section 2.3.3.1 for $2/m$ point group symmetry. Through these analysis, one can obtain nuclear and magnetic structures that are compatible with each other. The whole symmetry analysis to obtain the allowed magnetic configurations can also be performed using the computing program BasIreps (FullProf), which provides the list of Irreps for each magnetic site in the crystal [64]. In this thesis, we have used the group theory for crystal symmetry in order to check the compatibility of the resolved magnetic structure with the nuclear one for the LSMO thin film. More detailed analysis on this are presented in Chapter 4.

2.3.4 Single crystal diffraction experiments

In this section, we will explore the fundamentals of carrying out a single crystal diffraction experiment. We will see how different concepts defined above are useful in implementing and efficiently conducting a diffraction experiment. In addition, we will also review the concept of orientation matrix, an important term in executing single crystal diffraction measurements. Let's begin with the basic strategy behind a typical diffraction experiment.

2.3.4.1 A typical single crystal diffraction experiment

When a single crystal is mounted on an instrument for the first time, in a general orientation, the most probable scenario with monochromatic beam is that there will be no scattered intensity on the detector. This is because the crystal and the detector need to be oriented as per Bragg's law condition. A simple way to visualize and interpret this is through the construction of Ewald sphere. In case of elastic scattering, the final wavevector $\vec{K_f}$ is of the same length as $\vec{K_i}$ and the detector is oriented along the direction of $\vec{K_f}$. The Ewald sphere is drawn centered on the point of scattering and has a radius equal to the length of $\vec{K_i}$ ($\frac{2\pi}{\lambda}$) as shown in Figure 2.18. Reciprocal space points corresponding to each atomic plane are distributed in this 3D space with origin at the incident wavevector. The diffraction condition (Bragg's law) for a particular scattering plane is satisfied at a point where Ewald sphere intersects its reciprocal space point ($hk\ell$).

For comparison, in case of poly-crystalline samples, there are several different reciprocal spaces corresponding to each crystallite grain present in the sample. This means that at any general orientation of the sample or instrument, with sufficient number of crystallites under diffraction, it is more probable that there are some reflections intersecting the Ewald sphere. A similar scenario can also be imagined if instead of a monochromatic beam, a "white" beam (consisting of multiple wavelengths) is incident on a single crystal sample. Each wavelength will correspond to a Ewald sphere of different radius.

Even though the poly-crystalline peaks are relatively easier to measure, the patterns obtained from single crystals convey more information about the structure of the sample. This is because in poly-crystals there are several other factors contributing to the shape of Bragg peaks such as grain size, volume, and locally varying lattice constants. The detailed description in this thesis has been kept limited to elastic scattering on single crystal samples. During the experiments, the idea is to rotate the reciprocal space through Ewald sphere and measure intensity at desired intersection points. These measurements can be performed using two different ways: rotating crystal or rocking curve method. As the name suggests, in rotating crystal method, the sample is rotated in real space, thus the reciprocal lattice is also rotated. When the rotating reciprocal space points intersect the Ewald sphere, the diffraction condition gets fulfilled and the intensity is recorded. This way, full possible rotations of the sample along different axes generates the complete diffraction pattern of the sample

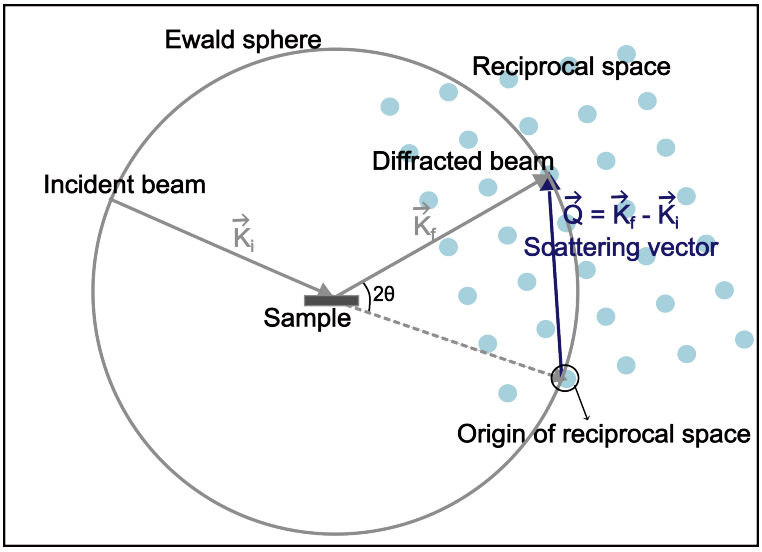

Figure 2.18: Scattering set-up with reciprocal space to illustrate the construction of Ewald sphere.

on a 2D detector.

The other method is rocking curve scans, which are performed by first moving the instrument set-up close to the diffraction condition of the reflection to be measured and then slowly rotating over a small range crossing the center of the peak. This type of scans are further classified as ω scans or ω-2θ scans (named depending on the type of rotation), where ω represents rotation of the sample along vertical axis and θ is the movement of detector.

In the diffraction experiments, the measured peak shape and intensity is a function of several other parameters than the structure factor. The following are few of the corrections needed to be taken into consideration before using the collected data for structural solution.

- Absorption by the sample can affect the intensity of the probing beam. It varies depending on the constituent elements of sample and the nature of probing beam (X-rays or neutrons). In some cases, it is too small to have any significant effect on the measured peaks but otherwise, corrections need to be applied for accurate structure determination.

- The measured peak shape is influenced by the thermal vibrations of atoms. At absolute zero temperature, the crystals have a perfectly rigid structure with atoms fixed at their respective positions, but the temperatures during diffraction experiments are generally significantly higher. This means that the atoms are under random thermal motion around their equilibrium positions. This leads to broader peaks in the diffraction pattern. Debye-Waller factor (or atomic displacement factor) is a measure of the average thermal motion of atoms inside a crystal [65]. It varies with temperature and atomic mass. Since the thermal vibrations decrease with temperature, the Debye-Waller factor is smaller at

lower temperatures. Mathematically, it is given by:

$$B = 8\pi^2\langle u\rangle^2 \tag{2.26}$$

where, $\langle u\rangle^2$ represents the mean square displacement of atoms around their positions. The measured intensity is proportional to $\exp\left(\frac{-2B\sin^2\theta}{\lambda^2}\right)$. It is possible to refine the B value during the structural refinement process.

- Since XRD experiments are conducted with an unpolarized beam of X-rays, a polarization correction needs to be applied to the measured intensity. For an unpolarized X-ray beam, the scattered intensity is given by:

$$I_s \propto I_0(\frac{1+\cos^2 2\theta}{2}) \tag{2.27}$$

where, I_0 is the incident beam intensity and $\frac{1+\cos^2 2\theta}{2}$ is known as the Polarization factor [66, 67]. In case, a monochromator is used in the experiment, the incident beam will be partially polarized and the Polarization factor then becomes $\frac{1+A\cos^2 2\theta}{1+A}$, where $A = \cos^2 2\theta_M$ and θ_M is the Bragg angle of the monochromator crystal. The measured intensity needs to be divided by this factor.

- Lorentz factor accounts for the length of time that a moving crystal spends in the diffraction position. Ewald sphere is an effective tool to also understand this effect. The speed at which each reciprocal space point intersects the sphere depends on the scattering angle. Points at higher scattering angle move faster and hence, spend less time at the intersection point with the sphere. This gives lower intensity as compared to points at lower scattering angles. There are formulae according to the geometric set-ups used in the experiment, that can be used to correct the measured intensity and obtain the right diffracted intensity for analysis [68].

- Correction related to Extinction factors were not taken into account considering the low thickness of the materials in focus.

Thus, the final measured intensity can be written as:

$$I \propto |F|^2(LF)(LP)(Abs) \tag{2.28}$$

where, $|F|^2$ is the square of structure factor, which includes the Debye-Waller factor as $\exp(-2w)$ and $w = B\sin^2\theta/\lambda^2$. LF, LP and Abs correspond to contributions due to Lorentz Factor, Lorentz Polarization and Absorption by the crystal respectively. A common way to solve crystal structures is by starting with an initial "guess" model of atomic positions and refining it until the diffracted intensities calculated from the model gives the best agreement with the measured intensities. This summarizes a typical single crystal diffraction experiment and data treatment.

2.3.4.2 Concept of Orientation matrix

Four-circle diffractometers are a popular tool for single crystal diffraction experiments. The name four-circle comes from the fact that there are four different types of rotations that allow precise control and adjustment of the crystal and detector positions. The four rotations are used to place the sample in desired diffraction conditions. It is to be noted that the X-ray diffractometer used in this project (SmartLab) was in fact used as a five-circle diffractometer. This is because the detector on SmartLab has two different motors corresponding to in-plane (horizontally) and out-of-plane axes of rotation.

Sample alignment is a crucial and first step for any diffraction measurement. It is necessary to identify and calculate the sample orientation required for each reflection. This is done with the help of orientation matrix.

Orientation matrix relates the frame of reference of the sample and the laboratory one in which the angular rotations are carried out. In order to calculate orientation matrix, one needs to know the unit cell parameters and observed angles of few measured reflections. This requires complex calculations and is usually done using programs available at the instrument computer. The general concept behind the calculation can be understood as follows. The conventions from Busing and Levy on four-circle single crystal diffractometer are followed [69].

The axes of rotation of the four angles construct a frame of reference called the instrument frame (see Figure 2.19(a)). The relation between laboratory Cartesian frame of reference and the instrument frame is illustrated in Figure 2.19(b). The detector position makes an angle γ ($= 2\theta$) with the incident beam, which is along y-axis in laboratory frame. Similarly, the χ axis in the equatorial plane makes an angle ω with the incident beam and angle χ is set by the ϕ axis. The zero position for ϕ is chosen arbitrarily. It is to be noted that the names of the angles can be different on different diffractometers.

The general sense of rotation for θ, ω and ϕ angles is dependent on the instrument geometry. For the sake of example, here it is considered to be clockwise (as per right-hand rule) for θ, ω, and ϕ angles and, anticlockwise for χ towards positive movement.

The laboratory Cartesian frame is related to the scattering vector ($hk\ell$) in reciprocal space, via the following relation:

$$V_1 = UB \begin{bmatrix} h \\ k \\ l \end{bmatrix} \tag{2.29}$$

where, V_1 is the position vector in laboratory Cartesian frame corresponding to the scattering vector, B is a matrix that transforms the crystal reciprocal lattice vectors into an orthonormal frame in reciprocal space and U is an orthogonal matrix relating the crystal Cartesian system to laboratory system when all the instrument angles are

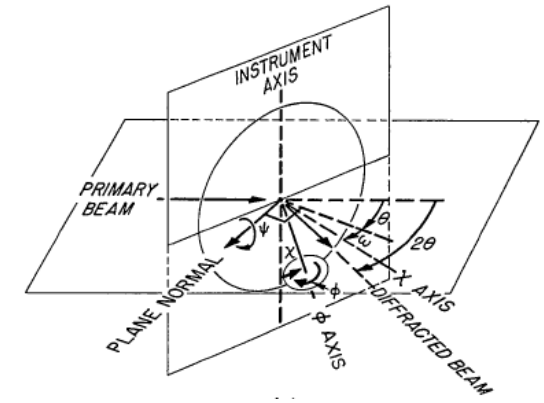

(a)

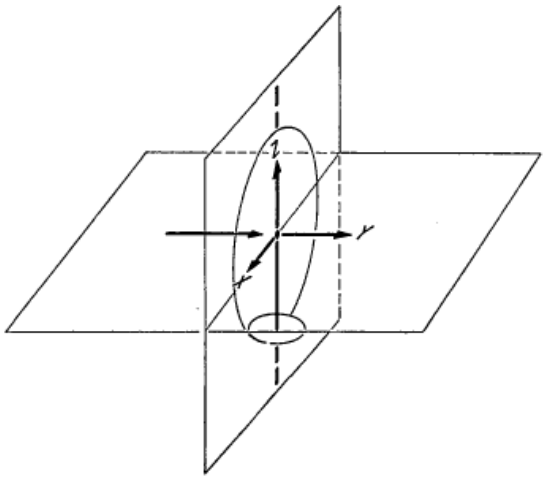

(b)

Figure 2.19: Schematic representation of four circle diffractometer axes. (a) The instrument angles and their axes of rotation. (b) The laboratory frame axes. The instrument angle axes and laboratory axes coincide when all the angles are set to zero. (adpated from [69])

zero. The matrix B is written as:

$$B = \begin{bmatrix} b_1 & b_2 \cos\beta_3 & b_3 \cos\beta_2 \\ 0 & b_2 \sin\beta_3 & b_3(\cos\beta_1 - \cos\beta_2 \cos\beta_3)/\sin\beta_3 \\ 0 & 0 & b_3(1 - \cos^2\beta_1 - \cos^2\beta_2 - \cos^2\beta_3) + 2\cos\beta_1 \cos\beta_2 \cos\beta_3)^{1/2}/\sin\beta_3 \end{bmatrix} \tag{2.30}$$

Here the b_i's and the β_i's are the reciprocal-lattice cell parameters and the angles of the unit cell respectively. In order to get the coordinates of vector V_1 after rotating the crystal, it is multiplied with the corresponding rotation matrices, defined according

to their rotation senses. In the current example, the matrices are as follows:

$$\begin{aligned}
\mathbf{\Phi} &= \begin{bmatrix} \cos\phi & \sin\phi & 0 \\ -\sin\phi & \cos\phi & 0 \\ 0 & 0 & 1 \end{bmatrix} \\
\boldsymbol{\chi} &= \begin{bmatrix} \cos\chi & 0 & \sin\chi \\ 0 & 1 & 0 \\ -\sin\chi & 0 & \cos\chi \end{bmatrix} \\
\mathbf{\Omega} &= \begin{bmatrix} \cos\omega & \sin\omega & 0 \\ -\sin\omega & \cos\omega & 0 \\ 0 & 0 & 1 \end{bmatrix}
\end{aligned} \tag{2.31}$$

If h, k, l are the indices of the plane under diffraction then the length of the scattering vector (reciprocal of inter-planar spacing, d in Å) in any Cartesian coordinate system can be written as:

$$q = (h_{c1}^2 + h_{c2}^2 + h_{c3}^2)^{1/2} \tag{2.32}$$

where, $\mathrm{h}_c = \mathrm{B} \begin{bmatrix} h \\ k \\ l \end{bmatrix}$ Equations 2.29 and 2.32 can be combined to write

$$V_4 = \mathbf{\Omega}\boldsymbol{\chi}\mathbf{\Phi}UB \begin{bmatrix} h \\ k \\ l \end{bmatrix} \tag{2.33}$$

where, $\mathrm{V}_4 = \begin{bmatrix} q \\ 0 \\ 0 \end{bmatrix}$. So, if we know the orientation matrix (UB), the angular rotations can be calculated using equation 2.33 for any ($hk\ell$) reflection of the sample. In the coming chapters, detailed explanation is provided on how this equation can be used to convert the angular scan coordinates to positions in reciprocal space ($hk\ell$).

Now, we will move the discussion from experimental methods towards theoretical calculations. Theoretical methods can be used to facilitate the experimental data analysis and effectively conclude results. Next section discusses a very common tool to carry out such calculations, Density functional theory (DFT) and its relevance to this project.

2.4 Density functional theory (DFT)

Though DFT calculations were not part of this project, the results obtained were used to analyze the experimental data more efficiently. In this section, the general idea behind DFT calculations is briefly described.

DFT is a computational method commonly used to calculate electronic properties of molecular or periodic systems. The central idea in DFT is to minimize the total energy of the system expressed as a functional of the electron density. Electron density map of a system represents the probability distribution of finding an electron. The total energy of the system includes terms from the kinetic energy of the electrons and nuclei, electron-nuclear and nuclei-nuclei interaction, and interaction of the electron with the surrounding potential created by the other electrons (Hartree exchange-correlation). The energy of the system is a functional of the ground state electron density [70].

The ground state electron density corresponding to the minimum energy is calculated using self-consistent cycle. Starting with an initial guess for the density, this procedure involves solving many one-electron Schrödinger equations (Kohn-Sham) iteratively until the global minimum energy configuration is reached [71]. The precise functional dependence of energy on electron density is not known. Therefore, approximations are used for potentials involving quantum-mechanical exchange and correlation between electrons.

Exchange-correlation functional is a key component in DFT calculations. There are several functionals available that are used as an approximations for exchange-correlation (Local Density Approximation - LDA, Generalized Gradient Approximation - GGA [72] etc.). Each functional has its own level of accuracy and applicability. Choice of a functional depends on the type of system being studied, information desired and computational resources available.

In this project DFT was used to perform geometry optimizations. It means that we start the process with a best "guess" geometry. The energy for this geometry is calculated first. Then, the atoms are moved a bit and the energy is recalculated. This process continues until the geometry with minimum energy is reached. The details of DFT work carried out by E. Rebolini [1] and M. B. Lepetit [2] for this project, along with the strategy, are presented in the related chapters.

With this, the chapter comes to an end. These are all the concepts and basics of methods that we will need to fully understand the work done in this project. Next, let's move to more technical aspects of the work. The next chapter is dedicated to explanations of technical specifications and usage of the instruments that are part of the thesis.

---

[1] Computational group ILL, 71 Av. Martyrs Grenoble France

[2] Theory group, ILL and Institut Néel, Grenoble France

Chapter 3

Experimental set-ups

Contents

What to expect in this chapter

Multiple techniques were employed to study the crystal structure and physical properties of the films in this project. This chapter provides an overview of the instruments used for these techniques. The first two sections are dedicated to the description of X-ray and neutron diffractometers. Then, the details about SQUID magnetometer, which was used for magnetic property measurements are written. In the end, a short introduction is provided to the techniques that were not part of the thesis work but were used for the analysis. These include thin film synthesis, characterization using transmission electron microscopy and density functional theory calculations.

3.1 SmartLab - X-ray diffraction

XRD experiments were performed at SmartLab, CEA-CNRS (Grenoble) using a Rigaku diffractometer. It is a multipurpose instrument for thin film analysis using diffraction and reflectivity measurements [73, 74]. One of the biggest challenges in XRD experiments on thin films is to deal with the large substrate signal. If the film peaks are too close to the substrate ones, it becomes difficult to detect them because they are relatively weaker in intensity. In addition, it is not easy to align the film samples for desired reflections on SmartLab, as there is no program available to calculate the orientation matrix and data reduction analysis. This means that each peak needs to be located manually. In this project, we did it by strategically by measuring reflections that can be aligned with some simple calculations. In fact, this was the first experiment set of single crystal diffraction measurements on thin films using this diffractometer. More details about the experiments and other sample specific issues in the measurements are discussed in the corresponding chapters. For now, we will focus on the overview of the instrument in terms of the geometry and technical specifications.

3.1.1 Technical details

The source is a standard Cu anode with a maximum power of 3 kW. It is also equipped with optional double bounce Ge (220) monochromator that selects only K_{α_1} radiation. There is a Ni K_β filter on the receiving side. The detector is a NaI scintillation point detector. The resolution and beam size can be selected using appropriate Soller slits on both incident and receiving sides. The primary beam size is 0.4 mm (vertical) $\times$ 12 mm (horizontal).

The different possible angular rotations that can be used to carry out measurements are shown in Figure 3.1. The angle of incidence (ω) can be varied using the incident beam set-up movement. The sample holder can be rotated along vertical axis (angle ϕ) and can also be tilted out-of-plane using χ-rotation. Finally, the detector position can be adjusted using two different motors for IP and Out-Of-Plane (OOP) movements denoted by angles $2\theta_\chi$ and 2θ respectively. This means that it was essentially used as a five-circle diffractometer. In this project, we have performed scans to measure OOP and IP Bragg reflections using two different geometrical set-ups. Most of the scans obtained were measured using 2 different angular rotations (2D scans), which gives us a 2D view of peak shape and intensity in the reciprocal space.

For both the types of measurements, it is important to first check the sample alignment properly. The normal to the sample surface must be parallel to the ϕ rotation axis passing through the center of the sample, correcting for substrate miscuts or glue in-homogeneity. There are 2 additional motors named R_x and R_y, that can used to align the sample properly. The height of the sample is adjusted with respect to the incident beam set-up using z translation axis. The size of the incident ray projected onto the sample surface can be chosen using appropriate slits. In addition, divergence of the beam is controlled using Soller slits. Soller slits are boxes with

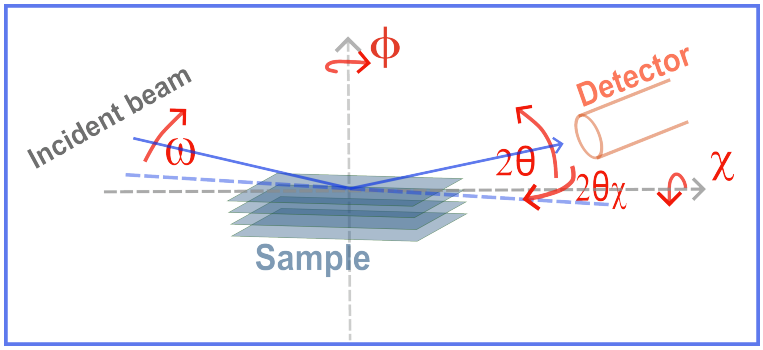

(a)

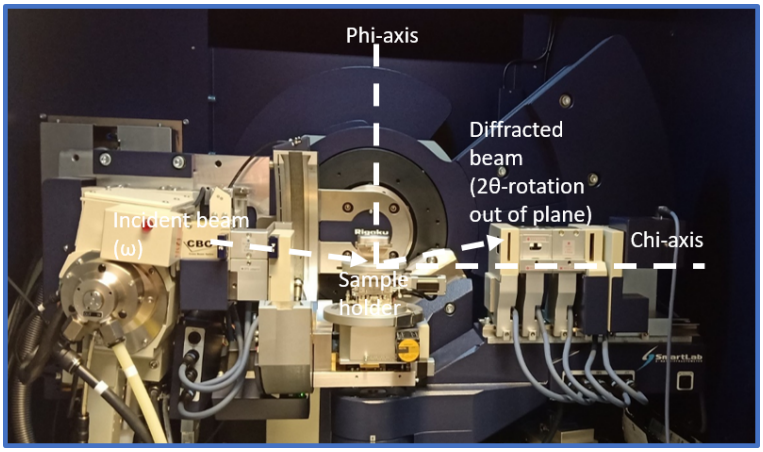

(b)

Figure 3.1: (a) Schematic of SmartLab diffractometers showing 5 different possible rotations. (b) A picture of the instrument with different rotation axes marked.

many metal sheets aligned parallelly with a fixed distance between them. The slits limit the range of angles of the X-ray beam that can pass through. X-rays that are outside this narrow angular range are blocked or absorbed by the slit material. Only X-rays within the specified angular range, defined by the distance between the slits, are allowed to pass through. Parallel slit analyzer (PSA) and Parallel slit collimator (PSC) are also used to manipulate the X-ray beam. They have same construction as a soller slit. PSA function as a filter, allowing beam through specific angular range to reach the detector while blocking other unwanted scattering. Choosing a bigger slit size will lead to higher number of incident/detected photons but the resolution will be compromised. One needs to choose the balance between intensity and resolution based on the nature of the sample and information required. For example: if the study involves ultrathin films, which have weak diffracted intensity, it is important to use bigger slits. However, care needs to be taken as compromising the resolution too much will also lead to loss of valuable information in the diffraction patterns.

In addition, the penetration of incident beam inside the sample depends on the incident angle. If the incident angle is below the critical angle for total external reflection, the X-rays will not penetrate into the film and the diffracted intensity will

be from a limited top surface of the sample. Larger angle leads to higher penetration depth and as a result, more contribution from the film and the substrate. As the incident angle is increased further, there is more absorption of X-rays by the sample, which can reduce the diffracted intensity. Furthermore, if the incident beam size is smaller than the sample size, it is necessary to perform corrections related to the film area under diffraction for each reflection. The final measured intensity is also altered by the size of slits on the detector side. Therefore, correction related to film area needs to be carried out taking into account both incident and receiving slit sizes.

3.1.2 In-plane and out-of-plane scans

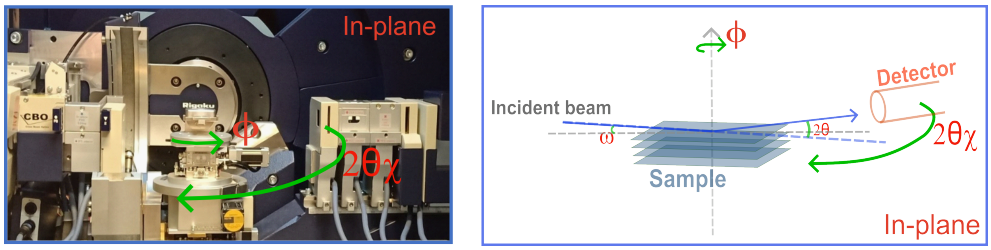

(a)

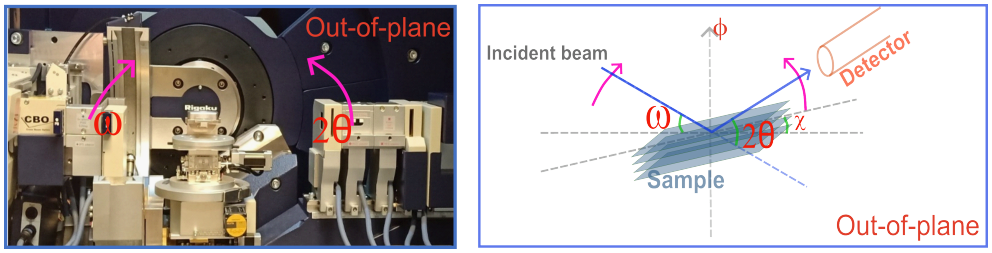

(b)

Figure 3.2: Schematics to show different methods of scans performed using SmartLab X-ray diffractometer and a picture of the instrument representing scan directions. (a) In-plane (IP) and (b) Out-of-plane (OOP).

The IP reflections are characterized by diffraction from lattice planes normal to the surface of the sample given by $(hk0)$ Miller indices family of reflections. The X-ray beam is employed on the sample with a grazing incidence, making the beam travel a long distance inside the film. The 2D scans are recorded while rotating the sample along vertical axis (ϕ) and performing $2\theta_\chi$ movement of the detector in the horizontal plane, hence called $2\theta_\chi$-ϕ scans. The incident angle (ω) and the OOP detector angle (2θ) are kept constant throughout the scan. The χ angle is also kept constant after correcting for the offset such that the sample stays horizontally flat.

On the other hand, the OOP reflections are the ones with $\ell \neq 0$, ℓ being the Miller index of a reflection. The sample is adjusted to access the desired reciprocal space point using χ and ϕ angles that are kept constant during the scan. The other two angles ($\omega - 2\theta$ rotations) are varied in order to perform the 2D scans. This type of

scans are useful in obtaining information about the film crystallography along both the surface and the normal to surface. The directions of rotations are marked in Figure 3.2.

3.2 D10/D10+ - neutron diffraction

The D10 instrument at Institute Laue Langevin (ILL) is a thermal neutron ($E \approx 25meV$) diffractometer, which has been increasingly used for magnetic structure determination of thin films. Recently, during the course of the thesis, the instrument underwent an upgrade (now called D10+), which has led to significant improvements in several areas of measurement.

A detailed technical description of D10 is provided below along with a discussion on its suitability for thin film measurements. The upgrades related to D10+ are described at the end. Figure 3.3 shows the layout of D10 and an image with thin film sample mounted.

D10 is a versatile diffractometer that can be used in four different configurations:

(a) Standard four-circle

(b) Standard two-axis

(c) Four-circle with energy analysis

(d) Two-axis with energy analysis

In this project, we have used the four-circle mode with energy analysis and the description has been kept limited to this configuration. The instrument set-up consists of Eulerian cradle, which is equipped with a helium-flow cryostat that allows cooling down to 1.6 K and 0.1 K with dilution. This rests on another motor that can be rotated on air cushions. The four different possible rotations are shown in Figure 3.4 and are defined as follows:

1. The sample holder is screwed to the Eulerian cradle and it can be rotated along an axis passing across it length. This rotation defines the angle ϕ.

2. The sample holder itself can be driven around the Eulerian cradle such that the sample always stays at the center of the circle. This angle of rotation is named as χ and the χ-axis lie in the equatorial plane.

3. The plane of the entire cradle can be rotated around the vertical axis (angle ω).

4. The detector set-up can be rotated in the horizontal plane making an angle 2θ with the incident beam direction.

It is to be noted that the sense of laboratory z-axis on D10 is opposite to the Busing-Levy convention discussed in chapter 2. This is done in order to have same sense of angular rotations. Thus on D10, 2θ, ω and ϕ follow left-hand rotation and χ is right-handed.

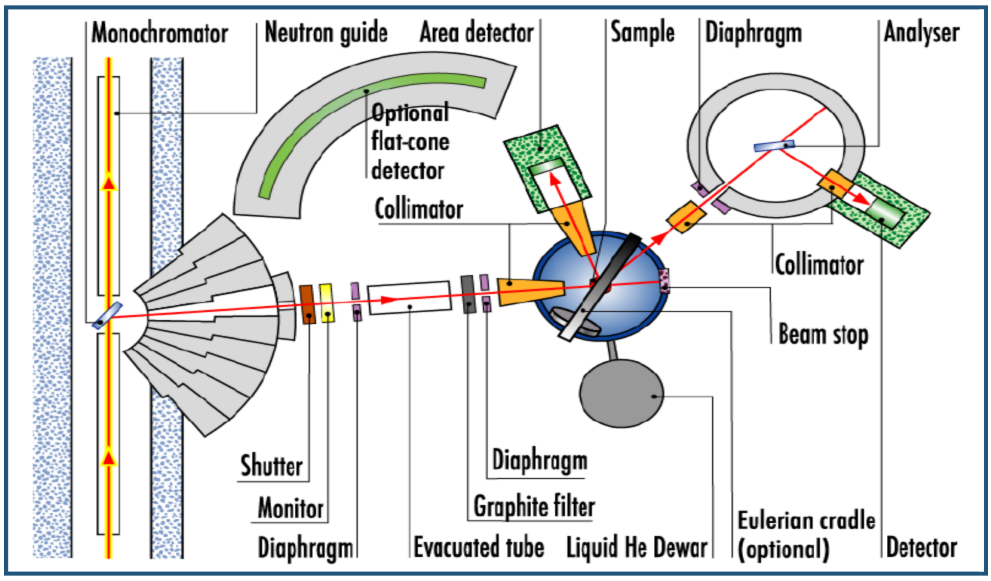

(a)

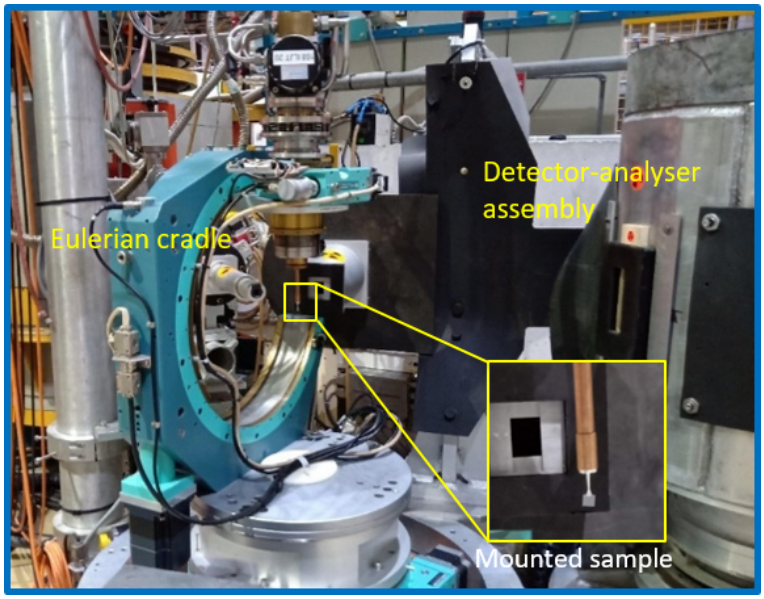

(b)

Figure 3.3: D10 diffractometer: (a) General layout with different parts of the instrument labeled (adapted from [75]). (b) A picture of the instrument showing a thin film mounted in four-circle mode.

3.2.1 Technical details

The full four-circle movements remain accessible even with the cryostat mounted. There are two ^{3}He detectors available. One is a position sensitive area detector (94 $\times$ 94 mm^2) and the other is a point detector, which is mounted on the analyzer table for energy analysis mode. The analyzer consists of a vertically focusing

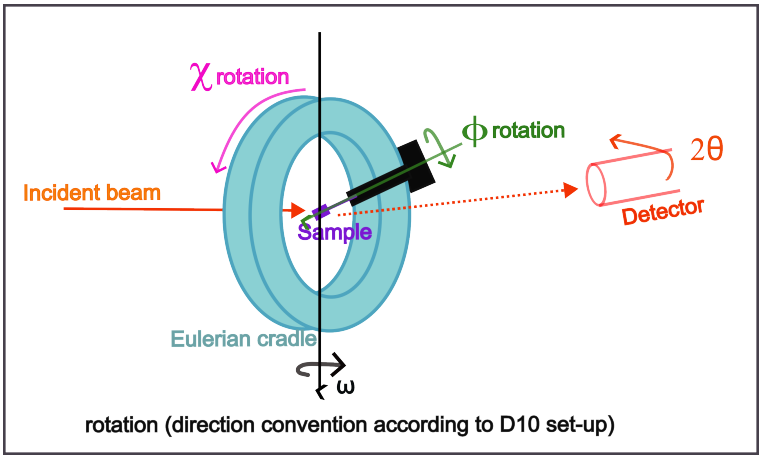

Figure 3.4: Schematic representing four possible rotations on D10 diffractometer equipped with Eulerian cradle.

pyrolytic graphite crystal to select the desired diffracted energy range. There are two monochromators (vertically focusing and continuously varying) that can be used to select incident wavelength in the range of 1 - 6 Å. There is a Cu (2 0 0) monochromator that gives wavelength in the range of 1 - 3 Å and the pyrolytic graphite (0 0 2) can select from 1.8 to 6 Å. The incident flux varies with the change in wavelength. To reduce the contamination due to second order harmonics ($\lambda/2$), two filters are available: pyrolytic graphite for wavelength in range 1.8 - 3 Å and Be for larger wavelengths.

The suitability of D10 for thin film diffraction is empowered by two important factors. The signal-to-noise ratio is crucial to detect diffraction peaks from thin films. D10 provides one of the best signal-to-noise ratio for instruments of this type and a very good resolution. Secondly, the signal from substrate is a big hurdle when it comes to thin film measurements. The energy analysis option allows to measure only the elastic signal and as a result, reduce the inelastic background coming from the substrate. The order of magnitude of elastic versus inelastic intensities depends on several factors such as sample, instrument etc., nevertheless it is possible that the inelastic signal is of the same magnitude in intensity as elastic. Therefore, it almost becomes necessary to use energy analysis in order to perform such measurements.

In spite of the mentioned advantages, ND on thin films remains a challenging task. The measurement time for each peak is very long ($\approx$ 4-6 hours for a scan of about 19 data points). This means that only a limited number of peaks can be measured. In addition, the integration of measured peaks is a delicate as one needs to be aware of the positions of substrate peaks. This is why, conventional data integration softwares cannot be trusted and the integration needs to be performed manually for each peak. There are several other sample specific difficulties that are discussed in the corresponding chapters of the thesis.

A typical thin film single crystal experiment on D10 can be described as fol-

lows. The goniometer head with glued sample is mounted on the Eulerian cradle and centered optically. At first, the sample alignment is carried out using substrate peak positions as they are much stronger and hence, easy to detect. Bi-dimensional detector is generally used for the initial alignment. The orientation matrix for the substrate is calculated using a few peaks. The peaks should be chosen such that all the dimensions of the sample can be centered properly. The substrate-film unit cell relation is used to transform the film peak indices into substrate unit cell setting. The scans are then programmed accordingly (in q-scan mode) in the Nomad software on the instrument computer. In this mode, the input for any scan is the range of Miller indices in substrate basis and the software automatically calculates the angular positions of the sample using orientation matrix. It is possible to calculate the film orientation matrix at a later stage of the experiment if there are sufficient film peaks available. With the film orientation matrix, one can directly provide the film Miller indices to be measured as the input. If the sample needs to be cooled down or heated, cryostat heads are mounted and same procedure is followed at the higher or lower temperature. The change in orientation matrix with temperature is directly related to the change in lattice parameters of the sample, assuming no phase transition.

For each scan, one can specify the monitor to be used, which is basically the number of neutrons incident per point in the scan. The level of monitor is chosen depending on the expected strength of the peak and statistics required. In order to compare the measured reflections, they first need to be normalized with respect to the monitor used.

3.2.2 D10+

The update on D10 was carried out during the time of long shut down at ILL (October 2021- February 2023). The shut down period was used to upgrade the neutron guides. During the same time-period, D10 was installed with new monochromators, new sample table and a new analyzer. The new monochromators are made of highly ordered pyrolytic graphite (HOPG) and Cu covering the wavelength range of 1 - 6 Å. The suppression due to second order harmonics is carried out using Be and HOPG filters. The initial measurements on D10+ indicate increase in flux up to a factor of 11. This is a significant advancement and very advantageous for experiments on thin films for which the diffracted signal is weak. In this project, experiments were performed on both D10 and D10+.

3.3 SQUID magnetometry

Superconducting Quantum Interference Device (SQUID) was employed to measure macroscopic magnetic properties of the epitaxial thin films. SQUIDs work on the principle of Josephson junction: two superconductors separated by a thin insulating layer. Changes in the magnetic flux coming from the sample are read through periodic modulations in the output voltage.

Josephson junction phenomenon
In a set-up of two superconductors separated by a thin insulating layer, the whole system behaves like a superconductor and electric current flows without any resistance. This is due to tunneling of Cooper pairs of electrons from one superconductor to another through the thin middle layer. Depending on the nature of current flowing, the junctions can be classified into two categories: direct current (DC) and alternate current (AC). AC SQUIDS (also called rf SQUID) are cheaper and easier to make but have lower sensitivity than the DC ones. SQUID based on DC type junctions was used in this project.

3.3.1 Working principle

A DC SQUID consists of two Josephson junctions fashioned parallel into a ring-shaped circuit (see Figure 3.5(a)). There is a defined critical current for every superconductor above which it looses its superconducting properties. As the magnetic field passing through the loop varies, it causes changes in the phases of electron wavefunctions, ergo, current passing through the junction also changes. As the current goes above the critical limit, there is resistance in the system and a voltage appears at the junctions (resistive mode). A fundamental property of superconducting rings is that the magnetic flux enclosed by them is quantized. The critical current changes with progressive increase or decrease in applied flux. Therefore, the output voltage changes periodically as depicted in Figure 3.5(b). One complete cycle of voltage corresponds to one quantum of magnetic flux, known as fluxon, given by $h/2e$ [76]. Thus, a SQUID in fact, is a flux to voltage transducer that converts tiny magnetic signals (one fluxon) into voltage signals.

In practice, a SQUID magnetometer is operated with a constant bias current (I_{bias}) slightly higher than the critical current. Screening current (I_s) changes from zero to maximum with magnetic flux quanta. A flux transformer with pickup loop is used to convey the magnetic field signal from the sample to the superconducting loop, as shown in Figure 3.5(c). When a magnetic field is applied, it produces a current in the pickup loop, which then produces equivalent flux in the SQUID junction. Any small changes in this flux can be detected by the SQUID with the help of bias current and voltage measurement as discussed above. Theoretically, SQUID magnetometers can reach sensitivity of about 10^{-9} emu order [9] (1 emu (electromagnetic unit) = 10^{-3} J/T). In reality, there are several factors that can contribute to lower

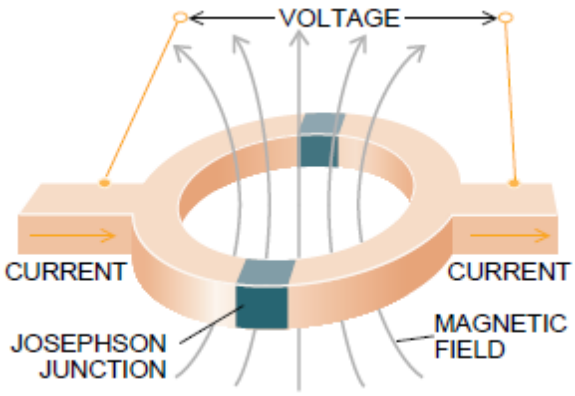

(a)

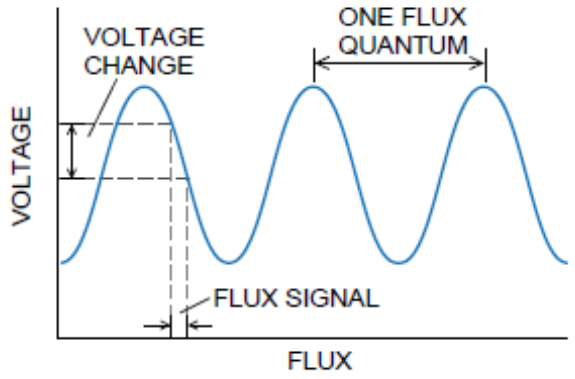

(b)

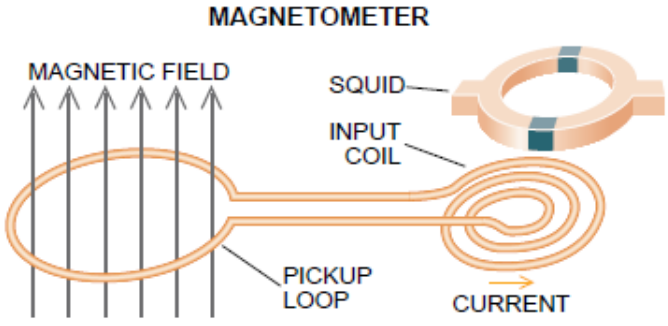

(c)

Figure 3.5: (a) Superconducting loop set-up in a typical DC SQUID (b) schematic representation of voltage oscillations with flux changes (c) model representing pick-up loop transmitting magnetic signal to SQUID (adapted from [76])

sensitivity and possible contamination in the measurements. A few such factors and the precautions to be taken are discussed below.

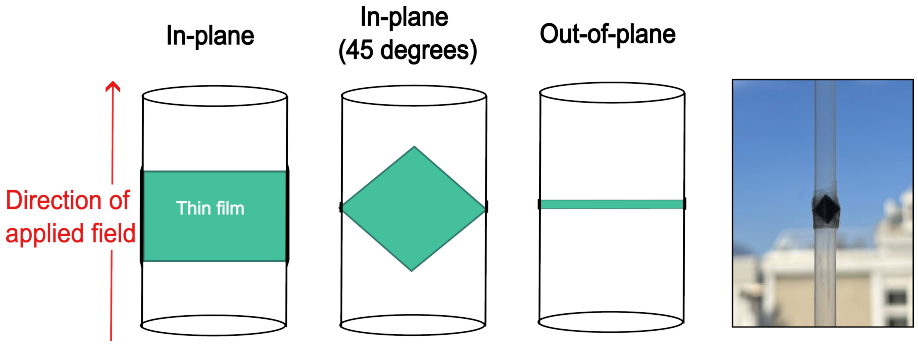

Figure 3.6: Different means of sample mounting for SQUID measurements using a straw. Rightmost image: One of samples mounted for measurement with field applied along 45 degrees in-plane direction.

- The sample is usually mounted using a non-magnetic drinking plastic straw. It is wedged inside the straw using non-magnetic adhesive tape, which is then mounted on one end of a rod (see Figure 3.6). This rod is then inserted into the sample chamber and the measurements are programmed in the MPMS (Magnetic Property Measuring System) Multivu software [9]. The first issue with this set-up is that although the straws are non-magnetic, they can contribute to the background signal by some extent ($\approx 10^{-7}$ emu signal) [8].

- Secondly, it is not easy to place the sample perfectly aligned along the desired direction inside the straw (see Figure 3.6). In the case of materials with magnetic anisotropy, this can lead to small offsets in the moment measurement.

- If the sample size is slightly bigger than the straw area, a tiny part of sample may penetrate outside the straw. In our case, the size of all the samples is $5 \times 5\ mm^2$, which is just enough to wedge the whole sample inside the straw.

- And finally, the straw should be free of any bends or curves as it may alter the sample alignment. One should also avoid cutting any extra holes in the region of the straw close to the sample as it can lead to additional diamagnetic signal. Any imhomogeneity in the straw magnetic profile will be detected by the pick up coils due to flux change. The straw should be clean and their re-use after one experiment should be avoided.

- There can be some experimental artifacts that can lead to instability in the measurements when the signal from sample is too weak. As a consequence, the acquisition of such data-points can be complicated and can present anomalous values. In case of a single such data-point, we have removed it from the presented data for better clarity on the plots. In addition, when an applied

magnetic field is removed, some flux gets pinned at the sample location, giving a weak magnetic field. This field generally assumes a direction opposite to the previously applied field. So, if the sample signal is weak it can alter the measured moment.

In spite of the above mentioned challenges, the realistic sensitivity in DC SQUID is still one of the best to measure thin film magnetism. The best possible data can be obtained by taking extreme care while mounting the sample.

3.3.2 Technical details

An MPMS (Magnetic Property Measurement System) XL SQUID at Institut Néel, Grenoble France, was used in this project. The instrument allows maximum possible applied field of 5 T and the temperatures can be varied in-between 3 - 320 K. The scans were performed in Reciprocal Space Option (RSO) mode in which, several sample movements through the pick-up coil are averaged to increase the sensitivity. Two different types of magnetic measurements were carried out.

- Temperature dependence of magnetization was studied by measuring the magnetic moment in a selected range of temperature at constant field. The data points were obtained at each selected step-size while cooling down or heating up the sample.

- Magnetic hysteresis loops were traced out by measuring the magnetization in varying field at constant temperature. At first, the field is applied along a particular direction of the sample and the strength is gradually reduced to zero while collecting data points at selected step size. The field is increased back to its starting value, but in the opposite direction. This whole process is repeated backwards to complete the hysteresis loop by tracing the magnetization curve, as explained in the previous chapter.

3.4 Thin film synthesis

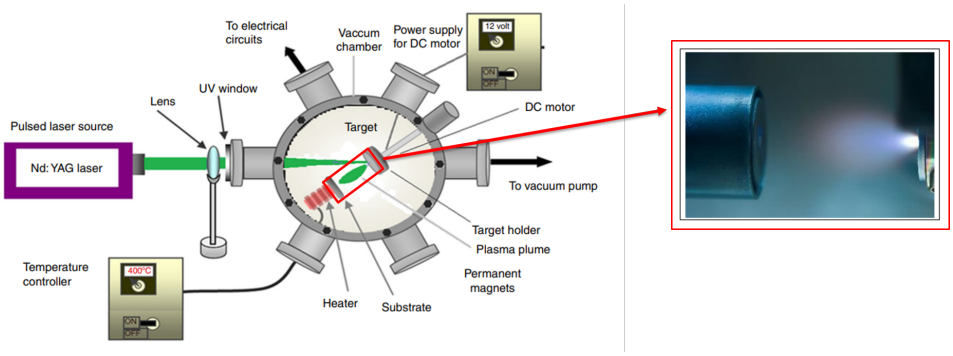

(a)

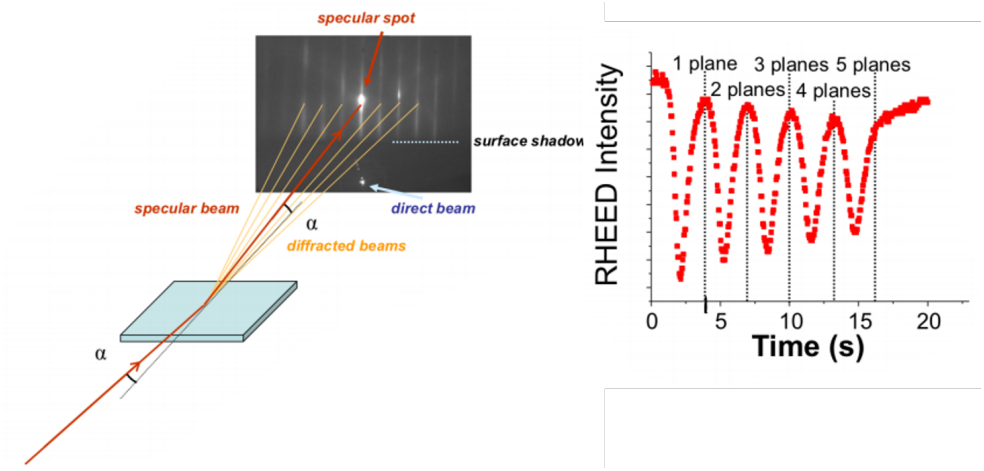

(b)

Figure 3.7: (a) Schematic of pulsed laser deposition set-up for thin film growth showing plasma created by laser evaporation of the target material. (b) Reflection high energy electron diffraction set-up: beam of electrons getting diffracted from the film surface at low angle of incidence. Right-side image shows surface sensitivity of the intensity of specular spot, (adapted from [77–79])

The film synthesis were not part of the PhD project and were carried out separately by B. Mercey and B. Domenges [1] at CRISMAT laboratory in Caen, France. A short overview of the synthesis process is provided in this section. The films were deposited using Pulsed Laser Deposition (PLD) technique [80]. PLD is a powerful method consisting of a target holder and a substrate holder in a vacuum chamber (see Figure 3.7(a)). The high-power laser almost instantaneously vaporizes the constituent material which then deposits layer by layer on the substrate. Molecular-beam epitaxy (MBE) was also utilized to carry out deposition of certain films [80, 81]. In MBE, the material elements of interest are evaporated individually in separate environments. The deposition rate is usually slower in MBE.

[1] CRISMAT, ENSICAEN-CNRS UMR6508, 6 bd. Maréchal Juin, 14050 Caen, France

The film growth is monitored using in-situ Reflection High Energy Electron Diffraction (RHEED) (Figure 3.7(b)). In RHEED, high energy electrons are scattered at a small incidence angle for surface characterization. One complete oscillation in RHEED intensity corresponds to deposition of one atomic layer. This way, precisely controlled deposition of multilayers can be achieved while maintaining epitaxy with the substrate. There are several parameters such as laser energy, substrate temperature, oxygen pressure that need to be optimized in order to synthesize high quality superlattices. The deposited structures were annealed in oxygen environment at high temperatures. Details of synthesis parameters are provided in the corresponding chapters.

3.5 Transmission electron microscopy

Initial characterizations of the films were performed by B. Mercey at CRISMAT lab Caen, France using Transmission Electron Microscopy (TEM). TEM is a powerful imaging technique that can be used to analyze internal structure and properties of thin samples. It is widely utilized to visualize quality of growth of thin films and their composition. As the name suggests, it involves transmitting a high energy beam of electrons through a thin film and the electron-atom interactions are used to produce high resolution images. These interaction can be elastic or inelastic in nature. The resulting electron image is formed based on the differences in electron transmission through different regions of the sample revealing finest details. In addition to imaging, TEM can also be used to perform electron diffraction. In diffraction mode, the electrons are diffracted from the crystal lattice. The diffraction pattern obtained carries information about the crystal structure and orientation. In this project, TEM measurements were performed using an ARM200F (double corrected JEOL TEM, 200 kV) microscope with z dependent contrast images along different sample directions.

With this section, we conclude the prerequisites portion of the thesis. The following chapters will delve into the literature review, present results, and engage in discussions regarding the various samples.

Chapter 4

$La_{0.67}Sr_{0.33}MnO_3$ thin film

Contents

What to expect in this chapter

In this chapter, the work done on LSMO film is described. Experimental challenges and complex data analysis are core parts of this study and are explained in details. Starting with a literature review, a brief introduction to the field of LSMO films is provided. Then, the different techniques used and the results obtained from them are discussed one by one; first XRD, then SQUID, and ND at the end. The overall work of this chapter in summarized in the conclusion at the end.

4.1 State of the art

Manganese oxide compounds of general formula $AMnO_3$ (A can be a rare-earth, alkali or alkaline cation) crystallize in perovskite type structure [1] and are commonly referred to as *manganites*. An ideal cubic perovskite structure is shown in Figure 4.1 using an ABO_3 schematic. It consists of B-O corner-sharing octahedra with cation A at the center of the cell on a 12 coordinated site. Any contraction, extension or tilt in the octahedra can lead to significant changes in the material's physical properties. Depending on the composition, manganites possess a variety of chemical and physical properties [84–88].

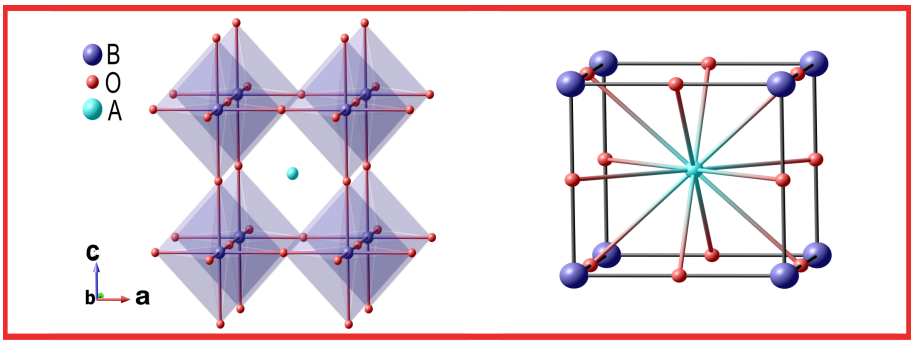

Figure 4.1: Schematic of an ideal cubic perovskite structure (ABO_3) showing B-O octahedron (left) and 12 coordinated cation A (right).

Doped manganites

Doping the manganites with suitable metals at site A leads to more fascinating physical properties such as magnetoresistance, half-metallicity etc. Doped manganites of general formula $La_xB_{1-x}MnO_3$ (B = Ca, Sr, Ba, Pb) have been intensively studied for more than 50 years. These compounds were first investigated by G. H. Jonker and J. H. Van Santen in 1950s, where they discussed the crystal structure and magnetic properties of B = Ca, Sr, Ba compounds [89–91]. Further research carried out on $La_xB_{1-x}MnO_3$ family of manganites revealed many exciting features of these compounds. They show a wide range of electronic (insulating to metallic), magnetic (AFM, FM and ferrimagnetic), and superconducting phenomenon, making them ideal candidates for various technological applications such as magnetic sensors, fuel cells, spin logic gates and thermoelectric devices [92–100].

4.1.1 Properties of bulk LSMO

The complex interplay of charge, lattice, spin and orbital degrees of freedom is particularly interesting in $La_{1-x}Sr_xMnO_3$ compounds. The complete complex phase diagram of $La_{1-x}Sr_xMnO_3$ is shown in Figure 4.2[101, 103]. Depending on the level

[1] Perovskite structure is named after a Russian mineralogist who discovered the $CaTiO_3$ perovskite mineral. The mineral was examined by German crystallographer Gustav Rose who determined its physical properties and chemical composition [82, 83].

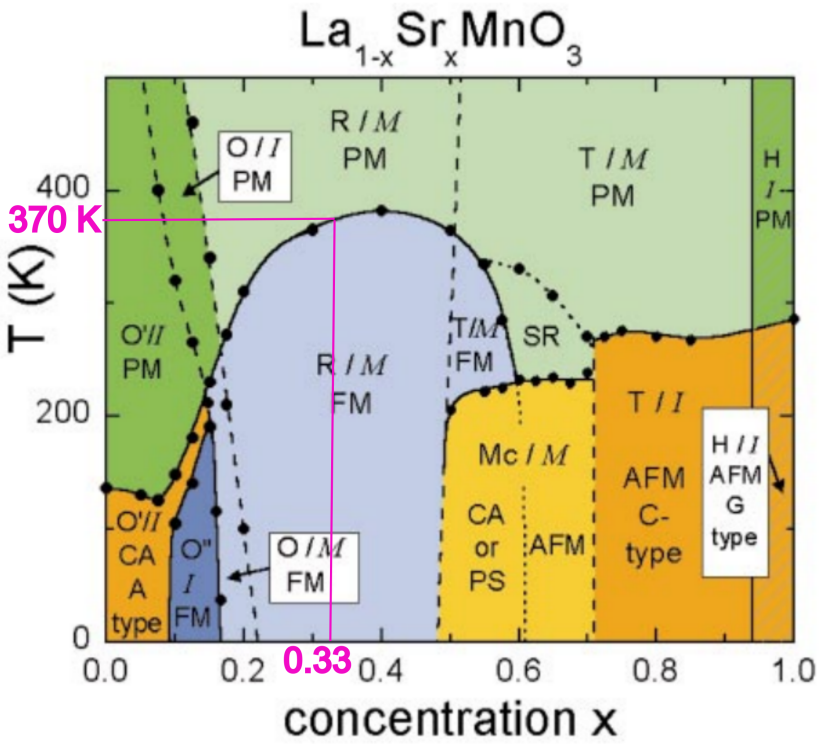

Figure 4.2: Phase diagram of bulk $La_{1-x}Sr_xMnO_3$ single crytals for the whole concentration range. The crystal structures (Jahn-Teller distorted orthorhombic, O′; orthorhombic, O; orbital-ordered orthorhombic, O′/; rhombohedral, R; tetragonal, T; monoclinic, Mc; and hexagonal, H) are indicated as well as the magnetic structures (paramagnetic, PM; short-range order, SR; canted, CA; A-type antiferromagnetic structure, AFM; ferromagnetic, FM; phase separated, PS; and AFM C-type structure) and the electronic state (insulating, I ; metallic, M)(adapted from [101]). Please note that the paramagnetic phase for x = 0.3 is written as metallic here, which is reported to be insulating due to higher resistivity[102].

of Sr doping, the physical properties and structures of these compounds vary over a wide range. The crystal structure is orthorhombic for low levels of doping ($x < 0.2$) and changes to monoclinic and hexagonal at higher x values [104, 105]. The magnetic ordering can vary from AFM (canted) to FM and then back to AFM as the Sr concentration increases. Our interest lies in the compounds with $x = 0.33$ as their range of properties makes them suitable candidates for spintronics, as discussed next.

Bulk $La_{0.67}Sr_{0.33}MnO_3$ (LSMO) crystallizes in $R\bar{3}c$ space group structure with lattice parameters $a = b = 5.5$ Å $c = 13.3$ Å in hexagonal unit cell as shown in Figure 4.3 [107]. It is found to be ferromagnetic below 370 K. This is the very close to the highest T_c in the family of La-Sr manganites, making them optimal materials for spin-based devices. The magnetic spin arrangement prefers [111] crystallographic direction (with rhombohedral structure) making it the easy-axis of magnetization and is associated with magnetocrystalline anisotropy [108]. It is also reported that at the

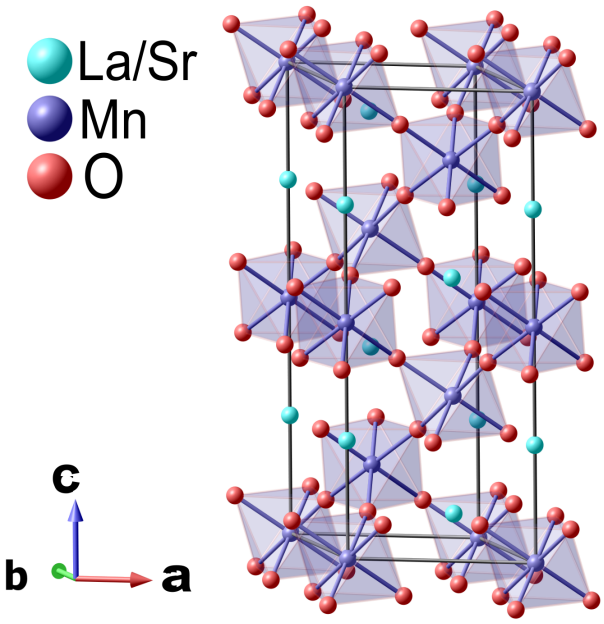

Figure 4.3: Crystal structure of bulk LSMO ($R\bar{3}c$ space group) in hexagonal unit cell setting (plotted using Mag2pol software [106] and data taken from [107]).

surface the magnetization lies in-plane along [110] direction possibly due to surface anisotropy [109].

In addition, these compounds are found to be half-metallic in the FM phase and their resistivity increases in paramagnetic phase [90, 91]. The half-metallic nature can be explained using DE mechanism [110, 111]. Due to doping of Sr^{2+} cations, there is a mixture of Mn^{3+} and Mn^{4+} ions in the compound. The electronic configuration of Mn^{3+} is $[Ar]3d^4$, which means it has 4 unpaired electrons in the d-shell as per Hund's rule. The fourth unpaired electron in Mn^{3+} follows a hopping mechanism through the oxygen atom. Since Mn^{4+} has its e_g orbital empty, the electron can occupy it without changing its spin (see Figure 4.4). This leads to conductivity for only one type of electron spin or in other words 100 % spin polarization, also know as half-metallic behavior.

There are two possible degenerate states of the DE mechanism in the case: $\psi_1 = Mn^{3+}O^{2-}Mn^{4+}$ and $\psi_2 = Mn^{4+}O^{2-}Mn^{3+}$. During the hopping process, the state changes from ψ_1 to ψ_2. Since the two states are degenerate, the system stays in its lowest energy configuration. The electron hopping is directly related to spin arrangement (parallel) of neighboring ions. In the paramagnetic phase, there is no ordering of spins and hence, no half-metallic conductivity.

The degeneracy of Mn^{3+} d-orbitals in these compounds is broken due to crystal field splitting in octahedral environment. It is further uplifted due to Jahn-Teller effect. The fourth unpaired 3d electron in Mn^{3+} can occupy either of the e_g doublet

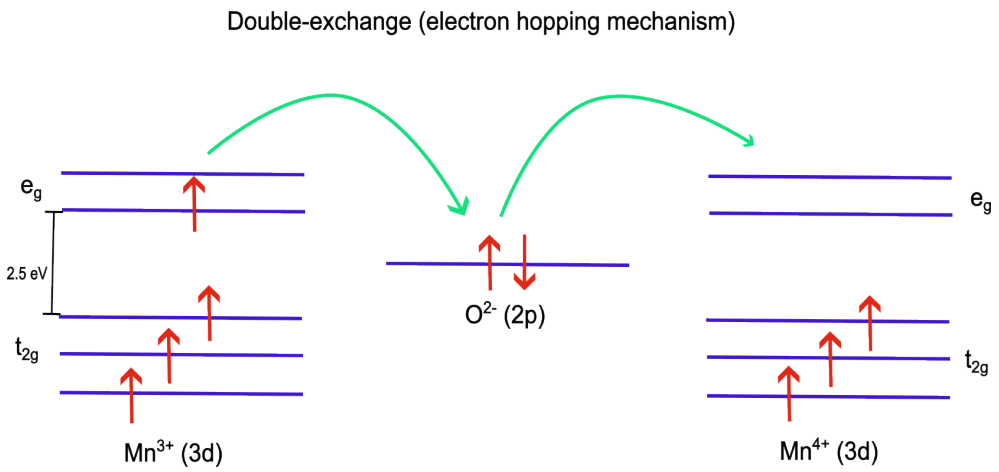

Figure 4.4: Schematic to illustrate the electron hopping mechanism during Double-exchange in Mn^{3+}-O^{2-}-Mn^{4+} in LSMO compounds.

orbitals. Depending on which orbital is occupied, there can be lattice distortions changing the oxygen octahedra network. If the bonds along z-direction are lengthened as compared to the $x - y$ plane, the electron occupies $3d_{z^2}$ orbital, due to lesser electronic repulsion along z. This type of changes in the atomic structure, can lead to alterations in the physical properties of the system. For example, it is reported that Jahn-Teller distortion is correlated to spin orientation in FM LSMO compounds [104]. Several compounds of this family have been identified to show magnetic order-disorder transition due to Jahn-Teller effect [105].

In addition, the presence of colossal and giant magnetoresistance has also been established in these compounds [112, 113]. These properties are highly desirable for spin-based devices as they confirm electric-magnetic coupling in the system. This phenomenon in LSMO is argued to be related to the double exchange mechanism as the conductivity of electrons is affected by the magnetic ordering in the system.

4.1.2 LSMO thin film

As discussed above, the interesting functional properties shown by LSMO compounds makes them ideal for spin-based devices, demanding their miniaturization in the form of thin films. This has led to a surge of interest in LSMO based thin films.

Epitaxial thin films of LSMO have been widely studied with different materials as substrate. It is well-known that the properties of epitaxial films are primarily governed by the strain due to substrate. This is related to the substrate - film lattice mismatch. The greater the lattice mismatch means that there will be a higher degree of strain and hence, different types of structural distortions can occur in the film. For LSMO, a variety of substrates has been investigated including $LaAlO_3$, $NdGaO_3$, STO, $(LaAlO_3)_{0.3}(Sr_2TaAlO_6)_{0.7}$ etc. [114–117]. Figure 4.5 lists commonly used substrates for perovskite materials on a line scaled to their in-plane lattice parameters [118]. The black arrow marks the lattice parameters of bulk LSMO in Rhombohedral unit cell setting. From this plot, one can easily see the suitable substrates for LSMO

films in the sense of lattice mismatch.

The lattice mismatch between STO and LSMO is only 0.64% (LSMO = 3.88 Å and STO = 3.905 Å). Bulk STO crystallizes in cubic P*m-3m* space group at 300 K and goes under a phase transition around 110 K [119]. The low temperature phase is tetragonal with I*4/mcm* space group [120]. This exact transition has not been reported in thin films of STO below 90 nm thickness. It is expected that LSMO films should be under tensile IP strain due to larger STO parameter. This will lead to reduction in OOP lattice parameter of the film as compared to bulk LSMO.

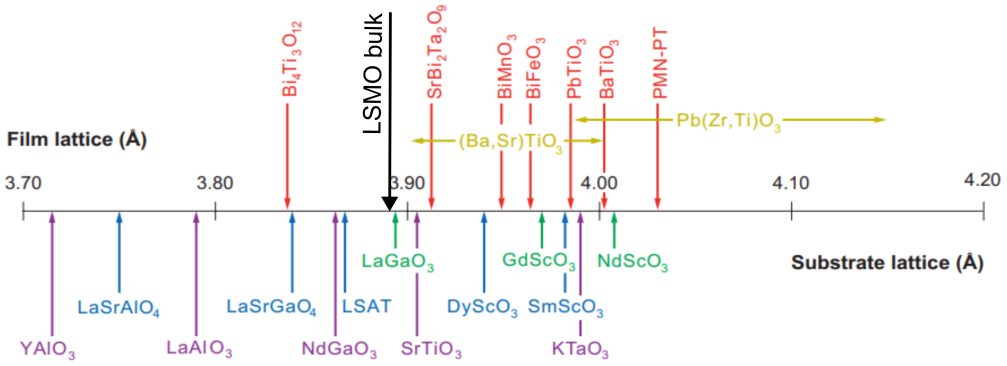

Figure 4.5: A number line showing the a-axis lattice constants (in Å) of some perovskite-related substrates (adapted from [118]). The black arrow marks the lattice parameter of bulk LSMO in rhombhohedral unit cell.

In addition to lattice parameters, several other quantities such as chemical reactivity, electric conductivity also need to be taken into account in order to have good quality epitaxial films. This is explained in-detail in Chapter 2. Overall STO has been established as a very suitable candidate for LSMO films.

Silicon (Si) is a crucial part of semiconductor industry. Therefore, there is high demand to create thin films with Si as a substrate for applications. However, they do not present a suitable choice for LSMO substrate. Several publications have shown that it is possible to do so by using a buffer layer of STO in-between Si and LSMO [121–124]. The lattice mismatch between Si and STO is about 1.7%. We have employed a similar strategy to study the behavior of LSMO films. In this chapter, we present our results on this sample of LSMO/STO/Si configuration.

Properties of LSMO/STO thin films

The field of research on LSMO thin films is vast and STO is one of the most commonly used substrate. In order to keep the discussion relevant, we will mainly focus on the magnetic and structural aspects of LSMO/STO thin films.

Similar to their bulk systems, LSMO thin films also show insulator-metal transition and giant magnetoresistance effects [17]. The electric and magnetic properties of LSMO/STO films can be manipulated largely depending on the thickness and growth conditions. The magnetic transition temperature is found to be higher for thicker films [16, 124]. At a thickness of 55 nm, the transition temperature is 360

K, which is very close to the bulk value. It is strongly depressed at lower thickness, reaching a value of about 150 K at 12 nm (see Figure 4.6). In addition, the IP magnetization is found to follow FM ordering [18, 21]. The overall easy-axis of the film lie in-plane and the possible origin of anisotropy is magnetocrystalline in nature due to strain [32]. At a very low thickness of about 3 unit cells, it is reported that there is co-existence of FM and AFM phases in the system [109].

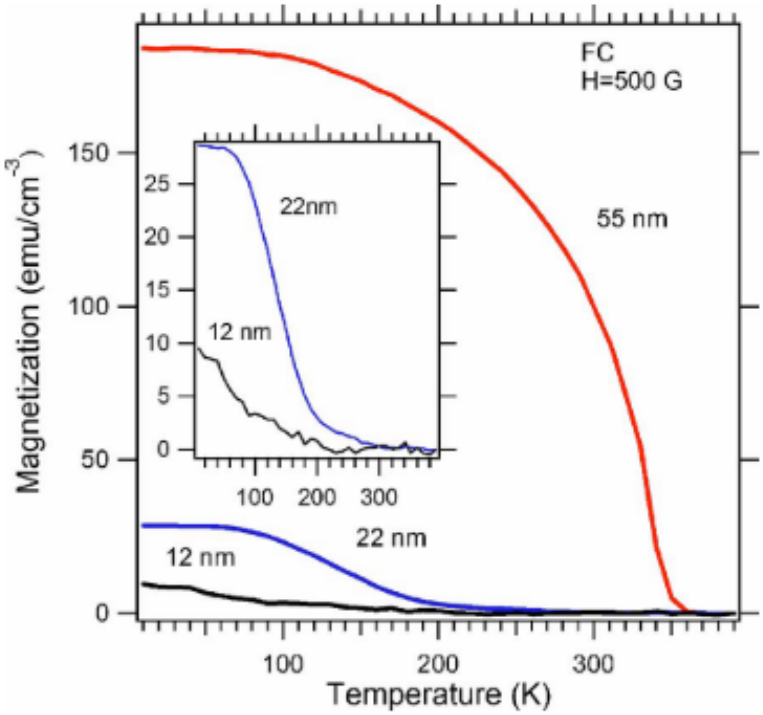

Figure 4.6: Temperature dependence of field cooled magnetization of LSMO/STO films of varying thickness, from 55 nm down to 12 nm. The inset shows the enlarged graphs of temperature dependence of magnetization curves for 22 nm and 12 nm thick films (adapted from [124]).

Furthermore, the magnetization is dependent on the oxygen environment during the film growth. It is argued that a low oxygen pressure leads to oxygen vacancies in the system and hence, weak magnetism [19]. This can result in low magnetic transition temperature. Furthermore, the magnetoresistance property is also thickness dependent and is shown by the films with thickness more than 9 monolayers [20].

In terms of crystal structure of these films, there is no clear knowledge of the atomic and magnetic arrangements inside the film. There are few studies that reported the nature of orbital occupation at the interface for low thickness films [26, 27, 125]. The structure at the interface is found to be surprising in terms of orbital occupation. The drastic changes in the properties at the low thickness are believed to be due to preferential occupation of $3d_{z^2}$ orbital (instead of $3d_{x^2-y^2}$), as a result of increased c-lattice parameter at the interface. This leads to decrease in DE mechanism

and reduction in the Magnetic transition temperature (T_M). This is why the first few layers in LSMO are termed as *dead layer*, and it is independent of the film thickness [25]. However, at present, there is no clear information available on the complete crystal structure of these films (at least for thickness higher than few monolayers).

Moreover, although the dramatic changes in the film's magnetic properties have been well-studied, there is still need for the overall magnetic structure picture. The OOP magnetic ordering is crucial for spin-based devices and yet, it is not well-established. This is probably because the determination of magnetic structure of thin films is a big challenge. The data analysis is not straightforward as shown in the subsequent sections. The huge potential of these films for technological applications demands complete nuclear and magnetic structure determination, which is the goal of this study in the thesis.

Following the above reasoning, we have chosen Si as a substrate for the LSMO film. A buffer layer of STO was incorporated in-between, in order to promote better growth of the film. The film is of composition ($[La_{2/3}Sr_{1/3}MnO_3]$(40 nm)/STO(20 nm)/Si) and surface size $5 \times 5\ mm^2$.

Film synthesis

The synthesis parameters for the LSMO are provided below for the reader's reference.

The LSMO film used in this study was deposited using Pulsed Laser Depostion (PLD) on a Si substrate with in-situ RHEED at CRISMAT lab, Caen. First, 20 unit cells of STO buffer layer were deposited using PLD, on top of the already Molecular Beam Epitaxy (MBE) STO at 650 °C, in 1.6×10^{-5} mbar pressure. Then, the deposition of 400 Å of LSMO (104 unit cells) was carried out, at 650 °C in a pressure of 4.2×10^{-4} mbar, in deposition atmosphere of 0.1% volume ozone and oxygen. The deposited film was cooled in 5.9×10^{-3} mbar pressure with a mixture of ozone (7% volume) and oxygen. The cooling rate was 50 °C/minute, after a 30 minute annealing period in the same atmosphere.

4.2 Characterization using TEM

In this section, results obtained using electron microscopy and electron diffraction are presented. The experiments and analysis were performed by B. Mercey and B. Domenges for initial characterization of the film. The detailed structural analysis were then carried out using XRD discussed in the next section.

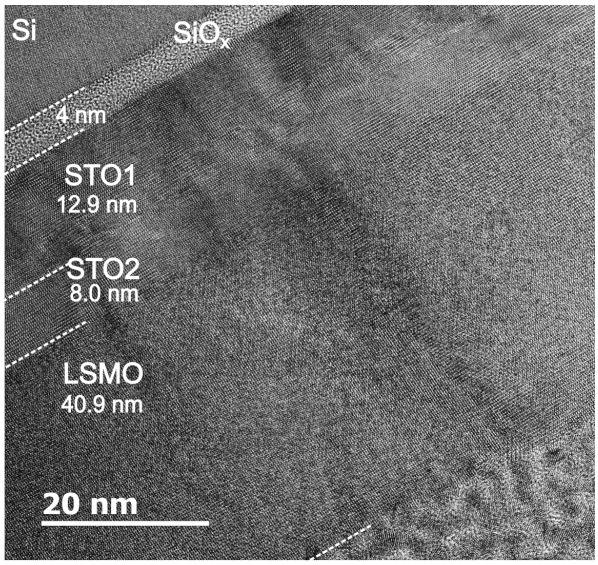

Figure 4.7: Transmission electron microscope (TEM) image of the LSMO thin film seen along [010] direction in STO unit cell, highlighting different layers.

Figure 4.7 shows a TEM image of the sample seen along [010] direction in STO unit cell, which is cubic with lattice parameter 3.9 Å. There are two layers of STO with thicknesses 12.9 nm and 8 nm, as expected from the deposition mechanism. The uniform stacking of layers along the c-axis (OOP direction) shows the quality of epitaxy of the film. The film thickness is determined to be 40.9 nm. A very thin layer (4 nm) of silicon oxide formed at the Si-STO interface probably due to oxidation after annealing the film. This can affect the growth of STO layer but since LSMO is deposited on the second STO layer, the epitaxy is well-maintained. The LSMO-STO interface shows no significant distortion or defects, which points to the fact that the film follows constraints from STO and under strain.

Electron diffraction measurements showed that there is a doubling of the LSMO unit cell as compared to STO. Here's how the doubling of unit cell can be inferred:

Figure 4.8(a) shows the electron diffraction pattern of the sample in $(-hh\ell)$ plane of STO unit cell. The peaks from LSMO in this plane belong to 3 families. If we go by the STO unit cell notations these peaks are described as follows. One is labeled in red; $(\frac{1}{2}\frac{1}{2}\frac{1}{2})_{\text{STO-cell}}$ and equivalent ones. The second and third families are in green; $(001)_{\text{STO-cell}}$ labeled 3.86 Å and $(110)_{\text{STO-cell}}$ labeled 2.72 Å. The peaks observed at $(\frac{1}{2}\frac{1}{2}\frac{1}{2})$ (in STO unit cell conventions) do not exist in the paramagnetic phase at RT.

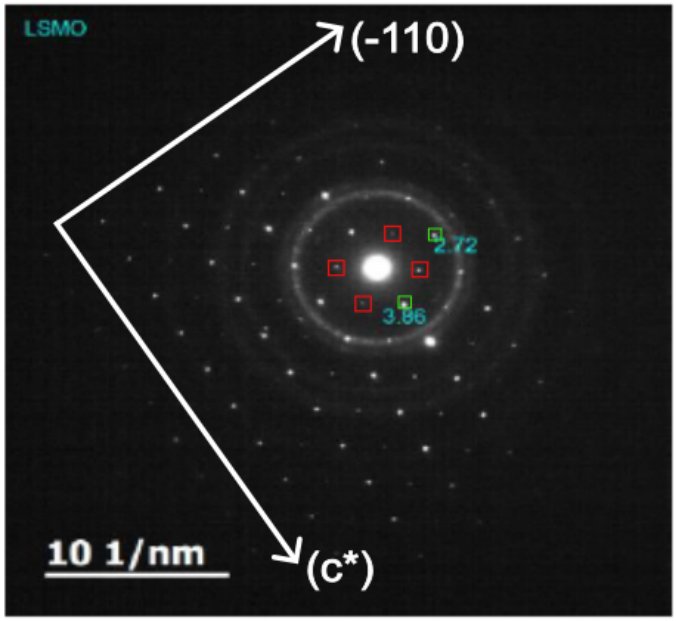

(a)

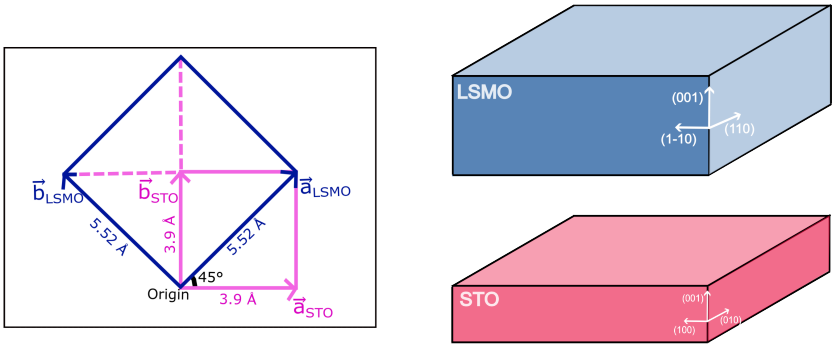

(b)

Figure 4.8: (a) Electron diffraction peaks measured on the LSMO film highlighting features that require unit cell doubling. The direction (-110) is in smaller STO unit cell notation. The peaks from LSMO in this plane belong to 3 families. One is labeled in red; $(\frac{1}{2}\frac{1}{2}\frac{1}{2})_{\text{STO-cell}}$ and equivalent ones. The second and third families are in green; $(001)_{\text{STO-cell}}$ labeled 3.86 Å and $(110)_{\text{STO-cell}}$ labeled 2.72 Å. The presence of $(\frac{1}{2}\frac{1}{2}\frac{1}{2})_{\text{STO-cell}}$ peaks shows that the unit cell must be doubled. (b) Relationship between STO and LSMO unit cells. There is rotation of 45° IP and it is doubled along the *c*-axis as well. Schematic on the right side shows crystallographic directions of the LSMO film and STO.

These peaks in LSMO doubled unit cell convention correspond to: family 1; $(0\ 1\ 1)_{\text{LSMO-cell}}$, family 2; $(0\ 0\ 2)_{\text{LSMO-cell}}$ and family 3; $(2\ 0\ 0)_{\text{LSMO-cell}}$. Therefore, the unit cell must be doubled IP as illustrated in Figure 4.8(b), rotated by 45° and doubled along the *c*-axis as well. The relation between the two unit cells is according to the

following equations:

$$\vec{a} = \vec{a'} + \vec{b'} \tag{4.1}$$

$$\vec{b} = -\vec{a'} + \vec{b'} \tag{4.2}$$

$$\vec{c} = 2 \times \vec{c'} \tag{4.3}$$

where, $\vec{a}$, $\vec{b}$, $\vec{c}$ are the lattice vectors in LSMO unit cell and $\vec{a'}$, $\vec{b'}$ and $\vec{c'}$ are the lattice vectors in smaller STO unit cell ($a = b = c = 3.9$ Å). The lattice parameters obtained for the LSMO cell are $a' = b' = 5.52$ Å and $c' = 7.7$ Å.

Please note that there is a 3^{rd} unit cell, which is of Si and we have used it to align the sample in ND measurements (Orientation matrix (UB-matrix) calculated based on Si diffraction peaks). We found that the thin SiO_x layer does not disrupt the epitaxy between STO and Si. The Si unit cell is cubic with lattice parameters 5.43 Åand it is aligned by 45° IP rotation with respect to the STO unit cell. Thus, the LSMO unit cell (double as per STO) is aligned on top of Si one with a lattice mismatch represented by the difference between their IP lattice parameters: 5.52 Å and 5.43 Å respectively. Using ND measurements discussed in Section 4.5, we confirmed this relation between LSMO and Si cells.

4.3 Nuclear structure using XRD

XRD experiments were performed on this sample using SmartLab Rigaku diffractometer at RT to study the nuclear structure of the film. The aim was to resolve the atomic positions of the LSMO film using structural refinements, that can be used later to refine magnetic structure using ND. These experiments were challenging in many ways. As there is no direct program available on SmartLab to measure diffraction peaks on such films, the peak centering was not easy. In addition, calculations related to different corrections to the intensity were performed by hand. New ways of integrating peaks were also developed. And finally, the low number of reflections in the data-set meant that the structural refinement had to be performed strategically combining FullProf with Python.

Incident wavelength of 1.54 Å was used. The reflections were measured using 3 types of scans; 2θ-ω 2D (OOP), $2\theta_\chi$-ϕ 2D (IP) and 1D (0 0 ℓ) scans. For 2D scans, the measured intensity was recorded as a function of the two rotating angles. In total, three experiments were performed; 2 for IP set-up and 1 for OOP. The incident intensity and resolution of each experiment was selected using specific slit sizes (also affects divergence of the beam). The details of instrumental parameters for each experiment are listed in Table 4.1. These parameters were used in calculating the film area under diffraction for each scan (described in-detail in next section).

Table 4.1: The size of slits used in different XRD experiments LSMO sample and the corresponding divergence (H-Horizontal, V-Vertical, deg-degrees). Open means that there was no slit used to reduce the size of the beam at the position.

		Out-of-plane	In-plane	
Type of slit	Direction	Run1	Run2	Run3
Incident slit	H	5 mm	2 mm	2 mm
	V	2 mm	0.3 mm	0.1 mm
Incident divergence	H	Open	0.5 deg	0.5 deg
	V	0.06 deg	0.06 deg	0.06 deg
Detector slit	H	Open	Open	Open
	V	2 mm	10 mm	10 mm
Detector divergence	H	5 deg	0.228 deg	0.5 deg
	V	0.5 deg	Open	Open

Measurement strategy

As mentioned in Chapter 3, it is not straightforward to measure reflections in a single crystal diffraction method on SmartLab diffractometer. Now we will review the experimental procedure in-detail, that was followed to perform such measurements.

At first, the sample was aligned with the beam height and corrected for horizontal offsets (defective flatness due to gluing procedure). In OOP geometry, (0 0 ℓ) scan was performed for 2θ up to 120°. It was a 1D scan varying the 2θ and ω values, keeping the sample fixed (ϕ and χ angles). We also recorded 2D scans using both IP

and OOP modes. The sample alignment process for these scans is described below.

- IP scans were measured using $2\theta_\chi - \phi$ rotations, i.e. detector - sample movement (please refer to Chapter 3 for detailed definitions of different rotations). In these scans, the source is fixed at grazing incidence and the sample's horizontal plane is also kept fixed after correcting for offsets. The detector moves only in the surface plane and sample rotation is with respect to the vertical axis. The detector's position for each peak was calculated using Bragg's law ($2\theta_\chi$). Then, a quick 360° ϕ rotation was carried out in order to locate the peak. In fact, this rotation would reveal 4 equivalent peaks of the chosen reflection, as we will see in the discussion later. Once the center $2\theta_\chi - \phi$ positions of the peak were obtained, we could simply plan the 2D scans around this position. The angular widths of the scans was decided keeping in mind to also include the peaks from the STO layer.

- OOP scans were slightly more complex to locate. In this case, one needs all the four angles to find the peaks as the sample needs to be tilted horizontally (χ can be non-zero) as well as the source moves during the scan ($\omega - 2\theta$). So first of all, 2θ is calculated using Bragg's law for the chosen reflection. Half of this angle gives us the position of the source, ω. The χ angle was calculated as follows. For all our thin films samples, we know that the [100] and [010] axis of STO are along the edges of the sample and the [001] direction is along surface normal. This was also verified during the measurements. Thus, the horizontal tilt of the sample i.e. χ angle for a particular reflection is given by the angle between the chosen reflection's vector in the reciprocal space ($hk\ell$) with the (0/0/1) vector. This can be calculated using simple vector algebra. Let us take an example.

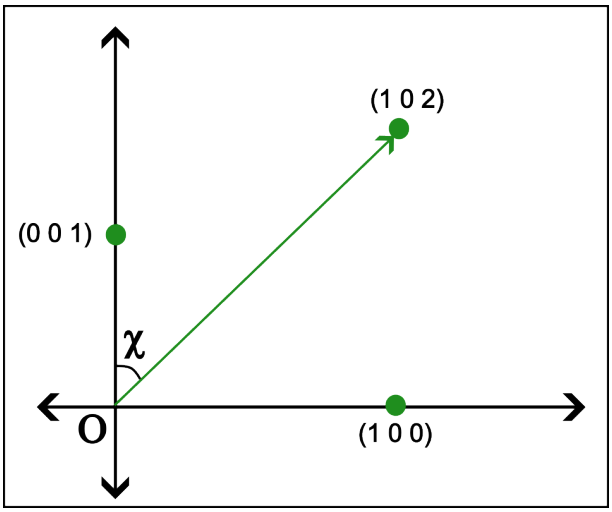

Figure 4.9: Schematic showing the angular position of (1, 0, 2) with (0, 0, 1) vector in reciprocal space plane ($h0\ell$). The reciprocal space points are not drawn to scale. The angle χ represents the horizontal tilt of the sample in XRD experiments.

Consider reflection $(1\ 0\ 2)_{\mathrm{LSMO}}$, which can be visualized in the reciprocal space as shown in Figure 4.9. By doing dot product of vectors $(0, 0, 1)$ and $(1, 0, 2)$, we find that the angle between them about 26.25°. This gives us the angle χ. Then, similar to IP scans, a 360° rotation of angle ϕ would give us the position of the peak. It is to be noted due to gluing the rotations of the sample are hindered in XRD. This is a significant difference between XRD on thin films and crystal samples. To overcome this, for some reflections, the χ angle was kept zero and the horizontal tilt of the sample was accommodated in the position of the source (ω). Doing so, allows more reciprocal space to explore through different rotations and hence, more reflections could be measured.

Now, we move to the data analysis part, starting with converting the measured angular scans to their corresponding reciprocal space mapping.

4.3.1 Calculating $(hk\ell)$ from diffractometer angles

The $(hk\ell)$ value (position in reciprocal space) corresponding to each data-point can be calculated from the corresponding diffractometer angles using the UB-matrix. It is useful to plot the scans against their reciprocal space points in order to analyze the peak shapes correctly and carry out the peak integration. Therefore, the UB-matrix was first calculated by-hand for each experimental data-set.

U-matrix (U-mat) basically relates the crystal frame of reference to that of the laboratory using a matrix representing the rotations carried out through angles ϕ, χ, and ω. In order to calculate the U-mat, a rotation matrix needs to be constructed that represents the offsets in the crystal and instrument coordinate systems. Then, the inverse of this matrix gives us the U-mat. To do this, we made use of the property; the two frames (orthogonal unit-vector triples) should coincide when all the instrument angles are set to zero. At first, we need to define the unit-vector triple for each frame. We know that the [100] and [010] direction of the STO unit cell are along the edge of the sample. This means that we can take one unit vector of instrument frame along this direction ($t_{1\phi}$). Busing-Levy conventions require that the third unit vector should be perpendicular to this one (ϕ-axis - ($t_{3\phi}$)) and the second one is only constrained to lie in the plane of t_{1c} and t_{2c}.

Let us take an example of the IP experiment. The rotation matrix (denoted by u_ϕ) is given by the multiplication of the $\mathbf{\Phi}$, $\boldsymbol{\chi}$, and $\mathbf{\Omega}$ matrices as defined in Chapter 2. While measuring the IP reflections, χ angle stays zero (after correcting for the offset during the alignment). This means that the χ rotation axis are aligned with the sample's coordinate system and there is no rotation needed for this. Similarly, the incident beam angle ω is also kept fixed during the experiment. As the exact position is arbitrary, it can also be taken as zero for the matrix calculation. Thus, 2 out of 3 axes are already aligned in the two frames at zero angular positions. We calculated the offset in ϕ angles using the fact that ϕ should be equal to $2\theta_\chi/2$ at the diffraction condition or we can say at the peak maximum. Therefore, ϕ offset was taken as average of the difference in ϕ and $2\theta_\chi/2$ values at the peak maximum of two non-parallel reflections (it was found to be 0.5° for Run2, -0.4° for Run3 and 2.3° for

OOP experiment). For the OOP set-up, there was also a χ offset of 0.2°. Using this, inverse of the u_ϕ matrix was calculated, which gives us the U-mat.

Then, the following equation 4.4 was used to calculate the (hkl) values for each data-point.

$$\begin{bmatrix} h \\ k \\ l \end{bmatrix} = B^{-1}U^{-1}\mathbf{\Phi^{-1}\chi^{-1}\Omega^{-1}\Theta_{mat.}} \begin{bmatrix} q \\ 0 \\ 0 \end{bmatrix} \tag{4.4}$$

Here, q was calculated using Bragg's law and $\Theta_{mat.}$ is used to convert q to θ-space from the reciprocal space represented by the rotation matrix given by $2\theta_\chi/2$. The other symbols have same meaning as described in Chapter 2. Figure 4.10 shows one of the measured 2D scans plotted against diffractometer angles and the corresponding Miller indices. In what follows, all the scans are converted in $\vec{Q}$ space. Further treatment on this data is discussed in the next section.

4.3.2 Corrections applied to the measured intensity

As discussed in Chapter 2, the measured intensity needs to be corrected for several factors that can alter the number of counts measured. This is done in order to obtain the right peak strength for crystal structure refinement. Following are the corrections that were applied to the measured XRD data.

- **(a) Film area under diffraction**
  The area of the film that contributes to diffracted intensity depends on three factors: the size of the incident beam, sample orientation during measurement and the detector slits sizes. First, the size of the incident X-ray beam, which is selected using soller slits (horizontal and vertical), keeping the resolution in mind. The larger slit width will give more photons but leads to lower resolution. In the OOP configuration, the incident beam size chosen was smaller than the film surface area, which means that the whole film did not contribute to the diffracted intensity. For the IP, the beam was big enough to cover the whole sample.

  Secondly, the sample orientation changes while measuring different reflections. So depending on the sample orientation, the film area under diffraction also changes. Therefore, it is necessary to normalize the measured counts/s with the projection of beam area onto the sample surface. In addition, the measured intensity also depends on the size of the detector slits.

  A python script was written to carry out these corrections for both, IP and OOP geometries. The general strategy applied is as follows: The beam imprint onto the sample (rectangular area) is calculated for both incident and detector sides. The film area that contributes to the measured intensity is the intersection of the sample surface ($5 \times 5\ mm^2$) with the smaller rectangular imprint out of the two sides (incident/detector). These surface areas are calculated using the equations below. Figure 4.11 illustrates the area calculations using a schematic.

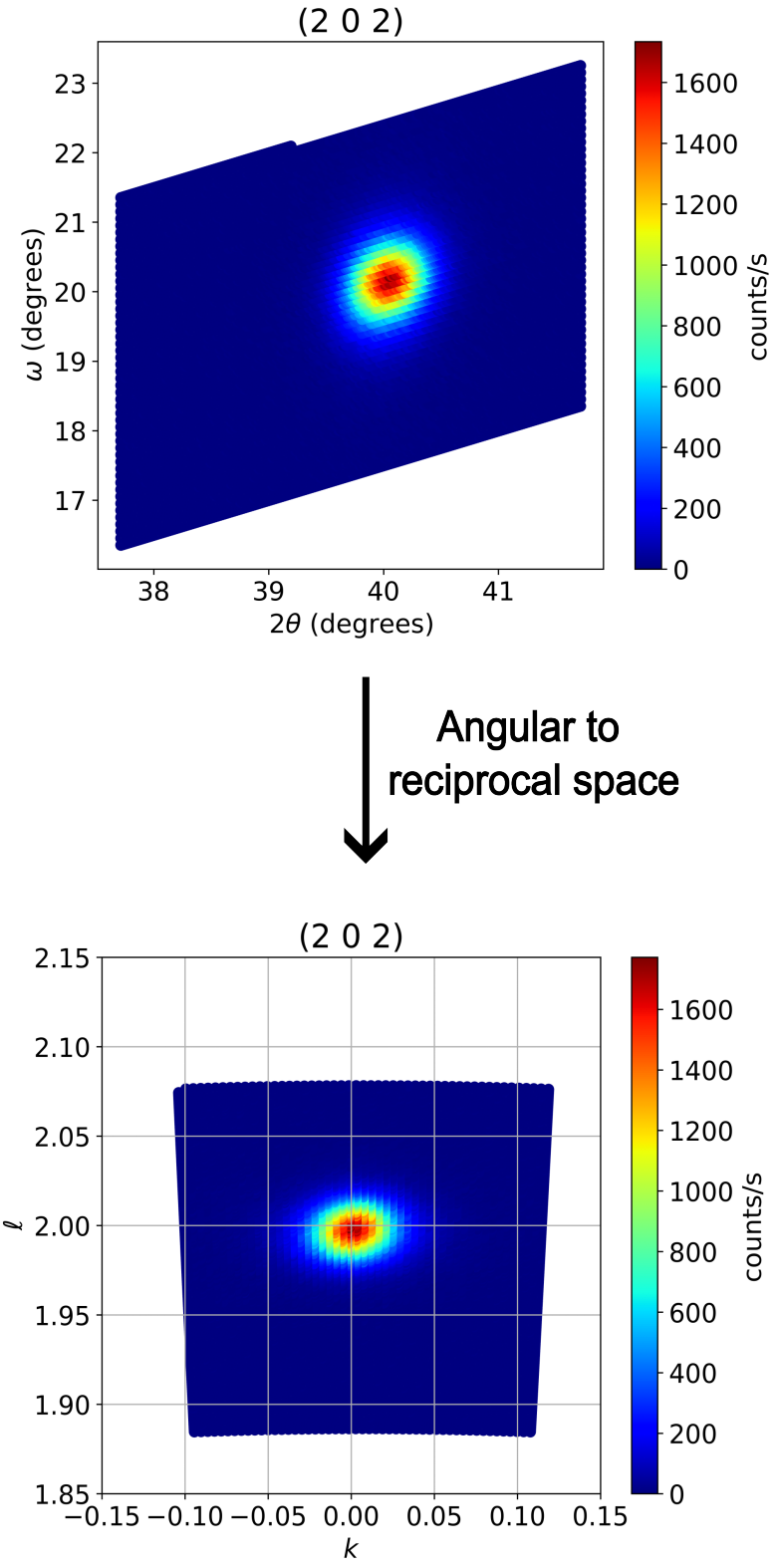

Figure 4.10: (2 0 2) reflection measured using 2D scans plotted against both the diffractometer angles and the corresponding $(hk\ell)$ indices calculated using UB-matrix (equation 4.4).

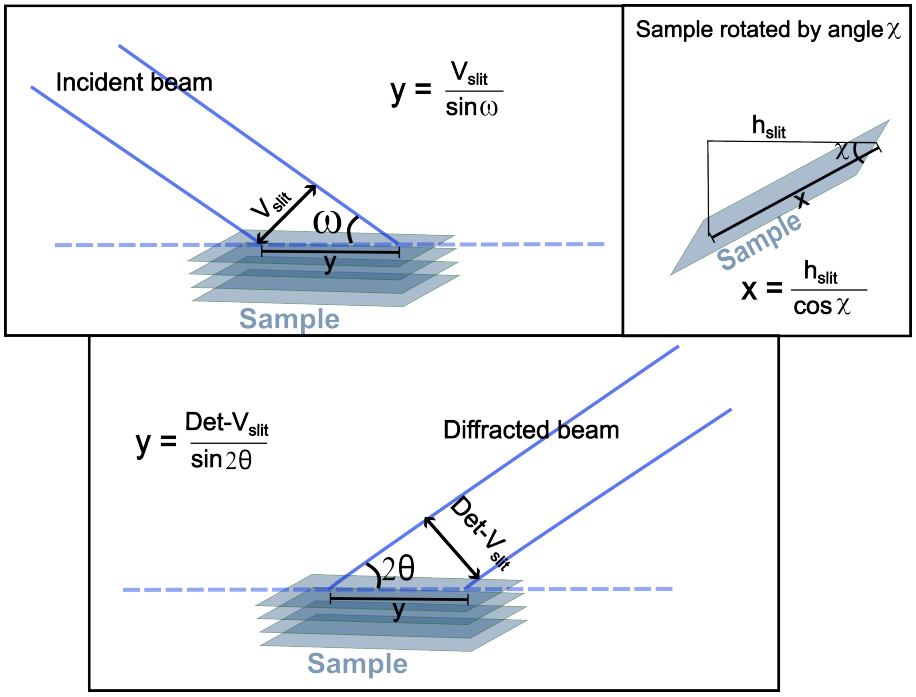

Figure 4.11: Schematic showing different sample orientations and beam imprints onto the sample. The equations used to calculate area under diffraction are also written for each schematic.

$$\begin{aligned} \text{Incident beam area on the sample} &= \frac{h_{slit}}{\cos\chi} \times \frac{v_{slit}}{\sin\omega} \\ \text{Beam area on detector side} &= \frac{h_{slit}}{\cos\chi} \times \frac{det_{vslit}}{\sin 2\theta} \end{aligned} \tag{4.5}$$

where, h_{slit}, v_{slit} and det_{vslit} are the horizontal incident, vertical incident and vertical detector slit sizes (in mm) respectively. The angular notations are the same as defined in Figure 3.1. The 2θ angle in the above formula changes to $2\theta_\chi$ for IP configuration. As an example, the beam and sample area overlap drawn using the Python script used for correction is shown for two different reflections in Figure 4.12. The beam imprint and the sample are drawn on 5×5 grid. The measured intensity is normalized with the area represented by the intersection between the beam and the sample.

- **(b) Lorentz factor and polarization**
  The correction factor associated with Lorentz factor is given by $\frac{1}{\sin 2\theta}$ [68]. Since a double bounce monochromator made of Ge (2 2 0) crystals was used for the OOP measurements, the final polarization correction includes $A = \cos^4 2\theta_M$ for the OOP reflections, where θ_M is the Bragg angle Ge (2 2 0). Thus, each data point (counts/s) was divided by $\frac{1+A\cos^2 2\theta}{(1+A)\sin 2\theta}$, combining both Lorentz factor and polarization factor, also knows as the Lorentz polarization factor.

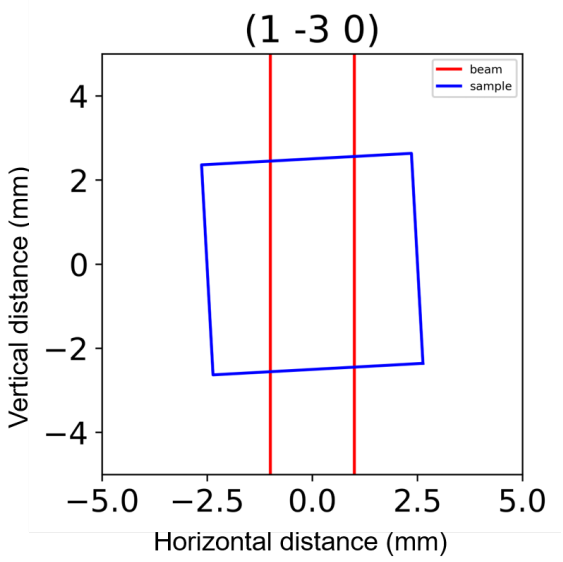

(a)

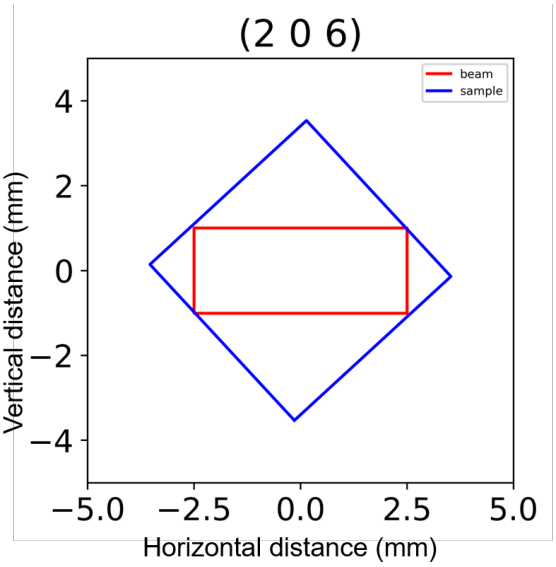

(b)

Figure 4.12: X-ray beam and sample area intersection at the positions of (a) (1 -3 0) and (b) (2 0 6) reflections, plotted using Python script designed to calculate the film area under diffraction.

- **(c) Divergence correction**
  As mentioned above, slits were used to limit the spread of the incident and diffracted beams. For the in-plane geometry, reflections were measured in two separate experiments (Run2 and Run3). In order to make the two data-sets comparable, it had to be made sure that the optical set-up is similar for both. The only difference in the two experiments was the width of slits used for horizontal divergence on the detector side (0.5° and 0.228°). This means that

more photons were counted in the measurements with 0.5° slit. Therefore, all the data points in this set were multiplied with (0.228/0.5) factor.

- **(d) Absorption correction**
  Absorption of X-ray beam by the sample can lead to significant decrease in the measured intensity depending on the type of sample and measurement. The scans were carried out in reflection mode, which means that the X-ray penetration in the sample was not large enough for significant absorption. To be thorough, the correction due to absorption by the LSMO film was carried out using the following procedure.

  Beer-Lambert's law of absorption says that:

$$I = I_0 \exp(-\mu x) \tag{4.6}$$

where, I_0 is the initial intensity and I is the final intensity after passing through a medium for distance x with absorption coefficient μ. The absorption coefficient μ is given by $\mu_m \times \rho$ (μ_m - mass absorption coefficient and ρ - density of the sample material). μ_m depends on the energy of the incident X-rays and it was taken from the NIST tables for Cu k_α radiation [126, 127]. The density was taken to be $6.16 g/cm^3$ (same as La for approximation).

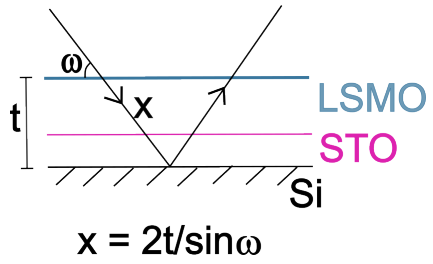

Figure 4.13: Schematic to show the path traveled by the X-ray beam inside the LSMO sample considering that it only penetrates up to top surface of Si.

In case of scattering from layers, the total path traveled by X-rays inside the sample is $2t/\sin\omega$ as shown in Figure 4.13. Substituting this in Equation 4.3.2, we get the expression:

$$I = I_0 \exp(-2\mu t/\sin\omega) \tag{4.7}$$

where, ω is half of 2θ at the Bragg condition for OOP reflections and it was kept fixed at 0.32° for IP set-up. Using this expression, I_0 was calculated for each experiment, which gives us the final intensity that can be used for structural refinement.

In the case of IP scans, the observed intensity of Si peaks was negligible at IP incident angle, which means that the beam penetration was only up to STO layer and the top surface of Si. The absorption is high because the beam traveled longer path inside the sample due to grazing incidence. Since the angle

of incidence (ω) was kept constant for all the IP reflections, it is the same for all the peaks and hence, only introduces a change in the scaling factor of the data-set. For the OOP reflections, the loss due to absorption was not large ($< 5\%$). Although, the higher incident angle suggests deeper penetration of X-rays in the sample, the path traveled by the beam inside the film is very short. Contrary to IP reflections, the correction was different for each reflection in the OOP set-up because the incident angle is not the same for all peaks.

4.3.3 Peak integration

After conversion to $\vec{Q}$ space and applications of the different normalization and corrections mentioned above, the data-set is ready for peak integration of the scans.

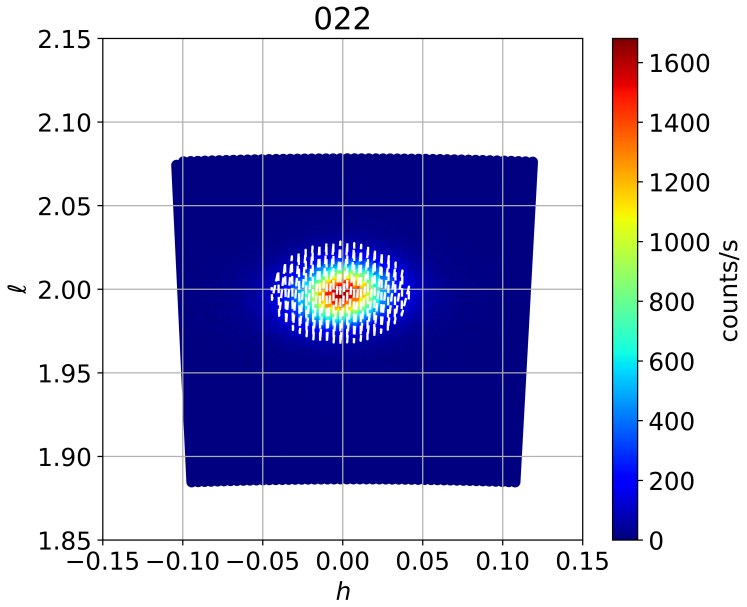

Figure 4.14: 2D XRD scan of (0 2 2) reflection highlighting the defined area of integration. The integrated intensity was calculated by summing the counts/s inside this region. The points outside the area were used to calcualte the average background.

Peak integration was not straightforward here due to various reasons. First of all, there is no software available to integrate such 2D scans with peaks from both LSMO and STO close to each other. Secondly, the shape of the LSMO peaks are not symmetric due to strain relaxation (developed later). Integrating such points using a 2D-Gaussian type shape leads to errors in integration. Therefore, it was decided to perform a numerical integration of the observed counts/s using homemade Python scripts. The procedure developed is as follows:

1. A radius of integration was defined for each scan as shown by the highlighted region in Figure 4.14. The circle drawn by this radius represents the part of scan that is included in the integrated intensity calculation.

2. All the points outside this spherical region were averaged in order to calculate the background.

3. The calculated average background was subtracted from each data-point inside the region. The sum of all these points then gives the final integrated intensity.

For the (0 0 ℓ) scan, the sum was carried out over all the measured points as it was a 1D scan and there was no need to define a radius of integration. Instead, the counts/s were summed up numerically in the peak region and the background was calculated from the rest of the data points. The so obtained intensities were used for structural refinement as observed square of structure factors.

4.3.4 Nuclear structure refinement

The lattice parameters of the LSMO film cell, obtained from various XRD peak positions are: $a_{LSMO} = b_{LSMO} = 5.522 \pm 0.006$ Å and $c_{LSMO} = 7.690 \pm 0.004$ Å with angles $\alpha = \beta = \gamma = 90°$. The a and b lattice constants of LSMO and STO are found to be exactly related by $a_{LSMO} = \sqrt{2} \times a_{STO}$, which confirms that the film follows in-plane constraints imposed by the STO layer. The 1D scan performed along [00ℓ] film direction, is shown in Figure 4.15. The strongest peak is $(0\ 0\ 4)_{Si}$ from the substrate Si (with cubic unit cell $a = b = c = 5.43\mathring{A}$). The $(0\ 0\ 2)_{LSMO}$, $(0\ 0\ 4)_{LSMO}$, $(0\ 0\ 6)_{LSMO}$, and $(0\ 0\ 8)_{LSMO}$ Bragg reflections of the LSMO film can be seen clearly. The peaks from STO layer are very close to the film peaks, but can be distinguished for $(0\ 0\ 4)_{LSMO}$ and $(0\ 0\ 8)_{LSMO}$ reflections thanks to the small thickness of STO buffer layer. Please note that since $(0\ 0\ 2)_{LSMO}$ and $(0\ 0\ 6)_{LSMO}$ are too close to the STO or Si peaks respectively, they could not be included in the data-set for the refinement later. These results confirm that the growth of the film is along c-axis for both STO and LSMO.

From the IP reflections ($\ell = 0$), it was found that there is complete overlap of the STO and LSMO peaks. This reaffirms the fact that the film follows in-plane symmetry and lattice constraints of the STO layer. Figure 4.16(a) shows 2D scans obtained for (3 1 0) and its equivalent peaks. All 4 peaks were found to be well-centered with intensities close to each other. These were measured at consecutive 90 ° rotation of the sample, indicating the presence of IP 4-fold symmetry in the film. In addition, Figure 4.16(b) shows a 1D cut of the 2D scans along ϕ, corresponding to maximum of each peak for clarity. The 4-fold symmetry presence was further established by similar behavior of other IP reflections.

Refinement procedure

In total, 56 reflections were measured out of which 16 are independent ones. Table 4.2 lists all the measured reflections. The average intensity of equivalent reflections was used in the refinement. This was done because for few reflections, the equivalent peaks were different in intensity. This could be due to misalignment of the sample or presence of crystallites. But since there was no further information available on this it was decided to use the average intensity. In addition, the contribution from STO layer to the integrated intensity was removed from each peak. For OOP reflections,

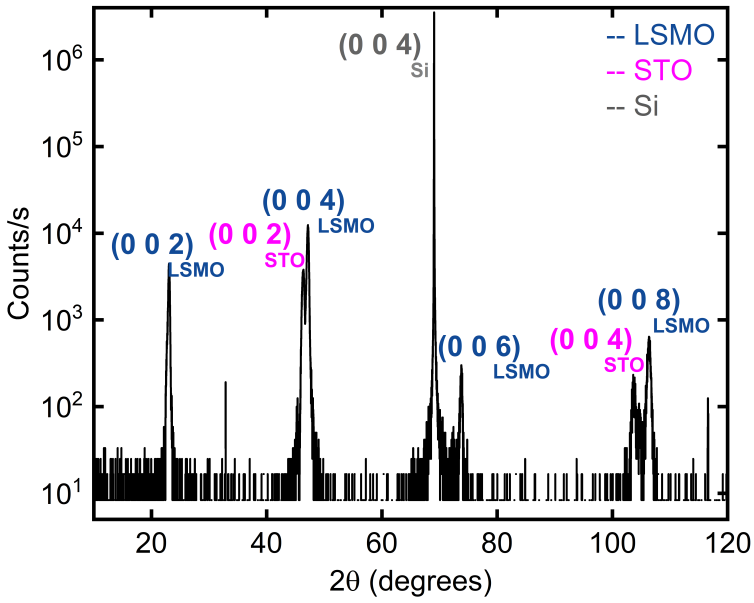

Figure 4.15: XRD (0 0 ℓ) scan showing peaks from Si (substrate), STO (in purple) and LSMO film (in blue). The intensity is presented on $\log_{10}$ scale.

Table 4.2: List of reflections measured on LSMO film using XRD, color coded according to IP (Run2+Run3), only (0 0 ℓ) and other OOP sets (Run1).

Reflections	Equivalent ones
(1 1 4)	(-1 -1 4), (1 -1 4), (-1 1 4)
(2 2 6)	(2 -2 6), (-2 2 6), (-2 -2 6)
(2 0 6)	(0 2 6), (0 -2 6), (-2 0 6)
(2 0 2)	(0 2 2), (-2 0 2)
(1 1 6)	(1 -1 6), (-1 -1 6), (-1 1 6)
(0 0 4)	
(0 0 8)	
(3 3 0)	(-3 -3 0), (3 -3 0)
(3 1 0)	(-1 -3 0), (1 -3 0), (3 -1 0), (1 3 0), (-1 3 0), (-3 -1 0), (-3 1 0)
(1 1 0)	(1 -1 0), (-1 1 0)
(1 5 0)	(-1 -5 0), (-5 1 0), (5 -1 0)
(2 0 0)	(0 2 0), (0 -2 0), (-2 0 0)
(2 2 0)	(2 2 0), (2 -2 2), (-2 2 0)
(4 0 0)	(0 4 0), (0 -4 0), (-4 0 0)
(4 4 0)	(4 4 0), (4 -4 4), (-4 4 0)

this was done by separately integrating the STO peaks in the same way as LSMO and then subtracting the obtained number from the total intensity. For IP, the procedure is not so simple because the two types of peaks completely overlap. In this case, theoretical structure factor of STO was calculated for all the peaks. The atomic positions were taken for the P$m\bar{3}m$ group[119]. The ratio of IP and OOP structure factors gave us an idea of IP intensities because we already have the OOP intensities. This way, contribution from STO was subtracted from the IP data-set as

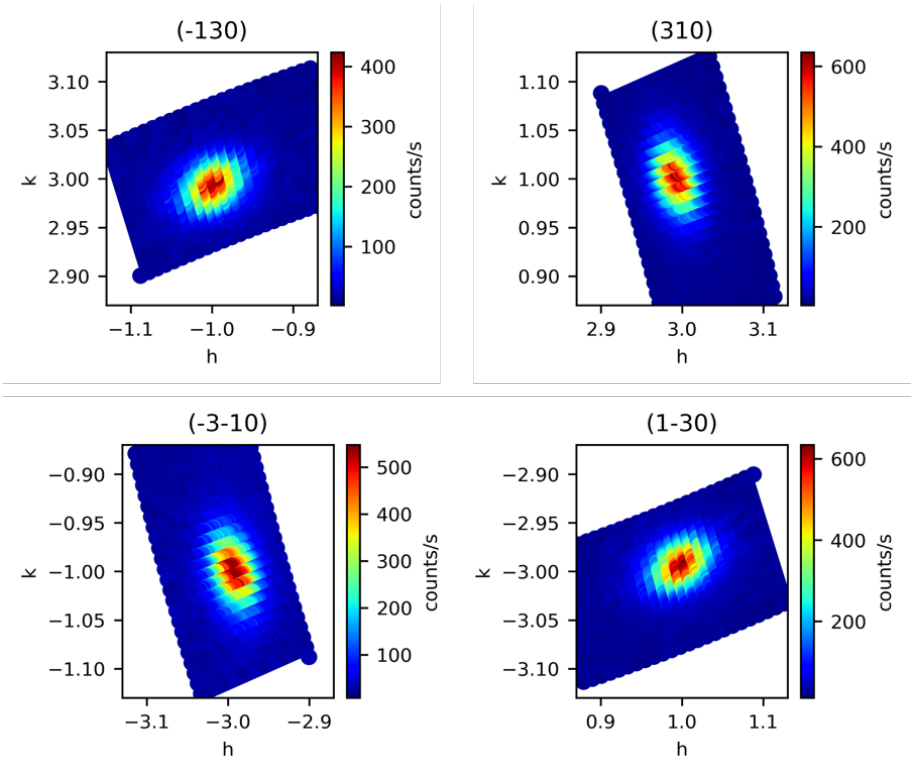

(a)

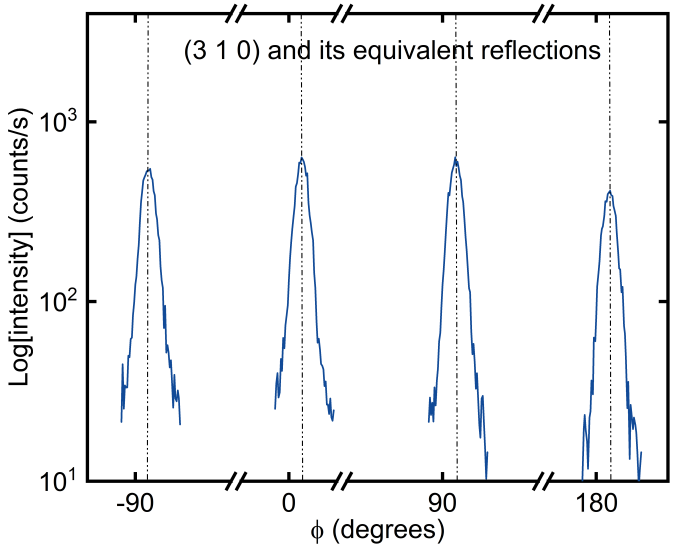

(b)

Figure 4.16: Proof IP 4-fold symmetry in LSMO film. (a) 2D scans of (3 1 0) and its equivalent reflections measured using XRD after consecutive 90 degrees rotation of the sample. (b) 1D cut of the 2D scans of (3 1 0) plotted against ϕ-rotation.

well.

The refinement was carried out by dividing the data into 3 different sets; IP (Run2 + Run3), only (0 0 ℓ) peaks and other OOP ones (Run1). Each data-set was refined with a separate scale factor due to different geometrical set-ups. As discussed in previous section, the measured intensity is significantly altered by the type of instrumental set-up, resolution and type of scan performed. Therefore, it was better to refine the 3 data-sets with independent scale factors. The refinement was performed using FullProf (FP) software package using least square fitting to compare the observed and calculated square of structure factors [128, 129]. The reliability of fit was measured using Rf-factor given by:

$$\text{Rf-factor} = \frac{\sum_i |F_{obs_i} - F_{cal_i}|}{\sum_i |F_{obs_i}|} \times 100 \tag{4.8}$$

where, F_{obs} and F_{cal} are the observed and calculated structure factors and the summation is carried over all the measured reflections. The theoretical structure factors are calculated in FP based on a structure model defined in the input file (PCR). The calculated and observed intensities are then compared and the least square fitting is used to find a configuration that gives minimum Rf-factor.

Electron diffraction results showed that the LSMO unit cell is double (by 45° rotation IP) in comparison to STO. From the lattice parameters, we know that the film cell is tetragonal in shape and the observed film peaks follow $h + k + \ell =$ even rule, which suggests that it is a body-centered cell. In addition, the presence of 4-fold symmetry IP is also established. Following these analysis, the refinement process was started with I$4/m$ space group model with atomic positions as shown in Table 4.3.

Table 4.3: Atomic positions and Wyckoff sites of the LSMO film atoms in I$4/m$ space group setting

Atom	WyckOff site	Relative atomic coordinates
Mn1	2a	(0, 0, 0)
Mn2	2b	(0, 0, 0.5)
La/Sr	4d	(0, 0.5, 0.25)
O1	4e	(0, 0, 0.25)
O2	8h	(0.23, 0.25, 0)

An important point to note here is that due to the low number of measured reflections, the first fit was obtained by refining only the scale factors. The next step was to try and optimize this geometry by manually making small changes in the structure. Since the x and y coordinates of oxygen atoms (O2 at *8h* site) were on non-special positions, there was possibility to refine these coordinates (only degree of freedom in this group). However, X-rays are not very sensitive to oxygen atoms and with such low number of reflections to fit, no good result could be obtained from this step. Removing the mirror plane along c-axis (I4 space group symmetry) gives possibility to optimize the z-positions of all the atoms, but the refinement is again unstable with many free parameters.

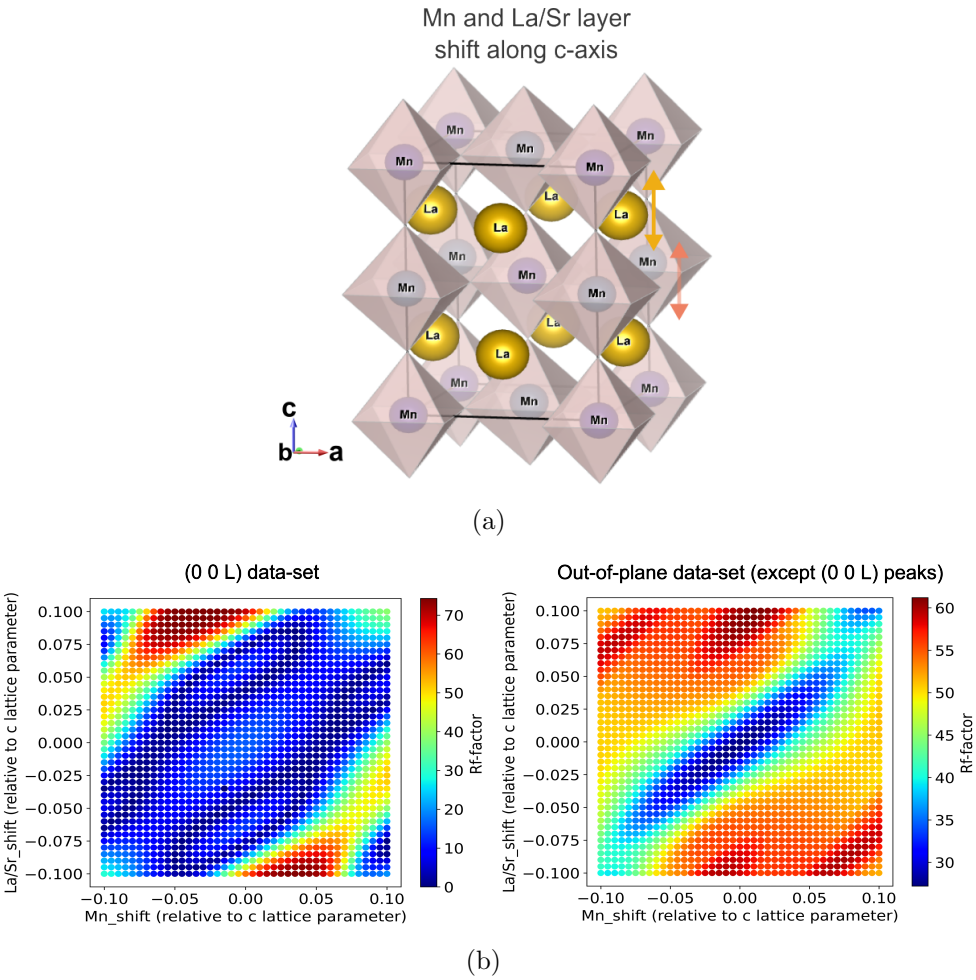

(a)

(b)

Figure 4.17: (a) Schematic representation of the LSMO film structure with markers indicating La/Sr and Mn layer movements along z-direction explored during the fitting process. (b) Rf-factors of XRD data-sets calculated against the shift in z-positions of Mn and La/Sr atoms (0 0 ℓ) and OOP data-sets.

To overcome this problem, FP was run through Python scripts and used only to evaluate the Rf-factor of a given geometry but not to refine it. At first, the z-positions of Mn and La/Sr atoms were moved in both directions on a 2D grid. The goal of this process was to see if there is any shift in La/Sr and Mn layers along z-axis as compared to the $I4/m$ space group special Wyckoff sites. The corresponding Rf-factor obtained for the (0 0 ℓ) and other OOP data-sets were plotted against the 2D grid of different possible La/Sr and Mn z-positions (see Figure 4.17). The shift is relative in reciprocal lattice parameter units. The IP Rf-factor is not shown because it stayed constant as the IP reflections are independent of z-positions of atoms. It can be seen that the minima of Rf-factors is close to the zero shift for both La/Sr and Mn. Since the number of reflections is low, it was not possible to determine the very small changes in shift.

To further analyze the diffraction data, the IP oxygen atoms, which are part of

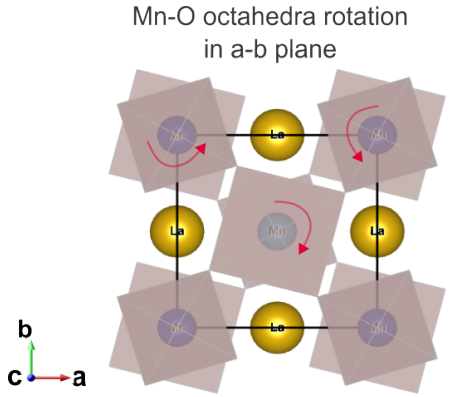

(a)

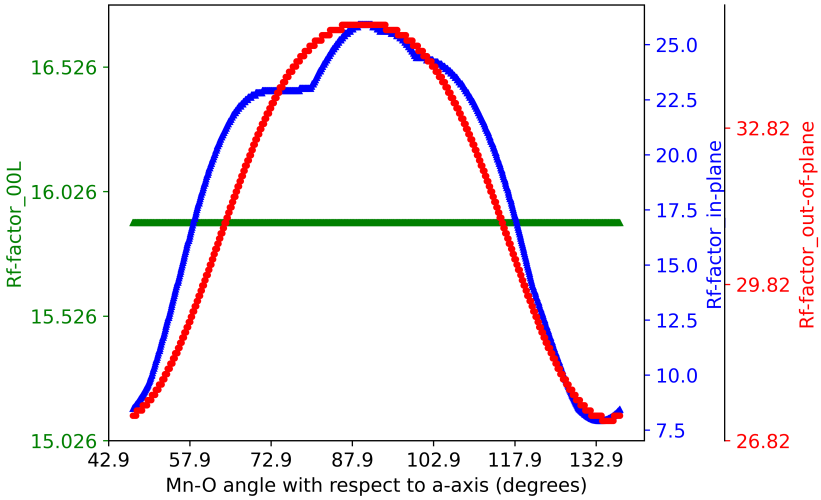

(b)

Figure 4.18: (a) Schematic representation of the rotation of Mn-O octahedra carried out in small steps. (b) Rf-factors of the 3 data-sets in XRD refinement calculated for rotation of IP Mn-O octahedra by moving oxygen atoms. The 3 data-sets are color coded: blue; IP reflections, green; only (0 0 ℓ), red; OOP reflections except (0 0 ℓ).

Mn-O octahedra were rotated. The rotation was performed in such a way that the 4-fold symmetry stayed preserved and the IP angle between O-Mn-O in the octahedra doesn't change. This was done by changing the x and y positions of the oxygen atoms surrounding Mn (rotation with respect to c-axis). The change in x and y was calculated using rotation matrices for 0.1° step-size in angle. The initial angle between O-Mn bond and the a-axis was about 47° and it was rotated by full 90° during the refinement. The Rf-factors of each data-set are plotted against this angle in Figure 4.18. The (0 0 ℓ) data-set is independent of this rotation and hence, the Rf-factor stays constant. It can be clearly seen that the minima of other 2 Rf-factors is close to the initial angle (47°). The structure return back to its original position after 90° rotation and hence, the Rf-factors also return to their minimum values.

Furthermore, a 3D loop was run in Python in order to move the z-positions of Mn and La/Sr atoms simultaneously with octahedra rotation. The plots obtained from this were 4D and hence, were analyzed by making 360° videos of the whole curves. The final results obtained also revealed that the data doesn't indicate any distortion in the octahedra environment and along c-axis.

In conclusion, it was found that the minima of 3 Rf-factors is at negligible distortions from the original structure. Thus, there is no indication that the mirror plane is absent and hence, the best possible fit of the nuclear structure is with $I4/m$ space group. The final structure is shown in Figure 4.19(b).

The Rf-factors obtained are as follows: Rf-IP = 8.5 %, Rf-(0 0 ℓ) = 16 %, Rf-OOP = 27.3 %. Figure 4.19(a) shows the comparison between $|F_{calc}|^2$ and $|F_{obs}|^2$ for different reflections. The relatively high value of OOP Rf-factor can be attributed to a couple of factors. Firstly, the sensitivity of the instrument to small misalignment during the measurements can be the cause of some misfit between the calculated and measured intensities. Second factor is a combination of possible La/Sr disorder in the system and strain-relaxation of the film. This is argued because the OOP peaks are asymmetric with a long tail on smaller 2θ side indicating increase in c lattice parameter. For instance, the $(2\ 0\ 6)_{\mathrm{LSMO}}$ and $(0\ 0\ 4)_{\mathrm{LSMO}}$ peaks are shown in Figure 4.20.

For $(2\ 0\ 6)_{\mathrm{LSMO}}$ along with the measured 2D scan, a 1D cut of the data passing through the peak center is also shown. The long tail on the left side can be clearly seen. This is in accordance with the fact that the film is gradually relaxing from strain. The bulk LSMO c value is about 3.88Å and film c is 3.845 Å(7.69 Å in doubled cell). The film tries to go back to its bulk like behavior resulting in increase in c lattice parameter. This increase in c leads to peaks at lower Q values, which is seen as the long peak tail here. As the relaxation is a percentage of the initial parameter, it is more visible for reflections far away in $\vec{Q}$. For the refinement, the total intensity was taken into account because it is very difficult to separate the different contribution from the peak curve, especially for reflections with low Q values.

It is to be noted that the data quality for such XRD measurements on thin films is not good enough to identify small distortions leading to symmetry breaking in the system. As explained in the integration and refinement process, the resolution is not the best because we need higher intensity to observe the film peaks and integration process is complex. As a result, small changes in the structure cannot be detected by the diffraction pattern. Nevertheless, the results obtained show that it is possible to perform thorough structural analysis in order to obtain valuable information about the film symmetry using such measurements.

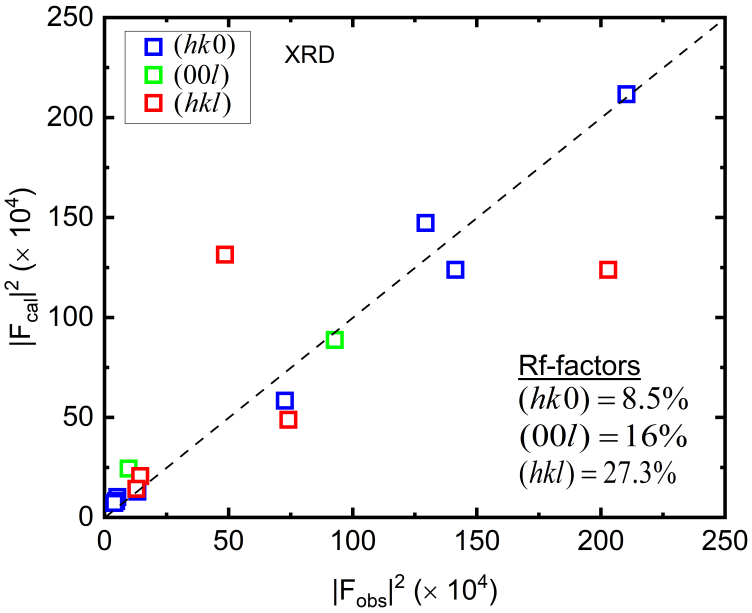

(a)

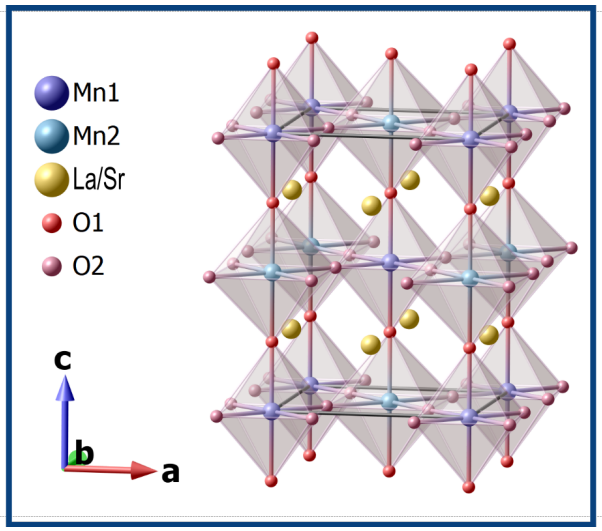

(b)

Figure 4.19: (a) Comparison of XRD square of structure factors: observed with the calculated ones of I4/m space group for LSMO film. (b) Nuclear structure of the LSMO film obtained from XRD refinement (I4/m space group). See table 4.3 for atomic positions.

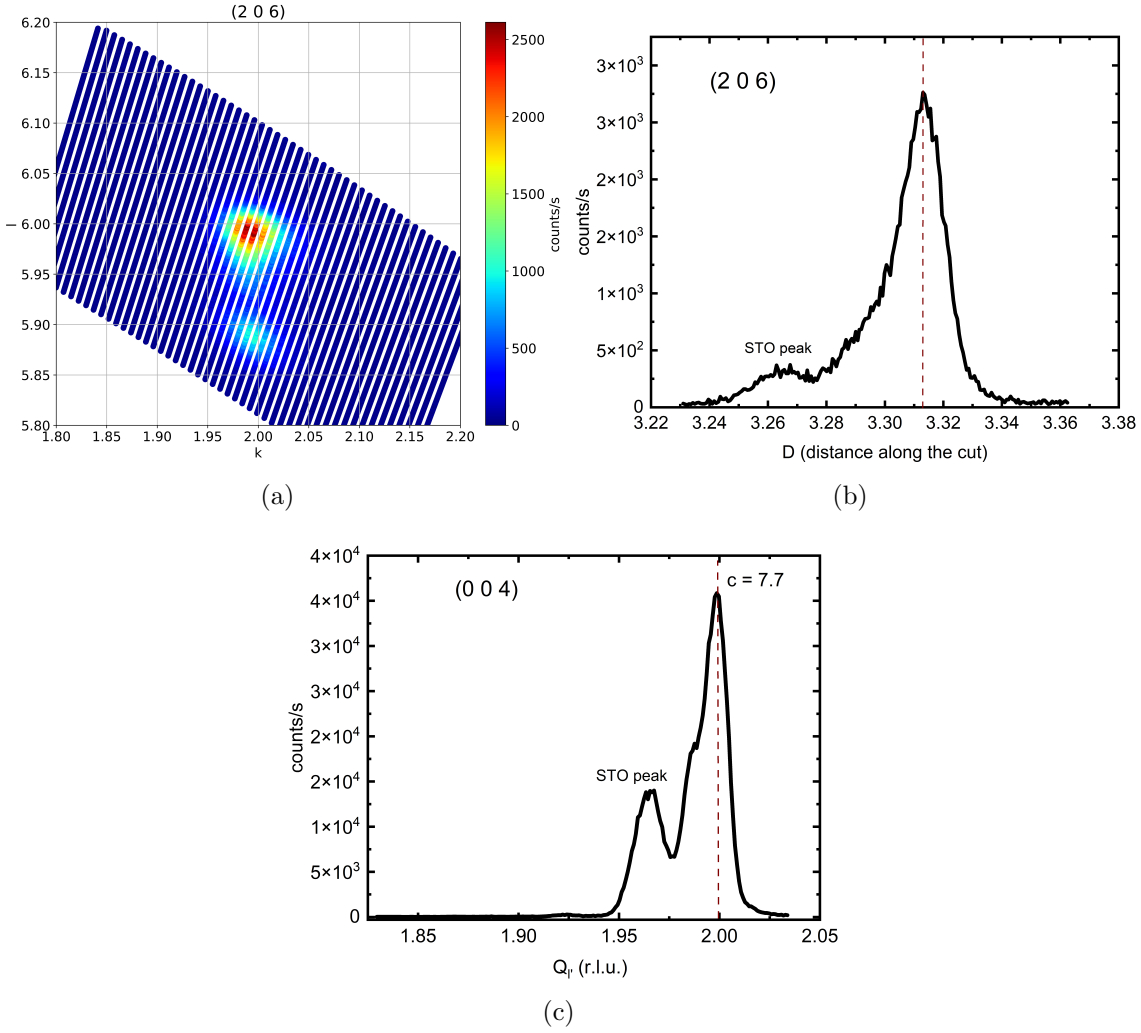

Figure 4.20: XRD scans showing relaxation in the film. (a) 2D scan of the $(2\ 0\ 6)_{\mathrm{LSMO}}$ reflection also showing the weaker STO (1 1 3) peak close to the film one. (b) 1D scan of the $(2\ 0\ 6)_{\mathrm{LSMO}}$ 2D scan passing through the peak maximum plotted against the distance along the LSMO line of cut. (c) 1D scan of the $(0\ 0\ 4)_{\mathrm{LSMO}}$ reflection plotted against the reciprocal lattice units of the STO unit cell. The STO peak is close to the film one shown by the marker. The obtained c lattice parameter is also marked.

4.4 SQUID magnetometry

In order to establish the magnetic structure, we first investigated the macroscopic magnetic properties of the film using SQUID magnetometer. Magnetic hysteresis were measured at various temperatures for fields applied along different film directions. Temperature dependence of the film magnetization was investigated by doing scans in the range of 20 - 300 K. In this section, we will discuss the results obtained on the magnetic properties of the film and hypothesize the possible magnetic spin arrangement in the system.

4.4.1 Temperature dependence of magnetization

The measured moments for field applied parallel (IP) and perpendicular (OOP) to film surface are plotted against temperature in Figure 4.21. The film was cooled down to 20 K from RT in a field of 0.25 T. Then, the moment was measured (in electromagnetic units - *emu*) in small steps while gradually increasing the temperature back to RT. Two different curves were measured for each film direction; in zero-field and 0.25 T field. The measured signal was divided by the total volume of the LSMO film to represent the magnetization in emu/cm^3 ($1\ emu = 10^{-7}$ Joules/Gauss). Please note that here we are assuming that the whole sample surface is evenly covered with the deposited film.

For all the three field directions (Figure 4.21 shows only [100] and [001]), the magnetization reduces as the temperature is increased and is close to zero above 260 K. This means that above this temperature, the material looses its magnetic ordering and goes to the paramagnetic state. So the magnetic transition temperature of the LSMO film is expected to be close to 260 K. The fitting of curve with Curie-Weiss law failed because the data-points in paramagnetic region are very close to the transition temperature. The mean field approximation does not hold in the close vicinity of transition point and measurements up to higher temperature are needed. The maximum achievable temperature in the used SQUID instrument is only 320 K. Therefore, we only take an estimated transition temperature of $\approx$260 K, to plan the ND measurements.

A small anomalous dip can be seen in the signal near the transition temperature. This can be an experimental artifact because of instability in SQUID when the measured signal is close to zero as discussed in section 3.3.

Furthermore, for the field applied along [100] and [110] (not shown here for plot clarity as it is very similar to [100]) film directions, the shape of the curve indicates FM behavior. There is increase in susceptibility (M/H) below the transition temperature. This type of variation is typical in ferromagnets. For the OOP direction, the applied field strength is not enough to observe the possible alignment of moments. The magnetization presents a very low decrease at low temperature. The nature of magnetic ordering was further investigated using magnetic hysteresis measurements.

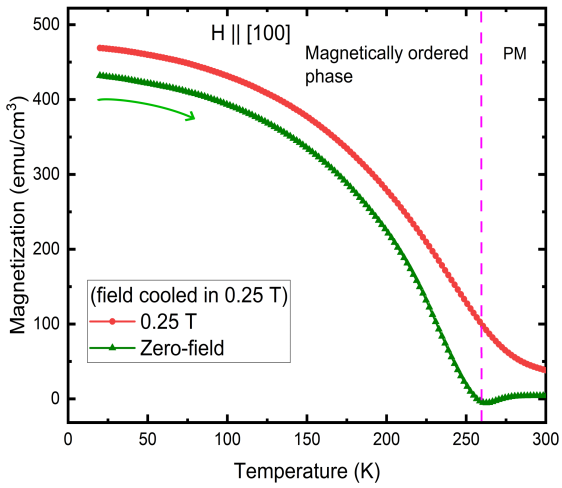

(a)

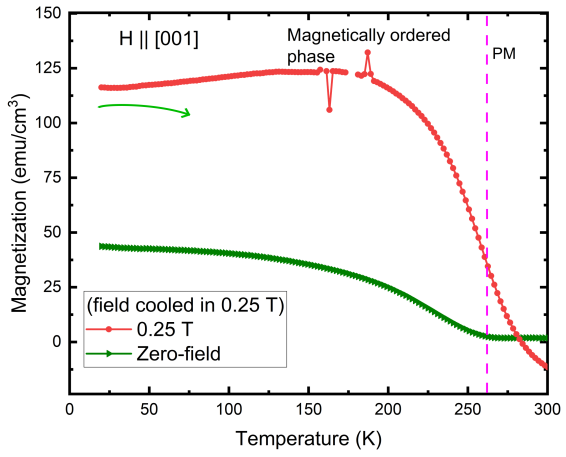

(b)

Figure 4.21: Temperature dependence of magnetization for applied field along [100] and [001], in 0.25 T and zero-field (field cooled). The dashed line near 260 K marks the transition from PM to magnetically ordered phase.

4.4.2 Magnetic hysteresis

The M(H) scans were performed on the sample at different temperatures within the range 20 - 300 K, for field applied along [100], [110] and [001] film directions. The applied field range was from +0.3 T to -0.3 T. The measured curves for [110] and [001] film directions, at different temperatures, are shown in Figure 4.22.

It can be clearly seen that for both film directions, the system shows negligible hysteresis at 300 K and there is a very small magnetic signal even at 0.3 T. For [100], this could be because of very little magnetization left in the system at 300 K as it is close to the transition temperature. These results show that magnetic signal from the substrate is very small and can be neglected for 0.3 T applied field.

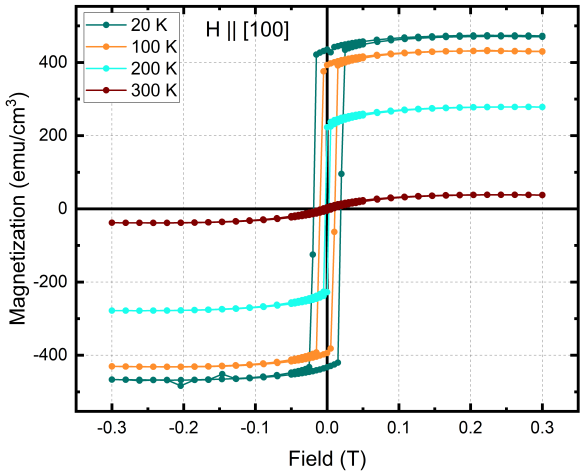

(a)

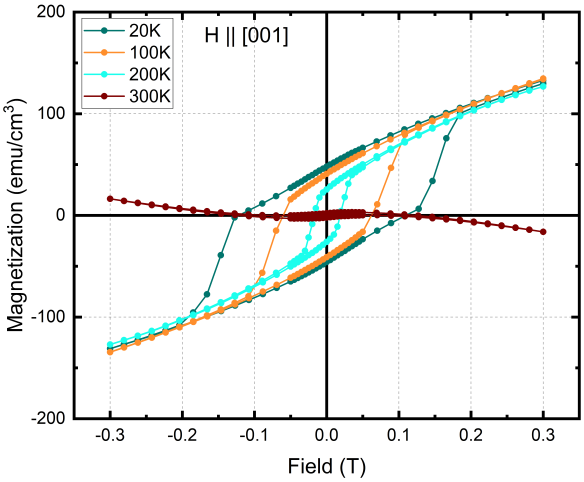

(b)

Figure 4.22: Magnetic hysteresis of the film measured at various temperatures in the range 20 - 300 K for field applied along [100] and [001] film directions.

For [001] direction, measured signal is low even at 20 K. This means that the substrate contribution can be of significant percentage. So, the 300 K data is subtracted for this direction.

As the temperature is reduced below 300 K, magnetic ordering starts taking place in the system and as a result the hysteresis area increases. It is highest for the curve at 20 K. This agrees well with the M-T scans discussed earlier.

Magnetic anisotropy at 20 K

Magnetic anisotropy in the film was analyzed by comparing the hysteresis curves for field applied along different film directions at 20 K. These are shown in Figure 4.23. The different parameters obtained from this plot are presented in Table 4.4.

The following remarks can be made based on these curves:

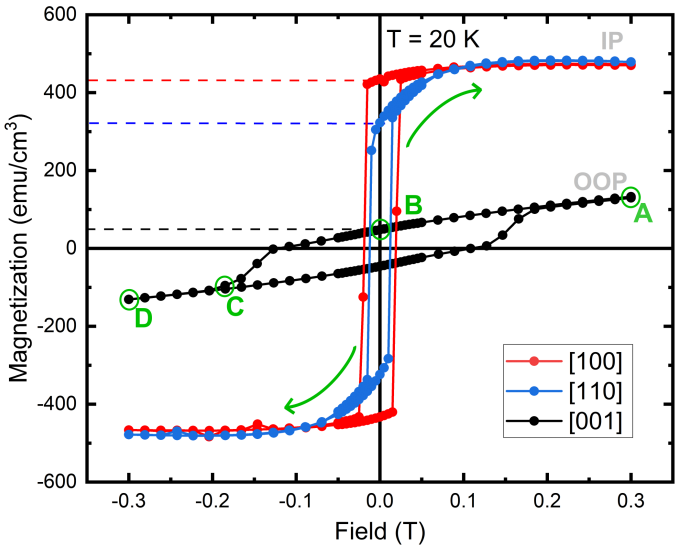

Figure 4.23: Magnetic hysteresis loops at 20 K for field applied up to 0.3 T along 3 different film directions: [100], [110] and [001]. Green arrow indicates the direction of measurement.

Table 4.4: Magnetic hysteresis parameters at 20 K for 0.3 T applied field. $M_{spon.}$ is the spontaneous magnetization, $M_{sat.}$ is saturated magnetization, and H_c is the coercive field.

Field directions	$M_{spon.}$ (emu/cm^3)	$M_{sat.}$ at 0.3 T (emu/cm^3)	H_c (T)
[100]	435	480	0.02
[110]	322	480	0.01
[001]	48	saturation not reached	0.1

- The difference in the shapes of IP and OOP hysteresis indicates presence of magnetic anisotropy in the system.

- **[100]** - The shape of hysteresis loop for IP measurements is typical of FM ordering. The moments along [100] direction are saturated in applied field of strength ≈ 0.1 T as indicated by the flat shape of the curve above this field. As the field is reduced below this value, the moments try to move towards zero-field magnetic configuration. This results in only slight decrease in the magnetization showing that the magnetic easy-axis is close to [100]. As the field direction is reversed (negative), the magnetization along [100] stays positive at first. This is because the current state of magnetic configuration corresponds to minimum energy (easy-axis) and a certain amount of energy is required to flip the spin directions towards the field. The field corresponding to this energy is called

coercive field (H_c) and it is 0.02 T for [100], indicating soft magnetic nature. The moment switch from [100] to [$\bar{1}$00] is instantaneous as indicated by the sudden reverse in magnetization sign. The moments then saturate along [$\bar{1}$00] direction as the applied field is increased above -0.1 T.

- **[110]** - The behavior of diagonal IP direction ([110]) is similar to [100] showing saturation above 0.1 T applied field. The H_c for [110] is 0.01 T and the moment direction switching is instantaneous like [100]. The spontaneous magnetization is about $1/\sqrt{2}$ times that of [100], which indicates about 45° rotation of moments. This is consistent with the fact that as the applied field along [110] is reduced below 0.1 T, the moments in-plane prefer to align along the [100] direction. The slope in the region of 0 to 0.1 T (blue curve in Figure 4.23) is a result of this rotation of moments.

- **[001]** - On the other hand, the OOP hysteresis behavior is slightly different. The moments are not saturated at 0.3 T and H_c is higher for this direction ($\approx$ 0.13 T) suggesting strong magnetic anisotropy. The shape of [001] hysteresis can be explained using points at different positions on the curve (see Figure 4.23). At point A, the moments are slightly oriented towards [001] direction (bigger c-component of the moment - μ_c) but are far from saturation. This is because it has a significant non-zero slope. At point B, the applied field is reduce to zero and the non-zero magnetization shows that the moments have an OOP component and are not completely IP. The ratio of μ_c and μ_a is about 0.1. As the field direction is reversed, the moments start to switch the direction of μ_c component and at point C, all have their μ_c component aligned to [00$\bar{1}$]. Increasing the field strength further towards point D leads to increase in μ_c as the moments try to align completely along [00$\bar{1}$].

- **5 T measurements:** In order to study the film's behavior in higher fields, similar hysteresis measurements were performed in an applied field of 5 T. These results are shown in Figure 4.24. The diamagnetic contribution from the substrate Si and STO layer is significant in such high fields. Therefore, it is necessary to subtract this signal for the accurate analysis of the film's magnetic properties. In addition to 20 K, the hysteresis curves were also measured at 300 K, in the paramagnetic phase of the LSMO film. It is expected that at 300 K, the signal mainly includes contributions from Si and STO. This dataset was subtracted from the 20 K measurements. For comparison, the subtracted signal is shown in figure 4.24(a) along with 20 K and 300 K measurements. The hysteresis cycles shown in Figure 4.24(a) are not a complete loop as the experiment was stopped at -4 T field, starting from 5 T. However, this does not affect the analysis and information can still be obtained about the film's magnetic behavior in 5 T.

  The hysteresis curves shown in Figure 4.24(b) are for field applied along [110] and [001] directions after subtracting the substrate contribution. For field along [001], ultimately the moments are completely aligned along [001] in a field of

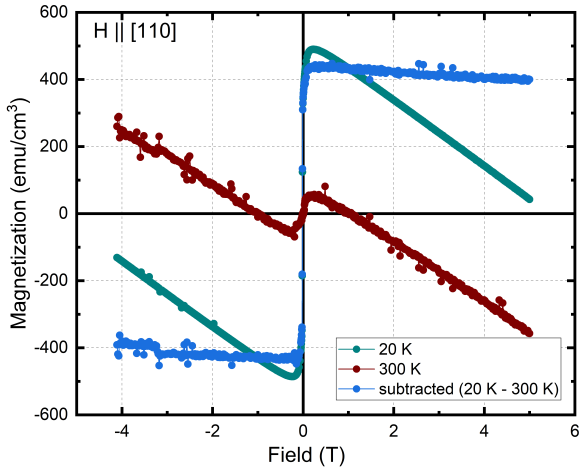

(a)

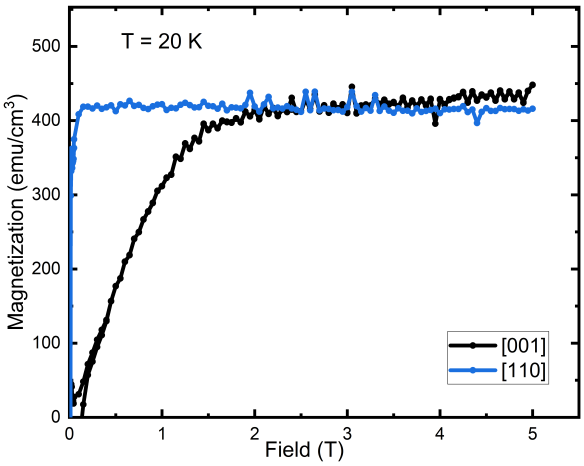

(b)

Figure 4.24: (a) Hysteresis measurements for 5 T field applied along [110] at 20 K and 300 K. The green curve shows the 20 K data after subtracting the substrate contribution (i.e. the data measured at 300 K). (b) Comparison of [110] and [001] hysteresis curves at 5 T at 20 K after subtracting the substrate contribution.

$\approx$ 2 T. Here, positive part of hysteresis from 0 to 5 T is shown. There are fluctuations in the subtracted data points and the reason is weak diamagnetic signal at 300 K that leads to instability in SQUID. Consequently, the subtraction carried out only gives an estimate but nevertheless, it is clear that the moments are saturated. For [110], no change was observed as compared to the 0.3 T hysteresis. The moments remain saturated till 5 T, as expected.

Possible magnetic structure

From these observations, it can be interpreted that the moments in zero field are aligned FM along [100] in-plane, with a component perpendicular to the surface

(OOP). Based on the shape of OOP hysteresis curves, two different scenarios can be hypothesized. Either the moments are coupled AFM along $\vec{c}$-axis with a small uncompensated magnetization given by the μ_c/μ_a ratio or the system is completely FM in nature with moment (μ_a, 0, μ_c). In order to distinguish between these two models and determine the moment size, ND measurements were performed as SQUID cannot provide clear information on this.

4.5 ND results

Neutron diffraction experiments were performed using D10 and the recently upgraded D10+ instrument at ILL. The goal of these experiments was to resolve magnetic structure of the LSMO film. We have obtained some valuable information about the film magnetic behavior using SQUID measurements and need to perform ND to resolve the microscopic nature of the moments. In this section, we will see what types of challenges are faced while performing such studies. Strategy applied in measurements and data analysis are discussed in-detail. Neutron diffraction peaks on such films present very low signal to noise ratio. This means that only a limited number of peaks can be measured within an allowed beamtime. Here, we will see how SQUID analysis can be used to better plan the experiments and apply constraints in magnetic refinement. At last, the resolved magnetic structure is presented along with the reasoning followed.

Let us first focus on the measurements carried out using D10. In this experiment, incident wavelength of 2.36 Å was selected using Pyrolytic graphite monochromator. Although the use of longer wavelength (as compared to 1.26 Å from Cu monochromator) limits the accessible $\vec{Q}$ (scattering vector) to lower values, the increase in flux by a factor of 6.19, which is important for thin film measurements. The analyzer on D10 can only move up to $2\theta = 95°$ due to the instrument's geometry. Reflections higher than this 2θ value were not accessible. A 10 mm slit was used for the incident beam, which means that the whole sample was under diffraction throughout the experiment and hence, no area correction was needed for the neutron data. The reflections were measured at various temperatures in the range of 20 - 300 K. The experimental planning and procedure is described next.

4.5.1 Experimental difficulties and planning

Below are the points that discuss the main difficulties faced in this experiment.

- Contrary to X-rays, performing 2D scans in ND is not practical considering the time and flux required. So only 1D scans are recorded with neutrons. These can be programmed as a q-scan choosing a direction to be scanned in reciprocal space or as an ω-scan [2]. This means that only a limited amount of information can be obtained. Especially in thin film cases such as this one, where there is relaxation effect, it is difficult to perform identical scans for each reflection. The relaxation effect can then be absent or visible on peaks depending on the scan direction, which makes it difficult to compare them for refinement. To overcome this problem, the measured data-set was divided into 2 sets of reflections based on the scan direction. This is explained in-detail in the refinement section.

- Diffraction peaks from the STO buffer layer had to be taken into account. For the complete IP data (h k 0), the set of two peaks overlap as the IP lattice parameters of LSMO and STO are equal. For the OOP case, the peaks are

[2] It can also be an $\omega - 2\theta$ scan depending on which angles were rotated during the scan.

close but distinct, due to small difference in their c-lattice parameters. Thanks to the small thickness of STO layer, it was possible to distinguish the LSMO peaks. In addition, care had to taken to avoid doing scans close to the Si peak positions as these are way more intense (1 mm thickness of Si) and it was not possible to locate film peaks nearby Si ones.

- As discussed before, the diffracted intensity from such thin films is very low. This means that higher monitors (more incident neutrons per data-point) had to be used to get good statistics. This leads to long measurement times for peaks. Typically, a 2 million monitor scan with 31 points required about 5 hours on D10.

- In order to program measurements as ω-scans (or $\omega - 2\theta$), one needs to provide the film UB-matrix for alignment. To calculate the UB-matrix, at least 3-4 well-centered film peaks with good intensity are required. It is not possible to do it quickly during the sample alignment because it takes long time to measure film peaks. But we know the Si peaks are intense and can be quickly measured. So it was better to align the sample on Si UB-matrix and calculate the film UB-matrix later if there are sufficient film peaks available. Therefore, the initial scans were programmed in q-scan mode using Si cell indices.

  The relationship between Si and LSMO film unit cells were used to transform the indices. For example, to measure (0 2 2) film peak, a q-scan along ℓ direction in reciprocal space of Si would be centered at (0 2 1.41). Si structure is cubic with lattice parameter 5.43 Å. So in Si unit cell $\ell_{film} = 2$ is $2 \times 5.43/7.7 = 1.41$. Bear in mind that this is for an ideal case scenario where IP epitaxy is perfect because the h and k indices are fixed at 0 and 2 respectively. And the lattice parameters are exactly 5.43 Å and 7.7 Å. In reality, it is possible that the film peak maximum is at slightly different position. This can also lead to off-centered peaks in the scans.

Experiment procedure

Keeping the above points in mind, the following procedure was followed in this experiment.

D10 provides the ability to calculate the UB-matrix using programs available on the instrument computer. To get a rough UB-matrix, at least 2 peaks are required. We started by measuring (0 0 4) peak of Si by manually aligning the angles in maximum signal position. Then, (-1 1 -1) was measured in a similar fashion. The angular positions of these two reflections were used to get a "rough" UB-matrix. Using this UB-matrix, a set of Si reflections (about 20) were measured using the area detector. It is common to have these reflections slightly off-centered because the UB-matrix is not good at this stage. That's why, it is helpful to use area detector that can cover more reciprocal space. The measured intensity is not an issue because we are interested in the positions of these peaks. The UB-matrix was then refined using the obtained positions of these reflections. The Si lattice parameter calculated using these peaks is 5.43 Å, as expected.

Then the set-up was moved to the analyzer mode, which includes a point detector. The same procedure was repeated in order to further refine the UB-matrix. Please note that this was carried out at RT so far. Now it was time to measure the film peaks but which ones? Since it takes long hours to measure a single peak, theoretical intensity of the peaks was calculated before-hand to decide which ones to measure.

Vesta software was used to calculate the theoretical structure factors of $I4/m$ space group for neutrons with 2.36 wavelength [130]. Top few most intense reflections were selected keeping in mind that the analyzer can only access 2θ up to 95°. At first, few reflections were measured using q-scans along ℓ and $h+k$ directions in the reciprocal space. These included (0 -2 2), (-2 0 2), (0 0 2) and (0 0 4) Si reflections, which were then used to calculate the first film UB-matrix. This matrix was used to measure more film peaks using ω and $\omega - 2\theta$ scans. The complete measured data-set is listed in Table 4.5. Most of the reflections were measured with 2 million monitor and few others with a 4 million one.

Table 4.5: List of reflections measured on LSMO film using D10 ND diffractometer at different temperatures, color coded according to type of scan; blue-ω-scan, orange-q-scan.

20 K	90 K	160 K	200 K	250 K	300 K
(0 0 4) (-2 0 2) (1 -1 0)	(0 0 4) (-2 0 2) (1 -1 0)	(0 0 4) (-2 0 2) (1 -1 0)	(0 0 4) (-2 0 2) (1 -1 0)	(0 0 4) (-2 0 2) (1 -1 0)	(0 0 4) (-2 0 2) (1 -1 0)
(2 -2 2) (0 -2 2) (-2 0 2) (0 0 4) (0 0 2) (1 -1 0)	(2 -2 2)	(2 -2 2)	(2 -2 2)	(2 -2 2)	(2 -2 2) (0 -2 2) (-2 0 2) (0 0 4) (0 0 2) (1 -1 0) (-1 -1 4) (-1 1 4) (-2 2 2)
					(0 0 2) (0 -2 2)

A set of 9 reflections was measured at RT (6 independent ones). The sample was then cooled down to 20 K. The above described procedure was repeated to calculate the film UB-matrix matrix. A set of 6 reflections (5 independent ones) was measured at 20 K (see Table 4.5). The idea was to use the 300 K data to fit the nuclear structure as it contains contributions from nuclear scattering only (in the paramagnetic phase). And to use the 20 K data, to find the magnetic configuration of the system. At 20 K, the system is magnetically ordered as seen in SQUID results and there is contribution from magnetic scattering as well.

In order to investigate the temperature dependence of the reflections, a few peaks were measured at several intermediate temperatures in the range 20 - 300 K. As it was not possible to calculate the UB-matrix at each temperature, these peaks were measured with q-scans in Si cell setting. These reflections included (0 0 4), (-2 0 2) and (1 1 0). The results of these measurements are discussed in the subsequent

sections.

4.5.2 Data treatment

Peak integration

The lattice parameters obtained using various peak positions at both 300 K and 20 K are listed in Table 4.6. The RT lattice parameters are well in-agreement with the XRD results and there is not much change as the temperature is reduced to 20 K. As a consequence, the UB-matrix calculated at 20 K was only slightly different from the RT one.

Table 4.6: Lattice parameters of LSMO film obtained using various ND peak positions at 300 K and 20 K. The error bars were calculated based on the step-size in 2θ.

Temperature (K)	a = b (Å)	c (Å)
300	5.51 ± 0.04	7.71 ± 0.02
20	5.52 ± 0.02	7.72 ± 0.02

Each peak was integrated using Gaussian fitting in OriginLab software [131]. The fitting function is as follows:

$$y = y_0 + \frac{A}{w_d\sqrt{\pi/4\ln(2)}}\exp\left(\frac{-4\ln(2)(x-x_c)^2}{w_d^2}\right) \tag{4.9}$$

where, y_0 is the background, w_d is Full Width at Half Maximum of the peak and x_c is the peak maximum position (see Figure 4.25). The area under the curve (A) gives the integrated intensity, which is used for structural refinement. For some peaks, it was not possible to obtain a good fit with all the parameters let free due to weak intensity. Therefore, the fit was carried out by fixing some of the parameters manually such as background or x_c. This results in a relatively slightly larger error bar on these peaks.

The integrated intensities were then corrected for Lorentz factor by multiplying them by $\sin 2\theta$. They were also normalized with respect to 2 million monitor. If a peak was measured with a higher monitor then the intensity was accordingly divided to make the structure factors comparable.

In order to obtain correct integrated intensities of the LSMO film, it was important to identify which peaks include contribution from STO. This is not directly known for ω and $\omega - 2\theta$ scans because the direction of scan needs to be calculated. To do so, each data-point in ω-scans was converted to corresponding $(hk\ell)$ indices using the UB-matrix matrices. The procedure followed was the same as discussed in section 4.3. The angular conventions were taken the same as for D10 (described in chapter 3). The same was done with lattice parameters of STO to calculate STO $(hk\ell)$ indices.

As an example, let us consider two equivalent peaks (-2 0 2) and (0 -2 2) at 300 K. The ω-scans measured for these peaks are shown in Figure 4.26. The corresponding

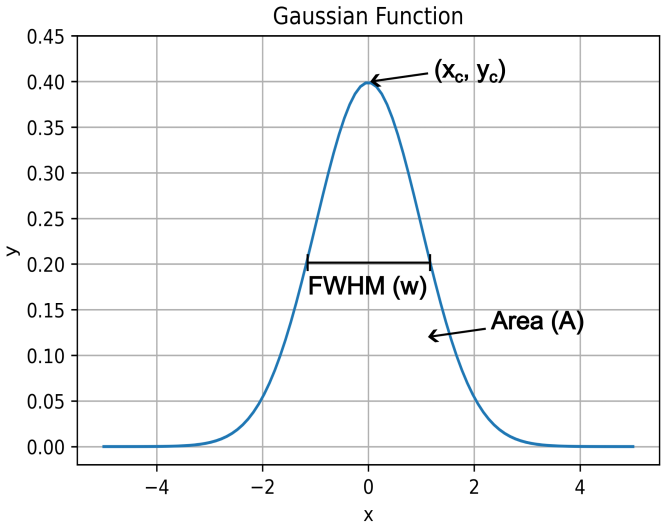

Figure 4.25: Schematic of a Gaussian function with marked important parameters.

$(hk\ell)$ for few data-points are also marked (blue-LSMO and purple-STO). As can be seen in the figure, the two scans move differently in the reciprocal space. For the (-2 0 2) peak, the scan does not record over the STO (-1 -1 1) peak. Whereas for (0 -2 2) peak, the scan direction is such that the STO peak position is crossed during the measurement. As a result, there is STO contribution on (0 -2 2) peak, while it is not included on (-2 0 2) peak scan. This is also apparent in the higher intensity of (0 -2 2) peak as compared to (-2 0 2). Similarly, the STO peak contributed to the intensity on (0 0 4) and not on (0 0 2). The (0 0 4) peak shape clearly indicated the smaller STO peak on the left side as visible on Figure 4.27.

For the structural refinement, it is important to be consistent with the STO contribution across all the reflections. If STO contribution is not present on few peaks, then it should be removed from all the other peaks. This is crucial for correct assessment of structure factors. In order to remove the STO contribution for such peaks, theoretical structure factors of STO reflections were calculated. Then, the same was done for LSMO structure in $I4/m$ space group. The ratio of squares of structure factors of STO and LSMO, was used to accordingly divide the total intensity. In addition, the effect of thickness was taken into account by dividing the structure factor of STO by 2, the STO layer being twice as thin as the LSMO one.

The same procedure was very effective for IP reflections as well, because for these reflections the LSMO and STO peaks overlap due to same IP lattice parameters. It is not possible to know from the peak shape whether STO peak is present on the scan or not. Therefore, with the help of calculated $(hk\ell)$ indices, the STO contribution was removed from the integrated intensity.

Finally, the data-set was divided into two categories based on the relaxation effect. As seen in XRD, the strain relaxation was observed in the form of long tail on the lower 2θ side of the peaks. It was also seen in ND peaks, but not on all of them. The relaxation effect is seen for scans with rather large values of $|\vec{Q}|$. Therefore, the data

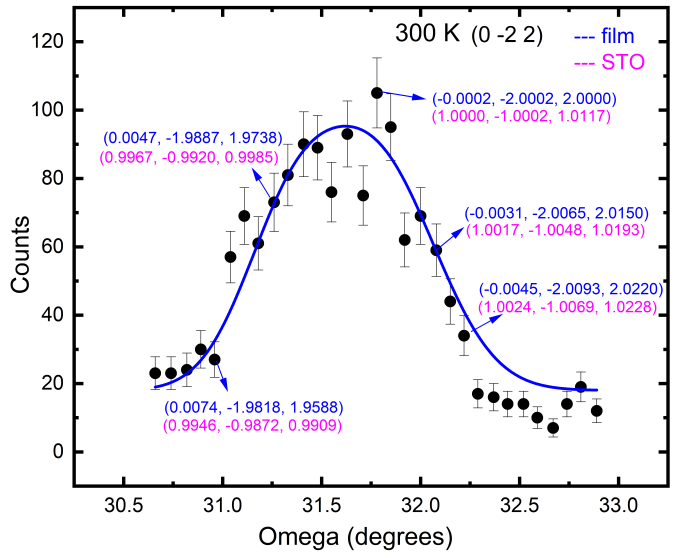

(a)

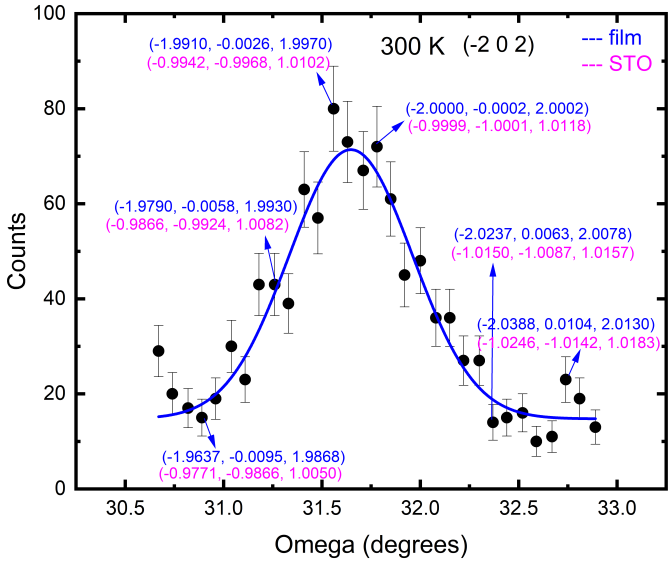

(b)

Figure 4.26: Two of the measured peaks on LSMO film at 300 K using D10 with marked reciprocal space points ($hk\ell$) for few data-points; (a) (0 -2 2) and (b) (-2 0 2). The monitor used was 2 million, taking about 5 hours of time to complete.

was divided into two sets based on whether the scan contains relaxation intensity or not, to refine them with separate scale factors. Set 1 included (0 0 2), (0 0 4) and (1 1 0) reflections. (0 0 4) peak clearly shows relaxation effect. And for (0 0 2) and (1 1 0) we interpret that the $\vec{Q}$ value is too low to see the relaxation effect and the scan includes relaxation effect intensity. Set 2 included the rest of the peaks as there was no relaxation seen on those even with sufficiently high $|\vec{Q}|$ values. The data-sets were then ready to be fitted with the structural models.

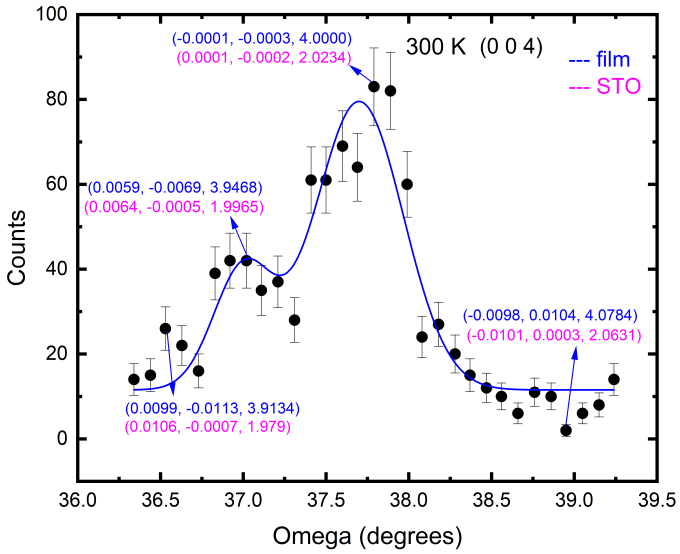

Figure 4.27: (0 0 4) peak of LSMO film measured using D10 at 300 K with plotted against ω with marked reciprocal space position of LSMO and STO both, for few of the data-points. The STO peak is clearly visible on the left side. The monitor used was 2 million.

4.5.3 Nuclear structure fit

The data measured at 300 K was used for the nuclear structure refinement as it is above the magnetic transition temperature, so only includes nuclear scattering contribution.

Fit with I4/*m* space group

From XRD analysis, it was found that the nuclear structure of the film follows I4/*m* space group symmetry. The ND peaks measured at 300 K were fitted with the same space group using FP software package. The comparison of observed and calculated square of structure factors is shown in Figure 4.28. Considering the low number of peaks in the data-sets, only scale factor was refined and the fit was found to be in agreement with the I4/*m* space group (Rf-factor = 10.4 %). A single Rf-factor was calculated by re-normalizing the data-sets using separate scale factors and finally fitting them all together.

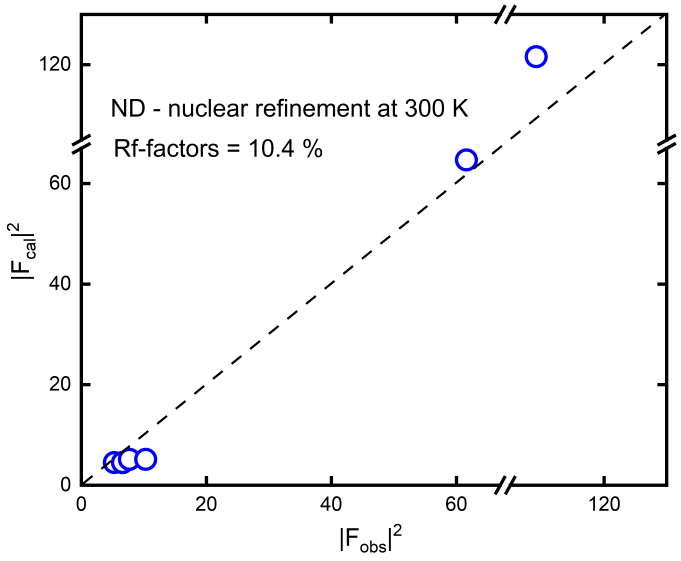

Figure 4.28: Plot showing comparison of the calculated and observed square of nuclear structure factors for the ND data at 300 K with I4/m space group for LSMO film.

4.5.4 Magnetic structure determination

The data measured at 20 K was used for magnetic structure determination as it includes contributions from both nuclear and magnetic scattering. Let us first review the changes observed in peaks as we reduced the temperature from RT to 20 K.

4.5.4.1 Temperature dependence of peaks

Figure 4.29(a,b) shows the temperature variation of integrated intensity of (0 -2 2) and (0 0 4) normalized to the 300 K peak. Magnetic transition occurs in the film close to 260 K. This means that at 300 K, there is no magnetic ordering in the sample and hence, no contribution from magnetic scattering. In Figure 4.29, it can be clearly seen that there is gradual increase in intensity while cooling below 260 K. This is due to contribution from magnetic scattering in the ordered phase.

In addition, Figure 4.29(c) shows the intensities of all the peaks measured at 300 K and 20 K. For almost all the reflections, there is good increase in the intensity at 20 K. These observations are well in-agreement with the SQUID results. For reference, the measured scans of (0 0 2) and (0 -2 2) reflections at 300 K and 20 K are also shown, in Figure 4.30.

The magnetic structure refinement was carried out by dividing the 20 K data into two sets in the same way as done for 300 K. In this refinement, the scale factors were kept fixed at the values obtained from nuclear fit at 300 K. Initial analysis revealed that there is no difference in the fits of FM and AFM ordered structures along c-axis. This is due to the nature of measured reflections. All the peaks have an even value of ℓ (Miller index), which means that the diffracted intensity is same for FM and AFM

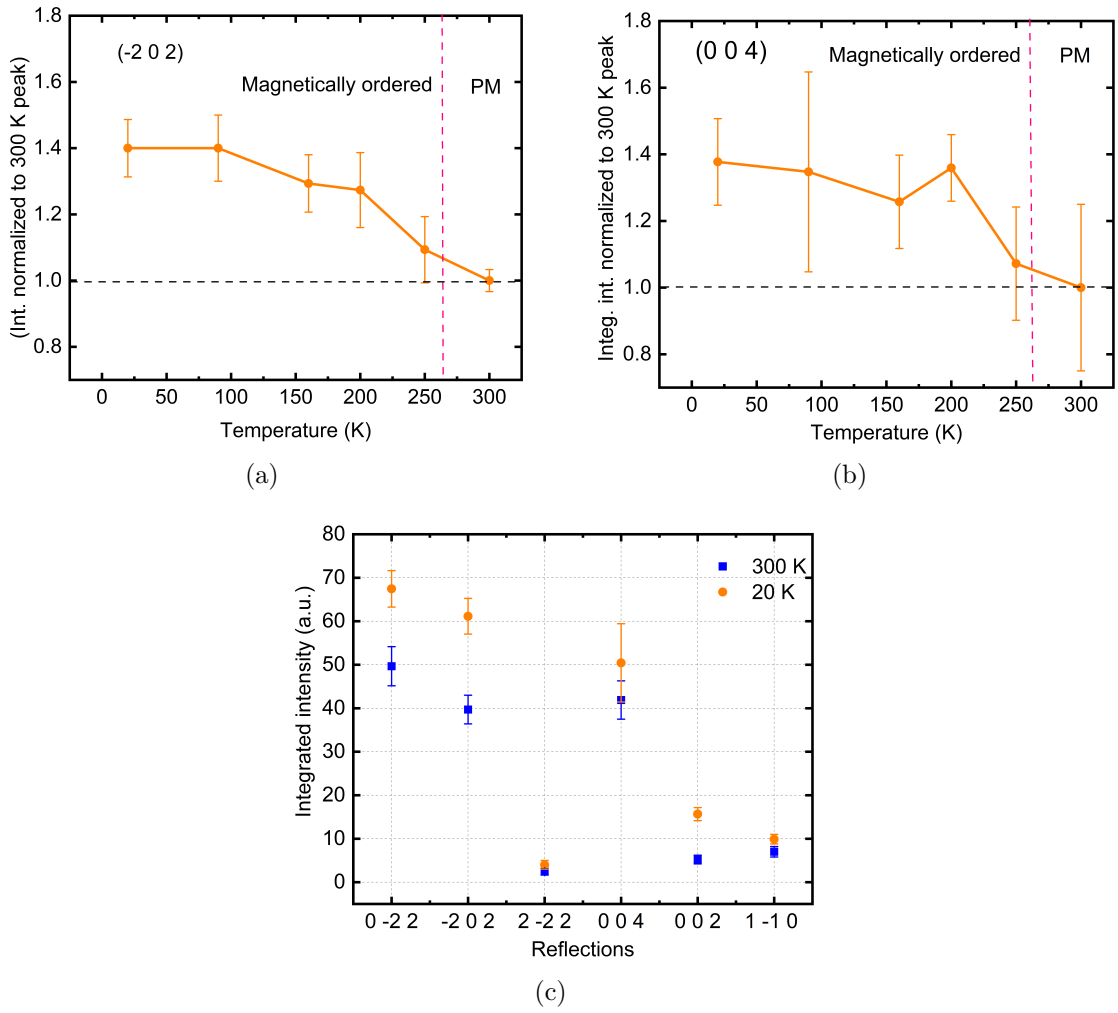

Figure 4.29: Integrated intensities of peaks measured with ND on LSMO film at various temperatures in the range 300 - 20 K: (a) (-2 0 2) and (0 0 4). (c) Comparison of integrated intensities of all the reflections measured at 20 K with the 300 K one.

structures. We analyzed several different models with FM and AFM ordering in the OOP direction. The obtained fit for 3 of the models with 20 K data-sets is shown in Figure 4.31(a). The calculated intensity is the same for all the models. Therefore, the recorded set of reflections is not enough to resolve the magnetic structure of the film and further measurements were needed.

To be noted that these are not all the possible models. The main goal here was to investigate the effect of nature of OOP ordering. The magnitude and alignment of the moment was refined using the complete data-set (explained later).

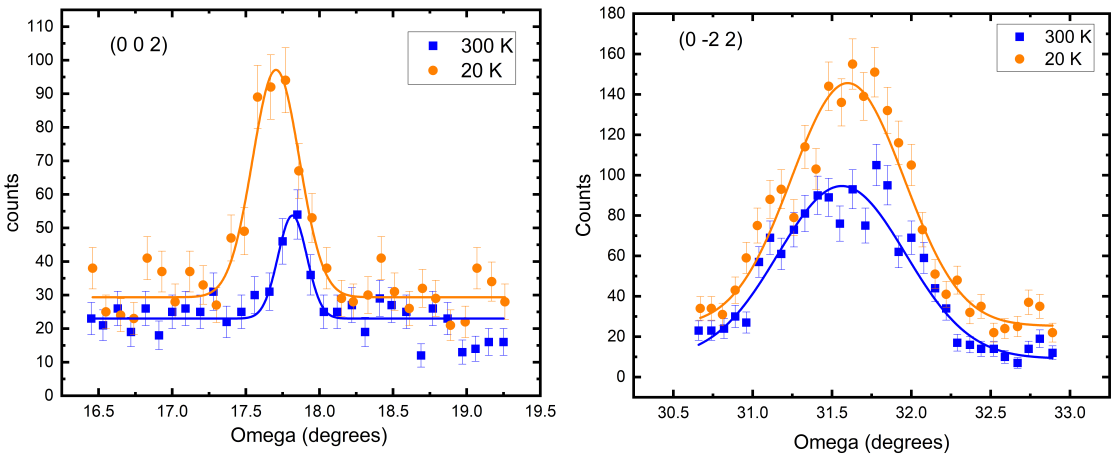

(a) (b)

Figure 4.30: ND (D10) peaks measured on LSMO film at 300 K and 20 K showing clear increase for both (0 0 2) and (0 -2 2) reflections.

To answer the question about magnetic ordering along *c*-axis, another experiment was performed on the upgraded D10+ instrument. Few reflections were identified that have zero nuclear contribution and are absent for FM structure, but should be significant in intensity for AFM ordering along OOP direction. The calculation was done by adding some "test" reflections with odd values of ℓ in the present data-set with a random amount of intensity. Then the fits for two models were compared again keeping the scale factor fixed at 300 K value. Figure 4.31(b) shows that the calculated magnetic structure factors of peaks (2 0 1), (1 1 1) and (1 0 1) are different for the two models and all zero for FM ordering. Thus, by measuring these reflections one should be able to resolve the nature of ordering along *c*-axis.

4.5.4.2 Measurements on the upgraded D10+

The measurements were performed with incident neutron wavelength of 2.36 Å. The procedure followed was similar to the previous experiment on D10. The main goal of this experiment was to measure selected AFM reflections at 20 K. At first, UB-matrix of the film was calculated at 300 K. The obtained lattice parameters are in-agreement with the previous measurements. The upgrade on D10 provided significant advantage in this study as decent increase in intensity was observed as compared to the previously measured peaks.

The (0 0 2) and (0 0 4) peaks measured on D10 at 300 K are compared with those from D10+ in Figure 4.32. Both the scans are normalized with respect to measurement time (145 minutes). As evident, there is big increase in intensity after the upgrade on D10. Thanks to this advancement, the measurement of AFM peaks, which are even weaker due to only magnetic scattering intensity, became possible.

The selected AFM peaks were measured at 20 K along with (0 0 2), (0 2 2) and (0 0 4). There was no significant increase in intensity observed this time on (0 0 2), (0 2 2) and (0 0 4) peaks. We expect this is due to off-centered UB-matrix at 20 K. This is because in this experiment the UB-matrix was not recalculated at 20 K and instead, the one from 300 K was used. This can lead to slight misalignment in the scans and hence, its possible that the measured intensity is lower. Nevertheless, this offset is not significant enough to discard our conclusions on AFM peaks.

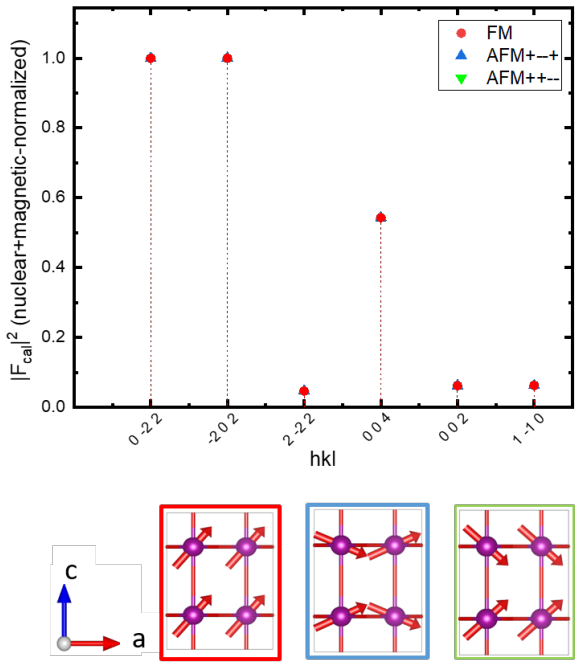

(a)

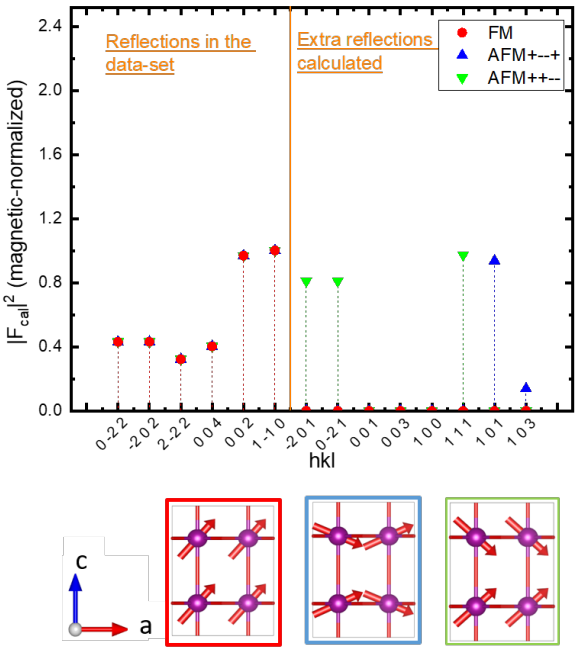

(b)

Figure 4.31: (a) Square of structure factors (nuclear+magnetic) of reflections measured at 20 K calculated using FP for different possible magnetic structure models along *c*-axis of the LSMO film. The structure factors are normalized to the maximum value. (b) Square of magnetic structure factors calculated using FP for reflections measured at 20 K and few extra ones that were added manually. The calculations were performed for various magnetic models in order to select few reflections to be measured in the experiment on D10+.

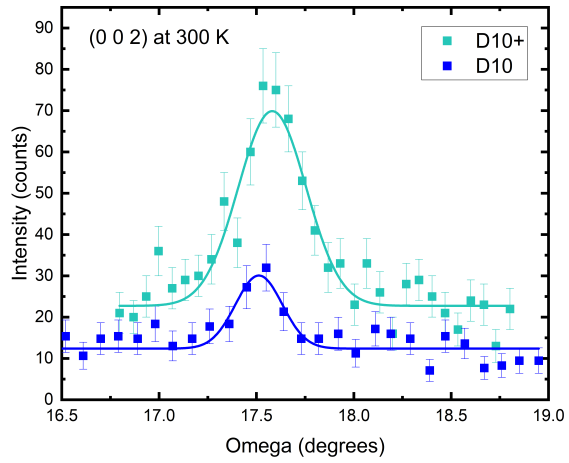

(a)

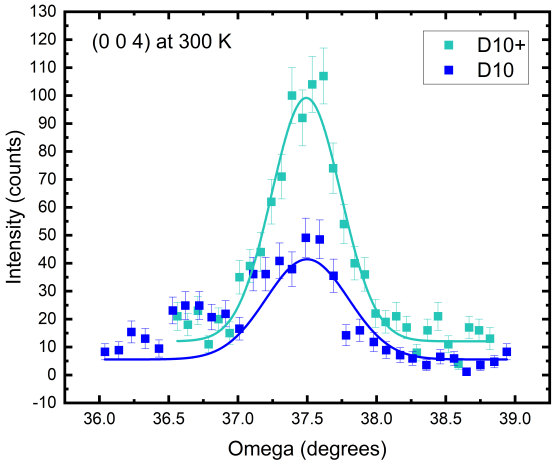

(b)

Figure 4.32: Comparison of LSMO film peaks (a) (0 0 2) and (b) (0 0 4), measured using D10 and D10+ at 300 K. The peaks are normalized to measurement time of 145 minutes each.

Magnetic ordering along c-axis

The four selected AFM reflections measured on D10+ are shown in Figure 4.33. As

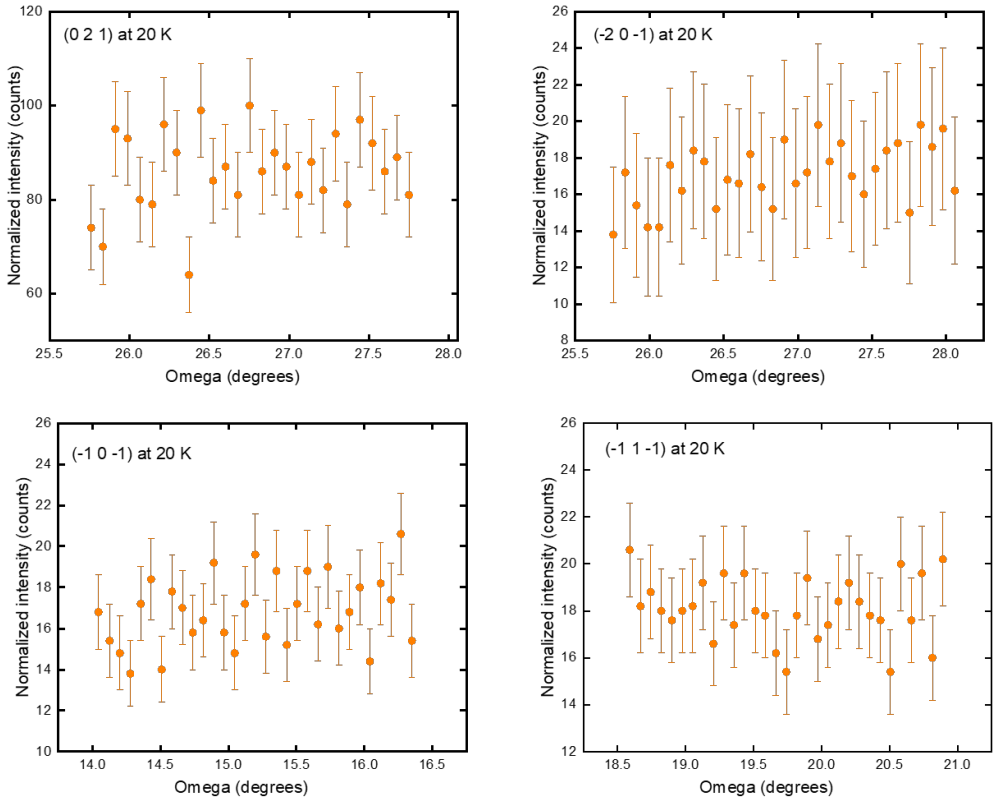

Figure 4.33: The 4 selected AFM reflections measured at 20 K on LSMO film using D10+ to investigate the nature of magnetic ordering along c-axis.

seen in Figure 4.33, no intensity was detected on any of the 4 reflections. This result clearly points to the fact that the magnetic ordering along c-axis in the film is FM in nature. The next step was to refine the magnetic structure with FM ordering along both IP and OOP directions.

4.5.4.3 Magnetic refinement

Now we turn our discussion back to the data-set measured at 20 K in the first experiment (on D10). This data-set was used to obtain the final magnetic structure. There are 5 reflections in total in this data-set, which makes the refinement challenging. Therefore, FP was run indirectly through Python script and the moment configuration was optimized step by step. We used a complete FM model with components along $\vec{a}$ and $\vec{c}$ axes (μ_a and μ_c). Since the $\vec{a}$ and $\vec{b}$ axes are equivalent in the film, two magnetic domains; moments along (μ_a, 0, μ_c) and (0, μ_a, μ_c) were used with 50% occupancy for each. In the magnetic refinement, the nuclear structure was described

in $P\bar{1}$ space group and scale factor was taken from the nuclear fit at 300 K. The propagation vector ($\vec{K}$) is (0, 0, 0).

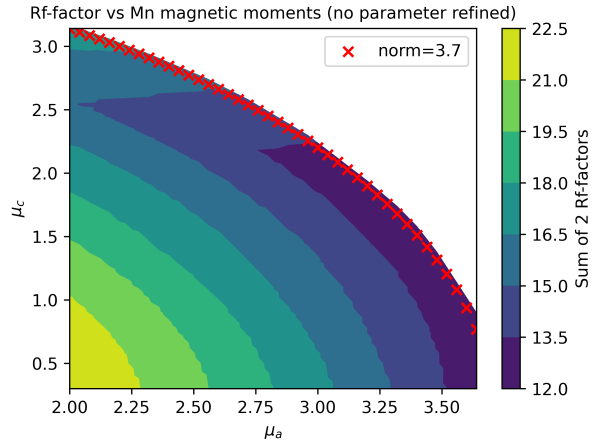

(a)

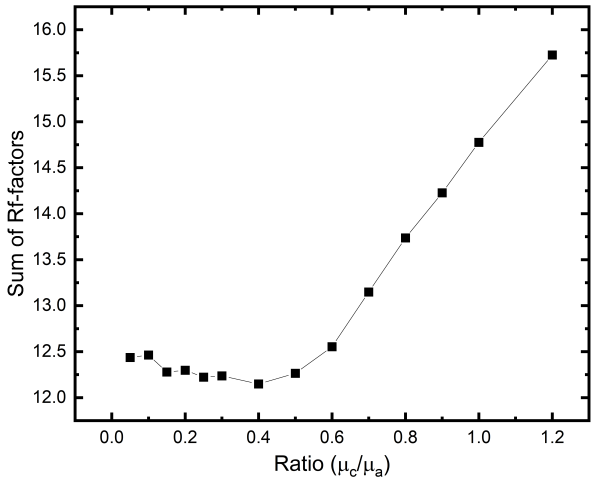

(b)

Figure 4.34: (a) Different values for μ_a and μ_c components of Mn moments in LSMO plotted against their corresponding calculated sum of Rf-factors. The red markers indicate points corresponding to norm of moment = 3.7 μ_B. (b) The sum of Rf-factors calculated for different possible ratio of μ_c and μ_a components, keeping the norm of moment fixed at 3.7 μ_B.

Theoretical magnetic moment of Mn ions in LSMO is $0.67\mu_{Mn^{3+}} + 0.33\mu_{Mn^{4+}} = 3.7\mu_B$ [3]. At first, in order to determine the moment size, Rf-factors were calculated for different magnitudes of Mn moment. The size of the moment was increased up to slightly over 3.7 μ_B in small steps by increasing both μ_a and μ_c. The obtained fit is shown in Figure 4.34(a). The red symbols on the plot correspond to norm of the

[3]Considering only spin moment contribution of 1 μ_B per Mn unpaired electron and no contribution from the orbital moment

moment $|\vec{\mu}| = 3.7\ \mu_B$, which is the theoretical limit. The color bar indicates trend in the sum of two Rf-factors (corresponding to 2 data-sets used). It is clear from this plot that the size of the moment is close to 3.7 μ_B as the sum of Rf-factors is lowest in that region. Furthermore, this plot also gives an idea about the magnitude of μ_a and μ_c components. It seems that the fit is better with μ_a component significantly larger than μ_c.

To analyze this further, fitting of the ratio of μ_c and μ_a components of moments was carried out while keeping the norm of the moment fixed at 3.7 μ_B per Mn. The results of this are shown in Figure 4.34(b). It was found that the sum of 2 Rf-factors is lowest in a range of 0.1 to 0.4 μ_c/μ_a ratio. The differences in the Rf-factors in this range are not big enough to pick one ratio over another. This is possibly due to low number of reflections. The complete structure was established using results from SQUID as discussed next.

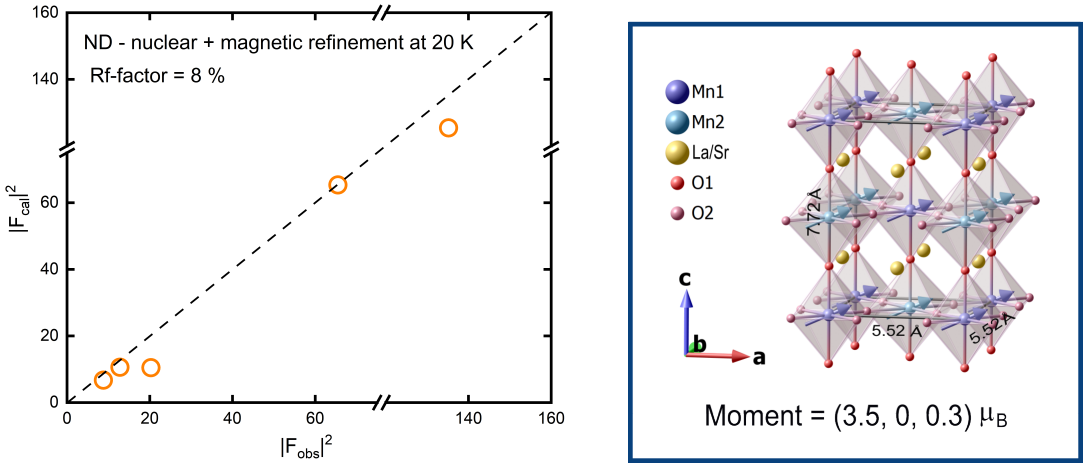

(a) (b)

Figure 4.35: (a) Comparison of calculated and observed square of structure factors of all the reflections measured on LSMO film at 20 K, for complete FM model with μ_c/μ_a ratio = 0.1. (b) The resolved magnetic and nuclear structure of the LSMO film. The OOP angle of the moments is exaggerated for clarity.

From SQUID, we found that μ_c is 0.1 times μ_a. We have used the ratio of components as a tool to compare the ND and SQUID results. This is because the conversion of SQUID signal from emu to μ_B is difficult in this case as an accurate determination of film volume on the sample is needed. ND results show that the magnetic structure is fully FM in nature and the fit of magnetic model with μ_c/μ_a ratio = 0.1 gives an Rf-factor of 8 %. The observed and calculated structure factors for this model and a schematic of the resolved magnetic structure are shown in Figure 4.35. The Mn moment is thus (3.5, 0, 0.3) μ_B. This shows that the moments are tilted slightly OOP (about 6°, exaggerated in Figure 4.35(b) for clarity).

For bulk LSMO, we know that the magnetic easy-axis is along [111] with FM ordering [109]. On the other hand, ultra thin films with thickness less than 3 nm

are found to favor co-existence of FM and AFM phases [18, 124]. In our case, the easy-axis are almost IP with a small tilt OOP. In this regard, we can say that the film is not fully relaxed at 40.9 nm thickness and is still far from bulk-like behavior. The direct determination of OOP ordering and the tilt completes the magnetic picture of these films. With information on the exact spin alignment, their utilization in spin-based devices can be further improved.

4.5.4.4 Space group symmetry analysis

The resolved magnetic structure is not compatible with the I*4/m* space group symmetry. The magnetic moment of Mn has both IP and OOP components. The Irreps of I*4/m* space group allow only one of IP and OOP components and not both together, which means that this type of structure cannot be represented using a single Irrep of space group I *4/m*. Although it is possible to represent the structure using more than one Irrep, it leads to extra terms in the Hamiltonian outside the block-diagonal form (equation 2.25). Therefore, the structure must be represented with a single Irrep. This may also require choosing a space group of lower symmetry. To find a compatible representation, the following calculations were performed.

Two types of symmetry analysis were considered; site-symmetry and the overall space group symmetry. At first, we will discuss the consequences of Mn site-symmetry. Site-symmetry deals with the constraints on the magnetic moments due to a symmetry operation present on the Mn position. Therefore, we needed to find a Wyckoff site with symmetry that allows both IP and OOP components of Mn moments simultaneously.

To do this, different Wyckoff sites were considered for Mn atoms in I*4/m* space group. Only the subgroups with body-centered unit cells were taken into consideration because we are dealing with site-symmetry and hence, there is no reason to remove the translation symmetry present due to body-centering. Figure 4.36 shows the point group chart highlighting the sub-point groups of *4/m*. Table 4.7 lists the possible Wyckoff sites for Mn in different point group settings.

As an example, consider the Mn atoms to be located on a 4-fold axis (Wyckoff site *2a*) of point group *4*. The Irreps for this site are shown in Table 4.8. Since Mn is located on a site with 4-fold symmetry, the magnetic moment ($\vec{\mu}_1 = (\mu_a, \mu_b, \mu_c)$) should transform as follows:

$$\begin{aligned} C_4\vec{\mu}_1 &= \vec{\mu}_2 = (-\mu_b, \mu_a, \mu_c) \\ C_2\vec{\mu}_1 &= \vec{\mu}_3 = (-\mu_a, -\mu_b, \mu_c) \\ C_4^3\vec{\mu}_1 &= \vec{\mu}_4 = (\mu_b, -\mu_a, \mu_c) \end{aligned} \tag{4.10}$$

Thus, if $\vec{\mu}_1$ belongs to Irrep A, then the constraints in equation 4.10 dictate that the moment $\vec{\mu}_1 = \vec{\mu}_2 = \vec{\mu}_3 = \vec{\mu}_4$, which is only possible if (μ_a, μ_b, μ_c) = (0, 0, μ_c). Similarly, Irrep B gives (0, 0, 0) and Irrep E allows (μ_a, μ_b, 0) moments. This concludes that if the Mn atoms are located on this site, the moments can only have either IP or OOP components and not both together. This is in contradiction with the solved magnetic structure, which has both IP and OOP components.

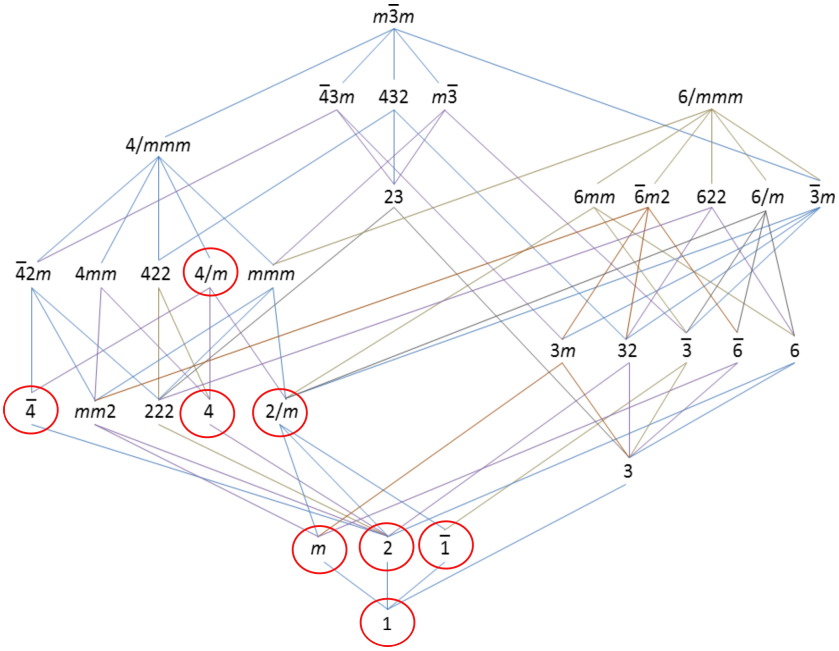

Figure 4.36: Point group chart highlighting the sub-point groups of *4/m* (red circles) used in symmetry analysis.

Table 4.7: Different possible Mn sites for *4/m* point group and few of its subgroups in body-centered unit cell (I) listed with site-symmetry

Space group	Possible Mn WyckOff site	Site-symmetry
I*4/m*	*2a*	..4/m
	4c	..2/m
	4e	..4
I*4*	*2a*	..4
	4b	..2
I*2/m*	*2a*	..2/m
	4d	-1
	4e	-1
	4f	..m
	4h	..2
P$\bar{1}$	*2i*	1

Table 4.8: Irreps calculated for point group *4* symmetry

Irrep	E	C_4	C_2	C_4^3
A	1	1	1	1
B	1	-1	1	-1
E	$\begin{pmatrix} 1 & 0 \\ 0 & 1 \end{pmatrix}$	$\begin{pmatrix} 0 & -1 \\ 1 & 0 \end{pmatrix}$	$\begin{pmatrix} -1 & 0 \\ 0 & -1 \end{pmatrix}$	$\begin{pmatrix} 0 & 1 \\ -1 & 0 \end{pmatrix}$

Similar analysis were carried out for other sites shown in Table 4.7. Our calculations revealed that if Mn atoms are located on site *4e* or *4f* in *2/m* point group, the site-symmetry allows moments with both IP and OOP components. However, it is also needed that the magnetic moment configuration is allowed by the overall symmetry of the space group and not just the site symmetry. We found that the overall space group symmetry of I*2/m* group does not allow FM coupling. This is explained in the following paragraph. The possible Irreps for I*2/m* group are shown in Table 4.9.

Table 4.9: Irreps calculated for I*2/m* space group

Irrep	E	C_2^z	i′	m_z'	t	t ∘ C_2^z	t ∘ i′	t ∘ m_z'
A_g	1	1	1	1	1	1	1	1
B_g	1	-1	1	-1	1	-1	1	-1
A_u	1	1	-1	-1	1	1	-1	-1
B_u	1	-1	-1	1	1	-1	-1	1
A_g'	1	1	1	1	-1	-1	-1	-1
B_g'	1	-1	1	-1	-1	1	-1	1
A_u'	1	1	-1	-1	-1	-1	1	1
B_u'	1	-1	-1	1	-1	1	1	-1

For instance, consider Mn atoms at site *4e* (in I*2/m* space group) that allows IP and OOP component in moments simultaneously. If the magnetic structure belongs to Irrep A_g, the transformations of moments of different Mn atoms can be written as shown in Table 4.10. The only possible solution allowed by these constraints is $\vec{\mu}$ = (0, 0, 0), which is not possible for this system. As another example, if the structure follows A_u Irrep, the moments transform in a slightly different manner (see Table 4.11). It can be easily deducted from the constraints that the A_u Irrep allows FM coupling OOP but IP the moments must be coupled AFM. This solution does not hold with our experimental observations.

Table 4.10: Magnetic moment transformation according to A_g Irrep with Mn at site *4e* in I*2/m* space group setting

Operator	Atomic coordinates	Moment $\vec{\mu}$
E	(1/4, 1/4, 1/4)	(μ_a, μ_b, μ_c)
C_2^z	(3/4, 3/4, 1/4)	(-μ_a, -μ_b, μ_c)
i′	(3/4, 3/4, 3/4)	(-μ_a, -μ_b, -μ_c)
m_z'	(1/4, 1/4, 3/4)	(μ_a, μ_b, -μ_c)
t	(3/4, 3/4, 3/4)	(μ_a, μ_b, μ_c)
t ∘ C_2^z	(1/4, 1/4, 3/4)	(-μ_a, -μ_b, μ_c)
t ∘ i′	(1/4, 1/4, 1/4)	(-μ_a, -μ_b, -μ_c)
t ∘ m_z'	(3/4, 3/4, 1/4)	(μ_a, μ_b, -μ_c)

Similarly, calculations for all the possible Irreps were performed for Mn at *4e* and *4f* Wyckoff sites. It was concluded that the I*2/m* space group is incompatible with

Table 4.11: Magnetic moment transformation according to A_u Irrep with Mn at site *4e* in I*2/m* space group setting

Operator	Atomic coordinates	Moment $\vec{\mu}$
E	(1/4, 1/4, 1/4)	(μ_a, μ_b, μ_c)
C_2^z	(3/4, 3/4, 1/4)	(-μ_a, -μ_b, μ_c)
i′	(3/4, 3/4, 3/4)	(μ_a, μ_b, μ_c)
m_z'	(1/4, 1/4, 3/4)	(-μ_a, -μ_b, μ_c)
t	(3/4, 3/4, 3/4)	(μ_a, μ_b, μ_c)
t ∘ C_2^z	(1/4, 1/4, 3/4)	(-μ_a, -μ_b, μ_c)
t ∘ i′	(1/4, 1/4, 1/4)	(μ_a, μ_b, μ_c)
t ∘ m_z'	(3/4, 3/4, 1/4)	(-μ_a, -μ_b, μ_c)

the resolved magnetic structure. This means that the space group symmetry needs to be lowered further. Further calculations revealed same results for I*2* and I*m* space groups. We found that P $\bar{1}$ space group is a possible option that's consistent with the magnetic moment configuration. The Mn atoms are taken at *2i* Wyckoff sites; (1/4, 1/4, 1/4) and (3/4, 3/4, 1/4). The possible Irreps for P$\bar{1}$ group are shown in Table 4.12.

Table 4.12: Irreps calculated for P-*1* space group

Irrep	E	i′
A_g	1	1
A_u	1	-1

Table 4.13: Magnetic moment transformation according to A_u Irrep with Mn at site *2i* in P-*1* space group setting. The Mn atoms are located on two different sites (both *2i* and the moment components of the second site Mn atoms are presented as $\vec{\mu'}$.

Operator	Atomic coordinates	Moment $\vec{\mu}$
E	(1/4, 1/4, 1/4)	(μ_a, μ_b, μ_c)
i′	(3/4, 3/4, 3/4)	(μ_a, μ_b, μ_c)
E	(3/4, 3/4, 1/4)	(μ_a', μ_b', μ_c')
i′	(1/4, 1/4, 3/4)	(μ_a', μ_b', μ_c')

The transformation of moments under the symmetry operations of P$\bar{1}$ space group with Mn at *2i* sites and according to Irrep A_u are shown in Table 4.13. It is clear that the moment $\vec{\mu} = (\mu_a, \mu_b, \mu_c)$ can be FM in nature along IP as well as OOP direction and can have both the components non-zero simultaneously. This is in agreement with the experimental observations. Therefore, the final resolved structure is represented in P$\bar{1}$ space group unit cell as shown in Figure 4.37.

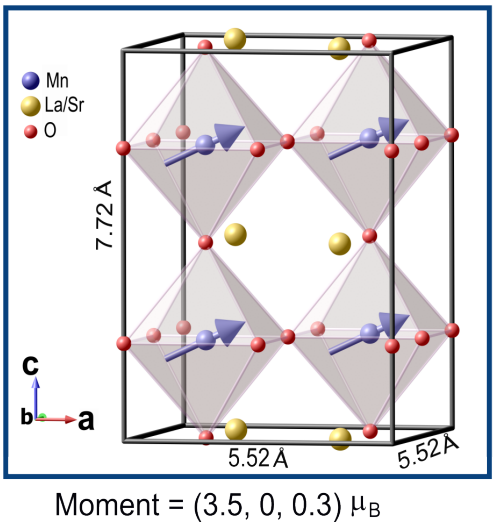

Figure 4.37: Resolved nuclear and magnetic structure of the LSMO film represented in $P\bar{1}$ space group. The OOP angle of the moments is exaggerated for clarity.

4.6 Conclusion

Summarizing the results of this chapter, we carried out diffraction studies and SQUID magnetometry on a thin film of LSMO.

The LSMO film was first characterized using TEM imaging. We found that the thickness of the deposited film is about 40.9 nm and a nice periodic stacking of layers was observed along the surface normal direction. A (0 0 ℓ) scan recorded using XRD showed peaks from the different materials in the sample: The substrate Si, the buffer layer STO and the LSMO film itself. Several other reflections were measured using 2D scans in IP and OOP modes. Despite the low thickness of the STO buffer layer, it was found that the LSMO film follows IP constraints imposed by STO. This was established using the IP peak positions. The lattice parameters obtained are: $a_{LSMO} = b_{LSMO} = 5.522 \pm 0.006$ Å and $c_{LSMO} = 7.690 \pm 0.004)$ Å. Furthermore, the presence of 4-fold symmetry was revealed by the measurement of equivalent reflections IP and the type of unit cell was confirmed to be body-centered tetragonal. Finally, the structural refinement was carried out on 15 independent measured reflections. The integrated intensities were obtained using Python scripts by summing over the recorded counts carefully, avoiding contribution from STO, and subtracting background. Several different corrections were also applied to the measured intensity including film area under diffraction, Lorentz factor and polarization. A rigorous refinement procedure using a combination of Python scripts and FullProf software package revealed that the LSMO film follows $I4/m$ nuclear space group symmetry.

Macroscopic magnetic properties were measured using SQUID magnetometer. Temperature dependence of magnetization showed that the film undergoes a magnetic transition to paramagnetic phase above 260 K. From magnetic hysteresis for field applied along different directions, we observed FM ordering characteristics for

IP directions: [100] and [110]. The OOP hysteresis, however, was not conclusive of the nature of magnetic ordering along [001]. To completely resolve the magnetic structure, ND measurements were conducted. The reflections measured in the paramagnetic phase at RT fitted well with the nuclear $I4/m$ space group. As we reduced the temperature, increase in the intensity was observed for several reflections as an effect of magnetic ordering in the system below 260 K. The magnetic ordering along c-axis was resolved by measuring selective reflections. These reflections were calculated to be non-zero for different AFM models along c-axis and zero otherwise. We observed no intensity for these reflections at 20 K, confirming that the magnetic structure is completely FM ordered. The magnitude and direction of the magnetic moment was refined by fitting the data-set measured at 20 K with different combinations of FM ordered structure. The fitting procedure involved optimizing the ratio of [100] and [001] components along with the size of the moment using Python scripts. The obtained magnetic structure of the LSMO film consists of moments along (3.5 0 0.3) μ_B with FM ordering.

In the first section of this chapter, we discussed about the need for complete nuclear and magnetic structure determination of LSMO films. They present huge potential for technological applications. The determination of nature of magnetic ordering and the out-of-plane tilt of magnetic moments using ND, is a significant addition to the manganese oxide film literature. Our findings offer considerable insight into the structural and magnetic properties of LSMO films that can be utilized for further improvements in their spintronic performance.

Overall, this chapter provides basis to carry out such studies on similar films to obtain crucial information about their atomic configuration.

Chapter 5

3-3 super-lattice

Contents

5.1 State of the art

5.1.1 Physics behind super-lattice structures

Super-lattice type structures are composed of epitaxial layers of different materials deposited alternatively on a substrate. Each material's layer thickness can vary from few atoms to few nanometers. Super-lattices are designed with a precise and periodic arrangement of the layers. The materials in each layer have distinct properties and the periodic arrangement allows for new, unique and interesting characteristics. Their behavior can be further manipulated by varying relative thickness of each component, periodicity, strain, and morphology. The intriguing properties of super-lattices have been well-utilized and researched for technological applications such as transducers, spin-transport and information storage. Numerous exciting super-lattices have been explored by researchers over the years such as $La_{0.7}Sr_{0.3}MnO_3/BaTiO_3$ (LSMO/BTO), $La_{0.7}Ca_{0.3}MnO_3$/BTO, $Pr_{0.85}Ca_{0.15}MnO_3$/BTO, $Pr_{0.85}Ca_{0.15}MnO_3$/STO, Fe/BTO, EuO/BTO, and Fe3O4/BTO [132–143].

One of the common and exciting combination for super-lattices include materials showing ferroic orders of magnetic and eletrical nature. In particular, LSMO/BTO has attracted significant attention showing strong ferroic order and magnetoresistive properties, making them well-suitable for spintronic devices. In this study, we will mainly control magnetic properties of LSMO/BTO super-lattices using the strain induced by the epitaxy. Let us have a look at the properties of bulk BTO first and then the LSMO/BTO super-lattices.

5.1.2 LSMO/BTO super-lattices

We know that the LSMO films are FM and BTO is known for showing ferroelectric behavior. This make a well suited combination for potential magneto-electric coupling in the system. Bulk BTO undergoes 3 distinct structural transitions with temperature: cubic-tetragonal at T = 393 K (ferroelectric Curie point), tetragonal-orthorhombic at T = 278 K, and orthorhombic-rhombohedral at T = 190 K [144]. It is to be pointed out these structural transitions are found to be absent in very thin films of BTO (60 nm) [145]. The lattice mismatch between cubic BTO and STO is about -2.3 % and between LSMO-STO, ≈ 0.7 %.

The quality of epitaxy has been reported to be very good on layered LSMO/BTO structures deposited on STO[001] substrates, showing single crystal like periodicity. Presence of magnetoresistive effects has also been established in these materials [29, 30]. The role of interface and strain is found to be crucial in determining their physical properties. The effect of thickness of different layers on magnetization of the sample has also been studied. The nature of magnetic ordering as well as magnitude of saturation magnetization were found to vary with changes in BTO and LSMO thicknesses. There was significant decrease reported in saturation magnetization with increase in BTO layer thickness (from 4 to 12 monolayers) and antiferromagnetic coupling is expected for samples with thin LSMO layers [30]. It was attributed to the

role of the strain in magnetic behavior of the sample. These studies were performed on samples with 4 to 12 monolayers of LSMO and BTO. In this project, we focus on super-lattices with only up to 3 monolayers of each material. Now we move to a review of the work already done on these super-lattices.

Work done prior to this on $(LSMO)_3/(BTO)_3$ super-lattices

One of the most desired property for spintronic devices is the Curie temperature (T_c) being significantly higher than RT. Strain in LSMO epitaxial films can be used to control the orbital ordering in Mn ions and alter the magnetic properties of the material such as T_c. This was theoretically predicted and experimentally verified on $(LSMO)_3/(BTO)_3$ (3-3) super-lattices by A. Sadoc et al. [28]. Large increase in T_c was achieved through orbital ordering manipulation. The idea behind this study can be explained as follows.

The 3d orbitals of Mn^{3+} ions undergo crystal field splitting due to Mn-O octahedra environment in LSMO. The two e_g orbitals are Jahn-Teller active, which means that there is further splitting between $3d_{z^2}$ and $3d_{x^2-y^2}$ orbitals. The 4^{th} unpaired electron in 3d shell occupies one of these two orbitals, stabilizing it over the other one. The preferred orbital by the electron is the one which presents lesser electronic repulsion, i.e. the one which is along the longer lattice parameters out of z- and IP $x-y$. The strategy applied in this work provides control over this orbital occupation. This is done by imposing appropriate in-plane strain through the substrate.

If one chooses a substrate with the in-plane lattice parameter $a > c_{\mathrm{LSMO}}$, the electronic repulsion will be stronger along the c-axis because of the shorter distance Mn-O along c-axis as compared to IP. Hence, the $3d_{x^2-y^2}$ orbital will be stabilized over $3d_{z^2}$. By same reasoning, in the case of $a < c_{\mathrm{LSMO}}$ the $3d_{z^2}$ orbital will be occupied. Both these possibilities are illustrated in Figure 5.1(a).

In thin films, the in-plane interactions are important and control the magnetic properties of the material. The occupation of $3d_{x^2-y^2}$ orbital leads to stronger in-plane orbital overlap, hence stronger magnetic interactions enhanced by delocalization . Consequently, this results in a higher T_c. This way, by applying appropriate strain through substrate, thin films with desired magnetic properties can be designed.

In general, thin films tend to relax the strain going away from the substrate interface. In order to keep the strong in-plane orbital overlap, the strain needs to be maintained throughout the structure. This was done by intercalation of BTO layers alternatively with the LSMO film (super-lattice structure) deposited on STO substrate. At RT, STO has lattice parameter $a = 3.905$Å, which is higher than bulk LSMO (3.88 Å). The condition for first scenario is satisfied so, $3d_{x^2-y^2}$ orbital should be occupied by the 4^{th} unpaired electron in Mn^{3+}.

A. Sadoc et al. demonstrated this phenomenon by combination of ab-initio calculations and magnetic macroscopic measurements [28]. It was theoretically predicted and experimentally verified that the T_c of 3-3 super-lattice is significantly higher as compared to LSMO film and bulk. In Figure 5.1(b), one can clearly see that there is magnetization present in the sample up to 600 K (loss of oxygen at higher tempera-

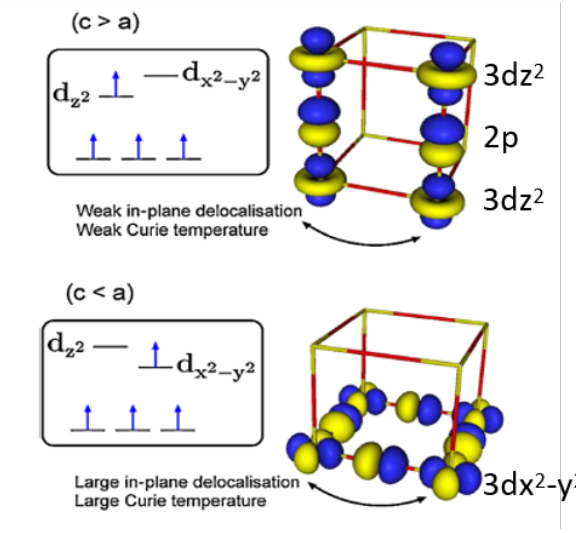

(a)

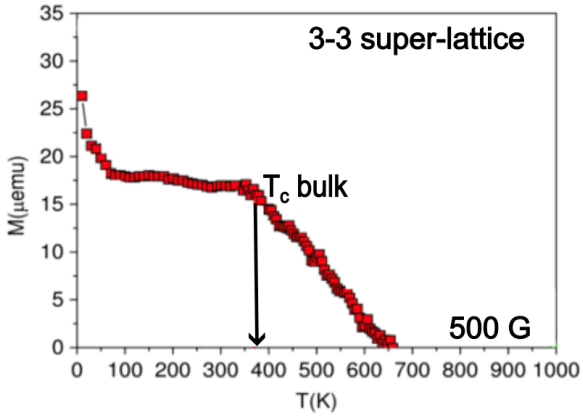

(b)

Figure 5.1: (a) Schematic representation of orbital ordering induced by cell distortions due to strain in LSMO. (b) Temperature dependence of the IP magnetization of 3-3 super-lattice showing significant increase in T_c due to orbital ordering caused by strain. Adapted from [28].

ture - degradation of the sample), making it a very suitable candidate for spintronic devices.

The theoretical calculations on geometry optimization of the 3-3 super-lattice using DFT showed that the two inter-facial layers of LSMO are not only extended in $\vec{a}$ and $\vec{b}$ directions, but also in the $\vec{c}$ direction. On the other hand, the middle LSMO layer was found to be contracted along the $\vec{c}$ direction. As per the length of lattice parameters, the interfacial layers were predicted to favor $3d_{z^2}$ orbital occupation ($c/a > 1$) whereas $3d_{x^2-y^2}$ for the middle one. It was hypothesized that these two layers contribute to two different magnetic phases observed on the M(T) curve shown in Figure 5.1(b); One below 25 K and second one up to 600 K.

The orbital occupation in this super-lattice has been experimentally analyzed by Zhang et al. who find contrary results. They used X-ray linear dichroism measurements to find that the preferred orbital is $3d_{x^2-y^2}$ in LSMO/BTO super-lattices [31]. The occupation of $3d_{z^2}$ by the middle layer was negated by their interpretations. However, the increase in T_c was not found to be as significant and thus, the findings are not conclusive. There are no other experimental studies on these super-lattices providing information on their crystal structure.

We are still far from the complete structural and magnetic picture of the 3-3 super-lattices. These materials are in-demand for their outstanding properties and open the way to design artificial structures with desired magnetic properties. However, structural characteristics and magnetic moment configuration needs to be established for their successful integration into devices. Thus, the goal of this study is to determine the nuclear and magnetic structure of these super-lattices combining experimental and theoretical techniques.

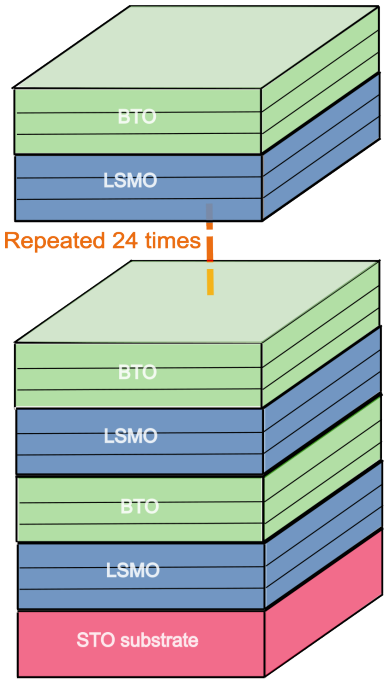

Figure 5.2: Schematic of 3-3 super-lattice sample showing repetition of layers of LSMO and BTO on STO substrate.

Table 5.1: List of different 3-3 super-lattice samples used for analysis, with their respective acronyms

Sample name	Configuration	Acronym
NG1118	$[(LSMO)_3(BTO)_3]_{24}$	A
NG1105	$[(LSMO)_3(BTO)_3]_{24}$	B
NG1102	$[(LSMO)_3(BTO)_3]_{24}$	C

To do so, we used samples prepared using the same synthesis techniques as discussed by A. Sadoc et al. to perform diffraction experiments and SQUID measurements. Performing single crystal diffraction experiments on such complex configurations comes with many challenges. Therefore, numerous neutron diffraction experiments were carried out on several samples to obtain significant information about the material. Table 5.1 lists all the samples used for the analysis. In addition, the DFT optimizations available from the previous work on 3-3, were also used for the analysis. Details on these calculations are provided in the next section.

5.1.3 DFT calculations

The preliminary work on 3-3 super-lattices using DFT was carried out by Aysegül Begüm Koçak in her PhD thesis [146]. The role of polarization from BTO layer and

octahedra rotations (antiferrodistortive - AFD) were studied to understand the magnetic behavior of these materials. It was found that the AFD motions are present only in the contracted layer of LSMO and enhance the preferential $3d_{x^2-y^2}$ occupation. In the elongated layers (inter-facial), $3d_{z^2}$ orbital is preferred and there is delocalization of electron to the empty Ti d-shell.

Further work on geometry optimizations was performed by E. Rebolini [1] and M. B. Lepetit [2], which is used in this project to better plan and analyze the diffraction results. Since in epitaxial structures, films normally follow the substrate constraints, the IP lattice constant was imposed to be same as STO for the super-lattice system. Keep in mind that the DFT optimizations were performed using a unit cell that's rotated by 45° IP in order to accommodate La/Sr disorder scenarios as described in the next paragraph. Thus, the IP lattice constants were 3.905 (STO bulk value at RT) $\times\sqrt{2}$ =5.51 Å. The optimizations were performed for the c lattice parameter and the atomic positions.

The calculations were performed using CRYSTAL package and the optimization were performed with Wu-Cohen GGA functional [72, 147]. One point of difficulty in these calculations was the La/Sr disorder. In periodic calculations, it is not possible to properly mimic the ionic disorder. Therefore, a whole set of calculations was obtained corresponding to totally ordered Sr ions and with average La/Sr ions. The unit cell used for these calculations was double IP as compared to the STO one (45° rotation IP) so the totally ordered case gives 9 different possibilities per calculation. The average La/Sr case included using average effective charge with different possible arrangements of La and Sr. The calculations were relatively easier with layers multiples of 3 because the Sr doping amount is $1/3^{rd}$ and hence can be accumulated well. If the doping amount were $1/5^{th}$, the size of the unit cell would have to be further increased, which leads to too big calculations and is not practical.

In addition, magnetic configuration was also taken into account while optimizing the atomic structure. A variety of different possible magnetic couplings (FM or AFM) among intralayer Mn ions were put as an additional constrain on the DFT optimizations. This way, a total of 27 geometries were obtained. These optimized geometries will be compared with the diffraction data in order to solve nuclear structure of the super-lattice.

[1] Computational group ILL, 71 Av. Martyrs Grenoble France
[2] Theory group, ILL and Institut Néel, Grenoble France

5.2 XRD

Information on the nuclear structure of the super-lattice was first obtained using XRD measurements on sample B with SmartLab diffractometer (unfortunately, sample A was not available anymore, discussed in-detail in the next section). A scan performed along (0 0 ℓ) direction is shown in Figure 5.3. Peaks from the super-lattice and substrate STO can be clearly observed and are marked in the figure. The $(0\ 0\ 6)_{3-3}$ peak is very close to the substrate peak. The c lattice parameter obtained is 24.10 $\pm$ 0.02 Å corresponding to the unit cell of 6 layers of LSMO and BTO combined, along perpendicular to the surface (c-axis) and that of STO is 3.9 Å. The spacing between STO and super-lattice peaks increases with ℓ and the peaks are well-resolved at higher values. The periodic positions of these peaks indicate that the structure grows in the [001] direction i.e. c-axis of STO, which is normal to the basal plane.

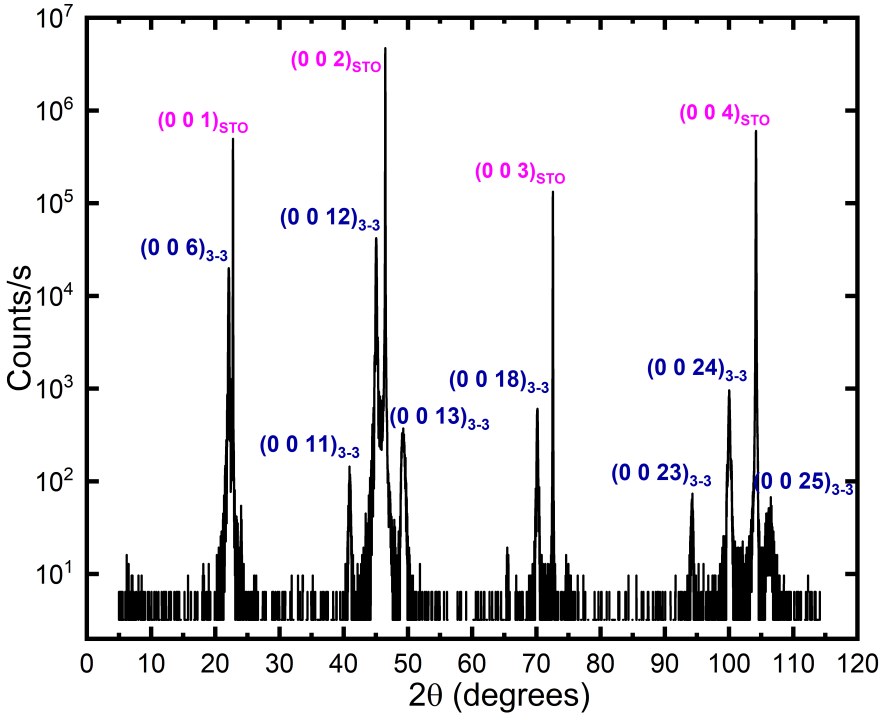

Figure 5.3: (0 0 ℓ) scan performed on sample B using XRD with peaks from the 3-3 super-lattice (blue) and the substrate STO (purple) clearly marked. The intensity on y-axis is presented on $\log_{10}$ scale.

Furthermore, the (0 0 ℓ) peaks were measured with better statistics in OOP geometry set-up using 1D $\omega - 2\theta$ scans and the results are shown in Figure 5.4. Several small satellite peaks can be clearly seen close to (0 0 6) and (0 0 12) main peaks. These are called Kiessig fringes. Kiessig fringes are a result of constructive interference between X-rays reflecting from the top and bottom surface of the super-lattice. The periodicity of these fringes is influenced by the thickness of the whole structure. For the (0 0 12) peak, these fringes are well-resolved up to $\theta = 2°$ (and

beyond) left from the main peak, highlighting the smoothness and good quality of the multilayers.

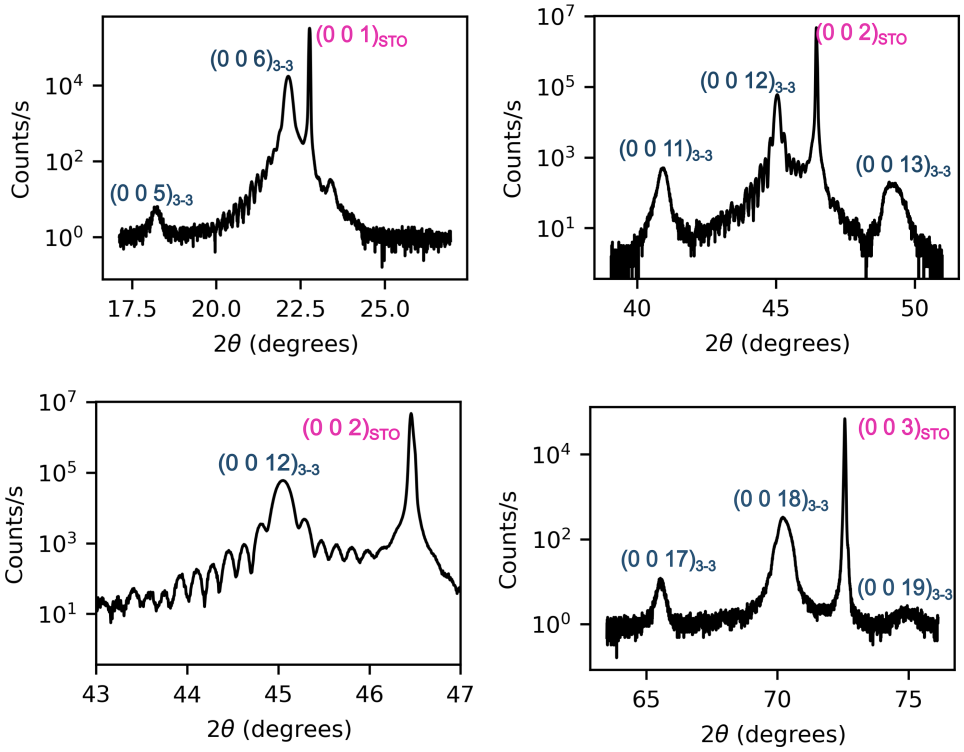

Figure 5.4: Some (0 0 ℓ) peaks measured on the 3-3 super-lattice sample B using XRD; (a) (0 0 6), (b) (0 0 12) along with (0 0 11) and (0 0 13), (c) enlarged view of the (0 0 12) peak to clearly show fringes, and (d) (0 0 17), 90 0 18) and (0 0 19) on one scan. Peaks from the 3-3 super-lattice (blue) and the substrate STO (purple) are clearly marked. The intensity on y-axis is presented on $\log_{10}$ scale.

The periodicity of these fringes was utilized for precise determination of the thickness using the following equation:

$$2t(\sin\theta_{n+1} - \sin\theta_n) = \lambda \tag{5.1}$$

where, t is the thickness of the film, λ is the wavelength of X-rays, and θ_{n+1} and θ_n are the positions of two consecutive fringes. Using this equation, we found the thickness of the super-lattice to be 59.7 nm. This is in agreement with the number of 24 times repetition of the stacking (24 $\times$ 24.1Å $\approx$ 58 nm).

In addition, very weak peaks such as (0 0 5), (0 0 17) and (0 0 19), which were not so obvious on the long scan (Figure 5.3), can be clearly seen on these scans.

In a similar way, several other peaks were measured including (1 1 6), (2 0 12), (2 0 18) amd (4 0 12) [3]. Out of these (1 1 6) was measured with its equivalent (1 -1 6) reflection as shown in Figure 5.5 (in a single crystal with in-plane 4-fold axis, these

[3]Please note that all the reflection indices of the super-lattice are presented in the IP doubled unit cell as compared to the STO one, to stay consistent with the notations used in DFT calculations.

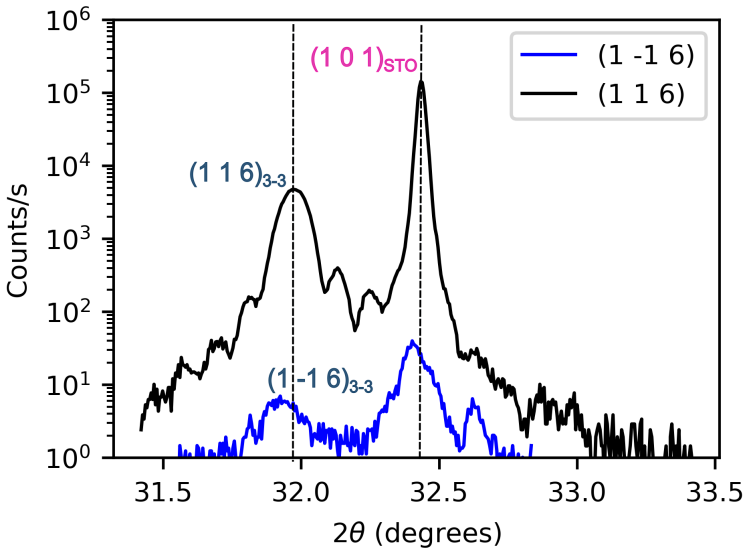

Figure 5.5: (1 1 6) and its equivalent (1 -1 6) peak measured on the 3-3 sample B using XRD. The dashed arrows marked show are to clearly show that the STO and 3-3 peaks are shifted and are not equivalent in both position and intensity. The intensity on y-axis is presented on $\log_{10}$ scale.

reflections should be equivalent). We confirmed that the in-plane film parameters are under strain from STO, with a relation of 45° rotation of the unit cell ($3.9 \times \sqrt{2} = 5.52$ Å). We observed that all the recorded peaks are symmetric in shape showing no sign of strain relaxation. This confirms the role of BTO layers in maintaining the strain throughout the film structure. Furthermore, it was found that there is big difference in the intensities and positions of the two peaks, even the substrate STO peak is shifted. This suggests that the substrate has crystallite domains and as we moved the sample to align for (1 -1 6) peak, the beam was diffracted from a different crystallite. This makes the measurement very challenging because the measured intensities cannot be compared if they are from different crystallites.

As a conclusion of this study, we confirm that the quality of the super-lattice is very good, but the overall quality of the sample B is impaired by the existence of different crystallites in the substrate. For this reason, we decided not to pursue a full XRD study as in the LSMO case. Thus, it was not possible to use this study to improve the knowledge of the positions of the atoms in the unit cell.

5.3 SQUID

Macroscopic magnetic measurements were performed on sample A using MPMS Quantum XL SQUID at Institute Néel. The purpose of these experiments was to obtain information about the nature of magnetic ordering in the system and the ratio of moment components along different crystallographic directions. This required measuring magnetic hysteresis for different applied fields along various directions. In addition, temperature dependence of the magnetization was also studied in the range 3 - 100 K. These results could help us hypothesize the possible magnetic structures of the super-lattice. While it is fairly possible to infer the behavior of a material's hysteresis from the magnetic structure, the reverse is not very straightforward. There is only a limited amount of conclusions that can be drawn from the SQUID results.

In thin film structures, depending on the magnitude of magnetization signal, the contribution from substrate can play a significant role in the analysis. For the super-lattice in consideration, it was necessary to subtract the STO data for correct analysis of the magnetic behavior.

The background subtraction (signal from the substrate - STO)
Usually, it is done by repeating the scans in paramagnetic phase of the film, that roughly includes signal from only the substrate. However, this approach was not possible for the 3-3 sample because the paramagnetic phase is above 600 K, which is not achievable with the SQUID MPMS instrument. Instead, this was done in the following way.

After doing the necessary measurements[4], the 3-3 sample was cleaned with HCl, which completely destroyed the deposited super-lattice. This sample was now with only the substrate STO. Therefore, we could use this cleaned sample data as a background (substrate signal) and subtract it from the sample data that was measured before cleaning it. This way, we extracted a clear "only super-lattice" signal.

Magnetic hysteresis measurements on the substrate with field (± 1 T) along [100] and [001] at 10 K are shown in Figure 5.6(a). The diamagnetic behavior of the substrate is clearly manifested in the negative slope of both the curves. There seems to be presence of very small ferromagnetic signal (area of hysteresis loop) in the substrate (not shown on the figure). Overall, the magnetic signal is very weak but the slope is significant to alter the super-lattice measurements (shown in Figure 5.8 later). The temperature dependent variation in magnetization is also shown in Figure 5.6(b) with 0.3 T applied field along [100] and [001] directions in the range of 3 - 100 K. No noticeable change is observed in the magnetization for both the directions. The anomaly close to 40 K is discussed in the next segment.

The super-lattice data, before and after carrying out the subtraction, is shown in the subsequent subsections to give an idea of the substrate contribution to the whole measured data.

[4]These measurements included complete SQUID data and 3 ND experiments described in the next section, but unfortunately not the X-rays

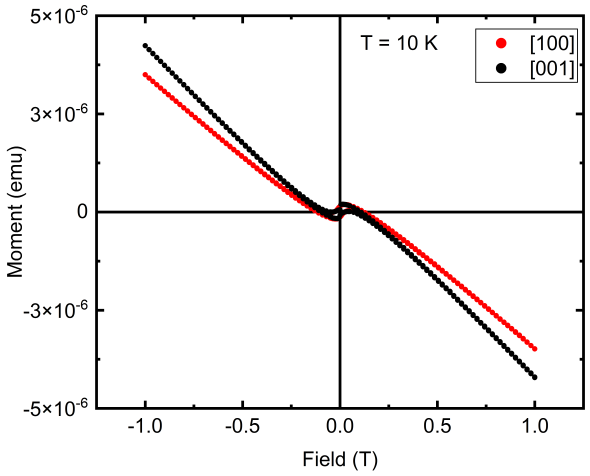

(a)

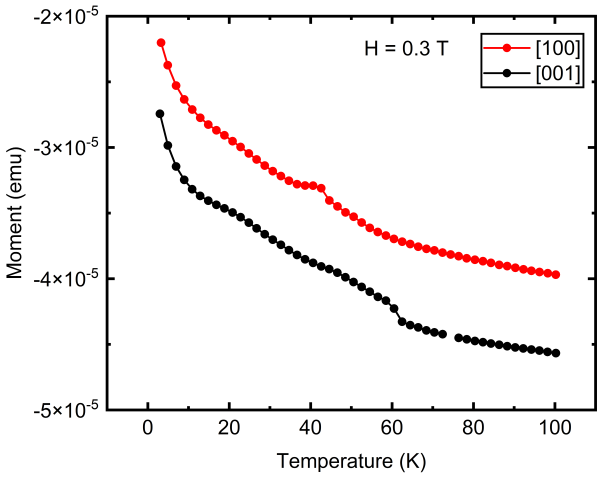

(b)

Figure 5.6: STO substrate magnetic measurements with field applied along [100] and [001] crystallographic directions of the super-lattice. (a) Hysteresis at 10 K in field of ±1 T. (b) Magnetization variation with temperature in range 3 - 100 K. The anomaly at 40 K is discussed in the next segment.

5.3.1 Temperature dependence of magnetization

The measured scans with 0.3 T field applied along [100] and [001] directions in the temperature range of 3 - 100 K are shown in Figure 5.7. For reference, measured data is shown along with the one after subtracting the substrate contribution. The moment is presented in units of emu. It is clear from these plots that there is no variation in magnetization of the super-lattice in this temperature range.

For the [001] direction, a small jump in the curve is observed in the range 40 - 50 K. This is possibly due to oxygen molecules trapped in the tape that holds the sample or improper purge airlock [148]. Solid molecular oxygen undergoes antiferromagnetic transition at 43 K, which can cause slight changes in the measured signal [149]. In

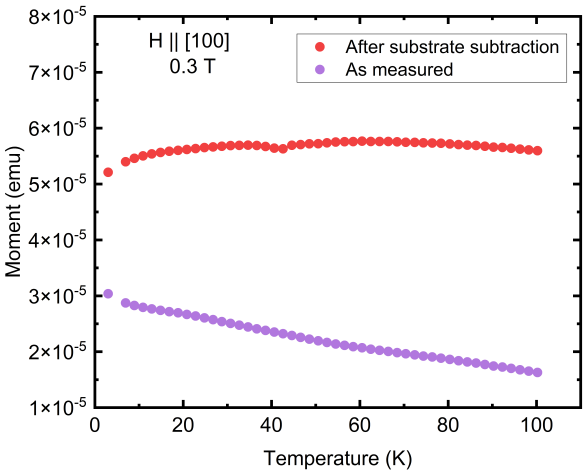

(a)

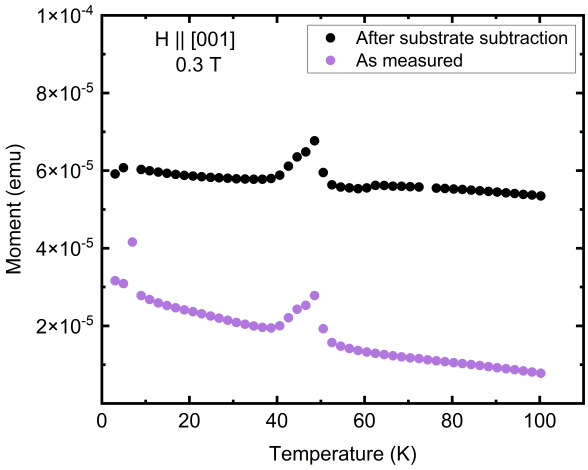

(b)

Figure 5.7: Temperature dependence of magnetization of 3-3 super-lattice in the range 3 - 100 K for 0.3 T field applied along (a) [100] and (b) [001].

the same experiment, these measurements were also performed in several fields (from 0.2 T to 0.7 T). A similar jump was observed in all the measurements indicating that it is field independent.

Thus, we conclude that in the range of 3 - 100 K, there is no change in the magnetization of 3-3 super-lattice. This was also confirmed by ND measurements discussed in the next section.

5.3.2 Magnetic hysteresis

The hysteresis scans were performed at 10 K for field applied along [100], [110] and [001] film directions. The applied field was varied in the range of +1 T to -1 T. The maximum field that can be applied with this instrument is 5 T. The hysteresis measured in 5 T showed that there is no effect as the field is increased from 1 T

to 5 T and the moments are not saturated [5]. Therefore, the detailed analysis are described with 1 T applied field. The obtained hysteresis loops are shown in Figure 5.8. In Figure 5.8(a), the hysteresis loops of [100] and [001] directions are plotted along with the substrate signal and the subtracted one, in units of emu (1 emu = 10^{-3} J/T). The negative slope seen in the measured curve is due to diamagnetic signal from the substrate. The comparison clearly shows that the effect of substrate signal is significant and the subtraction changes the loop shape completely.

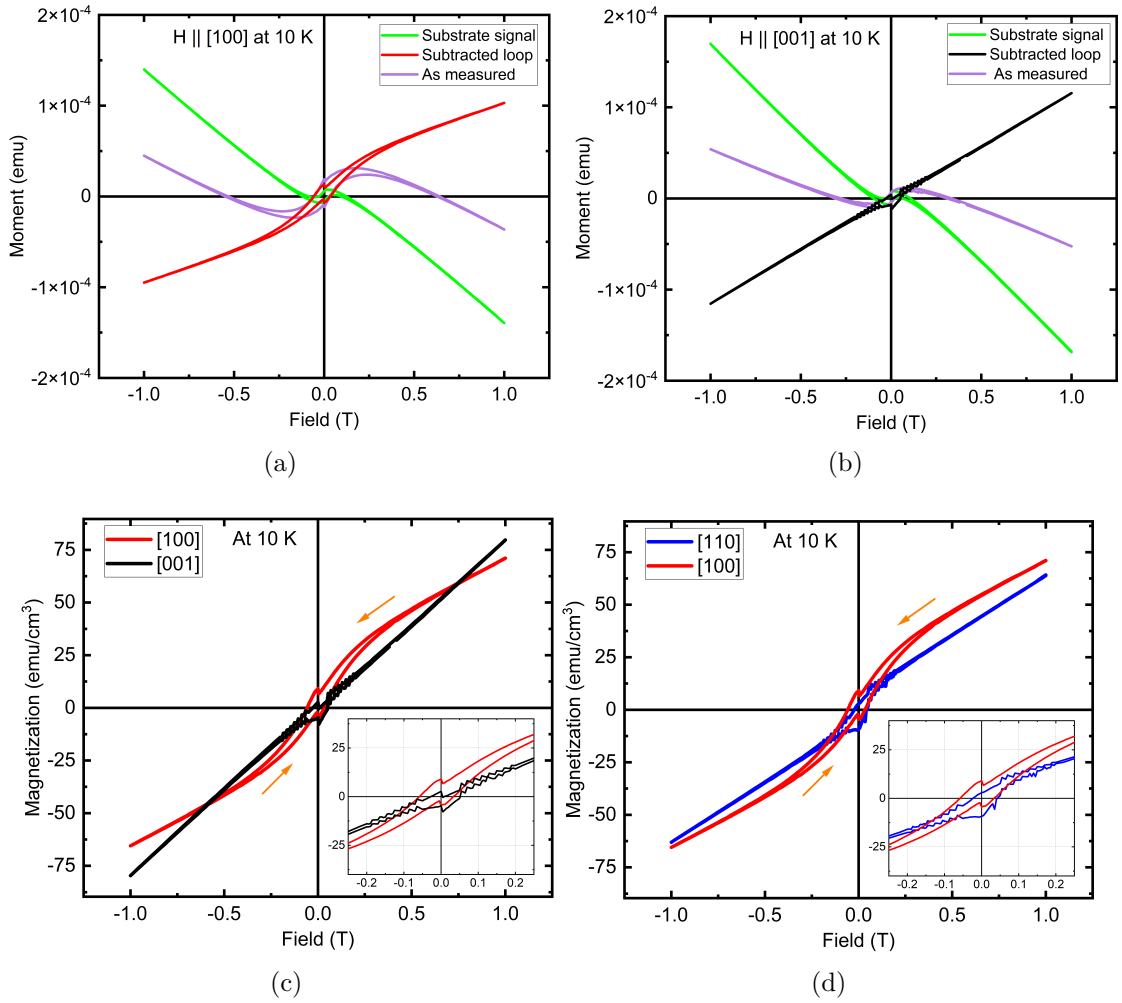

Figure 5.8: Hysteresis loops measured on the 3-3 sample for field applied along [100], [110] and [001] film directions: (a,b) Measured signal plotted along with substrate contribution and the subtracted one, against the applied field for [100] and [001] directions. (c,d) Comparison of hysteresis loops of the 3 directions in units of emu/cm^3. The comparison is separated in 2 plots: [100] with [001] and [100] with [110], for better clarity in the plot. The arrows mark the direction of measurement. The inset shows an enlarged view of the hysteresis curves.

Figure 5.8(b) compares the subtracted data of all the 3 directions; [100], [001] and

[5]The scan is shown at the end of Chapter 6, where we compare different super-lattice samples.

[110]. The magnetization signal is presented in units of emu/cm^3. Based on these plots, the following few preliminary points can be drawn regarding the magnetic properties of the material.

- The magnetization increases as the applied field is increased and the moments are not saturated in a field of up to 1 T, for all the three directions.
- The saturated signal is expected to be above 250 emu/cm^3 [6]. This means that the ferromagnetic component seen at low field is very small. It is only about 15 emu/cm^3, which is not large enough to take into consideration. (see the inset on Figure 5.8(c,d)) [7]. The values of spontaneous magnetization (magnetization in zero field) and magnetization at 1 T are summarized in Table 5.2.

Table 5.2: Magnetic hysteresis parameters of the 3-3 super-lattice measured at 10 K for 1 T applied field. $M_{spon.}$ is the spontaneous magnetization, M_{1T} is the magnetization at 1 T applied field.

Field directions	$M_{spon.}$ (emu/cm^3)	M_{1T} (emu/cm^3)
[100]	9	71
[110]	2.7	64
[001]	2.1	79

- This type of curves are usually due to AFM ordering in the system with a negligible uncompensated FM component. However, it can also be indicative of incommensurate magnetic structure and there is helical arrangement of spins in the system. From the ND measurements discussed in the next section, we did not find any evidence of incommensurate structure, therefore, henceforth, we will take only the AFM ordering in consideration for the SQUID analysis.
- Although all the 3 curves are almost linear in slope, there are slight differences in the shapes. The [100] direction has more curved shape at low field, which typically indicates a spin-flop transition. According to this transition, if field is applied along parallel to easy-axis, at some point the spins rotate perpendicular to the easy-axis modifying the slope of hysteresis curve. Then a continuous rotation of the magnetic moments occurs upon increasing the field. These two stages (before and after the transition) are depicted using a schematic in Figure 5.9. This suggests that the easy-axis of magnetization is [100].
- If we look at the [001] data in Figure 5.8(b), it presents a very straight line, typical of AFM when field is perpendicular to easy-axis. It crosses the [100]

[6] This is calculated based on the saturated signal observed for LSMO film sample in Chapter 4, assuming that both the samples' surfaces are completely covered with the deposited film.

[7] Please note that the sample used in the publication by A. sadoc et al. [28] was different and got damaged when temperature dependence was measured at 600 K, due to oxygen evaporation.

Figure 5.9: Schematic representation of the spin-flop transition observed on the 3-3 super-lattice for field applied along [100] direction. The blue arrows represent the direction of magnetic moments.

curve close to 0.7 T field. As the field is increased, the moments continuously align along [001] resulting in increase in the measure signal.

- For field along [110], the moments show interesting behavior. They tend to stay along the [100] easy-axis. This is how we verified this: we calculated the slope of [100] and [110] curves in the low field region. It was found that the [110] slope is about $\sqrt{2}$ times less than that of [100]. Now, since in SQUID we measure a projection of the moments along the field direction, it is clear that the moments were along [100] and what we measured was a projection of 45° along [110]. Further increase in field leads to continuous increase in the moment component along [110].

- The small steps seen close to the zero-field could be due to some artifact in SQUID due to low signal at zero field, as discussed in the Chapter 3.

Based on the above discussed results, the possible magnetic structure models are shown in figure 5.10. It is to be noted that the models are drawn based on an assumption that the structure is not incommensurate (more details on this in the ND section next). As mentioned, the moments prefer [100] in-plane direction, but the possibility of an out-of-plane component with antiferromagnetic coupling cannot be completely ruled out from macroscopic SQUID measurements. The different possible models are divided into three parts: moments in-plane [100], moments out-of-plane [001] and moments along diagonal (both [100] and [001] components). The models were prepared keeping in mind two facts: one is that there is no spontaneous magnetization and secondly, the hysteresis are indicative of AFM ordering in the system. Note that the unit cell used here is doubled along the *c*-axis to accommodate different possible AFM orderings (5.51 5.51 48.2). This change in unit cell is only to present the different models and the analysis are carried out in the original unit cell of dimensions (5.51 5.51 24.1).

In conclusion, we have used SQUID to obtain information on macroscopic magnetic properties of the super-lattice. We found that there is no significant change in the magnetization of the sample in the temperature range of 3 - 100 K. In the hysteresis measurements, the curves for all the 3 directions display shapes typical of AFM ordering. In addition, we observed characteristics of a spin-flop transition along [100] direction. The possible magnetic structures are drawn based on the shape of the hysteresis curves. SQUID results alone are not conclusive enough to resolve the magnetic structure. To complete the study, we planned to solve for the nuclear and magnetic structure of the sample using neutron diffraction measurements. A complete nuclear

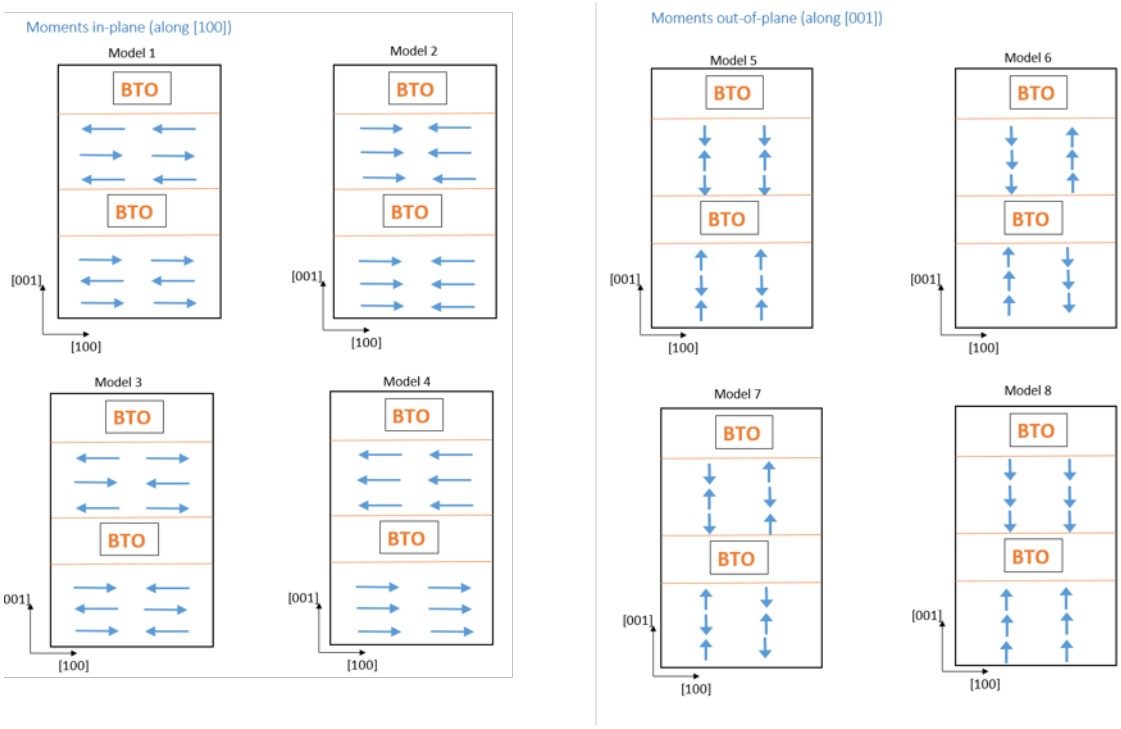

(a)

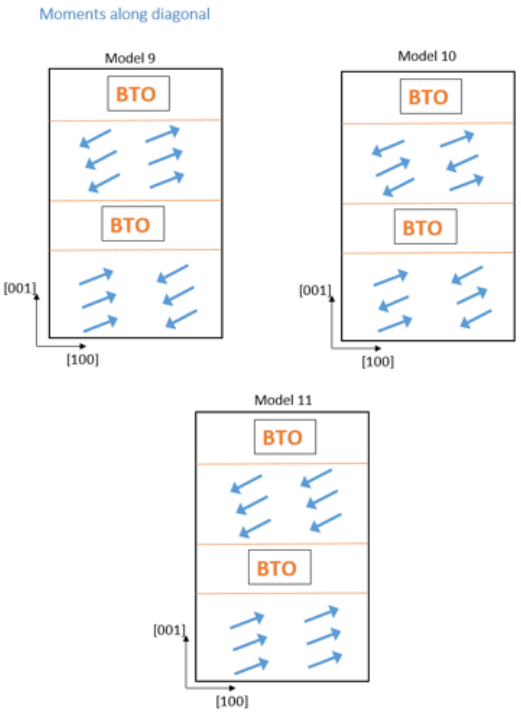

(b)

Figure 5.10: The possible magnetic structures of the 3-3 super-lattice derived from SQUID analysis divided into 3 categories: (a) Moments in-plane along [100] and moments out-of-plane along [001]. (b) Moments along diagonal out-of-plane.

structure can provide us detailed insights into the widths of different layers, which directly relates to magnetic properties via orbital occupation as discussed previously. These results are discussed in the next section.

5.4 ND

Single crystal ND experiments were performed on the 3-3 super-lattice to obtain information on its crystal and magnetic structure. In addition to the difficulties discussed earlier related to diffraction on thin film structures, this sample brings in more challenges. First of all, the magnetic transition temperature of the 3-3 super-lattice is close to 600 K. It is not possible to collect data in the paramagnetic phase because the sample gets destroyed at such high temperature. Secondly, the substrate STO undergoes a phase transition around 110 K [150], which makes it difficult to follow the diffraction pattern of the film at higher temperatures. So we can only work at low temperature (below 100 K) in the magnetically ordered phase. This makes it a complex study and significant input from DFT calculations is required. This is a good moment to note that the attempt to obtain nuclear and magnetic structures in the present study will be conducted by comparing DFT calculations and experimental results coupled with magnetic measurements.

Table 5.3: List of different ND experiments performed on 3-3 super-lattice samples.

Experiment date	Experiment acronym	Sample
September 2019	E1	A
January 2021	E2	A
March 2021	E3	A
October 2021	E4	C
(To be done)	E5	C

5.4.1 Results from different experiments

Five different ND experiments were performed on the 3-3 super-lattice samples. Table 5.3 lists all the experiments along with the samples used and experiment dates. As you'll see in the following discussions, obtaining conclusive data on such samples requires long measurement times. Therefore, each experiment was dedicated to resolve specific questions regarding the material's magnetic nature and collect valuable data to perform structural refinements.

September 2019 experiment (E1)
This experiment was performed on sample A before the start of my PhD and I was not present at this measurement. The 3-3 super-lattice sample A was held in a cryostat on the D10 diffractometer. Incident wavelength of 2.36 Å from a pyrolytic graphite monochromator was used. The energy analyzer option in 4-circle mode was used to reduce the signal coming from substrate and the film was oriented using the UB-matrix calculated from substrate peaks. In this experiment, about 15 peaks (sets of (00ℓ) and $(hk\ell)$) were measured at low temperatures (2 K to 100 K) using scans programmed in both q-scan and $\omega - 2\theta$ mode. Table 5.4 lists the complete data-set measured in this experiment. The obtained lattice parameters were found to be in

agreement with the substrate epitaxy: $a = b = 5.51$ Å ($3.9 \times\sqrt{2}$) and $c = 24.20\pm$ 0.04 Å, corresponding to a unit cell of 6 layers of LSMO and BTO combined.

Table 5.4: List of reflections measured on 3-3 super-lattice using ND (Experiment E1) at different temperatures. The rows are color coded according to the type of scan performed; orange highlighted ones were measured in $\omega - 2\theta$ mode while the rest in q-scan mode.

(h k l)	Temperature (K)
(0 0 2)	2
(0 0 3)	2
(0 0 4)	2
(0 0 5)	2
(0 0 6)	2, 10, 30, 45, 60, 75, 100
(0 0 7)	2
(0 0 8)	30, 45, 60, 75, 100
(0 0 9)	2
(0 0 10)	2
(0 0 12)	2, 10, 20, 40, 45, 75
(1 -1 12)	13
(-1 1 12)	13
(-2 0 11)	2
(-2 0 12)	2

In this data-set, one of the most intense peak is (0 0 12) and it is taken as a reference for integrated intensity determination (discussed in the refinement section later). The (0 0 6) peak is also very intense but since it is very close to the substrate peak (STO-(0 0 1)) it could not be integrated well. Few of the measured peaks are shown in Figure 5.11. No intensity was observed for several reflections such as (0 0 4), (-2 0 12), (0 0 10) etc. (not shown here).

In addition, temperature dependence of few peaks was also studied. The (0 0 12) and (0 0 6) were found to be independent of temperature (see Figure 5.11(a,b)). There is no change in the peak position and intensity with temperature in the range 2 - 100 K. The temperature variance of (0 0 8) peak suggested presence of two satellites at 60 K with no change in the central peak. It was believed that these satellites at $q = \pm$ 0.15 from the center, are an indication of incommensurate magnetic structure. This was further investigated in the experiment at the start of the PhD project (January 2021).

January 2021 experiment (E2)
The main goal of this experiment was to confirm the presence of satellites on (0 0 8) peak. The experiment was performed with the same wavelength and measurement conditions as E1. Several scans were performed at regular intervals in the temperature range of 30 - 80 K. The (0 0 12) peak and lattice parameters obtained in this

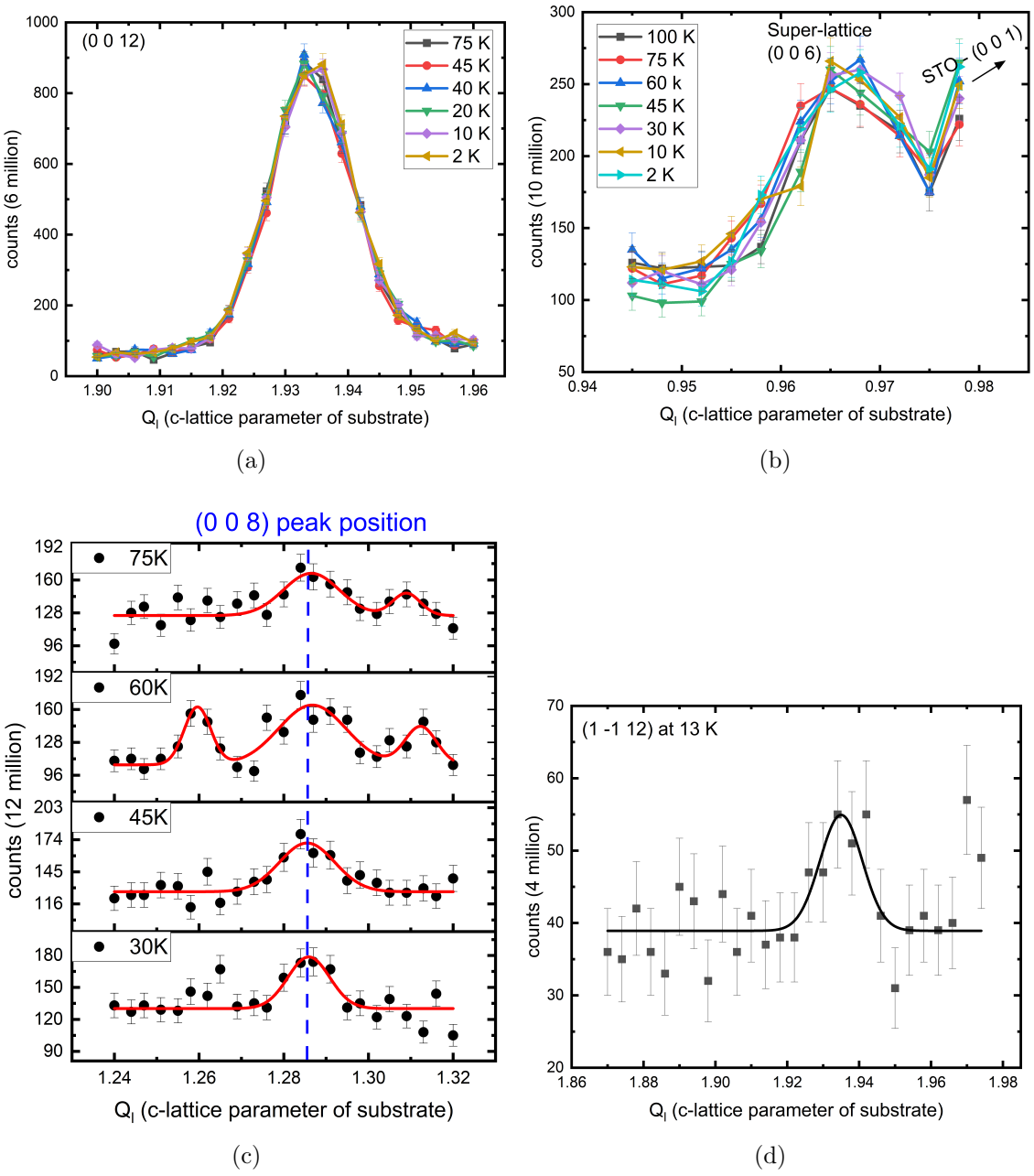

Figure 5.11: Few of the measured peaks on the 3-3 sample from September 2019 experiment, (a) (0 0 12) (b) (0 0 6) (c) (0 0 8) and (d) (1 0 12), at different temperatures counted with different monitors. The counting time is about 7 hours for 23 points with 12 million monitor.

experiment are in-agreement with the E1 experiment results. The (0 0 8) peaks were measured with 12 million monitor, which took about 12 hours for a scan of 23 points.

The measured (0 0 8) scans are shown in Figure 5.12. At 60 K, more than one scan were measured and the average intensity is plotted in Figure 5.12. As evident, no clear satellites were observed on the peak at any temperature in the range 20 - 80 K.

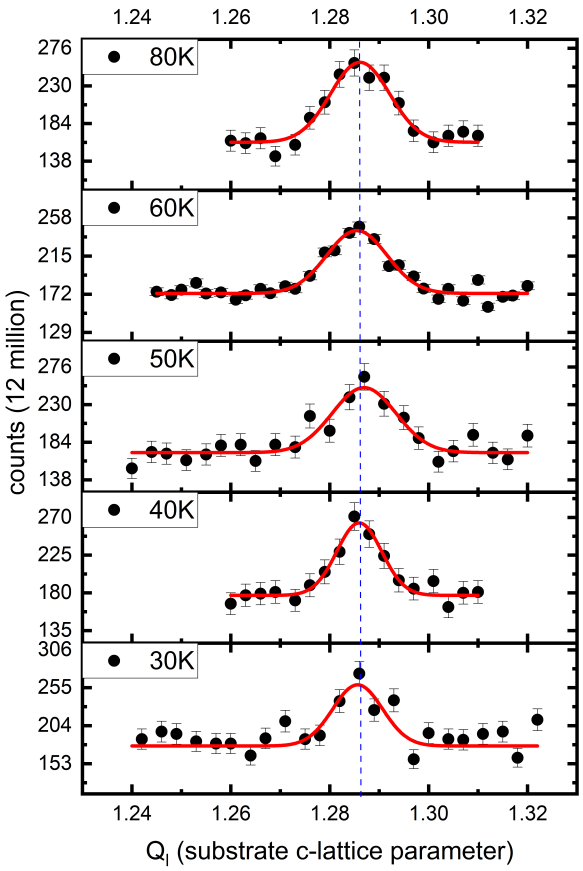

Figure 5.12: The (0 0 8) peak measured on the 3-3 sample in experiment E2 at different temperatures to investigate if there are any satellites as observed in E1 experiment.

Thus, the presence of satellites could not be confirmed. We speculate this might be due to one of the two reasons; either the statistics on peak in E1 were not good enough and the small satellites seen were experimental artifacts or the sample went under an irreversible transition due to repetitive application of high magnetic fields (up to 5 T) during SQUID measurements performed in-between the two experiments. At this stage of understanding, we believe the magnetic structure of the super-lattice is not incommensurate and will consider only commensurate possible structures henceforth.

Another point that needs to be added to this discussion is that we measured (0 0 8) peak on sample C as well (in experiment E4). Sample C was not exposed to high magnetic fields in SQUID before this experiment. No satellites were observed on this sample as well. This further strengthens the argument that the satellites observed in E1 were an experimental artifact. Next, we focused on measuring reflections to solve the nuclear and magnetic structure of the sample.

October 2021 experiment (E4)

We will discuss the results of this experiment here, breaking the chronology, as it

is relevant to the presence of (0 0 8) satellites. This experiment was performed on a new sample (C). The objectives were to investigate the presence of satellites on (0 0 8) on a new sample and collect reference data to compare with the upgraded D10+. The instrument went under upgrade during the shut down at ILL (October 2021 - February 2023) after this experiment. The peaks were measured with incident wavelength of 2.36 Å. The lattice parameters obtained are a = b = 5.51 Å ($3.9 \times \sqrt{2}$) and c = 24.25 ± 0.03 Å(calculated from (0 0 12) peak position). The (0 0 8) peak measured at 45 K and 60 K is shown in Figure 5.13.

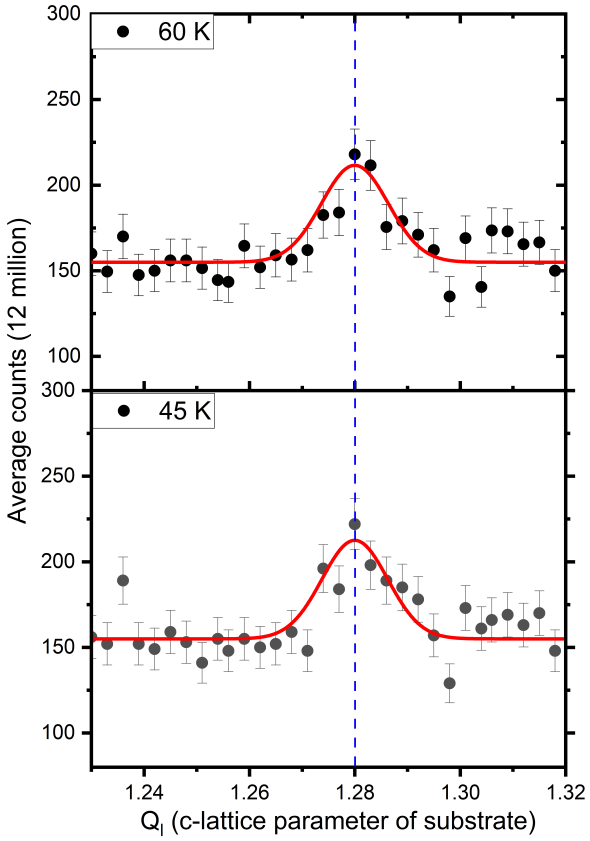

Figure 5.13: The (0 0 8) peak measured on the 3-3 sample C in experiment E4 at different temperatures to investigate if there are any satellites as observed in E1 experiment.

March 2021 experiment (E3)

The goal of this experiment was to measure reflections that can help us distinguish between different DFT optimized geometries and hence, solve the nuclear and magnetic structure. To select the reflections to be measured, we used the DFT optimized geometries. Nuclear structure factor of each set of atomic positions were calculated using the following equation:

$$F = \sum_{n=1}^{nlayers} \sum_{j=1}^{natoms} b_j \exp\Big(2\pi i(\vec{Q}.\vec{r}_j)\Big) \exp\left(\frac{-2B_j \sin^2\theta}{\lambda^2}\right) \tag{5.2}$$

where, b_j is the scattering length, B_j is the Debye-Waller factor at 30 K, $\vec{Q}$ and $\vec{r}_j$ are the reciprocal space vector and atomic position vector of atom j with respect to the origin of the lattice cell, respectively. The structure factor is calculated by summing over all the atoms in the super-lattice (*natoms* is the number of atoms in the unit cell i.e. $[LSMO]_3[BTO]_3$) and intensity is square of the structure factor. The values of scattering lengths and Debye-Waller factors for different ions are taken from literature [151–153]. This way, a whole list of reflections was generated with their corresponding intensities. For each reflection, the product of average intensity from all the geometries and standard deviation was calculated. From this list, top few reflections were selected so that different DFT geometries can be distinguished using the diffraction data.

Table 5.5: List of reflections measured on 3-3 super-lattice using ND (Experiment E3) at different temperatures in q-scan mode. The list is divided into 3 categories; $(0\ 0\ \ell), (2\ 0\ \ell),$ and$(2\ 2\ \ell)$.

(0 0 *l*)	(2 0 *l*)	(2 2 *l*)
(0 0 11)	(2 0 5)	(2 2 11)
(0 0 12)	(2 0 6)	(2 2 12)
(0 0 13)	(2 0 7)	(2 2 13)
(0 0 23)	(2 0 17)	
(0 0 24)	(2 0 18)	
	(2 0 19)	
	(2 0 20)	

An incident wavelength of 1.53 Å from Cu monochromator was used in this experiment to access larger reciprocal space as compared to 2.6 Å. In total, 15 reflections were measured on sample A at 30 K using q-scan mode. Table 5.5 lists all the measured reflections.

With this, the description of experiments conducted on this structure concludes. We will now shift our focus to the structural refinement carried using data-sets presented in Tables 5.4 and 5.5. To commence, let us review the procedure of peak integration.

5.4.2 Structural refinement

The integrated intensities were obtained by fitting all the reflections with Gaussian function using OriginLab software. Recalling the Equation 4.9 for Gaussian function:

$$y = y_0 + \frac{A}{w_d\sqrt{\pi/4\ln(2)}}\exp\left(\frac{-4\ln(2)(x-x_c)^2}{w_d^2}\right) \tag{5.3}$$

By fitting the measured peak with this equation, one obtains A(area), w_d (FWHM), and y_0 (background) fit parameters. Usually, peak area A is used as integrated intensity for structural refinement, whereas in this case, we have used the peak maximum (y_c). This is because we are using data-sets from 2 different experiments together for the refinement, in which scans were carried out with different wavelengths. Furthermore, within each experiment different scan modes were used. The scans programmed as q-scans using substrate UB-matrix, measure a different path in the reciprocal space than the ω-scans programmed directly with the film UB-matrix. This results in different peak shapes and widths. Therefore, to facilitate an accurate comparison of different reflections in each data-set, we decided to use the peak maxima value y_c for the refinement. Using the acquired fit parameters, y_c was calculated using the following equation:

$$y_c = \frac{A}{w_d \times 1.064} - y_0 \tag{5.4}$$

Henceforth, we will refer to y_c as integrated intensity for analysis in this chapter. Each scan was normalized with respect to monitor before performing the fitting. The obtained intensities were corrected for Lorentz factor. This way, 2 different data-sets (wavelength - 1.53 Å and wavelength - 2.36 Å) of integrated intensities were prepared.

The first step in the refinement process was to compare these sets of experimental intensities with those of DFT optimized geometries. This is detailed in the upcoming segment.

5.4.2.1 Results of DFT calculations

As explained before, the DFT calculations were used to perform geometry optimizations for the 3-3 crystal structure. A set of 27 geometries was obtained corresponding to different possible scenarios of La/Sr disorder and intralayer magnetic coupling in the system. All the geometries were obtained in either P$\bar{4}mm$ or P$\bar{4}$ space group. In simple terms, our aim was to obtain the atomic positions in different layers by fitting these geometries with ND data.

To do so, we calculated theoretical nuclear neutron diffraction intensities for all the DFT geometries using the procedure explained before in the experiment preparation (E3). These intensities along with the 2 experimental data-sets, were normalized with the (0 0 12) peak as it is one of the strongest peaks in the diffraction pattern. The intensities were then compared by further dividing the reflections into categories of $(0\ 0\ \ell), (2\ 0\ \ell), \text{and} (2\ 2\ \ell)$. Figure 5.14 shows the comparison with few of the DFT geometries and the rest were found further away from the experimental data.

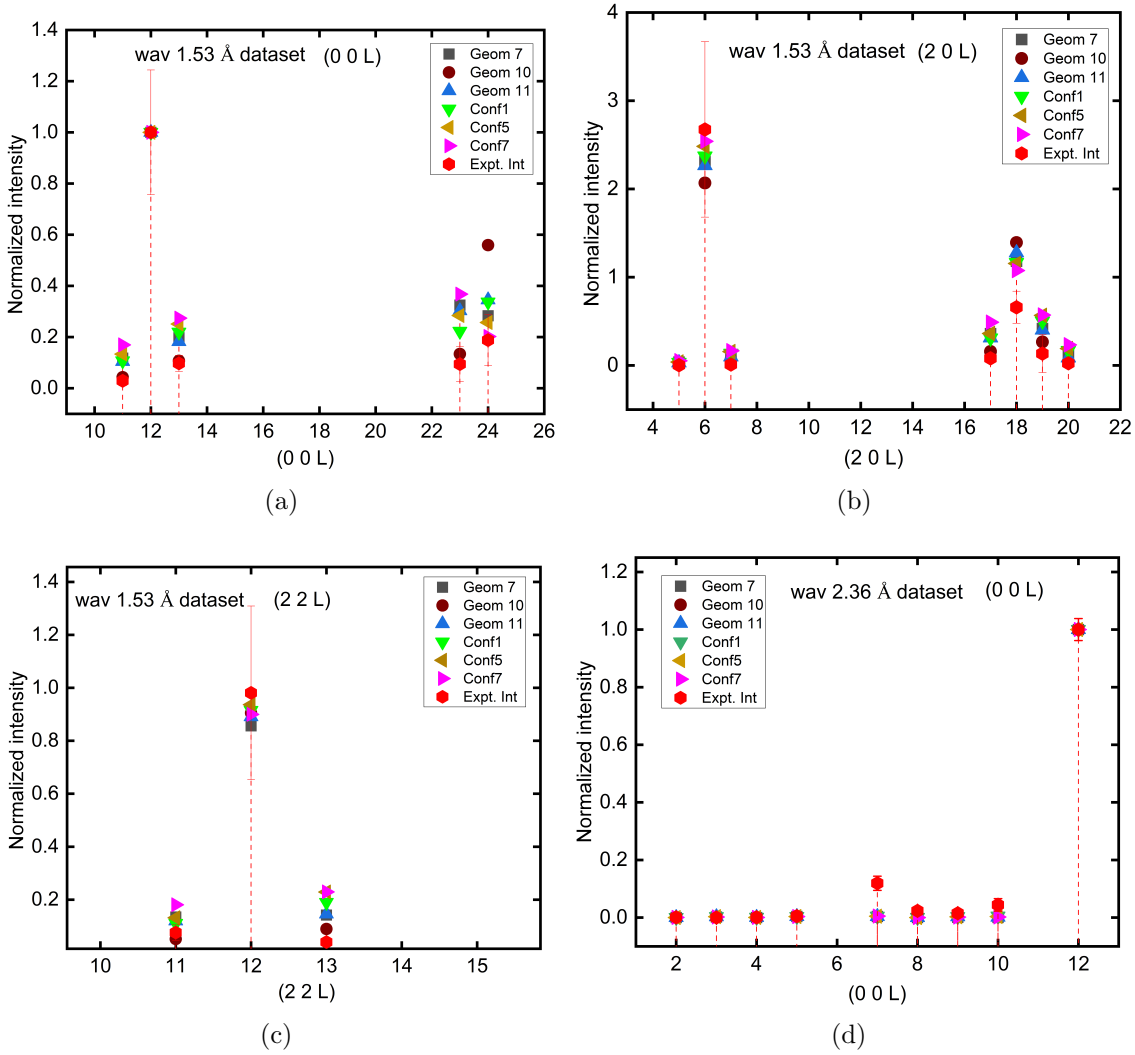

Figure 5.14: Plots showing comparison of experimental ND intensities with theoretical nuclear ND ones calculated for different DFT optimized geometries. The reflections are presented in categories of (0 0 ℓ), (2 0 ℓ), and(2 2 ℓ), separately for the 2 data-sets of wavelength - 1.53 Å and wavelength - 2.36 Å.

Figure 5.14(a-c) shows the plots comparing 1.53 Å data-set and the last subfigure (d) presents the (0 0 ℓ) reflections of the 2.36 Å data-set. For 2.36 Å, only (0 0 ℓ) reflections are presented as the remaining data-set consists of only 2 more peaks, that were used for analysis but not shown here explicitly.

From these plots, one can notice that none of the geometries display a perfect fit with the experimental data. However, there are at-least a couple that follow the same pattern as the experimental peaks. One such geometry is *Conf1*, which is consistently close to the experimental intensities across all the plots. In this geometry, the Sr atoms are located on the top layer out of the 3 LSMO layers. This is a good moment to note that the acronyms used for DFT geometries relate to their configuration. The geometries starting with *Geom* were those with FM intralayer coupling between Mn

ions and those with *Conf* name were AFM.

So we have found a closest match to experimental data from the DFT calculations, which is Conf1. The intensities from this structure are close to experimental values for most of the measured reflections, but there are a few peaks that don't fit at all. The (0 0 7) and (0 0 8) peaks show non-zero experimental intensity, however, there is no theoretical nuclear ND intensity on these reflections for Conf1. This is in fact true for all the DFT geometries.

One possibility is that these peaks are purely magnetic in nature. Since the peaks were measured at 30 K in the magnetically ordered phase, the recorded intensity could be due to magnetic ND. To verify this, we fitted different possible magnetic structures with Conf1 using FP, refining only the scale factor. These structures included all the intralayer AFM models from the 11 magnetic models prepared using SQUID results (see Figure 5.10). We found that none of the models showed any intensities on (0 0 7) and (0 0 8) peaks. Furthermore, we repeated the process with one of the FM geometries, *Geom*10 which also shows a decent fit with experimental data and obtained the same results.

Now, since no magnetic intensity was observed on these 2 reflections, we conclude that the experimentally observed intensity comes from nuclear ND. Since these reflections only depend on the z-positions of atoms, one needs to optimize the z-positions to obtain correct fit. Therefore, the next step in the refinement process was to optimize the z-positions of atoms. The idea was to try and alter the z-positions of atoms in Conf1 to see if this gives some non-zero intensity on these reflections as observed experimentally.

5.4.2.2 Optimizing the z-positions of atoms in Conf1

This optimization is not straightforward due to large number of independent parameters to refine. There are 36 independent atoms in the Conf1 unit cell (P*4* space group) and refining the z-position of each atom in FP with such small data-set is not possible. Therefore, we prepared Python scripts to strategically move different layers/atoms and use FP in the script to calculate the Rf-factors corresponding to each configuration. Even with this set-up, there were a number of possibilities to execute.

The plan implemented was as follows: The atoms were shifted along z-direction in small steps using *for* loops in Python and Rf-factors were obtained at each step. In parallel, the intensities of (0 0 7) and (0 0 8) peaks, which are the basis of these calculations, were also observed. A combination of relatively lower Rf-factors and non-zero intensity on (0 0 7) and (0 0 8) was the criteria to pick "good" geometries. In addition, it also had to be made sure that while moving different atoms, the bond lengths were not reduced too short, which can lead to a physically improbable structure. To avoid such scenario, a constraint was put on the minimum bond length. If in some configuration, any bond length were smaller than the decided value, that particular configuration was rejected and not taken into account for the fitting. As an example, the minimum Mn-O bond length was chosen to be 1.9 Å, which is expected for such systems. The fitted configurations were obtained as follows.

Fitted structures

As one can expect, there were a number of possible solutions presenting a reasonable fit, instead of one single geometry. These geometries were obtained by moving different atoms at different steps of the process, as we want to cover a broad spectrum of possible solutions in order to avoid a false minimum of energy in DFT calculations. One can imagine it as a tree branch, where the end-point of each sub-branch is a possible solution but they lie at different parts of the "energy" tree. Starting from the limb, the branch spreads into different directions, creating further sub-branches and so on. Each joint where a sub-branch is created, represents the choice of atoms that's shifted during the process. Therefore, by changing the sequence in which atoms were shifted, one can pick possible solutions from different "sub-branches". Let us review the results obtained from this optimization process.

For starting, we shifted the Mn and La/Sr atoms along z-direction by a distance of $\pm$ 0.48 Å in steps of 0.12 Å. This constituted a series of more than 8000 combinations (6 loops of 4 steps in each loop) and Rf-factors corresponding to each combination were calculated. From this, 20 smallest values of Rf-factors were picked. On this set of combinations, we found that there is increase in calculated intensities of (0 0 8) peak, while (0 0 7) was still negligible. In fact, this was true for the complete series of combinations. This means that the intensity observed on (0 0 7) and (0 0 8) experimentally is not due to shift in Mn and La/Sr atoms as compared to Conf1.

Moving Oxygen atoms

Since we did not observe any increase in intensity by moving Mn atoms first, we decided to start the optimization using oxygen atoms this time. We started the optimization by shifting oxygen atoms in the LSMO layer by 0.48 Å in steps of 0.12 Å. To do so, oxygen atoms were shifted layer-wise, meaning all the independent oxygen in one layer were moved by the same amount in each step. This resulted in a total of 6 different nested *for* loops, launched together to test different configurations. The results of this test are shown in Figure 5.15(a), presenting the Rf-factors corresponding to the 2 data-sets (2.36 Å and 1.53 Å). One can easily notice the oscillatory pattern in the values of Rf-factors, which represents the 6 *for* loops. This means that each *for* loop has similar effect on the diffraction pattern, which also makes sense because the relative distance between different oxygen atoms is the same in each loop. There was some increase observed in the (0 0 7) and (0 0 8) intensities. So we made a plan to zoom-in on this plot by restricting the *for* loops i.e. fixing some oxygen layers at one position while moving others.

This strategy was followed until we reached the pattern shown in Figure 5.15(b). The highlighted region represents the experimentally obtained intensity of (0 0 7) and (0 0 8) peaks including error bars. As can be seen, the (0 0 7) is close to the experimental range and (0 0 8) is still lower. Nevertheless, we obtained a better fit with the overall experimental data for these geometries. So, we picked one geometry (named oxy-6) from these and continued the procedure by moving Ba-Ti on this configuration.

Moving Ba and Ti

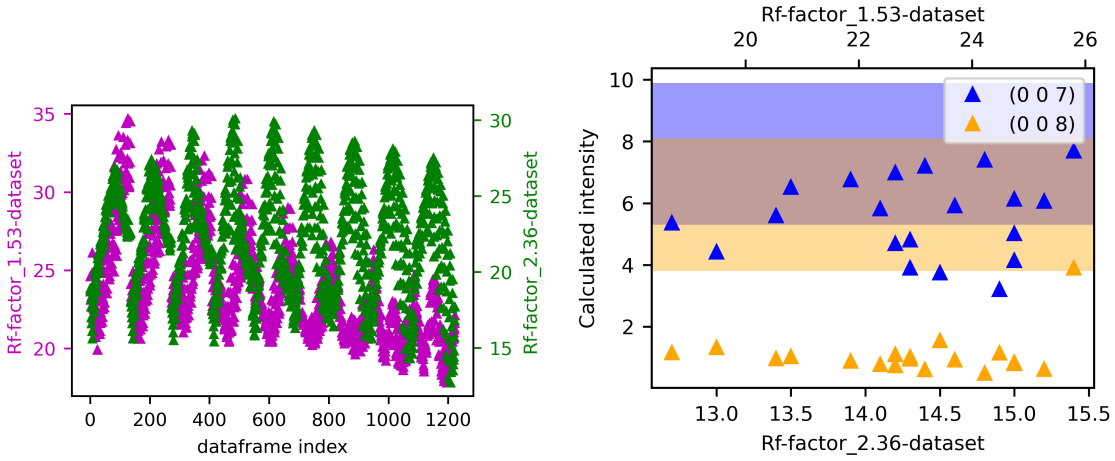

(a) (b)

Figure 5.15: Fitting DFT geometries of the 3-3 super-lattice with the experimental ND data. (a) Results of shifting the oxygen atoms along z–direction. The obtained Rf-factors corresponding to each configuraion are plotted. (b) The calculated intensities of (0 0 7) and (0 0 8) reflections for few of the lowest Rf-factors obtained. The highlighted region represents the experimentally obtained intensity of these peaks within error bars.

With Ba-Ti atoms, we found that there was an increase in the calculated intensities of both (0 0 7) and (0 0 8) but leading to slightly higher Rf-factors. The results are shown in Figure 5.16. Since there was no criteria to pick one "good" geometry over another, we picked one by random (named oxy-BaTi-41). In order to improve the overall Rf-factor,we then re-optimized the Mn and La/Sr atoms on this new geometry.

Moving Mn and La/Sr

Just as the ones discussed above, this process also consisted of 6 *for* loops; 3 for Mn layers and 3 for La/Sr. We found that this leads to improvement in the overall Rf-factors of both the data-sets while maintaining good fit for the (0 0 7) and (0 0 8) reflections. From the obtained results of this step, we picked the geometry corresponding to the best possible fit (named BaTi41-LaMn6592).

These obtained structures are shown in Figure 5.17, comparing them with the Conf1 structure. To compare them efficiently, we have used interlayer thickness as a parameter of comparison. As one can see, the interlayer thickness in fitted geometries is different from Conf1. The middle layer of LSMO was found to be contracted in the final experimentally fitted structure (BaTi41-LaMn6592). The BTO layers are slightly less thick and the interfacial Mn-Ti layers are elongated. The Rf-factors corresponding to these different configurations are listed in Table 5.6.

So, although these 2 configurations present intensity on (0 0 7) and (0 0 8) reflections, they are not exactly in-agreement with DFT results. To further study this difference, we performed DFT calculations to find the minimum energy corresponding

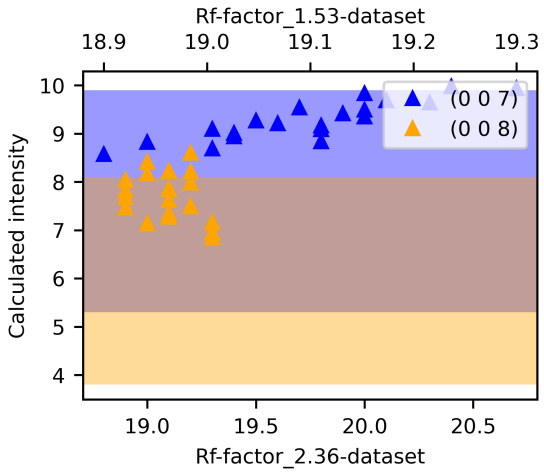

Figure 5.16: Fitting Oxy-6 configuration of the 3-3 super-lattice with the experimental ND data by shifting the Ba and Ti atoms along z–direction. The calculated intensities of (0 0 7) and (0 0 8) reflections for few of the lowest Rf-factors obtained. The highlighted region represents the experimentally obtained intensity of these peaks within error bars.

Table 5.6: The Rf-factors of fitted different 3-3 nuclear structures obtained by refining only the scale factors.

Geometry name	Rf-factor (wav 1.53 Å)	Rf-factor (wav 2.36 Å)
Conf1	33	31
oxy-BaTi-41	18.3	15.6
BaTi41-LaMn6592	16.7	9.6

to these structures. We found that they are not favorable by energy minimization calculations. Their energy is significantly higher than Conf1 (and other DFT geometries as well). Therefore, we arrive at a conclusion that the fitted configurations that we picked are not physically favorable as per DFT. It is possible that the DFT calculations on the fitted structures correspond to a pseudo minimum in energy and the global minimum could not be reached during the calculations. This can be a result of picking a geometry that's close to a pseudo minimum and hence, DFT calculations stayed in that range of energy. To verify this, we repeated the fitting process several times picking different geometries at each step. From these results, we established that the DFT calculations are, in fact, showing global minimum in energy and not a local one. We arrive at a conclusion that there is discrepancy between experimentally obtained structure and the one expected via DFT optimization.

To summarize, we performed several ND experiments on 2 samples of 3-3 type composition. Initial experiment on one sample suggested presence of satellites on

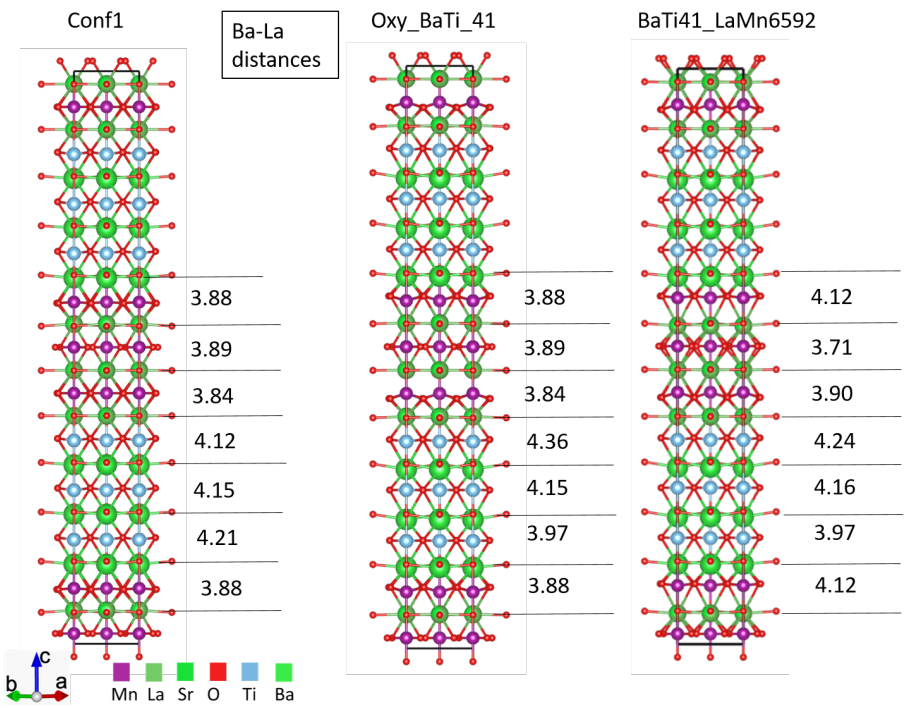

Figure 5.17: Nuclear structure configurations of the 3-3 super-lattice presented with doubling along the *c*-axis. The 3 structures presented are Conf1, oxy-BaTi-41 and BaTi41-LaMn6592. The widths of different layers are written in units of Å. Please note that La and Sr atoms are presented together on each corresponding site with their respective doping amounts. From DFT, Conf1 contains Sr on the top layer.

(0 0 8) peak at 60 K. This hypothesis was ruled out in a separate experiment on the same sample, where no satellites were observed. This was further corroborated using a different sample measured on the D10+ instrument. To resolve the nuclear structure of the film, several different reflections were measured at 30 K. We observed several nice peaks and established no temperature dependence of intensity in the range 30 - 100 K. We measured a set of reflections that were picked specifically to distinguish between different DFT geometries. All the recorded reflections were carefully integrated and used for structural refinement.

Due to large number of parameters, it was not possible to follow the usual refinement process. It was rather done by comparing the experimental data with DFT optimized geometries. The 3-3 nuclear structure(s) obtained using experimental ND data was found to be not reasonable for DFT. By meticulously analyzing the experimental data, we obtained several different geometries that showed good fit. However, the DFT calculations on energies of these systems showed them to be not feasible for ground state of this structure. Therefore, the analysis are not conclusive of the exact nuclear structure of this super-lattice.

There are some potential sources that might have contributed to the disparity between ND and DFT. To start with, it can be possible that right ingredients were not taken for the DFT optimizations. As explained before, the La/Sr disorder was

taken into consideration for DFT, however, it is only an estimate and may not reflect the true nature of the real structure. There is possibility of defects such as stacking faults that can alter the structure factor. This type of effect cannot be implemented in DFT process. In addition, there can be some finite thickness effects that could not be taken into account properly for theoretical intensity calculations. Therefore, we conclude that, although these analysis provided significant details about the sample behavior, the nuclear structure of the material cannot be concluded.

Obtaining magnetic structure was also part of the main objectives on this sample and this can be done without the conclusive nuclear structure. The results demonstrated previously have shown that the z-positions of Mn atoms have negligible effect on the intensities of (0 0 7) and (0 0 8) peaks. Since its only the Mn atoms that contribute to the magnetic ND intensity, we can work with the current Mn positions in Conf1. The next segment describes the analysis performed and proposes a plan to resolve the magnetic structure.

5.4.2.3 The plan to resolve magnetic structure

Given that there is a set of possible magnetic structures derived from SQUID and ND measurements, the idea is to measure specific reflections that can differentiate between different magnetic models. To identify such reflections, a few extra reflections were added in the data file manually, which were not experimentally measured. Then, a simple FP run for different magnetic models, keeping the scale factor fixed, gave us the expected intensity of these reflections. Figure 5.18 shows the magnetic intensities calculated for all the models. These reflections included only those, which have no nuclear contribution as they were non-integer $(hk\ell)$ indices.

From the figure, it can be clearly seen that there is no magnetic scattering contribution to the intensity of measured reflections (on the left of orange line). On the other hand, the extra added reflections (on the right of orange line), have significant magnetic intensity. This means that we can use these extra reflections as a mean to solve the magnetic structure of the system. This is a prospective work on sample C for a new ND experiment, which can be performed on D10+ in future.

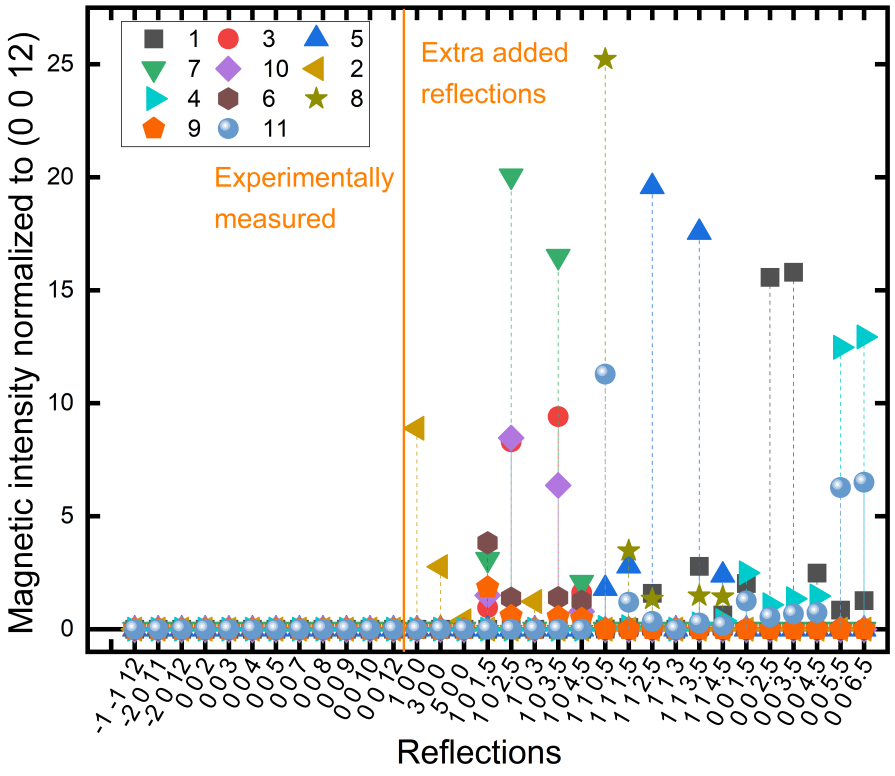

Figure 5.18: Comparison of calculated magnetic intensities of different reflections for the derived magnetic models using FullProf. The models are labeled with numbers from 1 to 11.

5.5 Conclusion

In conclusion, we investigated the crystal structure and magnetic properties of the 3-3 super-lattice ($(LSMO)_3/(BTO)_3$) sample using XRD, SQUID and ND techniques and obtained the following results.

With XRD, we measured a (0 0 ℓ) scan first on sample B, which is different from the samples used for SQUID and ND. From this scan, it was confirmed that the deposition of layers is of very good quality and the growth of the super-lattice is along the surface normal direction, as expected. The c-lattice parameter of the super-lattice unit cell was calculated to be 24.10 Å from the positions of peaks on the (0 0 ℓ) scan. Further scans along this direction revealed the Kiessig fringes pattern on (0 0 6) and (0 0 12) peaks. From the positions of fringes, the whole super-lattice thickness was obtained as 59.7 mm. This is in agreement with the number of unit cells deposited. Several other reflections were measured using 2D scans in OOP mode. The positions and intensities of equivalent reflections were found to be different on these scans. We concluded that the overall quality of the sample B is not very good due to presence of crystallites, making the XRD measurements very challenging. Thus, the data obtained is not suitable for nuclear structure refinement.

It is to be noted that the 3-3 sample used by A. Sadoc et al. was not available

for this study. This is because when the temperature dependence is measured up to 600 K, the sample gets destroyed due to oxygen evaporation. Therefore, all the samples used in this study are not tested in terms of magnetic signal at 600 K. The temperature dependence of these samples was recorded in the range 10 - 100 K and no change in the magnetization was recorded. This is different from what was observed by A. Sadoc et al. It was reported that there is a different magnetic phase below 25 K. In our samples, we did not observe this phase. We suspect that this is related to slightly different sample qualities due to stacking faults in the deposited layers. This type of defects can lead to discrepancies in the macroscopic magnetic properties of materials [154–156].

Macroscopic magnetic properties were investigate using SQUID measurements on sample A. The magnetic hysteresis measured along [100], [110] and [001] directions were found to be compatible with AFM ordering in the system with no residual magnetization. Although we cannot rule out the possibility of incommensurate magnetic structure, we focused on AFM ordering as we did not observe any incommensurate satellites peaks in the ND data. For the [100] direction, the hysteresis curve indicated a spin-flop transition at low field, making it the easy axis of magnetization. Furthermore, the [110] curve has a slope $\sqrt{2}$ times less than [100], confirming that the moments are along [100] at low field along [110]. For [001], we recorded a linear straight line suggestive of continuous moment alignment along the applied field. Finally, a set of possible magnetic structures was derived from these results, that can facilitate the planned ND experiments.

ND experiments were conducted on 2 different samples (A and C). Initially, (0 0 8) peak was argued to show satellites, which were not observed in another experiment on the sample A. Repeated measurements on the other sample also confirmed the absence of these satellites. Several reflections were measured at 30 K to solve the nuclear structure. This data was analyzed by comparative analysis performed using DFT optimized geometries. With thorough exploration, we established that the experimental ND data exhibits variations from the DFT predicted structures. We believe the source of this discrepancy is La/Sr disorder in the system. The DFT optimizations were indeed performed by taking disorder scenarios into consideration, however, it is not possible to implement other phenomenon such as stacking faults that can lead to modification in the nuclear ND structure factors. In the end, we propose a plan to resolve the magnetic ordering in the system without the need of detailed nuclear structure. It is to be noted that in Chapter 6, we present a comprehensive comparison of the properties of different samples analyzed in this project.

Chapter 6

3-2 and 2-3 super-lattices

Contents

What to expect in this chapter

In this chapter, the work done on 2 more samples is described. These samples were selected in order to study the effect of changing the numbers of layers on the LSMO/BTO super-lattices. In Chapter 5 we discussed the properties of (LSMO)$_3$/(BTO)$_3$ super-lattice. Now, we will review the changes in properties if 2 layers of LSMO or BTO are used instead of 3. The 2 samples studied are; [(LSMO)$_3$(BTO)$_2$]$_{29}$ (3-2) and [(LSMO)$_2$(BTO)$_3$]$_{29}$ (2-3). The surface dimensions of both the samples are 5×5 mm^2 with thickness of about 58 nm. At first, we will separately discuss the work done on these 2 samples and then, sum up the analysis by comparing the magnetic properties of all the samples at the end of the chapter. Let us commence with the results achieved on the 3-2 sample.

6.1 $[(LSMO)_3(BTO)_2]$ (3-2) super-lattice

The elementary bilayer unit in 3-2 sample comprises of 3 layers of LSMO and 2 of BTO repeated 29 times along the surface normal direction. We start with the X-ray diffraction studies performed on this sample.

6.1.1 XRD results

X-ray diffraction experiment was performed on the 3-2 sample using SmartLab Rigaku diffractometer at CEA, Grenoble. Through these measurements, we wanted to explore the 3-2 crystal structure and obtain information on the nature of layer stacking as compared to the 3-3 sample. Incident wavelength of 1.54 Å was used and the measurements strategy followed was the same as discussed in Chapter 4.

To investigate the stacking and epitaxy of layers along the surface normal direction, a (0 0 ℓ) scan was performed, which is shown in Figure 6.1.

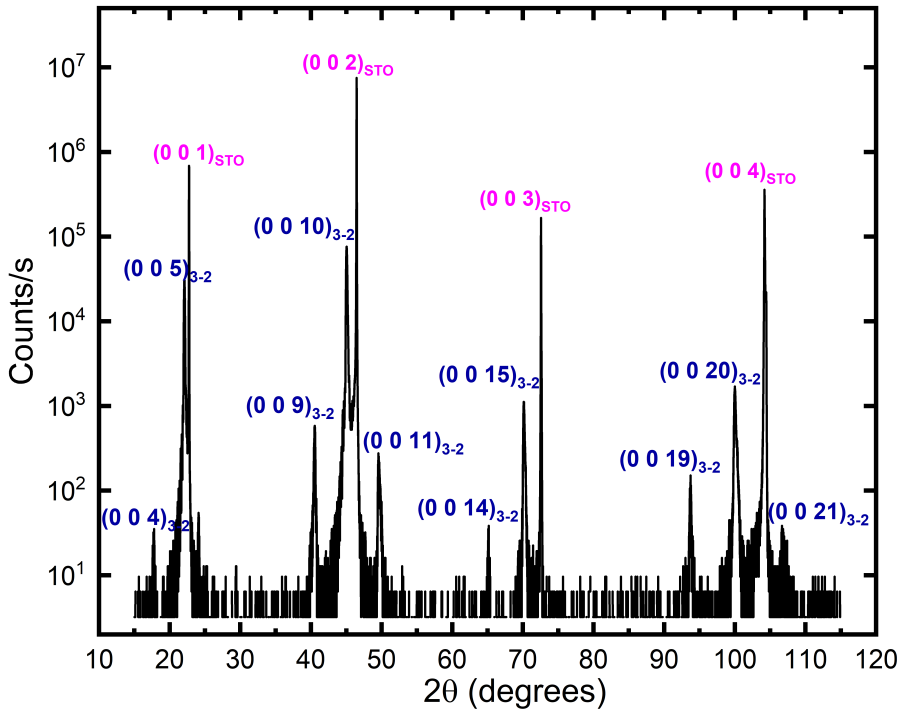

Figure 6.1: (0 0 ℓ) scan performed on $(LSMO)_3(BTO)_2$ sample using XRD with peaks from the 3-2 super-lattice (blue) and the substrate STO (purple) clearly marked. The counts/s are presented on $\log_{10}$ scale.

Here's some information that we can decipher from this plot. First of all, the c lattice parameter was calculated to be 20.10 ± 0.01 Å using the positions of peaks in 2θ as labeled in Figure 6.1. Since the unit cell is repeated 29 times along the surface normal (taken as the c-axis), the total thickness of the super-lattice can be obtained as: 20.10 Å × 29 = 582.90 Å or ≈ 58.3 nm. This is in agreement to what was expected

from the deposition. Secondly, based on the discussion in Chapter 2 about diffraction on super-lattices, we expect this sample to produce peaks at (0 0 5n), n being an integer. This is due to repetition of total 5 layers (3 of LSMO and 2 of BTO) in the structure. This is indeed what we see in the scan. The presence of (0 0 5), (0 0 10), (0 0 15) and so on peaks, reveals that the 5 layers of LSMO and BTO combined, are well-stacked and repeated periodically in the structure.

Furthermore, we also see peaks with ℓ indices other than multiples of 5, such as (0 0 4), (0 0 9), (0 0 11) etc. coming from the super-lattice. This is an indication that there is some modulation in the widths of different layers in the unit cell, but the difference is not very large as there is absence of other satellites such as (0 0 6), (0 0 8). However, structural refinements need to be performed to verify this. The STO peaks were found on the expected positions as calculated for cubic STO structure with lattice parameter $\approx$ 3.90 Å. The (0 0 5)$_{3-2}$ peak is very close to the substrate (0 0 1)$_{STO}$ peak as seen in the Figure 6.1 and separation between the (0 0 5n)$_{3-2}$ and (00n)$_{STO}$, increases with 2θ as a result of increase in scattering vector ($\vec{Q}$) magnitude, as expected.

In the quest to further resolve the nuclear structure, we performed 2D scans using the OOP mode ($\omega - 2\theta$ rotation). We first measured (1 1 5) and its equivalent reflections. Their positions in 2θ were calculated using in-plane lattice parameters assuming that the layers are under in-plane constraint from STO. To stay consistent with the LSMO film and 3-3 sample analysis, we have used the in-plane doubled unit cell as compared to STO, for this sample as well. The two unit cells are shown in Figure 6.2 using a schematic. This means that the in-plane lattice parameters are 3.90 $\times\sqrt{2}$ = 5.52 Å. These scans are shown in Figure 6.3. Let us review the results obtained form these plots.

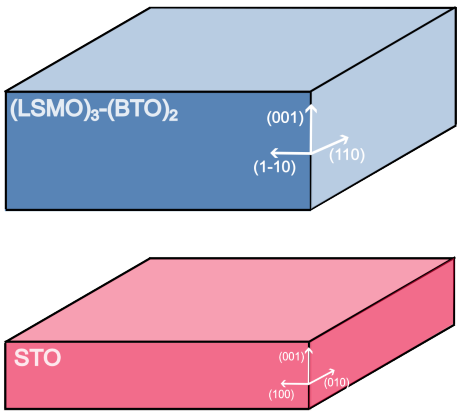

Figure 6.2: Schematic illustrating the relation between unit cells of STO and the 3-2 super-lattice. The 3-2 unit cell is double IP by a 45° rotation.

Figure 6.3(a) is the 2D scan of (1 1 5) peak, showing the more intense STO (1 0 1) peak on the right side. On this data-set, we selected 1D data-points by making a "cut" as represented by the dotted line on the 2D scan plot. In Figure 6.3(b), this 1D cut data is plotted and you can see the two peaks very clearly (intensity is plotted on log$_{10}$ scale). In addition to the main peaks, one can also notice some weaker extra

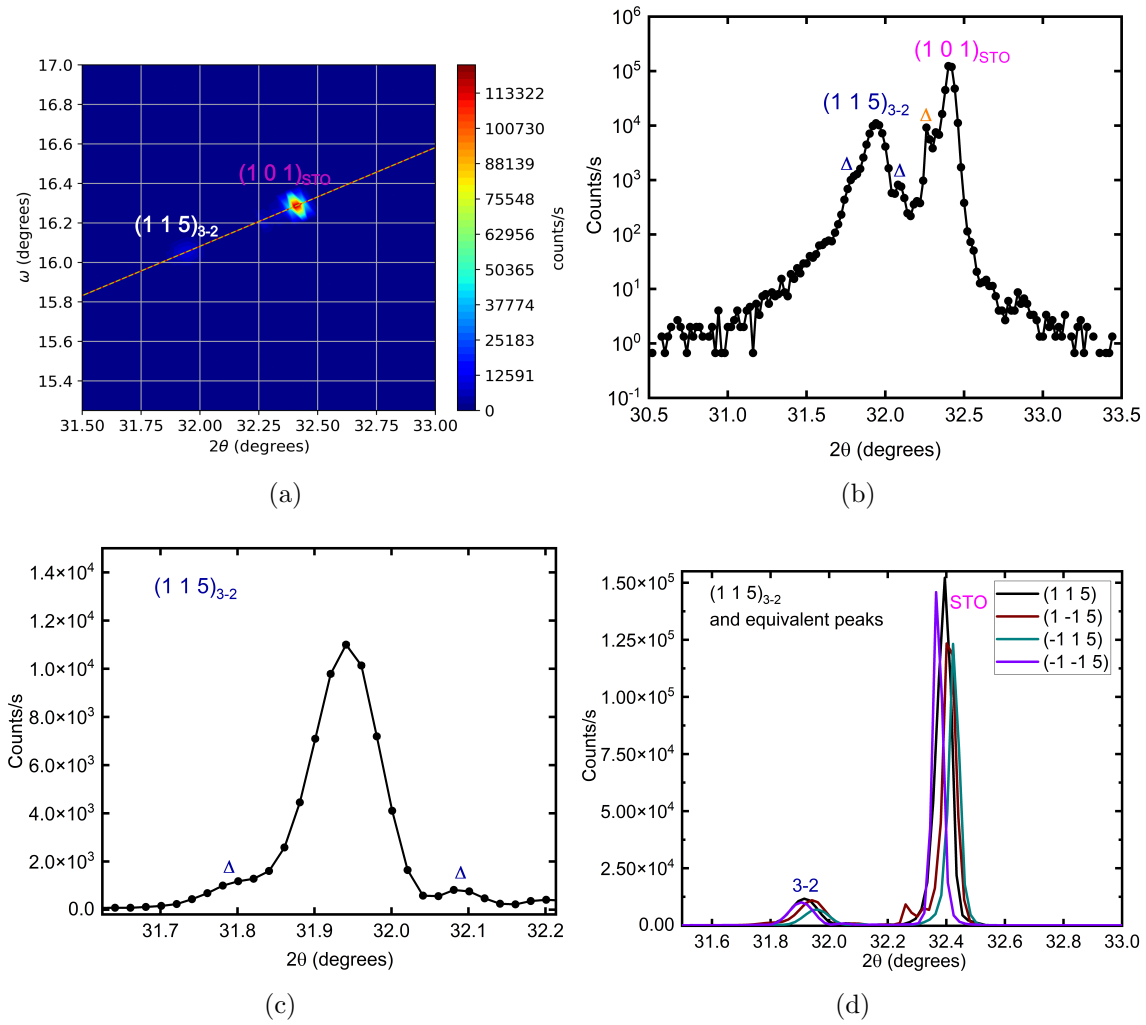

Figure 6.3: XRD measurements on $(LSMO)_3(BTO)_2$ sample using OOP scan mode. (a) 2D scan of (1 1 5) reflection showing peaks from STO and the super-lattice. The dotted line represents the direction of 1D cut made in this data-set to visualize the peaks better. (b) Log plot of the 1D cut of (1 1 5) scan plotted against 2θ to show the different peaks clearly. (c) A zoomed view of the (1 1 5) peak of 3-2 super-lattice showing small satellites on each side, a sign of Keisseg fringes. (d) Comparing (1 1 5) and its equivalent peaks by plotting 1D cuts of the 2D scans against 2θ.

peaks labeled with triangular symbols (blue and orange). Peaks with blue markers could be a result of Keisseg fringes. The intensity and resolution are not enough on this sample to clearly see the fringes and calculate the thickness of the film as done for the 3-3 sample. The orange marked peak, however, is doubtful to be from the film. It is very close to the STO peak and is believed to be from another crystallite of the substrate. More on this is elaborated in the results from the other conducted scans.

Figure 6.3(c) displays a zoomed view of (1 1 5) peak of the super-lattice. As

can be seen clearly, the peak is very symmetric. This confirms that there is no strain relaxation through change in lattice parameters in this sample, as observed for the LSMO film (Chapter 4). This confirms the role of BTO layers to maintain strain throughout the film. In Figure 6.3(d), we compare the (1 1 5) scan with its 3 equivalent reflections. Note that the intensity is plotted as counts/s (not on the $\log_{10}$ scale). In a hypothesis of a single crystal with a 4-fold axis along c, they would be equal in intensity and position. From this plot, one can interpret that the 4 scans are not equal as both STO and 3-2 peaks vary in intensity and position. This is another indication that there are crystallites in the substrate STO. These crystallites can lead to small changes in the lattice parameters and consequently, we should see the peaks shifted, with intensity proportional to the crystallite volume in the area of the sample under diffraction. Let us see what was observed on the other such scans.

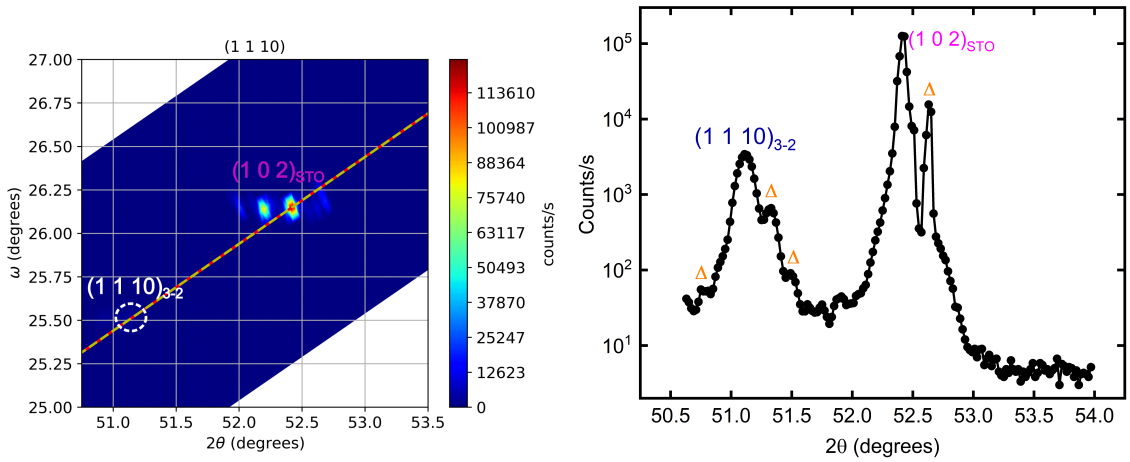

Figure 6.4: Single crystal XRD measurements on (LSMO)$_3$(BTO)$_2$ sample using OOP scan mode. (a) 2D scan of (1 1 10) reflection showing peaks from STO. The super-lattice peak is too weak to be seen on this plot, position marked in white circle. The dotted line represents the direction of 1D cut made in this data-set to visualize the peaks better. (b) Log plot of the 1D cut of (1 1 10) scan plotted against 2θ to show the different peaks clearly. Weak extra peaks observed are marked with orange triangles, believed to be from STO crystallites.

A 2D scan performed for (1 1 10) reflection is shown in Figure 6.4. On this 2D scan too, some extra peaks close to the STO (1 0 2) peak can be clearly spotted. The peak from the 3-2 super-lattice is too weak to be seen on the 2D scan plot (position marked in white circle). To plot them better, data along a 1D cut shown by the dotted line, is shown in Figure 6.4(b) (on a $\log_{10}$ scale). On this plot, along with the super-lattice (1 1 10) peak, some of the extra peaks can also be observed and are marked with orange triangular symbols. These peaks are believed to be from different crystallites present in the sample. They are less likely to be fringes as they are not symmetric in position with respect to the 3-2 peak. This type of peaks were also observed on 1D long scans of (0 0 10) and (0 0 20) reflections.

Although we were successful in locating and measuring the super-lattice peaks, these extra peaks, arguably coming from the STO crystallites, make it very challenging to align as well as integrate the peaks. The limitations in terms of XRD measurements on this sample are thus apparent.

In conclusion, XRD measurements on the 3-2 sample revealed that the sample is grown well with layers stacked along the surface normal direction. The lattice parameters were calculated to be 5.52 Å IP and 20.10 Å OOP. Please keep in mind that we will compare the 0 0 ℓ XRD scans of all the 3 super-lattice samples at the end of this chapter in order to extract information about the widths of layers in different super-lattices.

The film was confirmed to be under IP strain from the substrate STO, showing no signs of relaxation, as expected due to intercalation of BTO layers. Further scans displayed several extra weaker peaks close to STO as well as the 3-2 peaks. We argue that these are due to presence of multiple crystallites in the sample. This makes it difficult to perform conclusive analysis for the nuclear structure of this sample. However, these crystallites have little or no effect on macroscopic magnetic properties of the sample. Therefore, we now move to the magnetic properties of this material, starting with results from SQUID magnetometer.

6.1.2 SQUID results

Magnetic properties of the 3-2 sample were studied using SQUID, by measuring the magnetization in a varying field applied along different crystallographic directions. Our main objective behind these experiments was to see whether removing a BTO layer can affect the magnetic properties of the super-lattice and if so, what changes does it bring. Therefore, we measured the magnetic hysteresis at 10 K in a varying field up to 1 T applied along [100], [110] and [001] film directions. As done for the 3-3 sample, the contribution from STO needs to be subtracted from the measured scans in order to analyze the super-lattice behavior correctly. To do so, we applied the same strategy as the 3-3 sample.

The data measured on the "cleaned" 3-3 sample was treated as the substrate STO signal. At first, this data was normalized with respect to the weight of the 3-2 sample. After this correction, the data-set was subtracted from the scans measured on the 3-2 sample. Figure 6.5(a,b) shows the comparison between these curves. In Figure 6.5(a), the magnetic hysteresis curves measured for field along [100] on 3-2 and STO are shown, along with the subtracted one. Next we have the same curves for field applied along [001] direction in Figure 6.5(b). One can easily notice that the STO contribution is significant at such high fields and the subtraction brings substantial change in the curve shape. Note that the units for measured magnetic moment used in these two plots is *emu* in order to show the comparison clearly.

Finally in Figure 6.5(c), we compare the subtracted hysteresis loops of different directions. The units of magnetization used for this plot are emu/cm^3, assuming that the film is deposited on the whole sample surface. Here are a few notes on the magnetic properties of 3-2 super-lattice based on this plot:

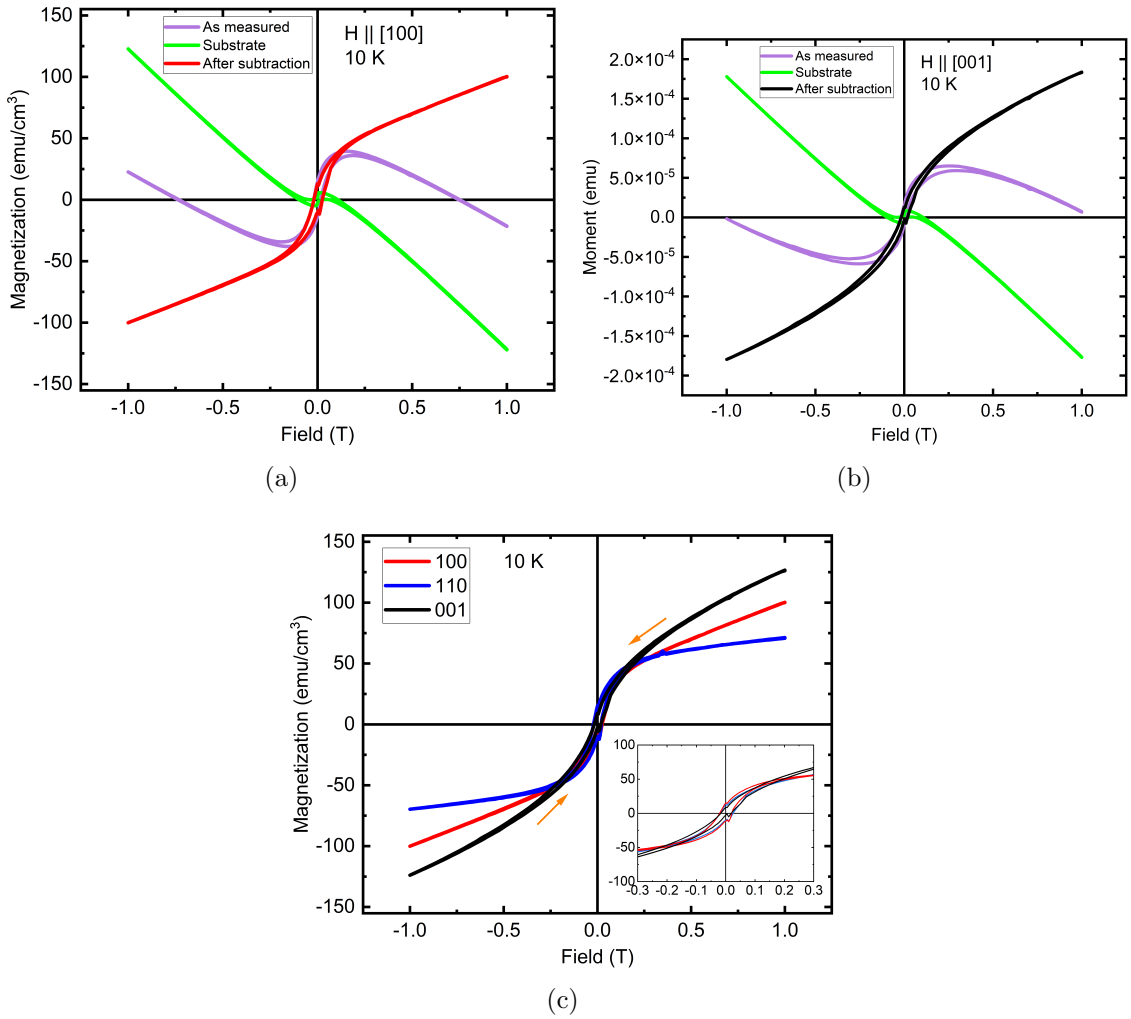

Figure 6.5: Magnetic hysteresis loops measured on the (LSMO)$_3$(BTO)$_2$ super-lattice for 1 T field applied along [100], [110] and [001] directions at 10 K. (a,b) The measured signal plotted along with the substrate STO contribution and the subtracted curve field along [100] and [001]. (c) Comparison of subtracted hysteresis loops of all the 3 directions with magnetization presented in units of emu/cm^3. The arrow marks the direction of measurement and the inset shows an enlarged view of the 3 hysteresis loops.

- First of all, the various magnetic hysteresis related parameters obtained from this plot are listed in Table 6.1. We see that the spontaneous magnetization is extremely small for all the directions, which means that in the absence of field the total macroscopic magnetization in the sample is negligible. This could be due to two possible reasons: either there is presence of domains with FM ordering in the system or the system is completely AFM. Let us see what the shape of the hysteresis loops tell us.

- The curves show no signs of magnetic domains in the system. The size of

Table 6.1: Magnetic hysteresis parameters of 3-2 super-lattice sample measured at 10 K for 1 T applied field. $M_{spon.}$ is the spontaneous magnetization, M_{1T} is the magnetization at 1 T applied field.

Field directions	$M_{spon.}$ (emu/cm^3)	M_{1T} (emu/cm^3)
[100]	15	100
[110]	13	70
[001]	9	126

hysteresis loops (shown in the inset on Figure 6.5) is too small to be taken into consideration for possible domains in the system. At this point, we can thus refute the possibility of FM ordering in the system. Furthermore, the hysteresis loops for field along [100] and [001] are not very typical but closer to AFM type of ordering than PM or diamagnetic. As the field strength is increased, the moments tend to align along the field and the net magnetization increases. Similarly, the net magnetization cancels out to almost negligible as we reduce the applied field to zero, due to anti-parallel alignment of moments.

- The [110] curve depicts an almost plateau shape, which can be an indication of saturation. However, the [100] and [001] curves show higher magnetization at this point. Since the saturation is achieved when all the moments are aligned along the field, it should correspond to the higher possible magnetization in the system. Therefore, clearly contradicting any saturation hypothesis of [110] curve. We assign this plateau shape to the presence of some magnetic coupling between different LSMO layers due to only 2 BTO layers in-between. This point is elaborated in the last section while comparing the magnetic properties of different samples.

- In general, the change in slope of hysteresis curves in antiferromagnets is due to spin-flip transition. On this sample, it is difficult to conclusively comment on any such behavior. This is because the change in slope is seen on all the directions and hence, easy-axis of the system, if there is one, cannot be identified from these measurements.

- In order to further explore the possibility of saturation, the hysteresis were repeated in a field of 5 T applied along [001] direction. The measured curve is shown in Figure 6.6, plotted after subtracting the STO contribution. As expected, the magnetization increases linearly with the applied field above 1 T and the shape shows no signs of saturation.

As a conclusion of SQUID measurements, we can say that the system follows AFM ordering along IP and OOP directions, with no residual magnetization in the absence of field. The measurements are not conclusive of any easy-axis behavior or any transitions of type spin-flop. The moments are not saturated in a field up to 5 T along [001], which showed the highest slope at 1 T among the 3 measured directions.

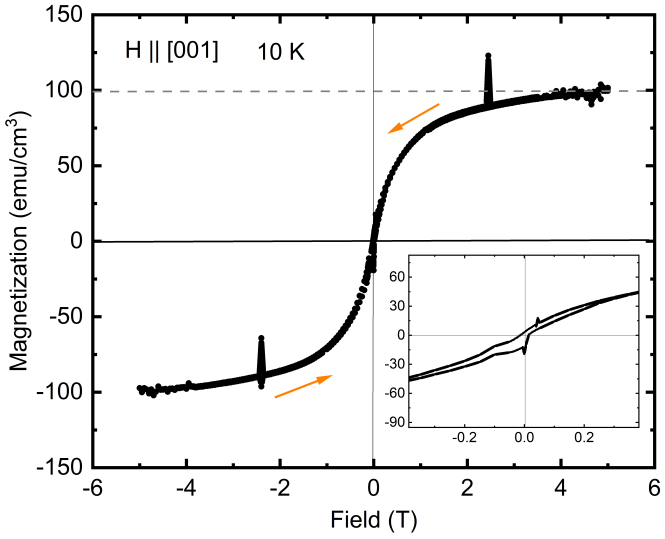

Figure 6.6: Magnetic hysteresis loops measured on the (LSMO)$_3$(BTO)$_2$ super-lattice for 5 T field applied along [001] direction at 10 K. The magnetization is presented in units of emu/cm^3. The arrow marks the direction of measurement and the inset shows an enlarged view of the hysteresis loop at low field.

Keep in mind that the magnetic hysteresis of all the samples used in this thesis are compared at the end of this chapter. Now we move to the ND studies on this sample. Presence of crystallites is not an issue for ND since the diffracted signal consistently originates from the entire sample. This signifies that all crystallites are subject to diffraction, and the resulting intensity reflects the average structure of the sample. Thus, it can allow us insights into the crystal and microscopic magnetic nature of the sample.

6.1.3 ND results

Single crystal ND measurements were performed using D10 diffractometer and the procedure followed was similar to the 3-3 super-lattice experiments (discussed in Chapter 5). As the substrate STO undergoes a structural transition close to 110 K, we decided to work below this temperature [150]. To stay consistent with the 3-3 measurements, all the peaks were measured at 30 K. The goal of this experiment was to measure maximum possible number of Bragg peaks that can give us information about the nuclear and magnetic structure of this sample. In order to identify the nuclear reflections to be measured, we used a DFT optimized geometry. We calculated the theoretical nuclear structure factors of different reflections for this geometry using Vesta software [130] and measured the few most intense peaks.

The film was held in a cryostat and incident wavelength of 1.53 Å was selected using pyrolytic graphite monochromator. The diffractometer was used in four-circle mode with the analyzer option. Since the STO peaks are much stronger than the super-lattice ones, the orientation of the film was done using STO peaks at room

temperature, and again at 30 K. Therefore, all the scans were programmed in q-scan mode ($\omega - 2\theta$ rotation) using STO lattice parameter indices. The lattice parameters obtained are: $a = b = 5.52 \pm 0.02$Å and $c = 20.08 \pm 0.05$Å (calculated using (0 0 10), (2 2 10) and (2 0 15) peak positions) for the unit cell doubled IP (see Figure 6.2 for reference). These values are in-agreement to the XRD results, with IP values suggesting constraint from STO.

Table 6.2: List of reflections measured on $(LSMO)_3(BTO)_2$ super-lattice by ND at 30 K.

(h k l)	(2 0 5)	(2 0 15)	(0 0 10)	(2 2 10)	(2 0 14)
	(0 0 9)	(2 0 4)	(2 2 9)	(2 0 16)	

In total, 9 reflections were measured as listed in Table 6.2 and few of them are shown in Figure 6.7. The scans were carried out with a 1 million monitor, taking about 4 hours to measure a 21 points scan.

The (2 0 5) peak in Figure 6.7(a) is very close to the STO (1 1 1) peak, which is much more intense[1]. The tail of this STO peak can be clearly seen in the plot. The dashed line represents the expected position of the (2 0 5) peak, which is suspected to be hidden by the STO peak. The same was observed for the (2 2 10) peak (not shown here). The second peak in Figure 6.7(b) is (0 0 10), which can be very clearly seen on the scan with a nice symmetric shape. The beginning of STO (0 0 2) peak can also be spotted at the end of the scan. This is one of the most intense peaks measured on this sample. In consistency with XRD results, we see no signs of strain relaxation on these peaks. Next, we show (2 0 15) peak in Figure 6.7(c), showing significant intensity. Similarly to other scan, the tail of STO (1 1 3) peak can be seen at the end of the scan. These are all the scans where we observed some intensity. The rest of the scans i.e. (2 0 14), (0 0 9), (2 0 4), (2 2 9) and (2 0 16) showed no peaks, even on multiple repeated scans with better statistics. As an example, (0 0 9) scan is shown in Figure 6.7(d) with dashed line marking the theoretically calculated position of the peak.

So in ND measurements, significant intensity is present on the peaks with ℓ multiple of 5, while no intensity is observed on the rest of the peaks. This means that the nuclear neutron diffraction structure factors of other peaks are very small and cannot be measured. Thus, ND cannot be used to obtain sufficient data-set on this sample required to resolve its nuclear structure. A detailed conclusion combining different diffraction results is presented in the next section.

Recalling the discussion in section 2.3.2.4 about diffraction on super-lattices, this can be an indication that the different layers of LSMO and BTO are almost equal in thickness. However, in XRD (0 0 ℓ) scan we saw that the peaks with ℓ not multiple of 5 ("satellites") are also present (see Figure 6.1). This points to the fact that the intensities of these peaks in ND are not enough to successfully integrate them, which

[1]Please note that the STO indices are represented in the smaller unit cell with $a = b = c = 3.90$ Å.

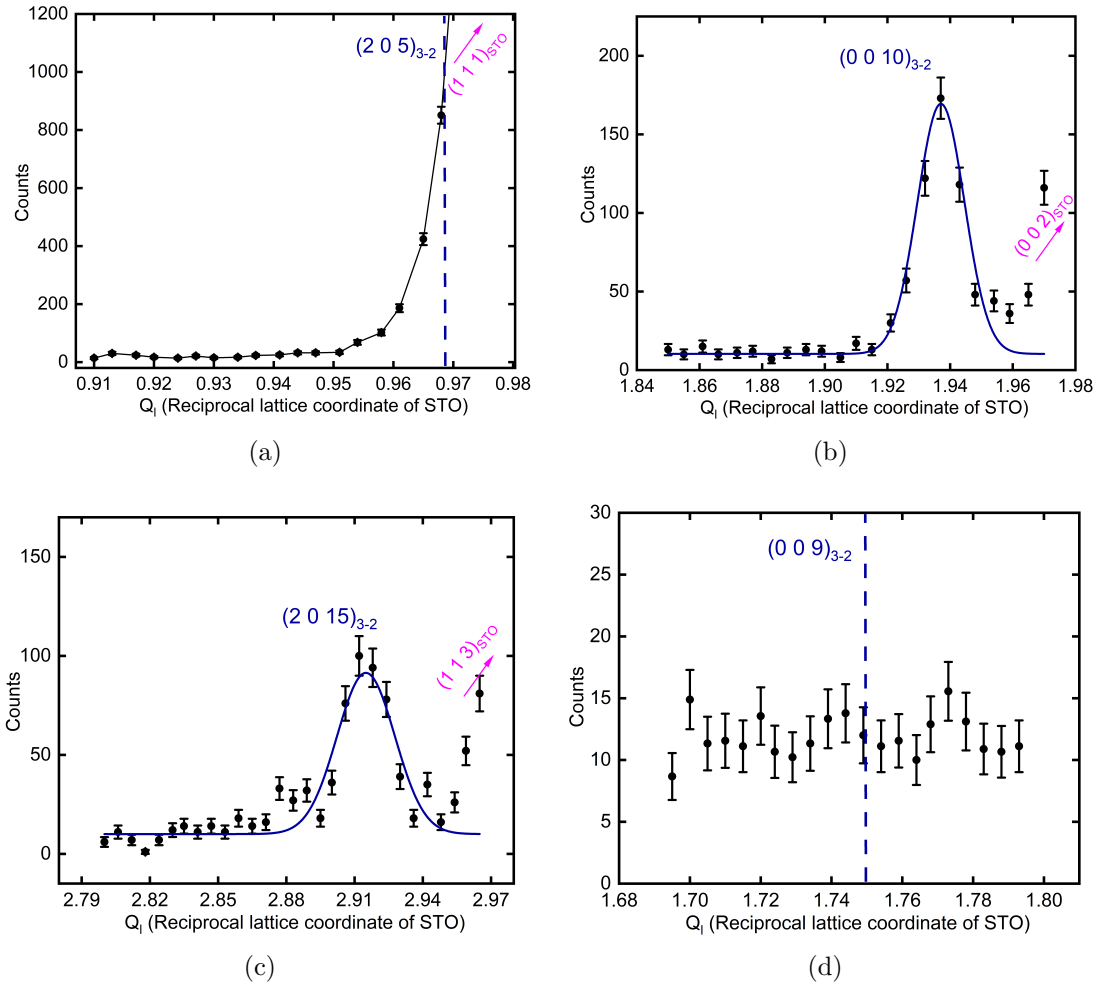

Figure 6.7: Single crystal ND measurements on (LSMO)$_3$(BTO)$_2$ sample using D10 instrument. (a-d) (2 0 5), (0 0 10), (2 0 15) and (0 0 9) scans, normalized to 1 million monitor. The counting time for a 21 points scan with 1 million monitor was about 4 hours.

was not the case for the 3-3 sample. Therefore, one can think that the layer widths' modulation in the 3-2 sample is not as extreme as in 3-3. We hypothesize that since 3-2 sample has only 2 layers of BTO, the different layers somehow stay locked with thickness similar to each other. This leads to weaker satellites that could not be measured with ND. With this notion, we conclude that it is not possible to perform structural refinement on the 3-2 sample using ND data.

6.1.4 Conclusion of the 3-2 sample analysis

In conclusion, we performed 3 different types of measurements on this sample, namely XRD, SQUID and ND. From SQUID, we observed the macroscopic magnetic properties of the system. We found that the material has no net magnetization in zero field and the possible arrangement of moment is AFM in nature. The hysteresis

measured along 3 directions i.e. [100], [110] and [001], showed different slope at low field, but no easy-behavior could be concluded. Finally, we also observed that the moments are not saturated in a field up to 5 T.

We used diffraction methods to obtain information on the crystal structure of the super-lattice. From XRD, we observed periodic peaks on the (0 0 ℓ) scan, establishing that the LSMO and BTO layers are well-stacked along surface normal direction. We also observed peaks with ℓ not a multiple of 5, a sign of different widths of the layers in the unit cell . The calculated IP lattice parameters of the super-lattice confirmed that the constraints from the substrate STO are successfully imposed. In addition, the 2D scans of (1 1 5) and (1 1 10) peaks revealed that the super-lattice peaks show no sign of strain relaxation. The 4 equivalent peaks of (1 1 5) family of reflections presented differences in intensities and peak positions (see Figure 6.3(d)). The 4 STO peaks on these scans also showed such differences. Furthermore, multiple unidentified extra peaks were observed on the (1 1 10) scan. We conclude that these peaks on (1 1 10) scan and the differences observed in (1 1 5) family of peaks, are due to presence of crystallites in the substrate. This makes the peak alignment and integration very challenging. Therefore, the data required to perform crystal structure refinement using XRD cannot be obtained on this sample. However, we can still comment on the widths of layers using the 0 0 ℓ scans, which is done at the end of this chapter by comparing these scans for all the super-lattices.

Using ND, we measured several reflections. The lattice parameters obtained were found to be in-agreement with the XRD ($a = b = 5.52 \pm 0.02$Å and $c = 20.08 \pm 0.05$Å). intensity was seen on the peaks with ℓ multiple of 5 with an exception of (2 0 5), which is very close to the STO (1 1 1) peak. One can easily interpret that the peaks were observed only on the scans with ℓ multiple of 5. Recalling the discussion in section 2.3.2.4 about diffraction on super-lattices, this can be an indication that the different layers of LSMO and BTO are almost equal in thickness. However, in XRD (0 0 ℓ) scan we saw that the peaks with ℓ not multiple of 5 ("satellites") are also present (see Figure 6.1). This points to the fact that the intensities of these peaks in ND are not enough to successfully integrate them, which was not the case for the 3-3 sample. Therefore, one can think that the layer widths' modulation in the 3-2 sample is not as extreme as in 3-3. We hypothesize that since 3-2 sample has only 2 layers of BTO, the different layers somehow stay locked with thickness similar to each other. This leads to weaker satellites that could not be measured with ND. The 3rd BTO layer thus allows some relaxation in terms of layer width along c-axis. In terms of magnetism, removing the middle BTO layer can result in some sort of coupling between different LSMO layers. Consequently, the magnetic hysteresis curves can show higher magnetism. This point is elaborated in the last section of this chapter, in which we will compare the magnetic properties of different super-lattice samples.

With this notion, we conclude that diffraction and magnetic measurements showed promising results on this sample, the presence of crystallites limits the XRD study whereas ND suffers from low intensity of peaks for structural determination.

6.2 [(LSMO)$_2$(BTO)$_3$] (2-3) super-lattice

The unit cell in 2-3 sample contains only 2 layers of LSMO with 3 of BTO and this is repeated 29 times along the surface normal direction (taken as c-axis here). Compared to 3-2, with this sample we wanted to investigate the effect of removing an LSMO layer on the magnetic and crystallographic behavior. This was mainly studied using SQUID magnetometer and ND. First, I present a (0 0 ℓ) XRD scan, which was measured by B. Mercey for initial characterization of the sample's quality. [2].

6.2.1 XRD - (0 0 ℓ) scan

The scan was measured with incident X-ray wavelength of $\approx$ 1.54 Å and in 2θ range of 10° - 60° as shown in Figure 6.8. Similar to 3-2, the (0 0 5) and (0 0 10) peaks can be seen clearly close to the STO (0 0 1) and (0 0 2) peaks. The c lattice parameter obtained from these peaks is 20.40 $\pm$ 0.01 Å. We can also see that the peaks are symmetric in shape, suggesting no relaxation, which can be expected after the results on 3-3 and 3-2 samples.

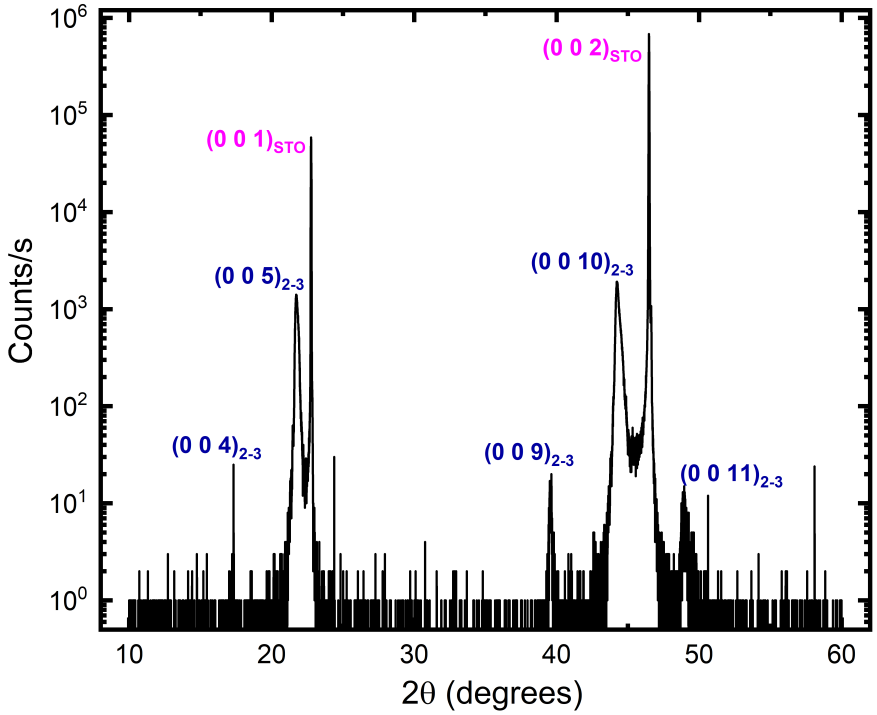

Figure 6.8: (0 0 ℓ) scan performed on (LSMO)$_2$(BTO)$_3$ sample using XRD with peaks from the 2-3 super-lattice (blue) and the substrate STO (purple) clearly marked. The counts/s are presented on $\log_{10}$ scale. Please note that this scan was performed by B. Mercey for initial characterization of the sample quality.

In addition, we can also see some of the satellites peaks namely (0 0 4), (0 0 9)

[2]Please note that on this sample we do not have any measurements from SmartLab.

and (0 0 11). Again, as explained in the 3-2 section, this is an indication that there is some modulation in the widths of different layers. To obtain further information related to this, we need to go to ND results. But first, let us discuss the macroscopic magnetic properties of the sample.

6.2.2 SQUID results

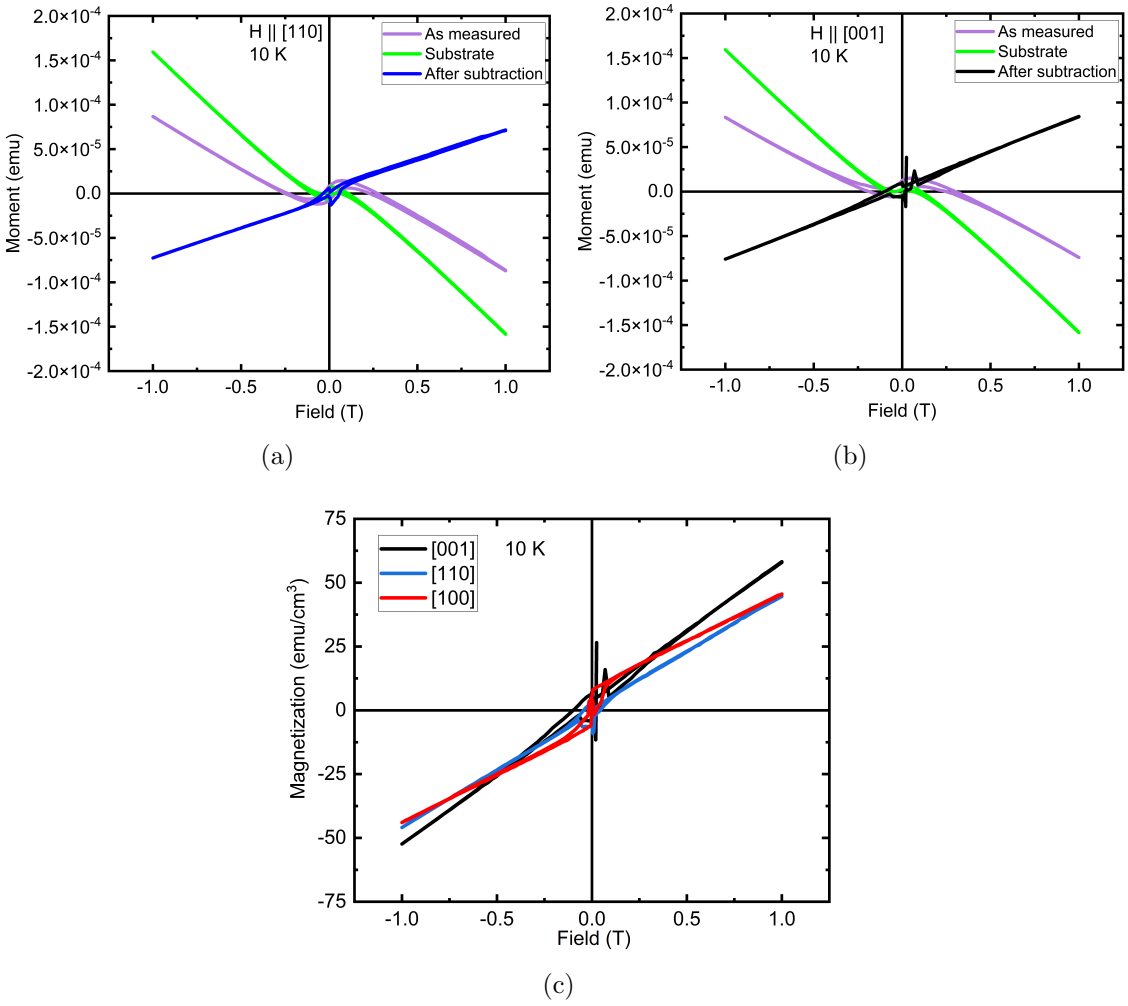

Figure 6.9: Magnetic hysteresis loops measured on the $(LSMO)_2(BTO)_3$ super-lattice for 1 T field applied along [100], [110] and [001] directions at 10 K. (a,b) The measured signal plotted along with the substrate STO contribution and the subtracted curve field along [110] and [001]. (c) Comparison of subtracted hysteresis loops of all the 3 directions with magnetization presented in units of emu/cm^3.

As for the other samples, the macroscopic magnetic behavior of this sample was also investigated by measuring its magnetic hysteresis loops in a varying field of up to 1 T applied along different crystallographic directions at 10 K. The STO magnetic contribution to the hysteresis curve was subtracted in the same way as done for

the other samples; *cleaned* 3-3 sample data (i.e. STO) was weight normalized and subtracted from the measured data-points. The comparison of the measured and subtracted curves is shown in Figures 6.9(a,b), in units of *emu* for better comparison. The subtracted curves are clearly very different from the measured ones. The [001] curve shows slight fluctuations in the signal close to zero field. We believe this is an experimental artifact because the signal is weak and can lead to some instability in the data acquisition.

In Figure 6.9(c), we compare the magnetic hysteresis for field along [100], [110] and [001] directions (the unit cell parameters are presented in the next section) in units of emu/cm^3 assuming that the whole sample surface is covered in film. The behavior of hysteresis is very similar to the 3-3 sample. We see a very small spontaneous magnetization on all the curves. Table 6.3 lists the value for each direction. Please note that due to fluctuations in the data close to zero field, the exact values of spontaneous magnetization could not be obtained. Nonetheless, it is evident that the magnitude is very small. Furthermore, the magnetization increases almost linearly with increase in field strength for all the directions. Based on these facts we can say that the ordering of magnetic moments is AFM in this sample.

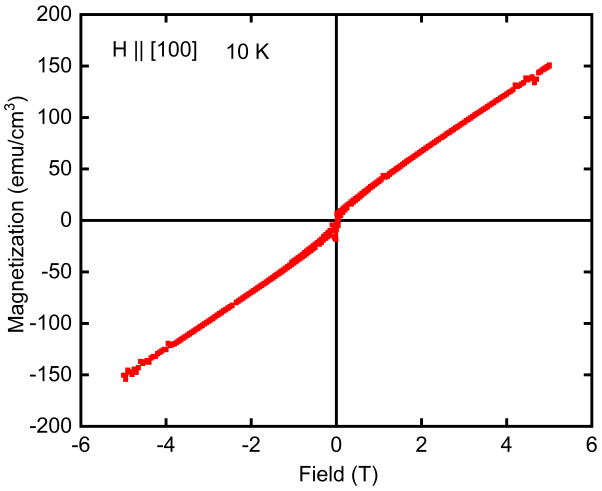

Figure 6.10: Magnetic hysteresis loops measured on the (LSMO)$_2$(BTO)$_3$ super-lattice in 5 T field applied along [100] direction at 10 K.

Furthermore, the [001] curve exhibits a distinctive behavior by intersecting with the other curves, mirroring the pattern observed in the 3-3 sample. The [100] is also different at low field, showing change in slope indicative of a spin-flop transition (see Figure 5.9. Consequently, we deduce that the easy-axis in this context aligns along the [100] direction. In contrast, the [001] orientation, being perpendicular to the easy-axis, demonstrates a linear progression with magnetic moments gradually reorienting towards the direction of the applied magnetic field as it increases.

The magnetic hysteresis were also measured in field up to 5 T for [100] direction. The results obtained are shown in Figure 6.10. The shape of the curve clearly shows that the moments are not saturated even in 5 T and higher field is required to reach

Table 6.3: Magnetic hysteresis parameters of 2-3 super-lattice sample measured at 10 K for 1 T applied field. $M_{spon.}$ is the spontaneous magnetization, M_{1T} is the magnetization at 1 T applied field.

Field directions	$M_{spon.}$ (emu/cm^3)	M_{1T} (emu/cm^3)
[100]	6	45
[110]	3	44
[001]	7	58

saturation. In addition, the magnetization increases linearly with field above 1 T. This further corroborates the mark that the system has AFM ordering of moments.

As a conclusion, we can say that the macroscopic magnetic properties of the 2-3 sample were found to be similar to the 3-3 sample. The ordering in this system is expected to be AFM, showing no spontaneous magnetization. [100] is argued to be the easy-axis of magnetization, displaying spin-flop transition at low field. Finally, the moments were found to be not saturated in an applied field of 5 T along [100]. Now, let us proceed to review the findings from ND.

6.2.3 ND results

We have performed single crystal ND experiment on this sample with a motive to obtain information on its crystal structure. An additional challenge in this study was that DFT optimizations are not available for this type of composition. Let me first explain the reasoning behind this.

Difficulties in performing DFT calculations on 2-3 super-lattice

In Chapter 5, we discussed the mechanism of DFT studies on LSMO/BTO super-lattice structures. For 3-3, there was possibility to mimic the La/Sr disorder in the system. This is because the doping level of Sr is $1/3^{rd}$ and since the number of layers repeated in the unit cell is a multiple of 3, one can accumulate well the different possible scenarios of disorder along the c-axis.

On the other hand, the 2-3 super-lattice contains 2 layers of LSMO in the unit cells. One possible option to include Sr as a doped element in this structure is 1 Sr atom out of 2 La positions in each unit cell, which amounts to 50% of doping concentration. This means that La/Sr disorder scenarios cannot be mimicked in this unit cell for the 2-3 sample. One can imagine multiplying the cell 3 times along a and b, but the calculations become very big for such a unit cell. Therefore, it was not possible to compute DFT optimized geometries in this case. With this in mind, let us continue to the ND results.

To overcome this problem, for the experiment on D10, the reflections to be measured were selected by modifying few of the DFT optimized geometries of the 3-3 super-lattice. The middle layer of LSMO was removed on these geometries and the theoretical nuclear structure factors were calculated for different reflections using the same procedure as discussed in Chapter 5 for the 3-3 sample. This way, a total of 13

Table 6.4: List of reflections measured on (LSMO)$_2$(BTO)$_3$ super-lattice by single crystal ND at 30 K, classified into categories of (0 0 ℓ), (2 0 ℓ) and (2 2 ℓ).

(0 0 l)	(2 0 l)	(2 2 l)
(0 0 7)	(2 0 4)	(2 2 9)
(0 0 9)	(2 0 8)	(2 2 10)
(0 0 10)	(2 0 9)	
(0 0 19)	(2 0 14)	
(0 0 20)	(2 0 15)	
	(2 0 16)	

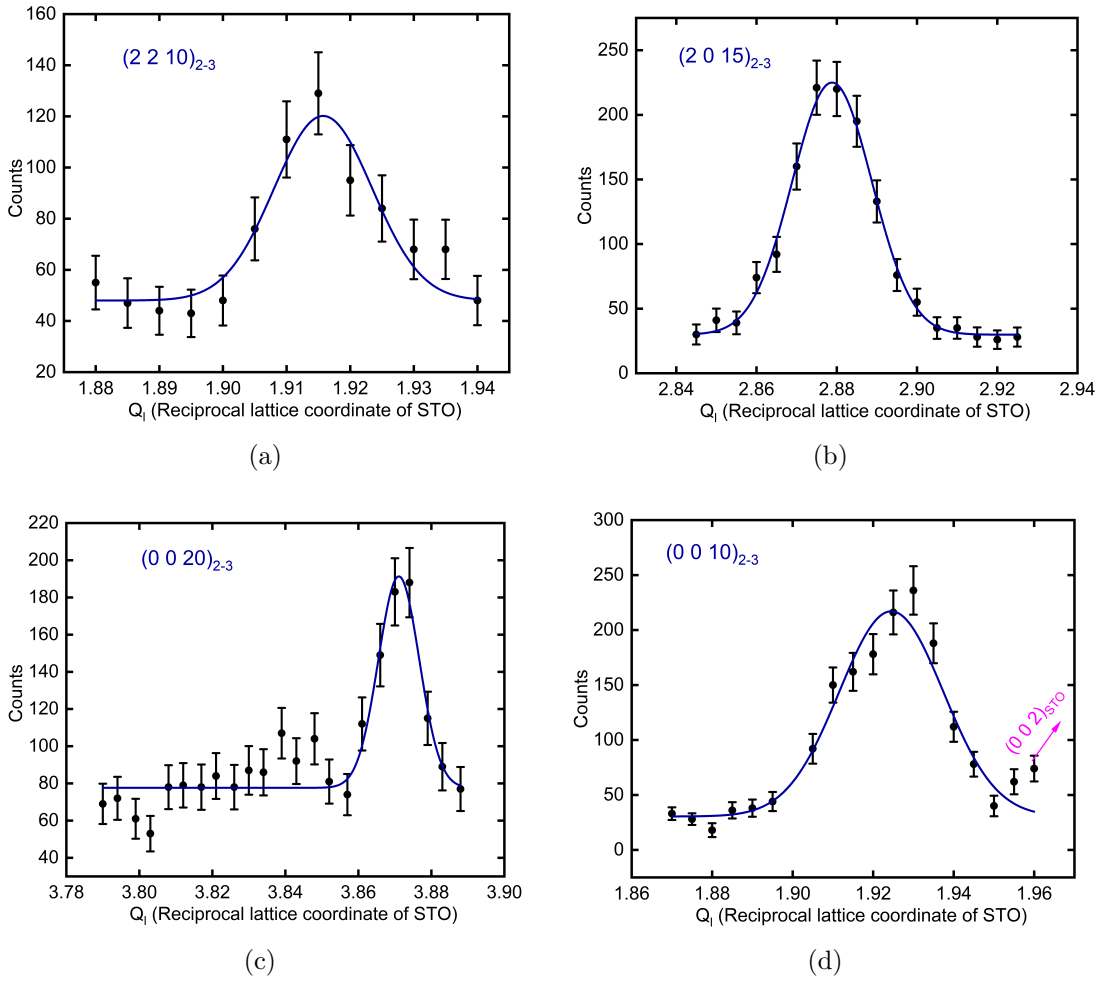

Figure 6.11: Single crystal ND measurements on (LSMO)$_2$(BTO)$_3$ sample using D10 instrument. (a-d) (2 2 10), (2 0 15), (0 0 20) and (0 0 10) scans, normalized to 2 million monitor. The counting time for a 21 point scan with 2 million monitor was about 5 hours.

reflections were identified to distinguish between different DFT geometries, as listed in Table 6.4.

The sample was oriented using STO peaks and the scans were carried out at 30 K in q-scan mode. The IP lattice parameters obtained are $a = b = 5.52$ Å, which is the 45° rotated unit cell with respect to STO cubic unit cell of dimension 3.90 Å, confirming that the super-lattice is under IP constraint from STO. The c lattice parameter calculated using several measured peak positions, is 20.30 ± 0.05 Å.

Figure 6.11 includes few of the scans performed. In Figures 6.11(a-c) plots, the peaks corresponding to (2 2 10), (2 0 15) and (0 0 20) can be clearly seen. The (0 0 10) peak in Figure 6.11(d) is found to be the strongest one. The (2 0 5) peak was found to be too close to the STO (1 1 1) peak and hence, could not be spotted (not shown here). The beginning of STO peaks can also be spotted at the end points of the (0 0 10) scan. In addition, all the peaks are symmetric in-shape and show no sign of strain relaxation, confirming the role of BTO layer in maintaining the strain.

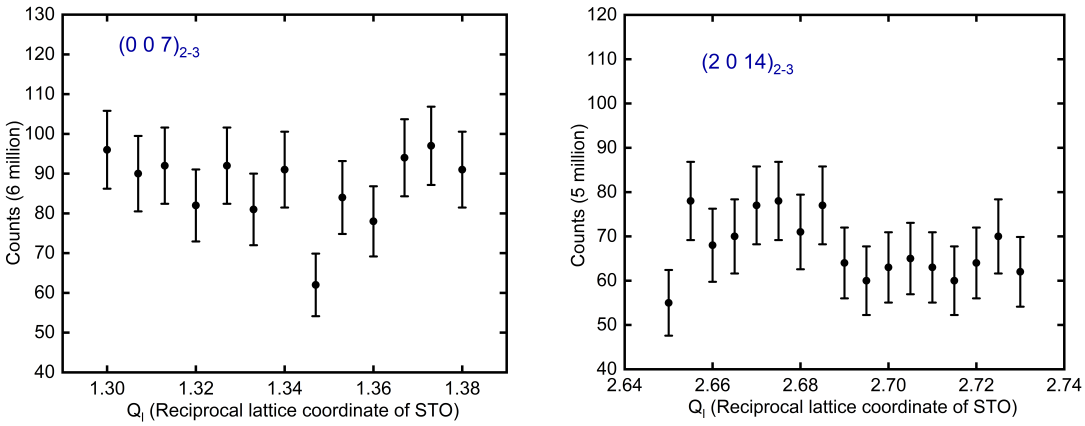

(a) (b)

Figure 6.12: Single crystal ND measurements on $(LSMO)_2(BTO)_3$ sample using D10 instrument. (a,b) (0 0 7)and (2 0 14) scans, with the monitor size mentioned on the y-axis.

Among the rest of the reflections, none showed any peak even with increased statistics of up to 5 million monitor. Two of such scans are shown in Figure 6.12 with their monitor size mentioned on the y-axis. These results are similar to what we observed on the 3-2 sample. We again come to the conclusion that the ND intensities on 2-3 structure are too weak to be observed and hence, it is not possible to perform structural refinement. Let us conclude the overall results of this sample.

6.2.4 Conclusion of the 2-3 sample analysis

We studied this sample using SQUID magnetometry and diffraction experiments.

Using SQUID, we measured its macroscopic magnetic properties. The hysteresis curves suggested AFM ordering in the system with no residual magnetization. The [100] hysteresis shows signs of spin-flop transition, making it the easy axis and for

[001] and [110], the magnetization increases almost linearly with the field. For [100], we also observed that the moments are not saturated in field up to 5 T.

The diffraction results were found to be similar to the 3-2 sample. In ND, we measured several reflections at 30 K. Good amount of intensity was observed on reflections with ℓ multiple of 5 and on the rest, no peak was obtained. The lattice parameters obtained were found to be in-agreement with the fact that the structure follows IP constraints from the substrate STO and the peak shape showed no signs of strain relaxation. In addition, the (0 0 ℓ) scan from XRD measurements showed that there are satellite peaks such as (0 0 4), (0 0 9) etc., corresponding to layer modulation in the structure. Therefore, following the discussion on 3-2 results, we concluded that with 2 layers of LSMO the structure of the super-lattice is possibly less distorted in terms of layer width as compared to 3-3 and as a result, the intensity of the satellites in ND is too weak to measure them for structural refinement.

With this, the analysis of 3-2 and 2-3 super-lattices come to an end. Now, we move to the comparison of magnetic hysteresis of all the samples used in this thesis: the LSMO film and 3 super-lattices.

6.3 Comparison of different samples

So far, we have discussed the crystal and magnetic properties of different samples individually, obtained using diffraction methods and SQUID macroscopic measurements. Now to conclude this study, we will compare the results of different samples. To remind the reader, these samples include: LSMO film on Si substrate with a buffer layer of STO, super-lattices of composition $(LSMO)_n(BTO)_m$ on STO substrate, where n and m are 3-3, 3-2 and 2-3. Let us start with a comparison of the super-lattice structures using the results obtained from XRD (0 0 ℓ) scans.

6.3.1 Structure: XRD results of super-lattices

We have evaluated the c-lattice parameter of each sample using the positions of different peaks on the (0 0 ℓ) scan. The obtained values and the corresponding peak used for the evaluation are listed in Table 6.5. Please note that we have chosen (0 0 10) (for 3-2 and 2-3), and (0 0 12) (for 3-3), and their neighboring satellites for these calculations as these peaks' positions are well resolved on all the scans. If we look at the c values calculated using the satellite peaks' positions for each sample separately, they are slightly different from their corresponding main peak value (except for 2-3). This can be an indication of incommensurability in the structure with possible origin in stacking faults. However, the resolution on these scans is not enough to conclusively comment on the shift in the satellite peak positions. Therefore, we will focus on the central peak values for further analysis.

Table 6.5: c-lattice parameters of the super-lattice samples calculated using different peak positions. The average thickness of each layer (c_{layer}) in different samples is also listed.

Sample	Reflection	$c \pm 0.01$ (Å)	$c_{layer} \pm 0.002$ (Å)
3-3	(0 0 11)	24.25	4.042
	(0 0 12)	24.10	4.017
	(0 0 13)	24.03	4.005
3-2	(0 0 9)	20.00	4.000
	(0 0 10)	20.10	4.020
	(0 0 11)	20.22	4.044
2-3	(0 0 9)	20.40	4.080
	(0 0 10)	20.40	4.080
	(0 0 11)	20.40	4.080

By simply subtracting the c values of different samples, one can obtain the thickness of some of the layers in the unit cell. In order to go to 2-3 sample from 3-3, the middle LSMO layer needs to be removed. Therefore, if we make a crude assumption that the rest of the layers are of similar thickness in both the samples, the middle LSMO layer thickness of 3-3 is given by the difference in the two samples' c values, which is 24.10 Å - 20.40 Å = 3.70 Å. So clearly from these analyses, we interpret

that the middle LSMO layer on 3-3 is significantly contracted as compared to the average layer thickness in the structure ($\frac{24.1}{6} = 4.02\mathring{A}$) as well as the bulk LSMO c value (3.88Å). This is consistent with what we obtained from the fit of the ND data. Though one needs to keep in mind that we have made a notable assumption here that the thicknesses of other layers are similar in the 2 samples. Moreover, although this contraction of middle layer was also expected from the DFT calculations as presented by A. Sadoc et al., the exact widths of different layers from ND were not found to be compatible with DFT. So we can say that the XRD results are in agreement with the ND analysis of 3-3, and are only qualitatively in accord with the DFT calculations.

Now we move to the comparison of magnetic properties of the super-lattices along with the LSMO film.

6.3.2 Properties: magnetic behavior

The magnetic hysteresis of all the samples are shown in Figure 6.13, with separate plots for each direction of applied field i.e. [100], [110] and [001]. Recalling that the unit cells used for all the analysis is different from the substrate STO bulk unit cell: rotated by 45° IP.

Here are some calculations performed to prepare these plots for precise and effective comparison between the different samples. First of all, the magnetic hysteresis chosen for comparison are the ones measured in applied field up to 1 T [3]. As pointed out in previous sections, the examination of hysteresis at higher magnetic fields did not yield any noteworthy additional insights, and it is important to note that the magnetic moments within the super-lattices did not reach saturation even under a magnetic field as high as 5 T. Secondly, the unit of magnetic moment taken for comparison is μ_B/Mn. The measured signal in *emu* cannot be compared as it is, because of different number of Mn atoms in the samples. For example, in LSMO film the number of total (or per cm^3) Mn atoms is different from the 3-3 super-lattice due to intercalation of BTO layers. Therefore, the magnetic signal was converted into units of μ_B/Mn using the following relation:

$$\begin{aligned} 1\ emu = 1\ erg/G &= 10^{-3}\ J/T \\ 1\mu_B = 9.27 \times 10^{-24} J/T &= 9.27 \times 10^{-21} erg/G \\ 1\ emu &= \frac{1}{9.27 \times 10^{-21}} \mu_B \end{aligned} \tag{6.1}$$

This way we obtain the size of magnetic moment per Mn ion for each sample. Please note that this calculation is based on the assumption that the surfaces of all the samples are covered uniformly with the deposited film. Now, let us examine some conclusions that can be drawn based on these comparisons:

- For the field along IP directions; [100] and [110], the moments in LSMO film are saturated at a low field of only ≈ 0.2 T. In Figure 6.13(a,b), it is evident that the super-lattice curves are far from saturation, even at 1 T field. The shape of

[3] Except for LSMO, which is for field up to 0.3 T.

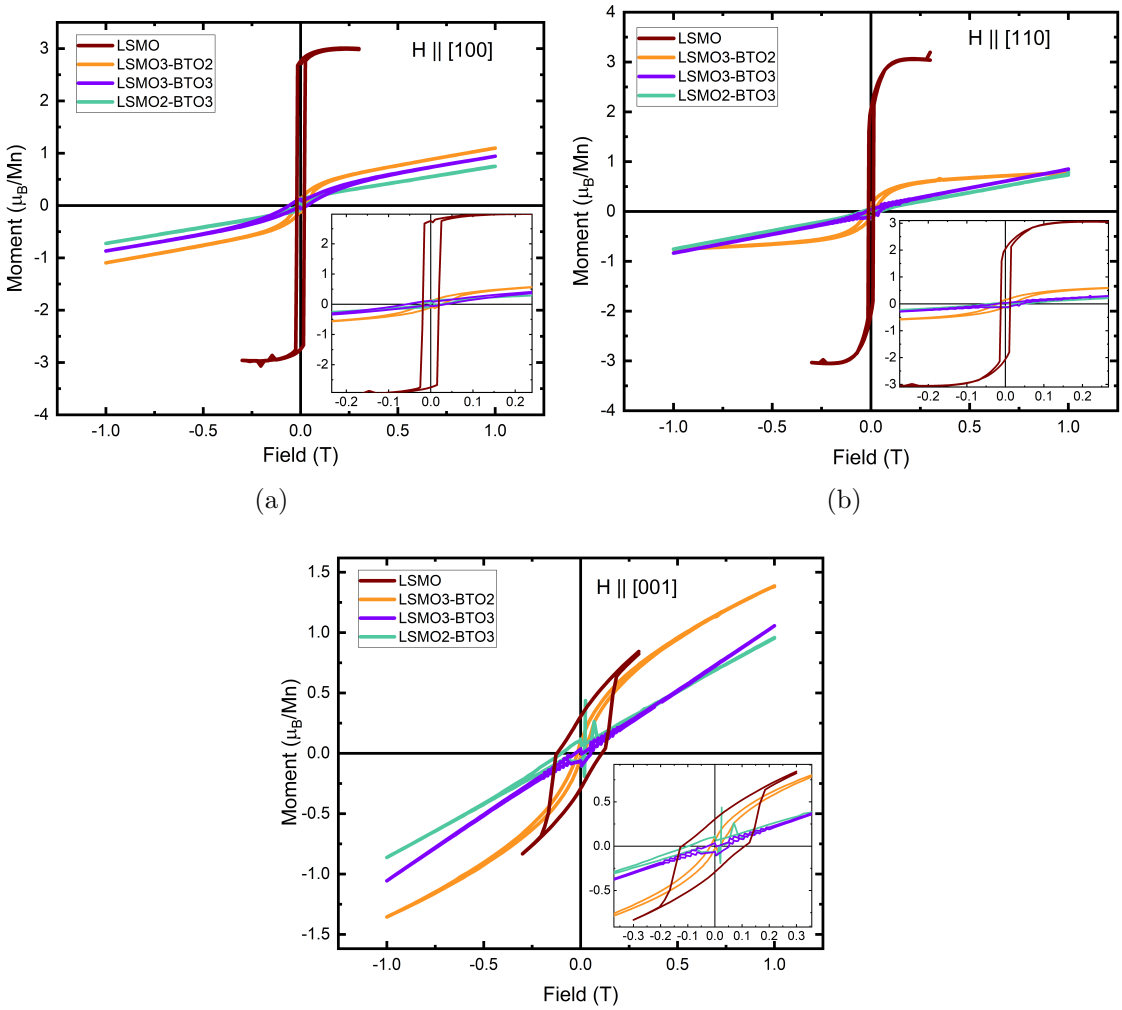

Figure 6.13: Comparison of magnetic hysteresis loops measured on the LSMO film and the super-lattices for 1 T field applied along [100], [110] and [001] directions. The moment is represented in units of μ_B/Mn, assuming the whole sample surface is covered uniformly with the deposited film.

hysteresis is also different. The LSMO film is typical of a FM ordering, whereas the 3 super-lattices showcase signs (almost straight line or possible indication of a spin-flop transition) of AFM ordering, with negligible uncompensated component at zero field. This highlights the effect of alternating BTO layers on the LSMO film.

- Turning the attention to magnetic anisotropy, the LSMO film clearly shows different magnetic behavior along [001] direction. It portrays that the moments gradually rotate with change in applied field. The saturation along this direction was reached above 2 T field (see Figure 4.24). On the other hand, the super-lattices show different directional dependence of magnetic properties. The

recorded curves on 3-3 and 2-3 samples displayed spin-flop like transitions along [100], demonstrating it as the potential easy-axis. The slope of magnetization at high field along [100] is very similar for the all the super-lattices.

- If we compare only the super-lattices, the slopes of increase in moment with field along [100] are similar for the 3 samples. Looking at the insets on Figure 6.13(a,b), one will find that the hysteresis loop of the 3-2 sample is slightly different from the other 2 in terms of shape, especially close to zero field. In addition, the [110] curve of 3-2 shows a plateau shape while the other 2 are almost linear. Our hypothesis is that this phenomenon is attributed to the composition of the 3-2 sample, which comprises only 2 layers of BTO, occurring after every 3 layers of LSMO. This configuration can result in some kind of coupling effect between different LSMO layers through the BTO layers, leading to a slightly more pronounced increase in the magnetic signal as the magnetic field is applied. In fact, this effect is seen for all the directions and is particularly evident in the [001] curves, as depicted in Figure 6.13(c). This means that this change in slope of the 3-2 curve is not due to any spin-flop transition as is the case for 3-3 and 2-3. As a result of this coupling, the 3-2 curve exhibits a higher magnetic moment compared to both the 3-3 and 2-3 configurations, indicating a larger magnetic moment size at the same magnitude of the applied magnetic field. The exact nature of this coupling cannot be obtained from the available measurements.

- The 3-3 and 2-3 curves are very similar in shape and moment size, indicating that removing one LSMO layer on 3-3 does not lead to any major alternations in the magnetic ordering.

To sum up, intercalation of BTO layers on LSMO film results in complete change in the magnetic ordering of the system. It is completely FM in LSMO film and turns to AFM ordering in the super-lattices. In addition, the magnetic anisotropy also changes. In LSMO, the [001] direction presents large anisotropy in terms of field required to align the moments. On the other hand, the super-lattice structures do not present such drastic differences along different directions. The 3-3 and 2-3 show signs of [100] being the easy-axis, but other than this the differences in the curves of the 3 directions are not as pronounced as LSMO. The 3-2 sample showed no conclusive evidence of the existence of any easy-axis.

This brings an end to the analysis of samples investigated in this thesis. In the next chapter, we will go through a summary of the key findings of this project and sum up the results in a broader perspective.

Chapter 7

Conclusion

In this thesis, we present an intensive study of the crystallography and magnetic properties of an epitaxial LSMO thin film and different super-lattices. Our study is motivated by two main factors. First is the potential of these materials for spintronic applications. The wide range of physical properties shown by these compounds such as magnetoresistance and half-metallicity, combined with versatility of thin films, makes them ideal for various spin-based devices. Secondly, the determination of nuclear and magnetic structure of epitaxial thin films using diffraction methods presents an exciting domain of thin film crystallography. As this is a relatively new field, we provide a foundational study of single crystal X-ray and ND on magnetic epitaxial thin films, through this thesis. The work can be subdivided into two main categories of samples as follows:

1. First is an epitaxial thin film of LSMO deposited on Si substrate with a buffer layer of STO in-between. The work on this sample included examining its nuclear and magnetic structure using diffraction and SQUID magnetometry.

2. The second category involved the super-lattice samples. In total, 3 samples were investigated, namely 3-3, 3-2, and 2-3, where the number corresponds to layers of LSMO and BTO in the unit cell, respectively. We chose these super-lattices in the search of potential candidates for the next generation of spintronic devices showing strong magnetism at RT. We performed single crystal X-ray and ND experiments on these samples in order to obtain their atomic structure. The macroscopic magnetic properties of the super-lattice samples were measured using SQUID and the changes were observed in comparison to the LSMO thin film. The obtained results of these 2 categories are discussed next.

Looking at the bigger picture, another important remark of this study is obtaining complete crystallographic information on such thin films using diffraction. The amount of challenges in these studies is considerable, from experimental difficulties to complex data treatments. One has to plan the measurements strategically and make coupled analysis using more than one technique to arrive at well-supported conclusions. In XRD section, we saw how complicated it is to align the sample and locate different reflections for measurements. In addition, the data treatment

required integrating the reflections in unconventional ways carefully avoiding contributions from substrate and performing UB-matrix calculations. Furthermore, the relaxation effect presented another hurdle to integration. In ND, long measurement times meant that a small number of reflections were available to refine the magnetic structure. This again required doing refinement in unconventional ways by exploring different configurations through Python scripts using Rf-factor from FP as a goodness of fit parameter. With this work, we established the basis for more such studies to dig into structural and magnetic properties of thin films.

Initial characterization of the film was performed using TEM and electron diffraction measurements. The LSMO film thickness is determined to be 40.9 nm. The quality of the epitaxy was found to be very good with layer by layer growth of the film along perpendicular to the surface. This confirms that it is possible to grow such films on Si substrates, which are a usual request in semiconductor industry.

XRD experiments revealed that there is presence of IP 4-fold symmetry and the unit cell is body-centered. Structural refinement process showed that the nuclear structure of the film follows $I4/m$ nuclear space group symmetry. From magnetic measurements, we found that the film undergoes a magnetic transition from paramagnetic to magnetically ordered phase below 260 K. Innovative magnetic structure refinement strategy using a combination of SQUID and ND established that the film is completely FM in nature and the magnetic moment was found to be (3.5 0 0.3) μ_B.

In comparison to bulk LSMO, the nuclear structure changes from $R\bar{3}c$ to $I4/m$, with origin in the strain imposed by the STO layer. Due to tensile IP strain from STO, the OOP lattice constant of LSMO is contracted (3.85 Å) as compared to bulk (3.88 Å). This results in a tetragonal shaped unit cell for the film. Based on the length of the lattice parameters, one can also expect that the $3d_{x^2-y^2}$ orbital is preferentially occupied over $3d_{z^2}$ in Mn^{3+}. Magnetically, the T_c value of the film is lower than the bulk (370 K). It is reported by several studies that the T_c of these films depends on film thickness and synthesis parameters [16, 19, 124]. So there is possibility to further optimize it for a value above RT. Furthermore, the bulk LSMO crystals contain FM ordering with [111] as the easy-axis. For the film, we have established that the moments prefer to be largely IP with a small OOP component. This behavior is possibly caused by magnetostatic anisotropy. Ideally, the magnetostatic anisotropy in thin films would require the moments to be completely IP, however the thickness of the film plays a role as well. We have obtained a small OOP component for this 40.9 nm thick film and it is possible that at smaller thicknesses, where surface effects are more prominent, the moments have zero OOP component. Interestingly, the ultra thin films of thickness less than 3 nm contain phases of both FM and AFM orderings. From this, we conclude that at such thickness (40.9 nm) the symmetry constraints from STO start to relax, with IP lattice parameters still frozen at constrained values. One may anticipate that at a somewhat smaller thickness, we can have FM films with fully IP magnetic moments. The exact knowledge of the magnetic moment configuration is crucial to actively harness these materials for various applications such as data storage. Thus, through magnetic structure determination, this study

allows considerable insights into the possible ways of utilizing these materials in spin-based devices.

The crystal structure and magnetic properties of the 3-3 super-lattice sample were investigated using XRD, SQUID and ND. The experimental methods in this work were complemented by DFT calculations for efficient analysis. XRD measurements showed that the super-lattice layers are of very good quality. No signs of strain relaxation were observed, which confirmed that the strain is maintained throughout the structure, courtesy of intercalation of BTO layers. Unfortunately, the presence of crystallites in this sample denied proper data acquisition for structural refinement. The comparative analysis of ND data with DFT calculations revealed a discrepancy between the two. One of the DFT optimized geometry with $P\bar{4}$ nuclear space group showed a decent initial fit with the ND data. However, through further analysis of the experimental data, we encountered variations in the widths of different layers. We attribute this difference to the La/Sr disorder and the possibility of defects such as stacking faults in the sample. This type of intricacies cannot be implemented easily in DFT optimizations. Through ND nuclear fitting and comparison of XRD (0 0 ℓ) scan with other samples, we also established that the middle LSMO layer on this sample is contracted. Although the exact geometry is not compatible with DFT, this phenomenon is in-agreement qualitatively with the DFT optimizations (also hypothesized by A. Sadoc et al. based on the DFT results [28]).

Magnetically, the sample showed characteristics of AFM ordering. However, the possibility of an incommensurate magnetic structure is not completely ruled out. No residual magnetization was observed along any of the 3 measured directions ([100], [110] and [001]). The [100] curve showed characteristics of a spin-flop type magnetic transition, making it the easy-axis of magnetization. A set of possible magnetic models was derived from these measurements that can be verified with the help of ND experiments.

Our exploratory study of the 3-3 sample has provided valuable insights. We successfully elucidated critical details concerning the sample's crystal structure and magnetic ordering. While our findings may not yield conclusive outcomes, they undeniably contribute significantly to the understanding of this sample's behavior. These findings include but not limited to, determination of the easy-axis of magnetization and critical details about the widths of different layers in the structure that can have direct effect on the orbital ordering and hence, magnetic properties. Furthermore, this study underscores the potential of analyzing diffraction results with theoretical calculations as powerful strategy for probing and unraveling intricate properties of materials in this category.

Future work on this sample can be dedicated to answering the questions related to alignment of magnetic moments. A plan is proposed in the thesis to further investigate the magnetic structure of the sample using ND.

The other 2 samples involved in this category were 3-2 and 2-3. The objective behind inspecting these samples was to observe their magnetic properties in comparison with the 3-3 and LSMO film, and provide structural insights as well. Let us first review the results of structural characterization. XRD measurements on the

3-2 sample showed some promising results. From the (0 0 ℓ) scan, the periodicity of the well-stacked layers of $(LSMO)_3(BTO)_2$ was confirmed. The presence of satellite peaks very close to $\ell = 5n \pm 1$ (n is an integer) was confirmed and the resolution was not enough to conclusively comment on any incommensurability in the nuclear structure due to stacking faults. An effort to obtain more information about the crystal structure via 2D OOP scans revealed some unidentified peaks, which we attribute to the presence of multiple crystallites in the sample. As a consequence, the full nuclear structure refinement using XRD was not possible.

ND measurements recorded intensity only for reflections with $\ell = 5n$, n is an integer. We did not observe any intensity on the rest of the reflections. Since XRD (0 0 ℓ) scan showed these other peaks with some intensity, we interpret that in ND the intensity is too weak for reflections other than $\ell = 5n$. We hypothesize that since these "satellite" peaks were observed on the 3-3 sample with ND, removing a BTO layer clearly has an impact on layers' widths such that the structure factor is too small in the 3-2 sample. The exact nature of this impact is not known at present. However, we suspect that the distortion among different layer widths in 3-2 is not as pronounced as the 3-3 structure. This can be caused by the fact that 3-2 has only 2 layers of BTO, which keep the system somewhat "locked" as in not allowing distortions. We attempted to resolve the structure of 2-3 sample as well and found similar characteristics as 3-2; only the reflections with ℓ multiple of 5 showed intensity. Therefore, we come to the conclusion that both 3-2 and 2-3 structures are not distorted enough in terms of layer widths as compared to 3-3, possibly due to increased constraints as a result of only 2 layers of BTO or LSMO, instead of 3.

Conclusion on all the samples

The macroscopic magnetic behavior of all the samples was studied in-detail. We have shown that the strain can be used as a tool to alter the magnetic properties of this type of materials. We established the magnetic structure of the LSMO film to be completely FM in nature. In addition, the film showed signs of strain relaxation in the diffraction measurements. At low thickness of less than 3 nm, where FM and AFM phases co-exist, the strain from the substrate is still maintained and there is no relaxation. We found a way to keep this strain sustained over the whole structure. This was done by intercalating layers of BTO after every few layers of LSMO, helping in preventing strain relaxation. Through diffraction, we verified that this, in fact, is true and no relaxation was observed on the super-lattice samples. As a consequence of this strain maintenance, these samples showed hysteresis curves typical of AFM ordering. In addition, the easy-axis of magnetization are believed to be IP for the 3-3 and 2-3 samples. In particular, the 3-3 sample is anticipated to be a potential spintronic candidate, as a very high magnetic transition temperature along with AFM ordering is the demand for the next generation of devices.

In addition to the successful results of the diffraction measurements, it is also important to mention the range of such measurements. From this study, we were also able to reveal the limitations in terms of what's possible with such diffraction measurements. The first and foremost requirement is that the quality of epitaxy with

respect to the substrate should be reasonable enough to locate the diffraction peaks of the film. In addition, for XRD, the overall sample must be of very good quality as well. As shown for the super-lattice samples, presence of crystallites limits the amount of obtainable information considerably. Moreover in ND, there are limitations in terms of measurable number of peaks in a given beamtime. Furthermore, if the peak intensity are not strong enough, one may not be able to integrate them as seen for 3-2 and 2-3 samples.

Prospective work

The nature of magnetic ordering in super-lattice samples was established using macroscopic magnetic measurements, however the question that remains unanswered is the exact arrangement of moments inside these systems. For the 3-3 sample, the proposed plan to resolve the magnetic structure is the next step. The set of identified reflections to be measured will provide us clarity on whether there is long range AFM ordering in the sample. In terms of crystal structure of this sample, we have given details on the widths of different layers. However, the crude layer width analysis and the "refined" geometries do not agree well with the DFT optimized ones. So far the La/Sr disorder in DFT calculations was taken into account by generating all possible configurations in the doubled cell and optimizing them individually. It would be interesting, although challenging, to test a Monte Carlo sampling of the different configurations in a bigger unit cell.

In addition, measuring high resolution (0 0 ℓ) scans using XRD can be very useful in determining whether there is any nuclear incommensurability due to stacking faults in different 3-3 samples. We attribute stacking faults to the differences observed in the macroscopic magnetic properties of the 3-3 samples (comparison with results from A. Sadoc et al.). Therefore, these scans can provide insights into the impact of possible stacking faults on the different analyzed samples.

Based on the results of 3-3, it will be interesting to attempt a similar kind of strategy for the 3-2 and 2-3 samples to resolve their magnetic structure completely. In addition, it can also be good test for the D10+ instrument to try and measure the 3-2 and 2-3 satellite peaks, which were not observed on D10. Furthermore, the intensity of satellite peaks on XRD (0 0 ℓ) scans can be measured with better statistics in order to also analyze the layer width hypothesis presented earlier.

Furthermore, since BTO is a ferroelectric compound, it will be interesting to investigate the presence of multiferroic nature in these super-lattices. Multiferroic materials show more than one type of ferroic ordering (electric and magnetic in this case) and in some cases the origin of these orderings is coupled, which can be utilized in many technological devices such as magnetic storage and magnetoelectric sensors.

Another interesting sample related to the super-lattices is combination of $La_{0.7}Ca_{0.3}MnO_3$/BTO layers that has also shown magnetism up to 1000 K [28]. An additional difficulty for this sample will be in terms of performing DFT calculations. This is because the size of Ca cations is very different from La ones and hence, the approximations taken for effective potential in DFT will not work. Nevertheless, it can be possible to perform XRD measurements first and investigate the effect of Ca cation on the width of different layers.

In terms of diffraction, the commissioning of D10+ provide a boost to such studies owing to the increase in incident flux on the instrument. This is a very suitable diffractometer for thin film studies and with the successful measurements on LSMO and super-lattices, we expect its increased utilization for similar investigations.

In broader perspective, this study helped us to understand and control the magnetic behavior of LSMO films using strain imposition. Therefore, providing a possibility of designing thin film structures with unique physical properties. By precisely creating this kind of artificial structures, they can be tailored for various kinds of applications. Though, the aim of integrating these materials into devices requires further inspection in terms of practical issues, we provide a fundamental idea that epitaxial strain can bring exciting properties into play, that will be useful in engineering materials for spintronic applications.

Bibliography

[1] Tomas Jungwirth et al. "Antiferromagnetic spintronics". In: *Nature nanotechnology* 11.3 (2016), pp. 231–241.

[2] Vincent Baltz et al. "Antiferromagnetic spintronics". In: *Reviews of Modern Physics* 90.1 (2018), p. 015005.

[3] EV Gomonay and VM Loktev. "Spintronics of antiferromagnetic systems". In: *Low Temperature Physics* 40.1 (2014), pp. 17–35.

[4] Sebastian Loth et al. "Bistability in atomic-scale antiferromagnets". In: *Science* 335.6065 (2012), pp. 196–199.

[5] Manfred Fiebig et al. "Ultrafast magnetization dynamics of antiferromagnetic compounds". In: *Journal of Physics D: Applied Physics* 41.16 (2008), p. 164005.

[6] Surendra Singh. "Neutron Reflectometry: a technique for revealing emergent phenomena at interfaces in heterostructures". In: *arXiv preprint arXiv:2303.13028* (2023).

[7] Boris P Toperverg and Hartmut Zabel. "Neutron scattering in nanomagnetism". In: *Experimental Methods in the Physical Sciences*. Vol. 48. Elsevier, 2015, pp. 339–434.

[8] M Sawicki, W Stefanowicz, and A Ney. "Sensitive SQUID magnetometry for studying nanomagnetism". In: *Semiconductor Science and Technology* 26.6 (2011).

[9] *Quantum design mpms multivu application user's manual (2001).*

[10] J Lindner and K Baberschke. "In situ ferromagnetic resonance: an ultimate tool to investigate the coupling in ultrathin magnetic films". In: *Journal of Physics: Condensed Matter* 15.4 (2003), R193.

[11] ZQ Qiu and Samuel D Bader. "Surface magneto-optic Kerr effect". In: *Review of Scientific Instruments* 71.3 (2000), pp. 1243–1255.

[12] Anthony Kevin Cheetham and Angus Paul Wilkinson. "Synchrotron X-ray and Neutron Diffraction Studies in Solid-State Chemistry". In: *Angewandte Chemie International Edition in English* 31.12 (1992), pp. 1557–1570.

[13] Maxim V Petoukhov and Dmitri I Svergun. "Analysis of X-ray and neutron scattering from biomacromolecular solutions". In: *Current opinion in structural biology* 17.5 (2007), pp. 562–571.

[14] George Edward Bacon and K Lonsdale. "Neutron diffraction". In: *Reports on Progress in Physics* 16.1 (1953), p. 1.

[15] Nancy L Ross and Christina Hoffmann. "Single-crystal neutron diffraction: present and future applications". In: *Reviews in mineralogy and geochemistry* 63.1 (2006), pp. 59–80.

[16] M. Huijben et al. "Critical thickness and orbital ordering in ultrathin $La_{0.7}Sr_{0.3}MnO_3$ films". In: *Phys. Rev. B* 78 (9 2008), p. 094413.

[17] A. Urushibara et al. "Insulator-metal transition and giant magnetoresistance in $La_{1-x}Sr_xMnO_3$". In: *Phys. Rev. B* 51 (20 1995), pp. 14103–14109.

[18] Hongyan Chen et al. "Thickness-driven first-order phase transitions in manganite ultrathin films". In: *Phys. Rev. B* 99 (21 2019), p. 214419.

[19] Shalini Kumari et al. "Effects of Oxygen Modification on the Structural and Magnetic Properties of Highly Epitaxial La0.7Sr0.3MnO3 (LSMO) thin films". In: *Scientific Reports* 10 (1 2020), p. 3659.

[20] R. Herger et al. "Structure determination of monolayer-by-monolayer grown $La_{1-x}Sr_xMnO_3$ thin films and the onset of magnetoresistance". In: *Phys. Rev. B* 77 (8 2008), p. 085401.

[21] M.A. Kouacou et al. "Magnetic and Transport Properties of Half-Metallic Ferromagnetic Compounds as the La0.7Sr0.3MnO3 Epitaxial Manganite Oxide Thin Films". In: *Journal of Applied Sciences* 8 (2008), pp. 4624–4630.

[22] P Wadley et al. "Antiferromagnetic structure in tetragonal CuMnAs thin films". In: *Scientific reports* 5.1 (2015), p. 17079.

[23] Kenta Shimamoto et al. "Tuning the multiferroic mechanisms of TbMnO3 by epitaxial strain". In: *Scientific Reports* 7.1 (2017), p. 44753.

[24] R Ibarra et al. "Noncollinear magnetic order in epitaxial thin films of the centrosymmetric MnPtGa hard magnet". In: *Applied Physics Letters* 120.17 (2022).

[25] Lina Chen et al. "Surface and interface properties of $La_{2/3}Sr_{1/3}MnO_3$ thin films on $SrTiO_3$ (001)". In: *Phys. Rev. Mater.* 3 (4 2019), p. 044407.

[26] A. Tebano et al. "Evidence of Orbital Reconstruction at Interfaces in Ultrathin $La_{0.67}Sr_{0.33}MnO_3$ Films". In: *Phys. Rev. Lett.* 100 (13 2008), p. 137401.

[27] R. Herger et al. "Structure determination of monolayer-by-monolayer grown $La_{1-x}Sr_xMnO_3$ thin films and the onset of magnetoresistance". In: *Phys. Rev. B* 77 (8 2008), p. 085401.

[28] Aymeric Sadoc et al. "Large Increase of the Curie Temperature by Orbital Ordering Control". In: *Physical Review Letters* 104.4 (2010).

[29] P. Murugavel and W. Prellier. "The magnetotransport properties of La0.7Sr0.3MnO3/BaTiO3 superlattices grown by pulsed laser deposition technique". In: *Journal of Applied Physics* 100.2 (2006), p. 023520.

[30] Xuan Shen et al. “Strain effects on magnetic characteristics of ultrathin La0.7Sr0.3MnO3 in epitaxial La0.7Sr0.3MnO3/BaTiO3 superlattices”. In: *Journal of Applied Physics* 112.12 (2012), p. 123919.

[31] Fei Zhang et al. “Increased Curie Temperature Induced by Orbital Ordering in La0.67Sr0.33MnO3/BaTiO3 Superlattices”. In: *Nanoscale Research Letters* 13.24 (2018).

[32] Y Suzuki et al. “The role of strain in magnetic anisotropy of manganite thin films”. In: *Applied Physics Letters* 71.1 (1997), pp. 140–142.

[33] H Guo et al. “Growth of epitaxial thin films of the ordered double perovskite La2NiMnO6 on different substrates”. In: *Applied physics letters* 89.2 (2006).

[34] T Roch et al. “Substrate dependent epitaxy of superconducting niobium nitride thin films grown by pulsed laser deposition”. In: *Applied Surface Science* 551 (2021), p. 149333.

[35] RA Rao et al. “Three-dimensional strain states and crystallographic domain structures of epitaxial colossal magnetoresistive La 0.8 Ca 0.2 MnO 3 thin films”. In: *Applied physics letters* 73.22 (1998), pp. 3294–3296.

[36] Hua Ma et al. “Strain effects and thickness dependence of ferroelectric properties in epitaxial BiFeO3 thin films”. In: *Applied Physics Letters* 92.18 (2008).

[37] Ping Sheng, Baomin Wang, and Runwei Li. “Flexible magnetic thin films and devices”. In: *Journal of Semiconductors* 39.1 (2018), p. 011006.

[38] MC Rao and MS Shekhawat. “A brief survey on basic properties of thin films for device application”. In: *International Journal of Modern Physics: Conference Series*. Vol. 22. World Scientific. 2013, pp. 576–582.

[39] Gunther Scheunert et al. “A review of high magnetic moment thin films for microscale and nanotechnology applications”. In: *Applied Physics Reviews* 3.1 (2016).

[40] James M Rondinelli, Steven J May, and John W Freeland. “Control of octahedral connectivity in perovskite oxide heterostructures: An emerging route to multifunctional materials discovery”. In: *MRS bulletin* 37.3 (2012), pp. 261–270.

[41] Anand Bhattacharya and Steven J May. “Magnetic oxide heterostructures”. In: *Annual Review of Materials Research* 44 (2014), pp. 65–90.

[42] Darrell G Schlom et al. “Strain tuning of ferroelectric thin films”. In: *Annu. Rev. Mater. Res.* 37 (2007), pp. 589–626.

[43] Mercy Mathews et al. “Step-induced uniaxial magnetic anisotropy of La: 67Sr: 33MnO3 thin films”. In: *Applied Physics Letters* 87.24 (2005).

[44] Hans Boschker et al. “Magnetic anisotropy and magnetization reversal of La0. 67Sr0. 33MnO3 thin films on SrTiO3 (110)”. In: *Journal of Applied Physics* 108.10 (2010).

[45] Hans Boschker et al. "Uniaxial contribution to the magnetic anisotropy of La0. 67Sr0. 33MnO3 thin films induced by orthorhombic crystal structure". In: *Journal of magnetism and magnetic materials* 323.21 (2011), pp. 2632–2638.

[46] Sandeep Kumar Chaluvadi et al. "Epitaxial strain and thickness dependent structural, electrical and magnetic properties of La0. 67Sr0. 33MnO3 films". In: *Journal of Physics D: Applied Physics* 53.37 (2020), p. 375005.

[47] Baomin Wang et al. "Oxygen-driven anisotropic transport in ultra-thin manganite films". In: *Nature communications* 4.1 (2013), p. 2778.

[48] C Adamo et al. "Effect of biaxial strain on the electrical and magnetic properties of (001) La0. 7Sr0. 3MnO3 thin films". In: *Applied physics letters* 95.11 (2009).

[49] S. Blundell. *Magnetism in Condensed Matter*. Oxford Master Series in Condensed Matter Physics. OUP Oxford, 2001. ISBN: 9780198505914. URL: `https://books.google.fr/books?id=0GhGmgEACAAJ`.

[50] Stephen J. Blundell. "Concepts in Magnetism". In: *Magnetism and Accelerator-Based Light Sources*. Cham: Springer International Publishing, 2021, pp. 39–62.

[51] Abhijit Biswas, Ki-Seok Kim, and Yoon Jeong. "Metal-Insulator Transitions and non-Fermi Liquid Behaviors in 5d Perovskite Iridates". In: (Aug. 2015).

[52] John B. Goodenough. "Theory of the Role of Covalence in the Perovskite-Type Manganites $[\mathrm{La}, M(\mathrm{II})]\mathrm{MnO}_3$". In: *Phys. Rev.* 100 (2 1955), pp. 564–573.

[53] Junjiro Kanamori. "Superexchange interaction and symmetry properties of electron orbitals". In: *Journal of Physics and Chemistry of Solids* 10.2-3 (1959), pp. 87–98.

[54] Philip W Anderson. "Antiferromagnetism. Theory of superexchange interaction". In: *Physical Review* 79.2 (1950), p. 350.

[55] Matthias Opel. "Spintronic oxides grown by laser-MBE". In: *Journal of physics D: Applied physics* 45.3 (2011), p. 033001.

[56] Sam Mugiraneza and Alannah M Hallas. "Tutorial: a beginner's guide to interpreting magnetic susceptibility data with the Curie-Weiss law". In: *Communications Physics* 5.1 (2022), p. 95.

[57] Kotarô Honda, Seisi Kaya, and Yosio Masuyama. "On the magnetic properties of single crystals of iron". In: *Nature* 117.2952 (1926), pp. 753–754.

[58] S Kaya. "On the magnetisation of single crystals of cobalt". In: *Sci. Rep. Tohoku Imp. Univ.* 17 (1928), p. 1157.

[59] D. S. Chuang, C. A. Ballentine, and R. C. O'Handley. "Surface and step magnetic anisotropy". In: *Phys. Rev. B* 49 (21 1994), pp. 15084–15095.

[60] Deviderjit Singh Sivia. *Elementary scattering theory: for X-ray and neutron users*. Oxford University Press, 2011.

[61] John C Lindon, George E Tranter, and David Koppenaal. *Encyclopedia of spectroscopy and spectrometry*. Academic Press, 2016.

[62] BERTAUT, E. F. "MAGNETIC STRUCTURE ANALYSIS AND GROUP THEORY". In: *J. Phys. Colloques* 32 (1971), pp. C1-462-C1–470.

[63] Rodrıéguez-Carvajal, J. and Bourée, F. "Symmetry and magnetic structures". In: *EPJ Web of Conferences* 22 (2012), p. 00010.

[64] Juan Rodríguez-Carvajal. In: *Physica B: Condensed Matter* 192 (1993), pp. 55–69.

[65] P. Debye. "Interferenz von Röntgenstrahlen und Wärmebewegung". In: *Annalen der Physik* 348.1 (1913), pp. 49–92.

[66] M. J. Buerger and Gilbert E. Klein. "Correction of X-Ray Diffraction Intensities for Lorentz and Polarization Factors". In: *Journal of Applied Physics* 16 (2004), pp. 408–418.

[67] B. D. Cullity. *Elements of x-ray diffraction*. Addison-Wesley Publishing Company, Inc., 1978. ISBN: 9780201011746.

[68] G. J. McIntyre and R. F. D. Stansfield. "A general Lorentz correction for single-crystal diffractometers". In: *Acta Crystallographica Section A* 44 (1988), pp. 257–262.

[69] W. R. Busing and H. A. Levy. "Angle calculations for 3- and 4-circle X-ray and neutron diffractometers". In: *Acta Crystallographica* 22 (1967), pp. 457–464.

[70] P. Hohenberg and W. Kohn. "Inhomogeneous Electron Gas". In: *Phys. Rev.* 136 (3B 1964), B864–B871.

[71] W. Kohn and L. J. Sham. "Self-Consistent Equations Including Exchange and Correlation Effects". In: *Phys. Rev.* 140 (4A 1965), A1133–A1138.

[72] Zhigang Wu and R. E. Cohen. "More accurate generalized gradient approximation for solids". In: *Phys. Rev. B* 73 (23 2006), p. 235116.

[73] S. Kobayashi. "X-ray thin-film measurement techniques". In: *Rigaku journal* 26 (2010).

[74] T. Mitsunaga. "X-ray thin-film measurement techniques". In: *Rigaku journal* 25 (2009).

[75] URL: `https://www.ill.eu/users/instruments/instruments-list/d10/description/instrument-layout`.

[76] John Clarke. "SQUIDs". In: *Scientific American* 271.2 (1994).

[77] URL: `https://crismat.cnrs.fr/synthese--conventionnelle/conventionnelle/`.

[78] Lecture notes from Pascal Turban, Univ. Rennes 1.

[79] Baig M. et al. "Pulsed laser deposition of SmCo thin films for MEMS applications". In: *Journal of Applied Research and Technology* (2016).

[80] M.J. Madou. *Fundamentals of Microfabrication: The Science of Miniaturization, Second Edition (2nd ed.)* CRC Press, 2002. ISBN: 9781315274225.

[81] N Cotón et al. "Synthesis from separate oxide targets of high quality La2−xSrxCuO4 thin films and dependence with doping of their superconducting transition width". In: *Superconductor Science and Technology* 26.7 (2013), p. 075011.

[82] Eugene Katz. "Perovskite: Name Puzzle and German-Russian Odyssey of Discovery". In: *Helvetica Chimica Acta* 103 (2020).

[83] Gustav Rose. "Beschreibung einiger neuen Mineralien des Urals". In: *Annalen der Physik* 124.12 (1839), pp. 551–573.

[84] J. M. D. Coey, M. Viret, and S. von Molnár. "Mixed-valence manganites". In: *Advances in Physics* 48.2 (1999), pp. 167–293.

[85] Myron B. Salamon and Marcelo Jaime. "The physics of manganites: Structure and transport". In: *Rev. Mod. Phys.* 73 (3 2001), pp. 583–628.

[86] Yoshinori Tokura et al. In: *Journal of the Physical Society of Japan* 63 (1994), pp. 3931–3935.

[87] P. Schiffer et al. In: *Physical Review Letters* 75 (1995), p. 3336.

[88] A. Urushibara et al. In: *Phys. Rev. B* 51 (1995), pp. 14103–14109.

[89] G.H. Jonker and J.H. Van Santen. "Ferromagnetic compounds of manganese with perovskite structure". In: *Physica* 16.3 (1950), pp. 337–349.

[90] J.H. Van Santen and G.H. Jonker. "Electrical conductivity of ferromagnetic compounds of manganese with perovskite structure". In: *Physica* 16.7 (1950), pp. 599–600.

[91] G.H. Jonker. "Magnetic compounds with perovskite structure IV Conducting and non-conducting compounds". In: *Physica* 22.6 (1956), pp. 707–722.

[92] C. W. Searle and S. T. Wang. "Studies of the ionic ferromagnet (LaPb)MnO3 III. Ferromagnetic resonance studies". In: *Canadian Journal of Physics* 47.23 (1969), pp. 2703–2708.

[93] C. W. Searle and S. T. Wang. "Studies of the ionic ferromagnet (LaPb)MnO3. V. Electric transport and ferromagnetic properties". In: *Canadian Journal of Physics* 48.17 (1970), pp. 2023–2031.

[94] A. H. Morrish et al. "Studies of the ionic ferromagnet (LaPb)MnO3 I. Growth and characteristics of single crystals". In: *Canadian Journal of Physics* 47.23 (1969), pp. 2691–2696.

[95] E. O. Wollan and W. C. Koehler. "Neutron Diffraction Study of the Magnetic Properties of the Series of Perovskite-Type Compounds $[(1-x)\mathrm{La}, x\mathrm{Ca}]\mathrm{MnO_3}$". In: *Phys. Rev.* 100 (2 1955), pp. 545–563.

[96] J. Volger. "Further experimental investigations on some ferromagnetic oxidic compounds of manganese with perovskite structure". In: *Physica* 20.1 (1954), pp. 49–66.

[97] A. Asamitsu et al. “A structural phase transition induced by an external magnetic field”. In: *Nature* 373 (1995), pp. 407–409.

[98] M. Viret et al. “Low-field colossal magnetoresistance in manganite tunnel spin valves”. In: *Europhysics Letters* 39.5 (1997), p. 545.

[99] H. Béa et al. “Tunnel magnetoresistance and robust room temperature exchange bias with multiferroic BiFeO3 epitaxial thin films”. In: *Applied Physics Letters* 89.24 (2006), p. 242114.

[100] Tapan Chatterji et al. “Orbital order–disorder transition in La1−xBaxMnO3 in the low-doping region”. In: *Solid State Communications* 131.2 (2004), pp. 75–80.

[101] J. Hemberger et al. “Structural, magnetic, and electrical properties of single-crystalline $La_{1-x}Sr_xMnO_3$ ($0.4 < x < 0.85$)”. In: *Phys. Rev. B* 66 (9 2002), p. 094410.

[102] M Paraskevopoulos et al. “Magnetic properties and the phase diagram of La1-xSrxMnO3 for x$\leq$ 0.2”. In: *Journal of Physics: Condensed Matter* 12.17 (2000), p. 3993.

[103] Masato Kubota et al. “Magnetic and electronic properties of (LaMnO3)5(SrMnO3)5 superlattice revealed by resonant soft X-ray scattering”. In: *Japanese Journal of Applied Physics* 53.5S1 (2014), 05FH07.

[104] Tapan Chatterji et al. “Jahn-Teller transition in $La_{1-x}Sr_xMnO_3$ in the low-doping region ($0lt; xlt;\ 0.1$)”. In: *Phys. Rev. B* 66 (5 2002), p. 054403.

[105] X. Xiong et al. “Correlation between coherent Jahn-Teller distortion and magnetic spin orientation in $La_{1-x}Sr_xMnO_3$”. In: *Phys. Rev. B* 60 (14 1999), pp. 10186–10192.

[106] Navid Qureshi. “*Mag2Pol*: a program for the analysis of spherical neutron polarimetry, flipping ratio and integrated intensity data”. In: *Journal of Applied Crystallography* 52 (2019), pp. 175–185.

[107] S J Hibble et al. “Local distortions in the colossal magnetoresistive manganates La0.70Ca0.30MnO3, La0.80Ca0.20MnO3 and La0.70Sr0.30MnO3 revealed by total neutron diffraction”. In: *Journal of Physics: Condensed Matter* 11.47 (1999), p. 9221.

[108] M Konoto et al. “Magnetic domain structure of a La 0.7 Sr 0.3 MnO 3 (001) surface observed by a spin-polarized scanning electron microscope”. In: *Applied physics letters* 84.13 (2004), pp. 2361–2363.

[109] Hongyan Chen et al. In: *Phys. Rev. B* 99 (21 2019), p. 214419.

[110] Clarence Zener. In: *Phys. Rev.* 82 (1951), pp. 403–405.

[111] Sayani Majumdar and Sebastiaan van Dijken. “Pulsed laser deposition of La1−xSrxMnO3: thin-film properties and spintronic applications”. In: *Journal of Physics D: Applied Physics* 47.3 (2013), p. 034010.

[112] J.-H Park et al. In: *NATURE* 392 (1998), pp. 794–796.

[113] Jose Maria De Teresa et al. In: *Science (New York, N.Y.)* 286 (1999), pp. 507–509.

[114] Ayan Ray et al. "Growth and optical properties of La0.7Sr0.3MnO3/ZnO heterojunctions". In: *2009 2nd International Workshop on Electron Devices and Semiconductor Technology* (2009), pp. 1–4.

[115] R. Bah et al. "Ferromagnetic resonance studies on colossal magnetoresistance films: Effects of homogeneity and light illumination". In: *Journal of Applied Physics* 99.8 (2006), 08Q312.

[116] Y. Suzuki et al. "The role of strain in magnetic anisotropy of manganite thin films". In: *Applied Physics Letters* 71.1 (1997), pp. 140–142.

[117] Belmeguenai et al. "La0.7Sr0.3MnO3 thin films on SrTiO3 and CaTiO3 buffered Si substrates: structural, static, and dynamic magnetic properties". In: 13 (2010), p. 5669.

[118] Darrell G. Schlom et al. "Strain Tuning of Ferroelectric Thin Films". In: *Annual Review of Materials Research* 37.1 (2007), pp. 589–626.

[119] K. Tsuda and M. Tanaka. "Refinement of crystal structure parameters using convergent-beam electron diffraction: the low-temperature phase of $SrTiO_3$". In: *Acta Crystallographica Section A* 51.1 (1995), pp. 7–19.

[120] Charles M. Culbertson et al. "Neutron Total Scattering Studies of Group II Titanates (ATiO3, A2+ = Mg, Ca, Sr, Ba)". In: *Scientific Reports* 10 (2020), pp. 2045–2322.

[121] Tetsuya Uemura et al. "Magnetic and Electrical Properties of (La,Sr)MnO3 Sputtered on SrTiO3-Buffered Si Substrate". In: *Japanese Journal of Applied Physics* 44.4B (2005), pp. 2604–2607.

[122] José Manuel Vila-Fungueiriño et al. "Epitaxial La0.7Sr0.3MnO3 thin films on silicon with excellent magnetic and electric properties by combining physical and chemical methods". In: *Science and Technology of Advanced Materials* 19.1 (2018), pp. 702–710.

[123] L. Méchin et al. "Epitaxial La0.7Sr0.3MnO3 thin films grown on SrTiO3 buffered silicon substrates by reactive molecular-beam epitaxy". In: *physica status solidi (a)* 209.6 (2012), pp. 1090–1095.

[124] A. K. Pradhan et al. "Magnetic properties of La0.6Sr0.4MnO3 thin films on SrTiO3 and buffered Si substrates with varying thickness". In: *Journal of Applied Physics* 103.2 (2008), p. 023914.

[125] Marie-Bernadette Lepetit, Bernard Mercey, and Charles Simon. "Interface Effects in Perovskite Thin Films". In: *Physical Review Letters* 108.8 (Feb. 2012).

[126] URL: `https://physics.nist.gov/PhysRefData/XrayMassCoef/tab3.html`.

[127] URL: `https://henke.lbl.gov/optical_constants/atten2.html`.

[128] H. M. Rietveld. "A profile refinement method for nuclear and magnetic structures". In: *Journal of Applied Crystallography* 2 (1969), pp. 65–71.

[129] Juan Rodríguez-Carvajal. "FullProf: A Program for Rietveld Refinement and Profile Matching Analysis of Complex Powder Diffraction Patterns (ILL, unpublished)". In: ().

[130] Koichi Momma and Fujio Izumi. "*VESTA*: a three-dimensional visualization system for electronic and structural analysis". In: *Journal of Applied Crystallography* 41.3 (2008), pp. 653–658.

[131] James G Moberly, Matthew T Bernards, and Kristopher V Waynant. "Key features and updates for origin 2018". In: *Journal of Cheminformatics* 10 (2018), pp. 1–2.

[132] Z. Yang et al. "Growth and structure investigation of multiferroic superlattices: [(La0.8Sr0.2MnO3)4n/(BaTiO3)3n]m". In: *Solid State Communications* 150.31 (2010), pp. 1432–1435.

[133] Yali Xie et al. "Strain induced tunable anisotropic magnetoresistance in La0.67Ca0.33MnO3/BaTiO3 heterostructures". In: *Journal of Applied Physics* 113.17 (2013), p. 17C716.

[134] A. Alberca et al. "Magnetoelastic coupling in $La_{0.7}Ca_{0.3}MnO_3/BaTiO_3$ ultrathin films". In: *Phys. Rev. B* 88 (13 2013), p. 134410.

[135] P. Murugavel et al. "The role of ferroelectric-ferromagnetic layers on the properties of superlattice-based multiferroics". In: *Journal of Applied Physics* 97.10 (2005), p. 103914.

[136] Sarbeswar Sahoo et al. "Ferroelectric control of magnetism in $BaTiO_3$/Fe heterostructures via interface strain coupling". In: *Phys. Rev. B* 76 (9 2007), p. 092108.

[137] H. F. Tian et al. "Strain induced magnetoelectric coupling between magnetite and BaTiO3". In: *Applied Physics Letters* 92.6 (2008), p. 063507.

[138] S. Cao et al. "Magnetoelectric coupling at the EuO/BaTiO3 interface". In: *Applied Physics Letters* 102.17 (2013), p. 172402.

[139] Hangwen Guo et al. "Interface-induced multiferroism by design in complex oxide superlattices". In: *Proceedings of the National Academy of Sciences* 114.26 (2017), E5062–E5069.

[140] Srinivasa Rao Singamaneni et al. "Magnetic properties of BaTiO3/La0.7Sr0.3MnO3 thin films integrated on Si(100)". In: *Journal of Applied Physics* 116.22 (2014), p. 224104.

[141] Rui Guo et al. "Interface-engineered electron and hole tunneling". In: *Science Advances* 7 (2021).

[142] Aysegül Begüm Koçak et al. "Control of the orbital ordering in manganite superlattices and impact on properties". In: *Physical Review B* 96.12 (2017), p. 125155.

[143] H. Lu et al. "Electric modulation of magnetization at the BaTiO3/La0.67Sr0.33MnO3 interfaces". In: *Applied Physics Letters* 100.23 (2012), p. 232904.

[144] Charles M Culbertson et al. "Neutron Total Scattering Studies of Group II Titanates (ATiO3, A2+ = Mg, Ca, Sr, Ba)". In: *Scientific Reports* 10 (2020).

[145] B. Wagué et al. "Structural studies of epitaxial BaTiO3 thin film on silicon". In: *Thin Solid Films* 693 (2020), p. 137636.

[146] Aysegül Begüm Koçak. "New theoretical concepts for designing oxide interfaces with exoticproperties for electronics and spintronics". Theses. Université Grenoble Alpes ; Université de Liège, 2017. URL: https://theses.hal.science/tel-01687743.

[147] Roberto Dovesi et al. "Quantum-mechanical condensed matter simulations with CRYSTAL". In: *WIREs Computational Molecular Science* 8.4 (2018).

[148] MPMS Application Note 1014-210B. *Oxygen contamination SQUID MPMS*. http://www.cmag.si/QD-OxygenContamination.pdf.

[149] Yu.A. Freiman and H.J. Jodl. "Solid oxygen". In: *Physics Reports* 401.1 (2004), pp. 1–228.

[150] P. A. Fleury, J. F. Scott, and J. M. Worlock. "Soft Phonon Modes and the 110°K Phase Transition in $SrTiO_3$". In: *Phys. Rev. Lett.* 21 (1 July 1968), pp. 16–19.

[151] URL: https://www.ncnr.nist.gov/resources/n-lengths.

[152] SJ Hibble et al. "Local distortions in the colossal magnetoresistive manganates La0. 70Ca0. 30MnO3, La0. 80Ca0. 20MnO3 and La0. 70Sr0. 30MnO3 revealed by total neutron diffraction". In: *Journal of Physics: Condensed Matter* 11.47 (1999), p. 9221.

[153] J Harada, T Pedersen, and Z Barnea. "X-ray and neutron diffraction study of tetragonal barium titanate". In: *Acta Crystallographica Section A: Crystal Physics, Diffraction, Theoretical and General Crystallography* 26.3 (1970), pp. 336–344.

[154] MA Hossain et al. "Interplay between intrinsic and stacking-fault magnetic domains in bi-layered manganites". In: *Applied Physics Letters* 101.13 (2012).

[155] J. Sort et al. "Role of stacking faults in the structural and magnetic properties of ball-milled cobalt". In: *Phys. Rev. B* 68 (1 July 2003), p. 014421.

[156] Keiji Doi et al. "Electronic and magnetic effects of a stacking fault in cobalt nanoscale islands on the Ag(111) surface". In: *Phys. Rev. B* 92 (6 Aug. 2015), p. 064421.